

Yingquan Peng  
Xinyong Dong *Editors*

# Proceedings of 2018 International Conference on Optoelectronics and Measurement

# Lecture Notes in Electrical Engineering

## Volume 567

### Series Editors

Leopoldo Angrisani, Department of Electrical and Information Technologies Engineering, University of Napoli Federico II, Naples, Italy

Marco Arteaga, Departament de Control y Robótica, Universidad Nacional Autónoma de México, Coyoacán, Mexico

Bijaya Ketan Panigrahi, Electrical Engineering, Indian Institute of Technology Delhi, New Delhi, Delhi, India  
Samarjit Chakraborty, Fakultät für Elektrotechnik und Informationstechnik, TU München, Munich, Germany

Jiming Chen, Zhejiang University, Hangzhou, Zhejiang, China

Shanben Chen, Materials Science and Engineering, Shanghai Jiao Tong University, Shanghai, China

Tan Kay Chen, Department of Electrical and Computer Engineering, National University of Singapore, Singapore, Singapore

Rüdiger Dillmann, Humanoids and Intelligent Systems Lab, Karlsruhe Institute for Technology, Karlsruhe, Baden-Württemberg, Germany

Haibin Duan, Beijing University of Aeronautics and Astronautics, Beijing, China

Gianluigi Ferrari, Università di Parma, Parma, Italy

Manuel Ferre, Centre for Automation and Robotics CAR (UPM-CSIC), Universidad Politécnica de Madrid, Madrid, Spain

Sandra Hirche, Department of Electrical Engineering and Information Science, Technische Universität München, Munich, Germany

Faryar Jabbari, Department of Mechanical and Aerospace Engineering, University of California, Irvine, CA, USA

Limin Jia, State Key Laboratory of Rail Traffic Control and Safety, Beijing Jiaotong University, Beijing, China

Janusz Kacprzyk, Systems Research Institute, Polish Academy of Sciences, Warsaw, Poland

Alaa Khamis, German University in Egypt El Tagamoa El Khames, New Cairo City, Egypt

Torsten Kroeger, Stanford University, Stanford, CA, USA

Qilian Liang, Department of Electrical Engineering, University of Texas at Arlington, Arlington, TX, USA

Ferran Martín, Departament d'Enginyeria Electrònica, Universitat Autònoma de Barcelona, Bellaterra, Barcelona, Spain

Tan Cher Ming, College of Engineering, Nanyang Technological University, Singapore, Singapore

Wolfgang Minker, Institute of Information Technology, University of Ulm, Ulm, Germany

Pradeep Misra, Department of Electrical Engineering, Wright State University, Dayton, OH, USA

Sebastian Möller, Quality and Usability Lab, TU Berlin, Berlin, Germany

Subhas Mukhopadhyay, School of Engineering & Advanced Technology, Massey University,

Palmerston North, Manawatu-Wanganui, New Zealand

Cun-Zheng Ning, Electrical Engineering, Arizona State University, Tempe, AZ, USA

Toyooki Nishida, Graduate School of Informatics, Kyoto University, Kyoto, Japan

Federica Pascucci, Dipartimento di Ingegneria, Università degli Studi "Roma Tre", Rome, Italy

Yong Qin, State Key Laboratory of Rail Traffic Control and Safety, Beijing Jiaotong University, Beijing, China

Gan Woon Seng, School of Electrical & Electronic Engineering, Nanyang Technological University, Singapore, Singapore

Joachim Speidel, Institute of Telecommunications, Universität Stuttgart, Stuttgart, Baden-Württemberg, Germany

Germano Veiga, Campus da FEUP, INESC Porto, Porto, Portugal

Haitao Wu, Academy of Opto-electronics, Chinese Academy of Sciences, Beijing, China

Junjie James Zhang, Charlotte, NC, USA

The book series *Lecture Notes in Electrical Engineering* (LNEE) publishes the latest developments in Electrical Engineering - quickly, informally and in high quality. While original research reported in proceedings and monographs has traditionally formed the core of LNEE, we also encourage authors to submit books devoted to supporting student education and professional training in the various fields and applications areas of electrical engineering. The series cover classical and emerging topics concerning:

- Communication Engineering, Information Theory and Networks
- Electronics Engineering and Microelectronics
- Signal, Image and Speech Processing
- Wireless and Mobile Communication
- Circuits and Systems
- Energy Systems, Power Electronics and Electrical Machines
- Electro-optical Engineering
- Instrumentation Engineering
- Avionics Engineering
- Control Systems
- Internet-of-Things and Cybersecurity
- Biomedical Devices, MEMS and NEMS

For general information about this book series, comments or suggestions, please contact [leontina.dicecco@springer.com](mailto:leontina.dicecco@springer.com).

To submit a proposal or request further information, please contact the Publishing Editor in your country:

#### **China**

Jasmine Dou, Associate Editor ([jasmine.dou@springer.com](mailto:jasmine.dou@springer.com))

#### **India**

Swati Meherishi, Executive Editor ([swati.meherishi@springer.com](mailto:swati.meherishi@springer.com))

Aninda Bose, Senior Editor ([aninda.bose@springer.com](mailto:aninda.bose@springer.com))

#### **Japan**

Takeyuki Yonezawa, Editorial Director ([takeyuki.yonezawa@springer.com](mailto:takeyuki.yonezawa@springer.com))

#### **South Korea**

Smith (Ahram) Chae, Editor ([smith.chae@springer.com](mailto:smith.chae@springer.com))

#### **Southeast Asia**

Ramesh Nath Premnath, Editor ([ramesh.premnath@springer.com](mailto:ramesh.premnath@springer.com))

#### **USA, Canada:**

Michael Luby, Senior Editor ([michael.luby@springer.com](mailto:michael.luby@springer.com))

#### **All other Countries:**

Leontina Di Cecco, Senior Editor ([leontina.dicecco@springer.com](mailto:leontina.dicecco@springer.com))

Christoph Baumann, Executive Editor ([christoph.baumann@springer.com](mailto:christoph.baumann@springer.com))

**\*\* Indexing: The books of this series are submitted to ISI Proceedings, EI-Compendex, SCOPUS, MetaPress, Web of Science and Springerlink \*\***

More information about this series at <http://www.springer.com/series/7818>

Yingquan Peng · Xinyong Dong  
Editors

Proceedings of 2018  
International Conference  
on Optoelectronics  
and Measurement

 Springer



*Editors*

Yingquan Peng  
China Jiliang University  
Xiasha, Hangzhou, Zhejiang, China

Xinyong Dong  
China Jiliang University  
Xiasha, Hangzhou, Zhejiang, China

ISSN 1876-1100

ISSN 1876-1119 (electronic)

Lecture Notes in Electrical Engineering

ISBN 978-981-13-8594-0

ISBN 978-981-13-8595-7 (eBook)

<https://doi.org/10.1007/978-981-13-8595-7>

© Springer Nature Singapore Pte Ltd. 2020

This work is subject to copyright. All rights are reserved by the Publisher, whether the whole or part of the material is concerned, specifically the rights of translation, reprinting, reuse of illustrations, recitation, broadcasting, reproduction on microfilms or in any other physical way, and transmission or information storage and retrieval, electronic adaptation, computer software, or by similar or dissimilar methodology now known or hereafter developed.

The use of general descriptive names, registered names, trademarks, service marks, etc. in this publication does not imply, even in the absence of a specific statement, that such names are exempt from the relevant protective laws and regulations and therefore free for general use.

The publisher, the authors and the editors are safe to assume that the advice and information in this book are believed to be true and accurate at the date of publication. Neither the publisher nor the authors or the editors give a warranty, expressed or implied, with respect to the material contained herein or for any errors or omissions that may have been made. The publisher remains neutral with regard to jurisdictional claims in published maps and institutional affiliations.

This Springer imprint is published by the registered company Springer Nature Singapore Pte Ltd. The registered company address is: 152 Beach Road, #21-01/04 Gateway East, Singapore 189721, Singapore

# Contents

## Part I Fiber Optics, Photonics and Optical Communication

<b>Large-range Bridge Beam-gap Displacement Sensors Based on Cantilever Beam with Fiber Bragg Grating</b> . . . . .	3
Guohui Lyu, Chunming Bi, Yan Zhang, Chaozheng Wang, Mingyang Wang, and Xu Jiang	
<b>Internal Photonic Modulation of Various Spatial Polarization Modes Using Digital Laser Transmission Across Fiber Optic Channels</b> . . . . .	12
Muhammed Fuzail Khan	
<b>Fiber Bragg Grating Thermal Gas Flow Sensor by 980 nm Laser Heating</b> . . . . .	27
Guohui Lyu, Jinling Zhang, Chaozheng Wang, Keda Wang, Yan Zhang, and Xu Jiang	
<b>Policy-Based Comparison-Triggered Defragmentation Mechanism for Elastic Optical Networks</b> . . . . .	37
Lingqi Luo, Xiaoling Liu, Jingwen Zhang, Cong Yu, and Jianhua Shen	
<b>Fabry-Perot Cavity-Based Optical Fiber Pressure Sensor</b> . . . . .	45
Hui Li, Qingchao Zhao, Jiasheng Ni, Long Ma, Faxiang Zhang, and Chang Wang	
<b>Modeling Method of Sunlight Interference Signal</b> . . . . .	52
Hao Guo, Na Ma, and Weiwei Liang	
<b>High-Efficiency Automatic Discovery of Optical Communication Device Based on MDNS</b> . . . . .	61
Yuhua Zhang, Xueguang Yuan, Yang'an Zhang, Qin Liu, and Yalei Chu	

<b>Adaptive Phase Estimation in the Presence of Nonlinear Phase Noise for Carrier Phase Recovery of PM-QPSK Signals in Coherent Optical Receivers</b> . . . . .	66
Faith Kwaku Deynu, Bo Xu, and Evans Wilson Akpari	
<b>The Plasmon in Square Quantum-Dot System with Few Atoms</b> . . . . .	73
Renglai Wu, Jun Quan, and Jiangli Song	
<b>Electrophysiological and Phototactic Behavior Studies of <i>Musca domestica</i></b> . . . . .	80
Wei-Wei Xu, Shun Kamada, Takanori Kozai, Tao Zheng, Takeshi Fujihara, Tomoya Konishi, and Masaru Kamano	
<b>High Temperature Sensor Based on Regenerative Fiber Bragg Grating</b> . . . . .	89
Guohui Lyu, Yu Sun, Yan Zhang, Chaozheng Wang, Xiaohang Liu, and Xu Jiang	
<b>Tunable NIR Filter with High <math>Q</math>-Factor Realized by Using TiN as Plasmonic Layer</b> . . . . .	98
Lingli Wang, Jun Tan, Yongming Shan, Guojun Jin, Yuying Wang, Limin Hu, Kai Xu, and Yanlong Meng	
<b>Research on Cascade Inner Microcavity-Based Fiber Sensor</b> . . . . .	107
Huifang Chen, Hai Wang, Kezhen Rong, and Tiantian Chen	
<b>Optical Fiber Sensor for Steady Micro-flow Rate Measurement</b> . . . . .	114
Zhicheng Zhu, Juan Kang, Qian Zhang, Yi Li, and Chunliu Zhao	
<b>Part II LEDs, OLEDs and Related Materials</b>	
<b>An Ultrathin Tandem Organic Light-Emitting Diodes with Very Low Driving Voltage and High Efficiency</b> . . . . .	123
Yanhong Deng, Jinjiang Wang, Liezun Chen, Xiangyu Jiang, Ke Xie, Yuqi Peng, and Yanqing Li	
<b>The Study of Working Mechanism of Organic Heterojunction Charge Generation Layer</b> . . . . .	133
Feiping Lu, Yuxiang Zhao, Yinglong Shi, Qing Liu, Xiaobin Liu, and Weijun Ling	
<b>Experimental Research and Theoretical Study of Cesium, Oxygen Activation on Defect AlGaN (0001) Surface</b> . . . . .	140
Zesen Liu, Liang Chen, Shuqin Zhang, Qingyang Meng, Zhenhuan Gu, and Jing Hua	
<b>Preparation of Er<sup>3+</sup>-Doped NaYF<sub>4</sub> and Its First-Principles Analysis</b> . . . .	148
Qingyang Meng, Shuqin Zhang, Liang Chen, Zhenhuan Gu, Zesen Liu, and Jing Hua	

<b>The Comparative Analysis of the LED and High-Pressure Sodium Lamp as Road Lighting</b> .....	155
Jianming Huang, Lei Zhang, Limin Hu, Yanhua Han, Mingzhong Xu, Weipeng He, Bin Ru, Haiyong Chen, Shaoqin Fu, Yu Xia, Yueming Yu, Zhangwan Wang, Qunjie Wu, Yan Shi, and Shiyu Wang	
<b>Distribution of Quantum Dots in Quantum Dots Enhancement Films</b> .....	159
Yuxue Feng, Zugang Liu, Renshi Chen, Xin Wang, Lei Li, and Hong Zhao	
<b>Part III Photo Detectors and Solar Cells</b>	
<b>Size Dependent Performances of Organic Photodiode Arrays</b> .....	167
Chen Liu, Junkang Zhong, Xinda Chen, and Yingquan Peng	
<b>High Photosensitivity Near-Infrared PhOFETs Based on PbPc:C<sub>60</sub> Bulk Heterojunction</b> .....	174
Qinyong Dai, Wenli Lv, Yingquan Peng, Wenli Lv, Sunan Xu, Yi Wei, Lei Sun, and Ying Wang	
<b>Thickness-Dependent Performance of Photosensitive Organic Field-Effect Transistors Based on Palladium Phthalocyanine</b> .....	180
Juanjuan Zhou, Wenli Lv, Sunan Xu, and Yingquan Peng	
<b>Channel-Length-Dependent Performances of Planar Photodiodes Based on Perovskite</b> .....	187
Guangmeng Liao, Kun Xu, Feiyu Zhao, Fobao Huang, Yuanlong Liang, Lan He, Yingquan Peng, and Rongzheng Ding	
<b>Green-Light Photoresponsive Organic Field-Effect Transistor by PTCDA/Pentacene Heterojunction</b> .....	194
Ying Tang and Binghan Song	
<b>Bending Characteristics of Flexible Organic Phototransistors Based on Copper Phthalocyanine</b> .....	202
Huabiao Zhu, Yuhuan Yang, Yingquan Peng, Wenli Lv, Sunan Xu, Yi Wei, Lei Sun, Ying Wang, and Fangzhi Guo	
<b>Preparation and Characterization of (C<sub>6</sub>H<sub>5</sub>C<sub>2</sub>H<sub>4</sub>NH<sub>3</sub>)<sub>2</sub>PbX<sub>4</sub> Perovskite Materials</b> .....	208
Meimei Hu, Zugang Liu, Qingyang Meng, and Qianmin Dong	
<b>Absolute Spectral Responsivity Calibration of Terahertz Detector</b> .....	216
Bin Wu, Hongchao Wang, Peng Wang, Peng Zhang, Wancheng Zhang, and Chengping Ying	

<b>Part IV Sensors and Measurement Technology</b>	
<b>Determining Hole Mobility of Zinc Phthalocyanine Thin Films by Light-Intensity-Dependent Current–Voltage Characteristics . . . . .</b>	<b>225</b>
Yinqin Ye, Fobao Huang, Yingquan Peng, Wenli Lv, Sunan Xu, Yi Wei, Lei Sun, and Ying Wang	
<b>Sensing Inter-dot Tunneling Using Nonlinear Absorption in Coupled Quantum Dots . . . . .</b>	<b>231</b>
Aihong Yang, Yan Xu, and Yandong Peng	
<b>Study on the Pressure of HF Gas Detection in High-Voltage Electrical Equipment by TDLAS Technology . . . . .</b>	<b>236</b>
Shiling Zhang, Qiang Yao, Xintian Li, and Yunqi Yue	
<b>Application Research of Adjustable Frequency DC-Spark in Oil Analysis Spectrometer . . . . .</b>	<b>245</b>
Zhen Wang, Mingfan Dai, Shenghua Zhou, Bangning Mao, and Yanqing Qiu	
<b>A Three-Dimensional Measurement Method Based on Binary Structured Light Patterns for Medical Electronic Endoscope . . . . .</b>	<b>251</b>
Pei Tao, JiaMin Xia, Bo Yuan, and Liqiang Wang	
<b>A Miniaturized Device for Measuring Flexure Angle of Flexible Fiber Data Gloves . . . . .</b>	<b>258</b>
Jin Zhang, Liqiang Wang, Bo Yuan, and Lei Zhang	
<b>Research Progress on Artificial Intelligence Human Sensor . . . . .</b>	<b>264</b>
Tianqi Zhao, Aiming Feng, Shangzhong Jin, Yan Shi, Bin Hou, and Yongqiang Yan	
<b>Investigation on Oil Spectrum Detection Technology Based on Electrode Internal Standard Method . . . . .</b>	<b>272</b>
Mingfan Dai, Zhen Wang, Shenghua Zhou, Bangning Mao, and Yanqing Qiu	
<b>Design of Compact Oil Particle Counter System Based on Microscopic Imaging . . . . .</b>	<b>281</b>
Zhonghui Cheng, Bin Shen, Dong Fu, Shangzhi Zhong, Yan Xuan, Tianhu Zhang, and Yanqing Qiu	
<b>Adaptive Phase Estimation in the Presence of Nonlinear Phase Noise for Coherent Optical Detection . . . . .</b>	<b>288</b>
Faith Kwaku Deynu, Bo Xu, and Evans Wilson Akpari	

**Preparation and Application of Semiconductor Fluorescent Probe . . . . . 294**  
Xin Wang, Jiaqi Chen, Jie Huang, Yuxue Feng, Zhenhuan Gu,  
and Zugang Liu

**Online Monitoring Study for SF<sub>6</sub> Composition by Optical Cavity  
Sensing Technology in High-Voltage GIS . . . . . 300**  
Shiling Zhang, Qiang Yao, and Meng Jiang

**Part I**  
**Fiber Optics, Photonics and Optical**  
**Communication**



# Large-range Bridge Beam-gap Displacement Sensors Based on Cantilever Beam with Fiber Bragg Grating

Guohui Lyu<sup>1</sup>, Chunming Bi<sup>1</sup>, Yan Zhang<sup>1</sup>, Chaozheng Wang<sup>1</sup>,  
Mingyang Wang<sup>1</sup>, and Xu Jiang<sup>2(✉)</sup>

<sup>1</sup> Research Center for Fiber, Optic Sensing Technology National Local Joint Engineering, and the College of Electronic Engineering, Heilongjiang University, Harbin, China

lvguohui@hlju.edu.cn

<sup>2</sup> College of Data Science and Technology, Heilongjiang University, Harbin, China

lvguohui@hlju.edu.cn

**Abstract.** The bridge beam-gap between the beam body of the high-speed railway bridge can reach 200–300 mm, and the traditional displacement sensor is inconvenient to measure. A large-range bridge beam-gap displacement sensor based on cantilever beam with fiber Bragg grating (FBG) is proposed in this paper. Based on the structural characteristics of the beam joint, fully utilized the effective space to enlarge the mechanical structure size of the cantilever beam to realize displacement sensing. The cantilever beam displacement sensing is simulated by ANSYS software. The sensor is designed and packaged according to the numerical simulation result. A beam-gap changing device is designed to develop the displacement experiment of the beam-gap. The results show that when the bridge beam-gap displacement varies from 0 to 200 mm, the linear correlation coefficient of the displacement–wavelength curve reaches 0.99852, and the displacement detection sensitivity is 4.53 pm/mm, which meets the requirements of beam-gap displacement monitoring. The sensor is structure simple, easy to package layout, convenient to expand the range by lengthening the cantilever beam, well durability, and suitable for long-term online monitoring applications of large-size beam-gap displacement.

**Keywords:** Fiber bragg grating (FBG) · Displacement sensor · Bridge beam-gap · Cantilever beam structure

## 1 Introduction

In recent years, with the rapid development of China's high-speed railway, many large-span high-speed railway bridges have been built. The high-speed railway bridge beam will expansion and deformation with the action of temperature change, load, concrete shrinkage and creep. Therefore, when the large bridge body is spliced, enough space should be left between adjacent two beam ends. In the actual application of the bridge, it is necessary to monitor the size of the beam joint in real time, to sense the



change of beam joint which will have great influence on the track structure of high-speed train. If the beam-gap is too large, the bearing spacing of the beam ends will increase, and the vertical and lateral displacement will be caused in the middle of the adjacent rail support points. The large gap will make the train produce an impact on the track and the substructure, reducing the travelling comfort of passengers and shortening the service life of the track and components, and at the same time, stress concentration in the rail is easy to cause serious consequences of the breakage [1–4]. In actual engineering, when the track passes through the beam joint mentioned above, in order to ensure the continuity and smoothness of the track, it is necessary to lay the bridge beam-end expansion device between the two beam ends, the beam end and the abutment or at the hinge position of the bridge. The device ensures the safety of the track structure in bridge expansion [5].

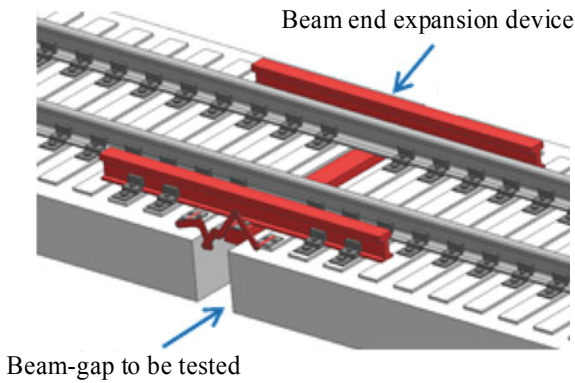


**Fig. 1** Beam-gap of high-speed railway bridge

The track circuit of high-speed rail produces strong electromagnetic interference to the traditional electronic displacement sensor, which affects the accuracy of displacement measurement. The displacement sensor based on FBG has the unique advantages of all-optical measurement and anti-electromagnetic interference, which is also suitable for online monitoring of beam joints displacement on high-speed rail lines. At present, most of China's high-speed railway bridge lines use the supporting beam-end retractor device designed by BWG Company [6]; the structure is shown in Fig. 1. Due to the complicated structure of the hinged beam-end retractor device of BWG Company, after the device is laid, the remaining space on both sides of the rail is insufficient, it is difficult to lay the traditional long probe displacement sensor. It is urgent to study a large-range beam-gap displacement sensor suitable for this kind of working condition.

In this paper, a large-range beam-gap displacement sensor based on cantilever beam with FBG is designed based on the actual working conditions. And the space between the beam bodies is fully utilized to enlarge the structure of the cantilever beam. It acts not only as an elastic sensitive component but also as a telescopic probe. The sensor installation and layout are convenient. As shown in Fig. 2, the Z-type sensor studied in this paper is compared with the traditional one-dimensional long probe displacement sensor.

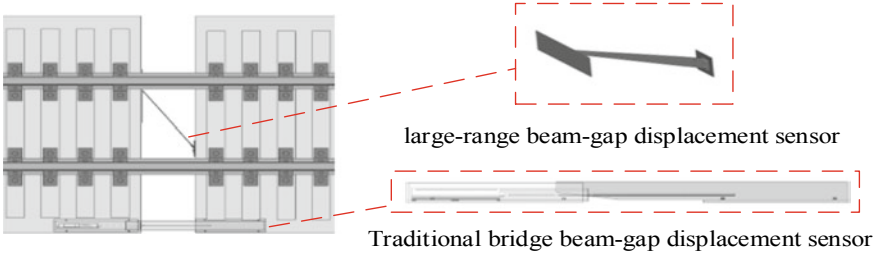


**Fig. 2** Comparison of beam-gap displacement sensor

## 2 Principle

### 2.1 Fiber Bragg Grating Sensing Principle

Fiber grating is a diffraction grating made by forming a periodic refractive index modulation in a core by a physical process such as laser writing. It is an optical passive device with small volume, low welding loss, full compatibility with optical fiber, and burying into the smart material and other advantages. And its resonant wavelength is sensitive to changes in the external environment such as temperature, strain, refractive index, and concentration. So it has been widely used in the field of sensing, the wavelength satisfied the Bragg condition (1) can be reflected by Bragg grating [7].

$$\lambda_B = 2n_{\text{eff}}\Lambda \quad (1)$$

where  $\lambda_B$  represents the Bragg reflection wavelength, which is the center wavelength;  $n_{\text{eff}}$  represents the effective refractive index in the core region of the fiber;  $\Lambda$  is the period of the Bragg grating.  $n_{\text{eff}}$  and  $\Lambda$  are easily affected by the external environment (such as temperature, strain, acceleration), causing the wavelength  $\Delta\lambda_B$  that meets the Bragg reflection condition to drift. When the external conditions change, such as temperature, axial stress, and lateral stress, it can lead to changes in the FBG period and the refractive index, and the total changes caused by these three external conditions can be expressed as [8]:

$$\frac{\Delta\lambda_B}{\lambda_B} = (1 - P_e)\varepsilon_x + (\alpha + \xi)\Delta T + \left[ -\frac{1 - 2\nu}{E} + \frac{n^2}{2E}(1 - 2\nu)(2P_{12} + P_{11}) \right] \Delta P \quad (2)$$

In the formula, in the right end, three terms respectively indicate the influence of axial strain, temperature, and lateral stress on the wavelength drift, where  $P_e$  is the effective elastic coefficient, 0.22 for the quartz fiber;  $\varepsilon_x$  is the axial strain;  $\alpha$  is the expansion coefficient of the material;  $\xi$  is the thermo-optic coefficient;  $\nu$  is the Poisson's ratio;  $E$  is the elastic modulus;  $P_{ij}(ij = 1, 2)$  is the linear electro-optic coefficient;  $\Delta T$  and  $\Delta P$  are the values of the external temperature and the external transverse pressure, respectively.

## 2.2 Equal-Strength Cantilever Beam Sensing Principle

The cantilever beam is a metal beam structure with one end fixed and one end free; it is widely used in the field of optical fiber sensing applications. According to the cross-sectional shape of the cantilever beam, it can be divided into equal-section cantilever beam and equal-strength cantilever beam. The FBG is solidified on the equal-strength cantilever beam, and the cantilever beam is fixed at one end. When the other end is deformed by force, the wavelength change in the FBG is detected; after calibration, it can be used to measure the change in the displacement. For equal-strength cantilever beams as shown in Fig. 3, when the measured force  $F$  acts on the free end of the beam, the strain at a certain position on the surface of the equal-strength beam can be calculated as follows [9].

$$\varepsilon_x = \frac{6(L-x)}{EAH} F \quad (3)$$

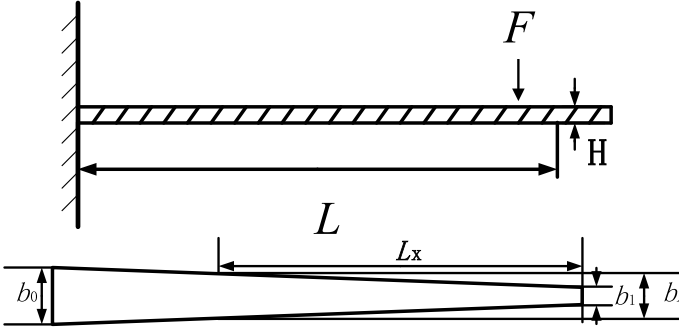


Fig. 3 Cantilever beam structure schematic

In Eq. (3),  $x$  is the distance from a certain position to the fixed end;  $\varepsilon_x$  is the strain value at  $x$ ;  $L$  is the length of the beam;  $E$  is the elastic modulus of the material of the beam;  $A$  is the section of the beam area;  $H$  is the thickness of the beam. For isosceles trapezoidal cantilever beams, the cross-sectional area at different distances from the fixed end is different, that is,

$$A_x = Hb_x = H \frac{b_1L + b_0(L-x)}{L} \quad (4)$$

Substituting (4) into (3), the strain at a point on the cantilever beam can be obtained.

$$\varepsilon = \frac{6L(L-x)}{Eh^2b_1L + Eh^2b_0(L-x)} \quad (5)$$

When the cantilever beam is subjected to axial strain, the fiber Bragg grating attached to the cantilever beam is also subjected to axial strain. The relationship between the wavelength drift of the fiber Bragg grating and the external strain when the fiber Bragg grating is only subjected to axial strain is:

$$\frac{\Delta\lambda_B}{\lambda_B} = (1 - P_e)\varepsilon \quad (6)$$

Substituting (5) into (6), the formula for wavelength drift of isosceles trapezoidal cantilever beam surface fiber Bragg grating can be obtained.

$$\frac{\Delta\lambda_B}{\lambda_B} = (1 - P_e) \frac{6L(L-x)}{Eh^2b_1L + Eh^2b_0(L-x)} \quad (7)$$

### 3 Design and Simulation Analysis of Large-Sized Equal-Strength Cantilever Beam

#### 3.1 Structural Design of Large-Sized Equal-Strength Cantilever Beam

In this paper, the isosceles trapezoidal structure is used to design large-sized cantilever beams, which can ensure the stability of the structure and reduce the weight of the structure. In order to ensure the good flexibility and strength of the cantilever beam, we choose 65 Mn as the material, and its tensile strength can reach 925 MPa. In practical engineering applications, the size of the cantilever beam can be designed according to the actual width of the beam to be tested. The large-sized cantilever beam design structure is shown in Fig. 4.

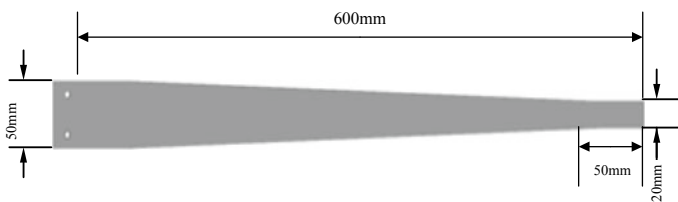


Fig. 4 Large-sized cantilever beam design structure

#### 3.2 Displacement Simulation Analysis of Large-Sized Equal-Strength Cantilever Beam

In this paper, the mechanical simulation analysis of the deformation process of large-sized cantilever beam is carried out. In the process of finite element analysis, a limit position board is added to the upper and lower ends of the cantilever beam as the fixed end and the moving end, respectively; overall, it looks like a Z-shaped structure. When

the lower splint is fixed and the upper splint is moved by the equidistant displacement, the strain distribution of the cantilever beam under different displacement conditions is simulated.

The specific simulation results are shown in Fig. 5. The displacement of the moving end of the large-sized cantilever beam changes from 0 to 200 mm.

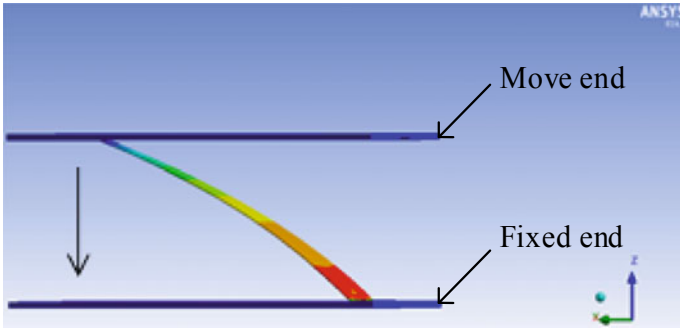


Fig. 5 Large-sized cantilever beam simulation

When the vertical downward equidistant displacement is applied to the upper clamping plate, the strain data is obtained by ANSYS software and processed by Origin software. The fitted curve is shown in Fig. 6, the displacement strain curve of the cantilever beam has good linearity, and the fitted value is up to 0.9998.

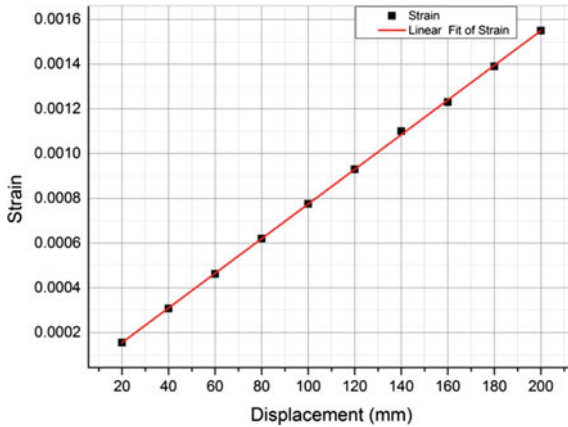


Fig. 6 Large-sized cantilever beam strain-displacement curve

## 4 Packaging and Manufacturing of Large-Range Beam-Gap Displacement Sensor

The manufacturing process of the large-range bridge beam-gap displacement sensor based on cantilever beam with FBG is that the FBG is cured to a selected position on the metal surface of the cantilever beam. Polishing the surface of the cantilever beam of the FBG with sandpaper to make it clean and smoothing. Then wipe the surface with alcohol, place FBG at the centerline of the cantilever beam. A two-component high-strength resin is spot-coated on both ends of the grating region of the FBG, and a certain quality metal block is suspended at one end of the fiber to produce a predetermined pre-strain of the FBG, and the high-strength resin will be completely cured after 24 h. Assembly drawing of large-range beam-gap displacement sensor is shown in Fig. 7.

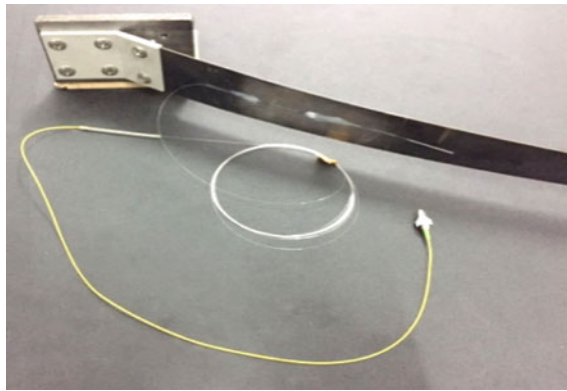


Fig. 7 Assembly drawing of large-range beam-gap displacement sensor

## 5 Experimental Study on Calibration of Beam-Gap Displacement Sensor

### 5.1 Displacement Sensor Calibration Device

In order to analyze and measure the sensing characteristics based on the large-range beam-gap displacement sensor, a simple displacement calibration device is designed to simulate the displacement of beam-gap, and the displacement change can be accurate to the order of millimeters. The calibration device is assembled by two identical standard punched aluminum alloy parts. Each standard part has 86 small holes with a diameter of 3.1 mm. The center distance of the hole is 5.08 mm.

The calibration device has a total length of 432 mm, a width of 23 mm, and a height of 21 mm. The whole is fixed on the experimental platform for experiments. During the experiment, the moving distance of block is between the two holes and squeezes large-range cantilever beams while moving the block horizontally, so that the

bending degree of the cantilever beam can be changed by changing the position of the moving block. The displacement sensing calibration device also includes a FBG wavelength demodulator and a computer with a software for collecting analysis data, as shown in Fig. 8. During the calibration process, the wavelength of the FBG at different displacements is collected by the demodulator and then transmitted to the PC through the network cable.

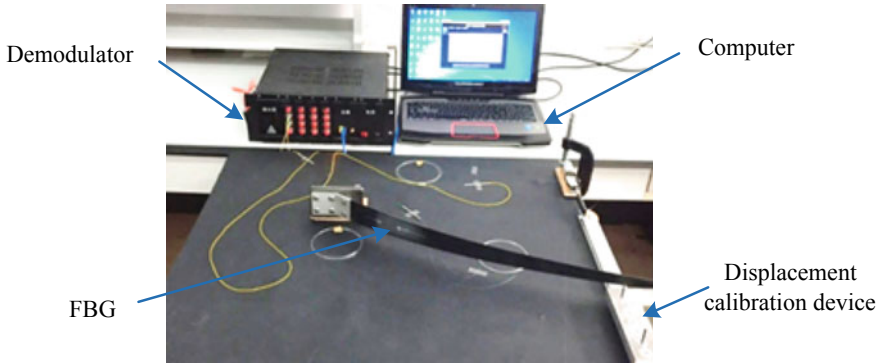


**Fig. 8** Displacement sensor calibration test platform

### 5.2 Displacement Sensing Calibration Test

Displacement test of bridge beam-gap displacement sensor based on cantilever beam with FBG is started from the zero point of the sensor, the displacement is smoothly increased to the maximum measured value of 10.16 mm, and the output value of each verification point during the forward stroke is recorded. The measurement range is from 0 to 203.2 mm, and the data is recorded for every 10.16 mm.

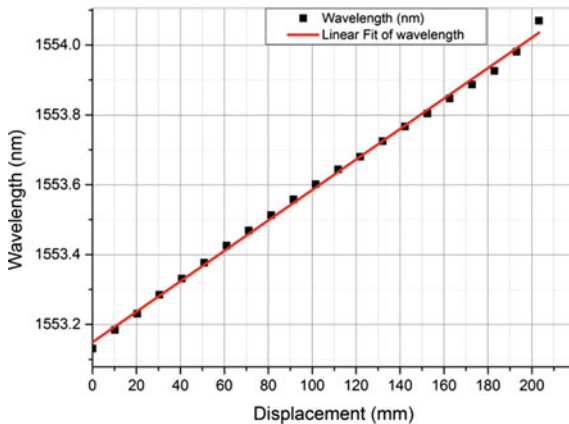


**Fig. 9** Displacement sensor experimental FBG wavelength fitting Curve

Linearly fit the curve of Fig. 9, the fit equation is:

$$y = 1553.2 + 0.00434x$$

It can be seen from the calculation that the linear correlation coefficient of the displacement sensor is 0.99841, and the sensitivity of the displacement sensor is 4.53 pm/mm, which meets the requirements of long-term online monitoring of beam displacement changes.

## 6 Conclusion

In this paper, the large-range bridge beam-gap displacement sensor based on the cantilever beam with FBG is designed and manufactured for the actual demand of the displacement monitoring of the high-speed railway bridge beam joint. The cantilever beam structure as the elastic sensitive component is designed into a telescopic probe, the cantilever beam, and the two concrete sides of the beam joint form a Z-shaped folding structure, which makes full use of the beam-gap space for installation and layout. The software simulation and experimental calibration curves of the sensor are linear, and the linear correlation coefficients are 0.9998 and 0.99841, respectively. The two are highly consistent, indicating that the displacement sensor based on large-sized equal-strength beam is feasible, and the displacement sensitivity is 4.53 pm/mm. The structure is simple and convenient, and it is suitable for application in the long-term online monitoring of high-speed railway bridge beam joints.

## References

1. Wang, X., Wu, L.Q., Zhou, Y.: The long-term settlement deformation automatic monitoring system for the Chinese high-speed railway. *Shock Vibr.* **2015**, 1–12 (2015)
2. Qiu, Y.J., Zhang, X.J., Wei, Y.X.: Influenced of train speed ballastless on dynamic characteristics of track subgrade. *J. Traffic Transp. Eng.* **2**, 1–5 (2007)
3. Luo, Q., Cai, Y.: Research on deformation limit and reasonable length of high-speed railway bridge and bridge transition section. *Railway Stan. Design* **20**, 2–4 (2000)
4. Hu, J.J.: Reasonable use of track temperature regulator on steel beam of Shuangta Bridge. *Railway Constr.* **2**, 14–15 (1995)
5. Li, Y.L., Xiang, H.Y., Wan, T.B., Ren, H.Q.: Performance of train running over expansion joints at beam ends of long-span railway bridge. *J. China Railway Soc.* **2**, 94–99 (2012)
6. Tian, C.X., Yin, M.G., Wang, P.: Thoughts on the use of telescopic adjusters for seamless lines on bridges. *Railway Eng.* **2**, 85–86 (2006)
7. Morey, W.W., Meltz, G., Glenn, W.H.: Fiber optic Bragg grating sensors. *Proc. SPIE* **11** (69), 98–107 (1989)
8. Chen, D.X.: Research on dynamic characteristics of fiber Bragg grating accelerometer. Wuhan University of Technology (2004)
9. Wang, Q.Y.N.: Design and study of fiber sensor based on cantilever beam of uniform strength. *Control Autom.* **26**(04), 107–108 (2010)





# Internal Photonic Modulation of Various Spatial Polarization Modes Using Digital Laser Transmission Across Fiber Optic Channels

Muhammed Fuzail Khan<sup>(✉)</sup>

University of Johannesburg, Johannesburg, South Africa  
mfuzailk@gmail.com

**Abstract.** A subsequent feature of the digital laser is the inexpensive ease to generate shapes digitally using electronics, rather than employing costly spatial optical lenses. This leads to a possibility of internally modulating data using digitally generated shapes, specific to a mode of electric field polarizations.

**Keywords:** Laser · Polarization · Modulation · Fiber optic

## 1 Introduction: Digital Laser and Spatial Modes

The common methods to modulate digital information using a laser are to either directly switch the driving source ‘On’/‘Off’ or use an electro-optic modulator (EOM) to externally split the laser beam with constructive/destructive interference in relation to the digital ones/zeroes, before combining the beams [1].

Another unique method exists, wherein spatial modes are employed to internally modulate transverse modes, which are patterns of radiation that determine the intensity distributions [2]. The simplest mode is the Gaussian mode. The longitudinal component in the propagation direction  $z$  is found to be negligible in comparison with the transverse component emanating in the  $x$  and  $y$  directions. Therefore, a mode is more commonly referred to as transversely polarized, wherein the light is not completely confined in the core but considered as a weakly guided approximation solution of the wave equation. The fundamental mode is known as a linearly polarized (LP) mode with rectangular symmetrical coordinates  $LP_{01}$ .

Polarization is defined in relation to the electric field intensity distribution which dominates in the transverse direction over its longitudinal magnetic component, described as an originating point charge moving in an elliptical pattern in the plane of the propagating light source [3]. The ellipsoid geometry includes the ratio of major to minor axis, the angular orientation and handedness (direction of rotation) which combine to describe the state of optical polarization. Some specific variations such as linear and circular polarizations of the general elliptical polarization can be observed when certain boundary conditions are met [4]. An alternative mathematical representation to describe light state of polarization (SOP) was proposed by George Gabriel Stokes using the Poincare sphere and Stokes parametric matrices [5] (Fig. 1).

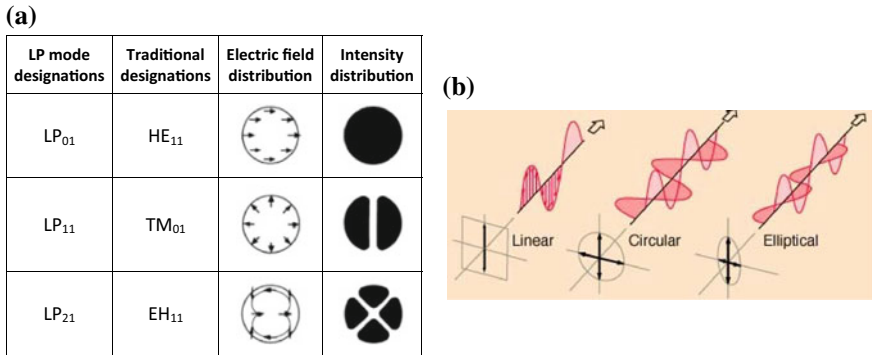


**Fig. 1** a Electric field vectors and intensity profiles of LP modes b Optical state of polarizations

### 1.1 Phase Relationship Analysis of the LP<sub>11</sub> Polarized Mode

The lower order LP<sub>11</sub> gray-scale image is sampled at incremental radial angles (ranging from 0° to 360°) and applied as the input arguments to the ‘improfile’ function found in MATLAB Image Processing Toolbox, the output of which is a 2D array plot of image intensity values as a function of the angle (Fig. 2).

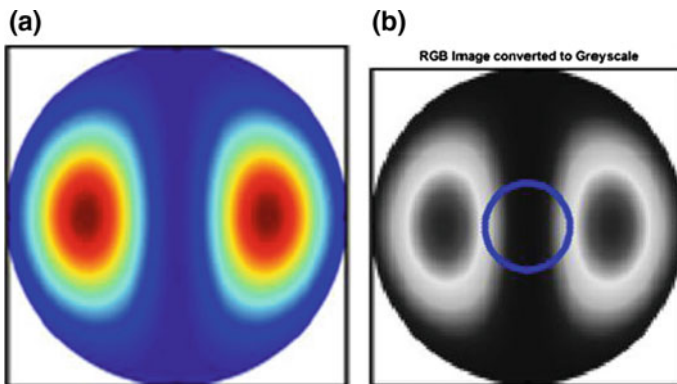


**Fig. 2** a LP<sub>11</sub> light shape in RGB b Gray-scale conversion with an overlaid sampling circle

The waveform follows a continuous sinusoidal graphic, where the maximum image intensities of the two lobes occur on the  $x$ -axis starting in an anticlockwise rotation at 0° and 180° with a period of 360°, which can be approximated by the cosine trigonometric function.

The image intensities of both the lobes are of equal value with 180° phase shift between the electric field orthogonal components, revealing a linear antipodal polarized shape as confirmed by the Poincaré sphere for the LP<sub>11</sub> mode which correlates closely to the Differential Phase Shift Keying (DPSK) modulation scheme.

The fast Fourier transform (FFT) is subsequently applied to the continuous image intensity waveform. The Fourier coefficients corresponding to angles of maximum amplitude intensity values are applied as a complex parameter to the ‘stokes’ function found in MATLAB Phased Array System Toolbox (Fig. 3).

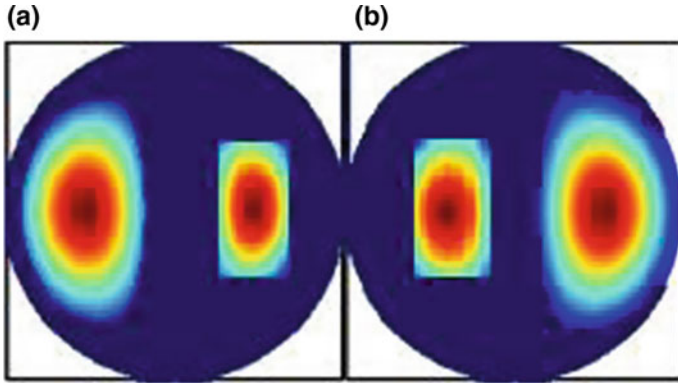


**Fig. 3** Internal modulation of LP<sub>11</sub> mode with image patterns representing a: **a** ‘1’ bit symbol **b** ‘0’ bit symbol

Thus, the two lobes of a LP<sub>11</sub> light shape mode can be internally modulated, by switching between the image patterns with differing orthogonal field intensities and phase shifts. The orthogonal component related to the lobe with lowest power intensity will be below the amplitude threshold at the detector, while the other higher intensity orthogonal component will be detected at the corresponding phase.

The switching of image patterns in relation to the digital bit stream and phase shift detection of the light carrier wave electric field components enables the transmission of one bit per symbol similar to the conventional externally modulated DPSK transmission.

## 1.2 Phase Relationship Analysis of the LP<sub>21</sub> Polarized Mode

Following a similar approach to LP<sub>11</sub> above, the higher order LP<sub>21</sub> gray-scale image is sampled (Fig. 4).

The maximum image intensities of the four lobes occur at a 45° azimuth in each cartesian quadrant starting in an anticlockwise rotation at 45°, 135°, 225° and 315° with a period of 180°, which can be approximated by the sine or cosine trigonometric function.

The image intensities of each lobe are of different values with a 90° phase shift between the electric field orthogonal components, revealing an elliptical polarized shape as confirmed by the Poincare sphere for the LP<sub>21</sub> which correlates closely to the Quadrature Phase Shift Keying (QPSK) modulation scheme.

Thus, the four lobes of a LP<sub>21</sub> light shape mode can be internally modulated, by switching between the image patterns with differing orthogonal field intensities and

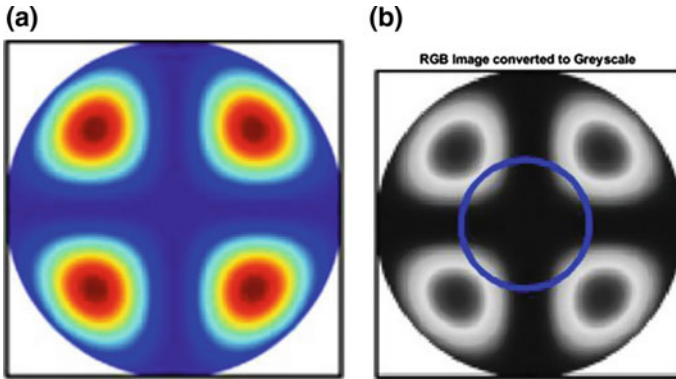


**Fig. 4** a  $LP_{21}$  light shape in RGB b Gray-scale conversion with an overlaid sampling circle

phase shifts. The orthogonal component related to the lobe with lowest power intensity will be below the amplitude threshold at the detector, while the other higher intensity orthogonal components will be detected at their corresponding phases (Fig. 5).

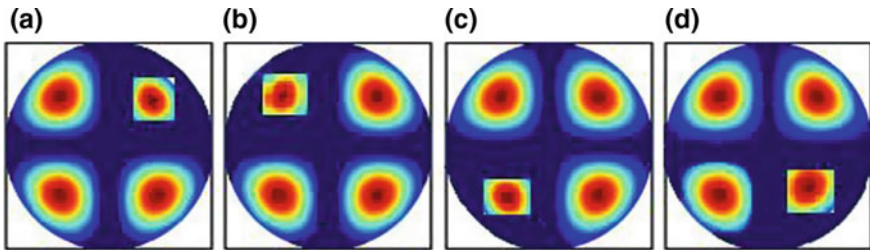


**Fig. 5** Internal modulation of  $LP_{21}$  mode with image patterns representing a: a '00' bit symbol b '01' bit symbol c '10' bit symbol d '11' bit symbol

The switching of image patterns in relation to the digital bit stream and phase shift detection of the light carrier wave electric field components enables the transmission of two bits per symbol, similar to the conventional externally modulated QPSK transmission.

## 2 Practical Block Diagram for a Transmission Model Using Internal Modulation of Digitally Generated Light Shapes to Transmit Data

See Fig. 6.

Light shapes produced from the various polarization modes (which are dualities of externally modulated constructs) can be easily switched from one shape pattern to another via a firmware command in relation to the binary information stream, where a

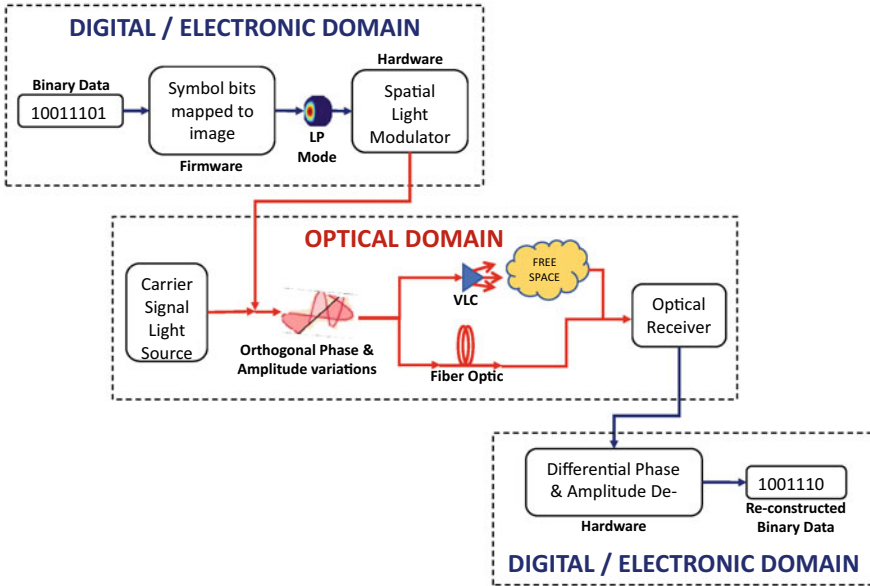


**Fig. 6** A design solution block diagram which uses digital laser hardware to internally modulate information before transmission over a fiber optic channel

gray-scale digital hologram picture (which represents a specific bit period symbol) is written to the spatial light modulator (SLM) hardware [6].

High speed SLM types such as grating light valve (GLV) and digital micromirror devices (DMD) capable of Giga bit per second speeds are required, to match and clock synchronize the central processing unit (CPU) transmitted data rate and the refresh rate of the SLM image projection, which standard liquid crystal display (LCD) SLMs cannot cope with [7].

The binary encoded data stream can be digitally modulated internally together with the digital hologram image via a programmable routine and SLM hardware, producing shapes of light corresponding to a specific polarization mode index where the phases of light carrier waves are manipulated for transmission across a fiber optic channel, which can then be detected using conventional demodulation techniques and existing hardware [8].

Thus, the entire modulation of the transmission phase is implemented in the digital domain, such that no physical change out, realignment or additional high cost customized optical elements are needed to produce the different shapes of light or polarized modes. Another advantage of using internal modulation over external modulation is that no electrical to light conversion EOM hardware such as a Mach-Zehnder interferometer (MZI) is required outside the laser cavity before transmission.

## 2.1 Experiment 1: A Digital Laser Modulator Prototype

The design solution in Fig. 6 above is practically tested by building a prototype line-of-sight (LOS) version for a visible light communication (VLC) application as shown (Fig. 7).

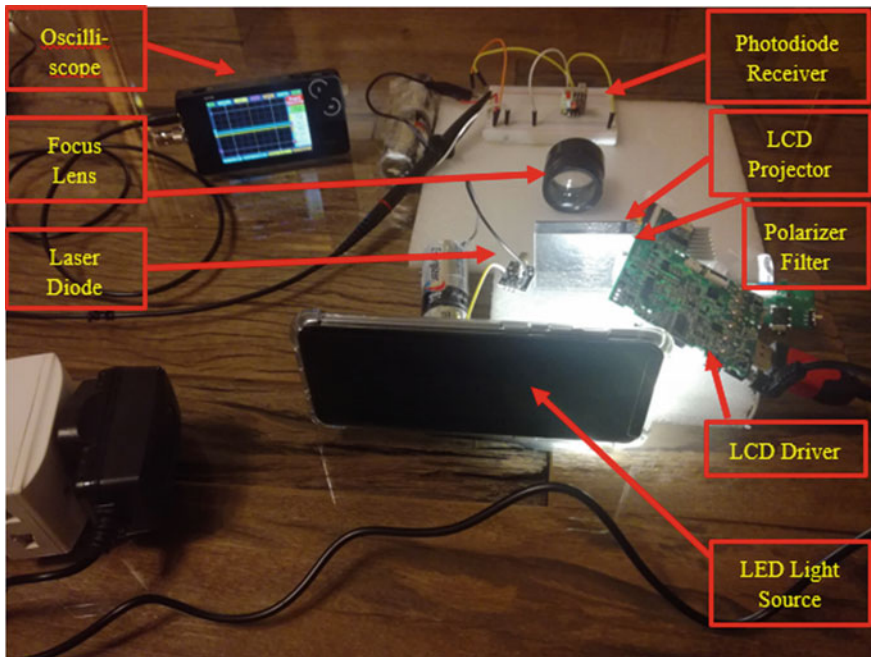


**Fig. 7** Practical implementation of a digital laser spatial mode modulator in a VLC application

The gray-scale images in Fig. 3 are transmitted via HDMI cable from a computer to the LCD driver, which spatially projects the image after passing through a polarizer filter using a collimated light emitting diode (LED) backlight source. A 540 nm laser diode is used as the carrier signal which is superimposed on the image projection using an optical focusing lens.

The oscilloscope output signals at the 540 nm photodiode receiver are displayed below. As can be seen in Figs. 8 and 9 below, when switching from the image pattern of Fig. 3a, b a phase shift of 50 ms occurs, thus validating the above theoretical analysis of phase shift occurrences between orthogonal field components in polarized modes.

One of the apparent advantages of this prototype design is the once off hardware investment cost allowing transmission of higher order modes, by simply generating new image patterns on a computer which is then digitally sent to the spatial projection modulator.



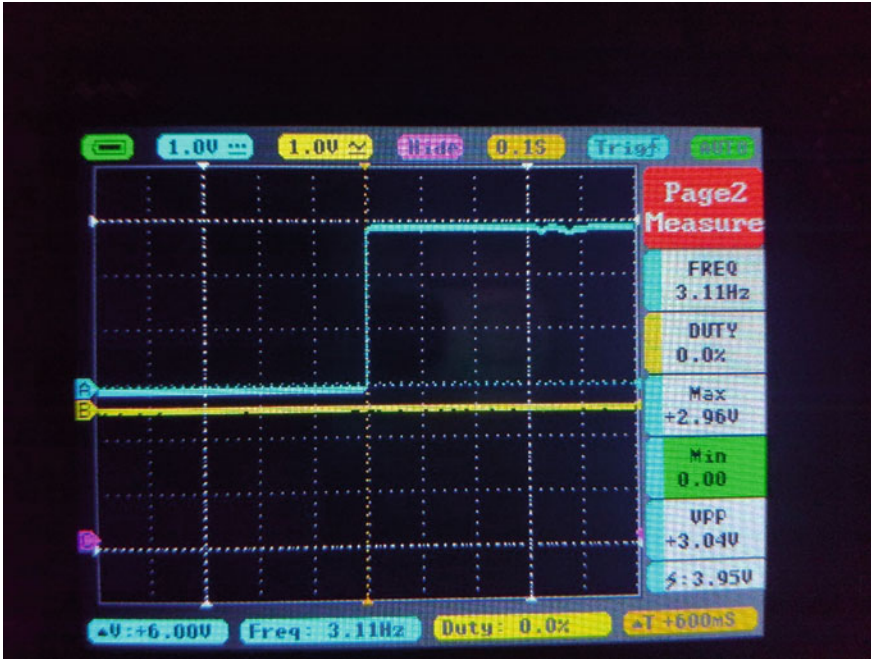


Fig. 8 Signal intensity output with no phase shift when the image from Fig. 3a is projected

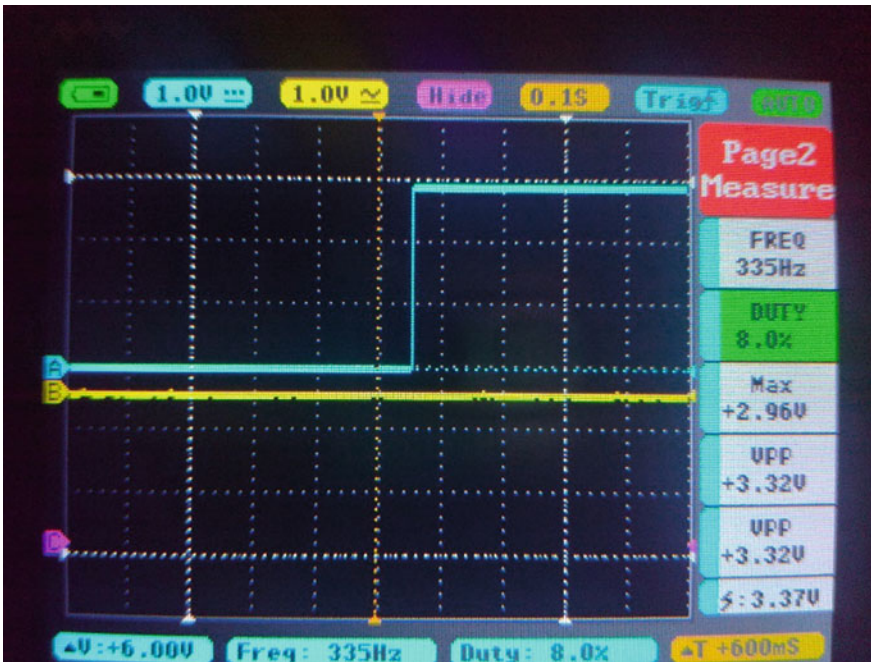
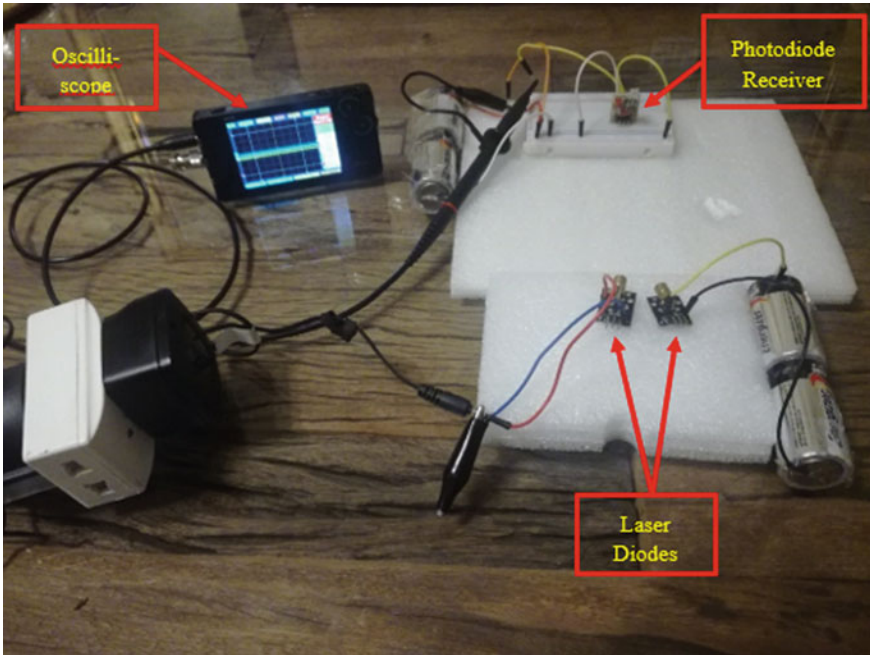


Fig. 9 Signal intensity output with a 50 ms phase shift when the image from Fig. 3b is projected

## 2.2 Experiment 2: An Alternate Spatial Mode Modulator Prototype

See Fig. 10.

In this alternate implementation, the gray-scale images in Fig. 3 are simulated and correlated by using two 540 nm laser diodes, where each laser represents one of the side lobe orthogonal components.



**Fig. 10** Alternate practical implementation of a digital laser spatial mode modulator in a VLC application

To achieve a digitized modulation of logical ‘1’s and ‘0’s, one of the lasers is driven at a higher voltage (having a larger spot size and intensity) level compared to the other laser and vice versa. Thereby achieving a similar switching effect between the projected image patterns as demonstrated in the implementation above.

The oscilloscope output signals at the 540 nm photodiode receiver are displayed below. As can be seen in Figs. 11 and 12 below, when simulating the switching effect from the image pattern of Fig. 3a, b a phase shift of 50 ms occurs, thus also independently validating the above theoretical analysis of phase shift occurrences between orthogonal field components in polarized modes.

The main drawback of this alternate prototype is the requirement for an increase in laser diodes proportionate to the polarization mode index, which will become costlier and impractical for transmission of higher order modes.



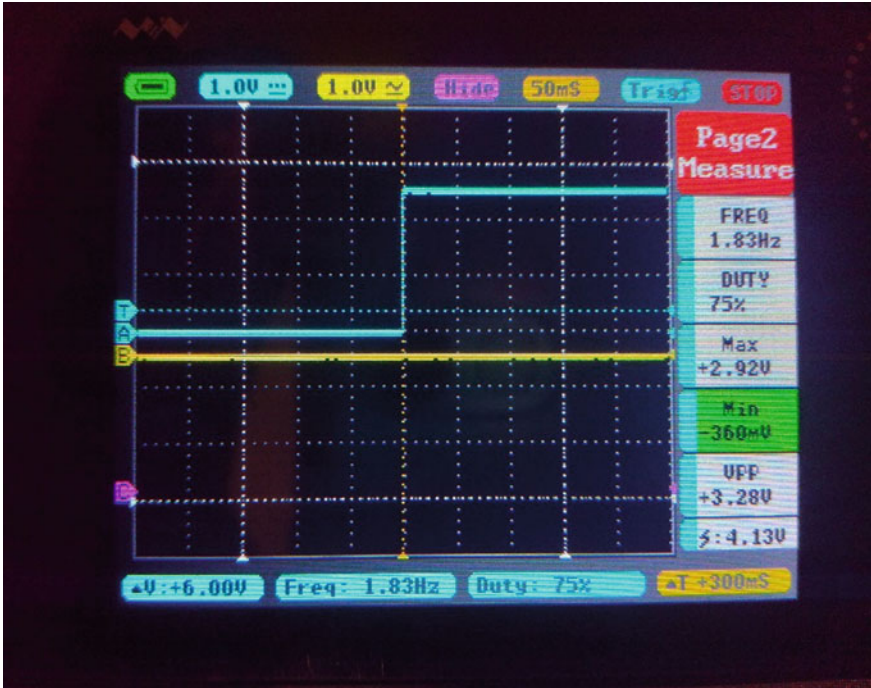


Fig. 11 Signal intensity output with no phase shift when the image from Fig. 3a is simulated

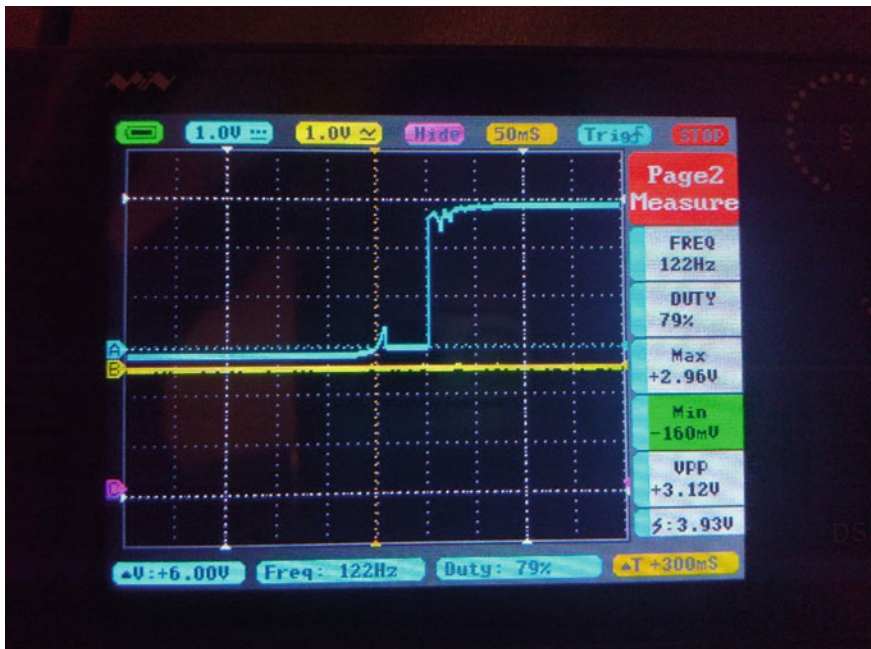
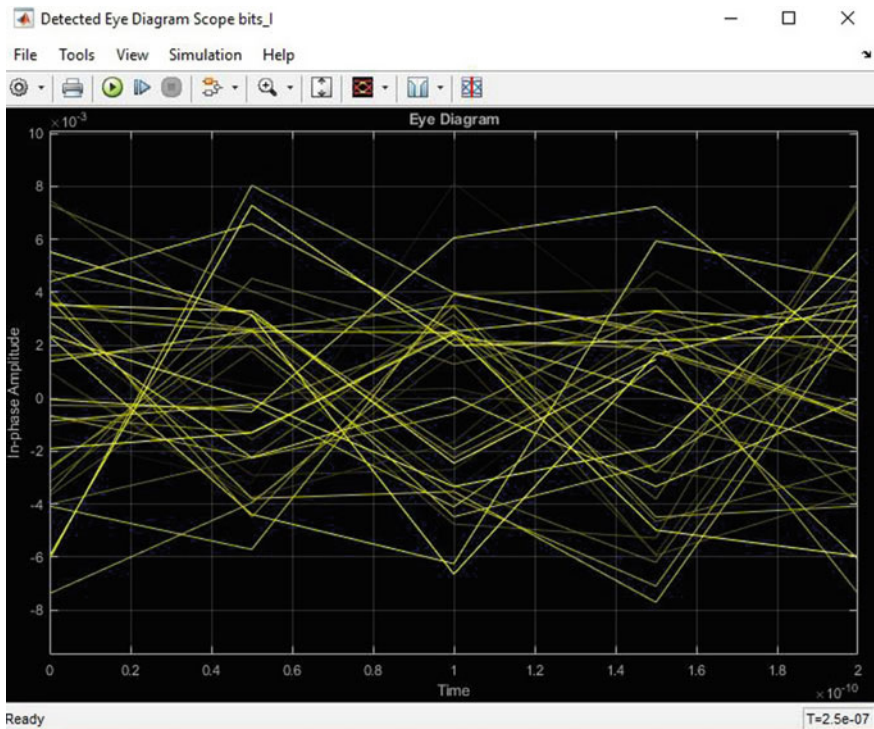


Fig. 12 Signal intensity output with a 50 ms phase shift when the image from Fig. 3b is simulated

Focusing on a fiber optic application, the above block diagram design in Fig. 6 is simulated to mimic internal polarized mode modulation by implementing a software-based model in MATLAB and SIMULINK, accounting for real-world multi-mode fiber optic transmission channel noise and non-linear fading effects in conjunction with various digital modulation and detection techniques [9, 10]. The output results from the fiber optic transmission simulation are explicated in the following subsections.

### 2.3 Internal Modulation of $LP_{01}$ Image Shape Patterns

The fundamental linear polarized mode is  $LP_{01}$  as depicted above. Internal modulation of this  $LP_{01}$  mode is achieved with a digital laser, by toggling the SLM using a computer-clocked frequency, to project a  $LP_{01}$  image shape when representing the ‘On’ bit state and not producing any shape during the ‘Off’ bit state (Fig. 13).



**Fig. 13** Eye diagram of the  $LP_{01}$  transmission at the input of the optical receiver

The detected eye diagram below shows a reduced eye opening with the presence of noise, waveform distortion and attenuation.

The threshold detection between bit states is difficult to correctly distinguish due to the large amount of jitter. As noted from the simulated Bit Error Rate (BER) which is in the order of  $e^{-2}$  at higher bit transmission rates.

The performance of  $LP_{01}$  modulated photonic systems is severely degraded due to fiber impairments dominated by fiber dispersion and non-linearity over long transmission distances.

Such deterioration in the performance due to fiber non-linearity results in the occurrence of high-power spectral components at the carrier signal frequencies of the modulated optical signals. In general, return to zero pulses have broader spectra which are more susceptible to fiber dispersion effects compared to non-return to zero pulses.

## 2.4 Internal Modulation of $LP_{11}$ Image Shape Patterns

The next lower order linear polarized mode is  $LP_{11}$ . Internal modulation of this  $LP_{11}$  mode is achieved with a digital laser, by toggling the SLM using a computer-clocked frequency, to project a  $LP_{11}$  image shape pattern when representing the '0' bit state and switching to a different  $LP_{11}$  image pattern during the '1' bit state, as depicted in Fig. 3. above.

This effectively alternates the optical transmission power of a light wave carrier over the FO medium between the 'On' bit state and 'Off' bit state, by changing the phases of the light carrier waves electric field components, to transmit one bit per symbol (Fig. 14).

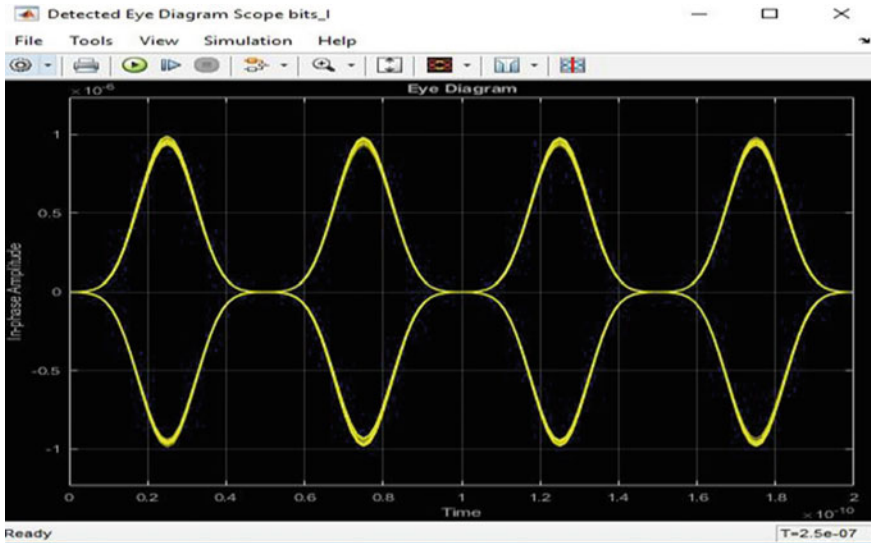


**Fig. 14** Eye diagram of the  $LP_{11}$  transmission at the input of the optical receiver

As evident in the simulated BERs which is in the order of  $e^{-6}$  and from the detected eye diagram above,  $LP_{11}$  modulation offers a greater SNR improvement over  $LP_{01}$  modulation when using an optical-balanced receiver.

Other advantages include a high tolerance to fiber non-linearity, such as intra-channel self-phase modulation (SPM) and inter-channel cross-phase modulation (XPM). The spectra of  $LP_{11}$  modulated waveforms do not contain high-power frequency components which offer more resistance to fiber non-linearity.

## 2.5 Internal Modulation of $LP_{21}$ Image Shape Patterns

An ascending linear polarized mode index is  $LP_{21}$ . Internal modulation of this  $LP_{21}$  mode is achieved with a digital laser, by toggling the SLM using a computer-clocked frequency, to project a  $LP_{21}$  image shape pattern when representing the bit states for the in-phase arm and switching to a different  $LP_{21}$  image pattern during the bit states for the quadrature arm, as depicted in Fig. 5 above (Fig. 15).

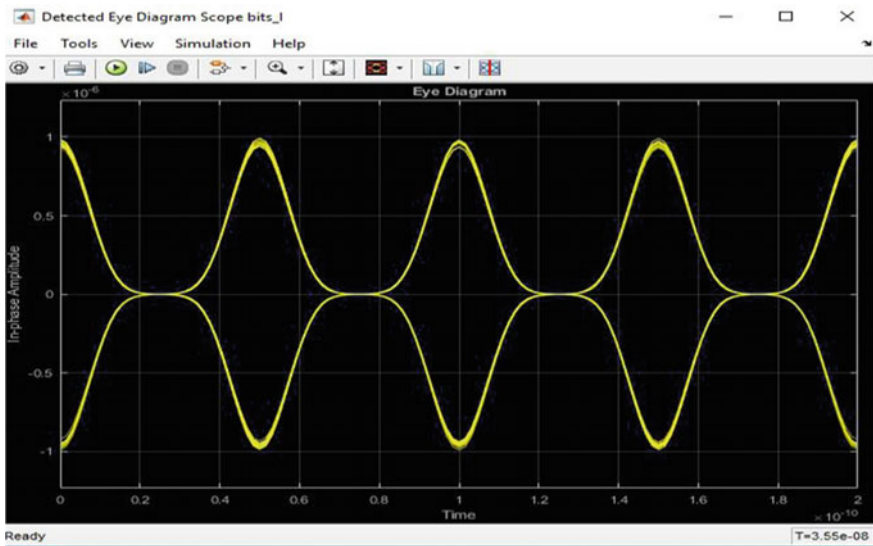


**Fig. 15** Eye diagram of the  $LP_{21}$  transmission at the input of the optical receiver

As evident in the simulated BERs which are in the order of  $e^{-6}$  and from the detected eye diagram above,  $LP_{21}$  modulation offers greater transmission rates over  $LP_{11}$  modulation by transmitting twice as many bits per symbol, although the optical-balanced receiver is of higher complexity in comparison with the  $LP_{11}$  receiver.

The spectra of  $LP_{21}$  modulated waveforms also do not contain high-power frequency components which offer more resistance to fiber non-linearity.  $LP_{21}$  demodulation and detection circuitry are more complex requiring more effort to reconstruct the information stream.

### 3 Performance Summary

The test results indicate that a digital laser hardware implementation combining internal modulation with conventional amplitude and differential phase demodulation can be closely correlated with the performance, i.e., spectral efficiency and BER, of external modulation techniques.

Albeit with reduced cost as polarized modes can be digitally generated and manipulated via software. In comparison, external techniques require expensive customized physical optical elements (i.e., filters, mirrors and lenses).

Furthermore, internal modulation employs a SLM which is a once off hardware investment cost which can produce any amplitude or phase modulated polarized mode at will, by changing the software input to the SLM. Whereas external modulation requires beam splitters, an electro-optic phase modulator hardware such as MZI and multiplexers in conjunction with individual optical elements for a specific polarized mode, necessitating change-out of the optical element to produce other polarized modes. The table below summarizes the various BER calculations for each LP mode (Table 1).

**Table 1** BER performance comparisons between various LP modes

LP mode	Simulated BER @ 100 km Tx distance	Statistical BER @ 100 km Tx distance	Semi analytic BER @ 100 km Tx distance	Simulated BER @ 1000 km Tx distance threshold	Simulated BER @ 7870 km Tx distance threshold	Simulated BER @ 7900 km Tx distance threshold
LP <sub>01</sub>	0.06957	0.0119	0.0419	0.1355		
LP <sub>11</sub>	9.9e-06	3.08e-06	1.73e-06		1.23e-02	
LP <sub>21</sub>	9.9e-06	1.55e-06	1.25e-06			1.6e-02

The simulated BER is the result of the above design block diagrams implemented in SIMULINK, while the statistical BER using ‘erfc’ and the ‘semianalytic’ MATLAB functions are also used for comparison.

Further results are shown for each mode, in relation to the threshold transmission distance for which the BER is beyond the acceptable tolerance levels required for reliable communications.

## 4 Conclusion

### 4.1 Achievements

The rationale for seeking alternate ways to improve data transmission rates and increasing channel capacities, while lowering the cost of implementation and maintaining spectral efficiency, were drivers for the development of internal modulation

techniques via manipulation of digitally generated shape patterns. Internally modulated LP modes reveal a duality with direct and external modulation methodologies. A practical internal modulated solution for implementation using a digital laser source for data transmission was developed in SIMULINK and MATLAB.

Digital laser technology does not require expensive customized optical elements to produce light shapes, coupled with the ability to change the light shape patterns on-the-fly within the electrical domain, thus enabling internal digital modulation of data is proven as the next evolutionary step in multi-mode optical fiber communications.

## 4.2 Future Research

### Demodulation by Image Processing of Received Light Patterns

A cost-effective coherent detection method is to consider building an optical correlator, comprising of Fourier transform lenses, beam splitter and SLMs. The received light signal is split and passed through a lens and projected onto a SLM detector which has been programmed with a filter for specific features of interest. The other split signal is passed through a lens and projected onto a separate SLM detector with no filtering. The output from both SLMs can be fed to a computer routine which correlates the light images to demodulate the symbol bits.

### Twisted Light Transmission Via Over the Air

Internal modulation can be used in conjunction with high-speed planar light valve (PLV) SLMs, to modulate the orbital angular momentum polarized light shapes as wireless non-line-of-sight transmission in free space over an unguided medium. This solution can also be adapted to visible light communication (VLC) technology using a Light Emitting Diode (LED) source in high speed line of sight communications.

### Integrated Optical CPUs

The compact nature of the digital laser and high-speed SLMs combined with LP mode phase modulation can be used to increase motherboard bus data speeds and save real estate on the central processing unit (CPU) hardware design, thereby eliminating the need for bulky optical elements currently used.

## References

1. Le Nguyen, B.: Optical fiber communication systems with MATLAB and simulink models, 2nd edn. CRC Press, Taylor and Francis Group, New York (2014)
2. Lan, X.J.: Laser technology, 2nd edn. CRC Press, Taylor and Francis Group, New York (2010)
3. Photonics Handbook. Polarization Mode Dispersion, <http://www.photonics.com/EDU/Handbook.aspx?AID=25148>. Last accessed
4. Katsunari, O.: Fundamentals of optical waveguides, 2nd edn. Elsevier, USA (2006)
5. Milione, G., Sztul, H.I., Nolan, D.A., Alfano, R.R.: Higher-order Poincare sphere, Stokes parameters, and the angular momentum of light. *Phys. Rev. Lett.* **107**, 053601 (2011)

6. Ngcobo, S., Litvin, I., Burger, L., Forbes, A.: A digital laser for on-demand laser modes. *Nat. Commun.* **2**(1), 22–58 (2006)
7. Payne, A., De Groot, W., Monteverde, R., Amm, D.: Enabling high data-rate imaging applications with grating light valve technology. In: *Photonics West-Micromachining and Microfabrication Symposium*, CA, USA (2004)
8. Proakis, J.G.: *Digital communications*, 4th edn. Mc Graw-Hill, New York (2001)
9. Le Nguyen, B.: MATLAB simulink simulation platform for photonic transmission systems. *Int. J. Commun. Netw. Syst. Sci.* **2**(2), 91–117 (2009)
10. Iannone, E., Matera, F., Mecozzi, A., Settembre, M.: *Nonlinear optical communication networks*. Wiley, New York (1998)





# Fiber Bragg Grating Thermal Gas Flow Sensor by 980 nm Laser Heating

Guohui Lyu<sup>1</sup>, Jinling Zhang<sup>1</sup>, Chaozheng Wang<sup>1</sup>, Keda Wang<sup>1</sup>,  
Yan Zhang<sup>1</sup>, and Xu Jiang<sup>2(✉)</sup>

<sup>1</sup> Research Center for Fiber, Optic Sensing Technology National Local Joint Engineering, and the College of Electronic Engineering, Heilongjiang University, Harbin, China

lvguohui@hlju.edu.cn

<sup>2</sup> College of Data Science and Technology, Heilongjiang University, Harbin, China

1995042@hlju.edu.cn

**Abstract.** This paper aims at solving the explosion-proof problem in the field of electronic thermal flow meter measuring gas flow, a new thermal flow sensor based on optical fiber heat transfer instead of heating resistor was developed, fiber Bragg gratings are used in place of conventional thermistors to measure the temperature of gaseous media and heat dissipating units, heated light source using 980 nm semiconductor laser, replacement of traditional heating resistors with photothermal conversion films for all-optical no-electricity measurements, intrinsically safe all-optical measurement design is implemented, the risk of explosion from heating circuits is minimized. Experimental results show good agreement between flow and temperature difference, the average mass flow resolution is 0.072 g/s, the method to increase measurement sensitivity is discussed.

**Keywords:** Fiber bragg grating · Thermal mass flowmeter · King's law · Constant power method · Photothermal conversion film

## 1 Introduction

Gas flow measurement is the key in the natural gas industry. In recent decades, thermal mass flowmeter (thermal mass flowmeter, tmf) has been widely used in many kinds of pipelines and different types of gases [1, 2]. Good reproducibility and other advantages are widely used in gas flow measurement [3].

In traditional gas flow measurement applications, thermistors are often used as temperature sensing components. In order to prevent short circuits or sparks, the explosion-proof mechanism must be carefully designed, especially in the electric heating section. At the same time, it should be pointed out that in recent years, in order to reduce safety risks, the gas industry needs new technologies to replace traditional electric heating flow sensing instruments.

We have proposed an FBG-based sensor for measuring the flow of gas, which has many advantages compared to traditional electronic sensors [4], such as electroless



measurement, anti-electromagnetic interference, intrinsic safety and high sensitivity, easy to achieve multi-parameter measurement. It is also ideal for temperature and pressure measurements in flammable and explosive environments. For FBG-based thermal flow sensors, the structural design of the heat dissipation body is a challenging part. In this paper, based on the special requirements of gas flow measurement in flammable and explosive environment, a thermal flow sensor based on FBG is proposed. The 980 nm laser is used as the heating source, and the photothermal conversion structure which is different from the optical fiber dislocation welding scheme is designed. The experiment shows that the sensor can realize the full light flow measurement of explosion-proof safety.

## 2 Principle

### 2.1 Measurement Scheme

This paper proposes a fiber-grating gas flow sensor based on the measurement of temperature difference to achieve flow measurement. Figure 1 shows the measurement principle diagram. Two FBG-based temperature sensing units are integrated in the measuring pipeline. One of the temperature sensing units is equipped with a light heating module to form a photothermal conversion unit. The 980 nm laser of the light source outputs a constant optical power for heating the photothermal conversion unit, and the temperature difference between the two FBG temperature sensing units is monitored in real time by the fiber-grating demodulation device. When there is no flow in the pipeline, the temperature difference between the two FBG temperature measuring units is the largest. When there is flow in the pipe, the gas flow will take away the heat of the heating unit, causing the temperature of the heating unit to drop. In a short time, due to the constant heating power and flow rate, the temperature of the heating unit will stop falling and tend to be stable. Therefore, the temperature difference between the two temperature measuring units will reach a lower stable value relative to the no flow condition. The larger the gas flow rate, the smaller the temperature difference. By measuring the temperature difference, the gas flow in the pipeline can be obtained.

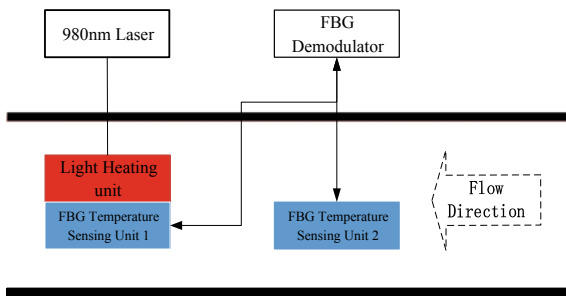


**Fig. 1** Diagram of the optical sensor of gas flow

## 2.2 Measurement Principle

The basic measurement principles used in TMF can be divided into two categories. According to the basic principles, TMF can be divided into thermal distributed (thermal profile flowmeter) TMF and Kim's law (King's law thermal mass flowmeter) TMF. The principle of flowmeter designed in this paper is based on Kim's Law. According to King's Law, the heat dissipation rate of the heating wire in the gas flow field can be expressed as [5, 6]:

$$\frac{H}{L} = \Delta T \cdot \left[ \lambda + 2(\pi \cdot \lambda \cdot c_v \cdot \rho \cdot U \cdot d)^{\frac{1}{2}} \right] \quad (1)$$

In formula (1),  $H/L$  is a heat dissipation rate per unit length of the heating wire when the gas flows, and the unit is  $J/(m \cdot h)$ .  $\Delta T$  is the average elevated temperature of the heating wire in  $K$ .  $\lambda$  is the thermal conductivity in units of  $J/(h \cdot m \cdot K)$ .  $CV$  is the constant volume specific heat capacity, and the unit is  $J/(kg \cdot K)$ .  $\rho$  is the gas density in  $kg/m^3$ .  $U$  is the flow rate of the gas in  $m/h$ .  $d$  is the diameter of the heating wire in  $m$ .

Two temperature measuring elements are, respectively, placed in the measuring pipe, and one of the temperature measuring elements measures the temperature  $T$  of the gas. The other temperature measuring element has a self-heating function and is heated as a heat dissipating body by a certain power, and its temperature is  $TV$  higher than the temperature  $T$  of the gas. When the gas flow rate is increased, the heat on the self-heating temperature measuring element is taken away, so that the temperature of the self-heating temperature measuring element is lowered, and the temperature difference between the two temperature measuring elements is  $\Delta T = TV - T$ . When the gas is stationary and the flow rate is 0, the temperature  $TV$  is the highest, then the temperature difference  $\Delta T$  between the two temperature measuring elements is maximum; the larger the gas flow rate, the heat exchange flow between the heat dissipating body and the airflow is taken from the heating body. The more heat that is taken, the lower the temperature  $TV$  and the lower the temperature difference.

When the heat dissipating body and the flowing gas in the pipe are in thermal equilibrium state, the relationship between the heating power  $P$  consumed by the heat dissipating body and the heat  $W$  dissipated by the heat dissipating body is:

$$W = f \cdot P \cdot L \quad (2)$$

In formula (2),  $f$  is a constant and  $L$  is the length of the heating wire. According to the heat conduction theory, the relationship between the heat loss of the heat dissipation body and its heat dissipation rate is:

$$W = H/L \cdot L \quad (3)$$

The relationship between the power  $P$  of the heat dissipation body and the temperature difference  $\Delta T$  is:

$$W = f \cdot P \cdot L = \Delta T \cdot \left[ \lambda + 2(\pi \cdot \lambda \cdot c_v \cdot \rho \cdot U \cdot d)^{\frac{1}{2}} \right] \cdot L \quad (4)$$

$$P = \Delta T \cdot \left[ \lambda + 2(\pi \cdot \lambda \cdot c_v \cdot \rho \cdot U \cdot d)^{\frac{1}{2}} \right] / f \quad (5)$$

From Eq. (5), the flow rate of the gas can be calculated, multiplied by the coefficient between the point flow rate and the average flow velocity of the pipe and the density of the gas and the mass flow rate  $q_m$  of the gas flow area.

$$\frac{P}{\Delta T} = D + E \cdot q_m^k \quad (6)$$

In Eq. (6),  $E$  is a coefficient related to the physical. In Eq. (6),  $E$  is a coefficient related to the physical properties of the gas to be tested. If the composition and physical properties of the gas to be tested remain stable,  $E$  can be considered as a constant.  $D$  is a constant related to the actual flow of the gas. When a constant heating power is supplied to the heat dissipating body, the mass flow rate of the gas at this time can be calculated by measuring the temperature difference  $\Delta T$  between the two temperature measuring elements, which is called constant power metering method. The flow meter designed in this paper adopts the constant power measurement method. According to the above formula, there is a significant negative correlation between the mass flow rate  $q_m$  and the temperature difference  $\Delta T$ . The larger the  $q_m$ , the lower the  $\Delta T$ .

### 2.3 FBG Temperature Measurement Principle

FBG is a reflective narrow-bandwidth optical filter component. When incident light enters FBG, the incident light is divided into two as transmitted light and reflected light [7] and the reflected light needs to satisfy the Bragg condition of FBG,

$$\lambda_B = 2 \cdot n_{\text{eff}} \cdot \Lambda \quad (7)$$

In formula (7),  $\lambda_B$  is the Bragg wavelength reflected by the FBG;  $n_{\text{eff}}$  is the effective refractive index of the fiber core;  $\Lambda$  is the grating period of the FBG. Differential Eq. (7)

$$\Delta \lambda_B = 2 \cdot \Lambda \cdot \Delta n_{\text{eff}} + 2 \cdot n_{\text{eff}} \cdot \Delta \Lambda \quad (8)$$

When the external parameters such as temperature, pressure, strain, and vibration change slightly, the  $\Lambda$  and  $n_{\text{eff}}$  of FBG change, which causes the Bragg wavelength of FBG to drift, and the single parameter variation and Bragg wavelength shift. There is a certain relationship between the quantities, so the Bragg wavelength of the FBG is modulated by changes in the external environmental parameters. Then, using the FBG wavelength demodulation device to demodulate the value of the Bragg wavelength, the change information of the physical parameter to be measured outside can be obtained, which is the basic sensing principle of FBG.

### 3 Thermal Flow Sensor Design

#### 3.1 Structural Design of Large-Sized Equal-Strength Cantilever Beam

The overall design of the fiber-optic thermal gas flow sensor includes a metering pipe section with a flange, and the FBG temperature sensing unit 1 with the light heating unit and the FBG temperature sensing unit 2 are sequentially integrated in the flow pipe section, as shown in Fig. 2.

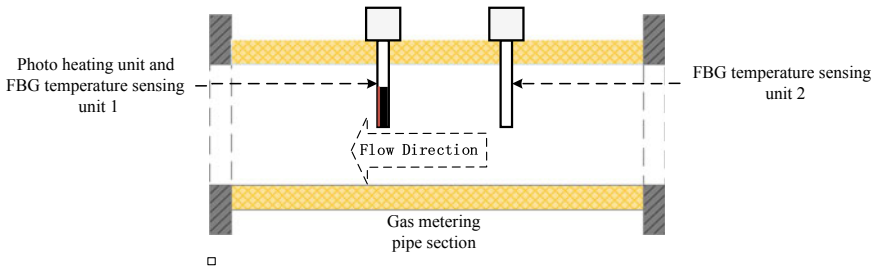
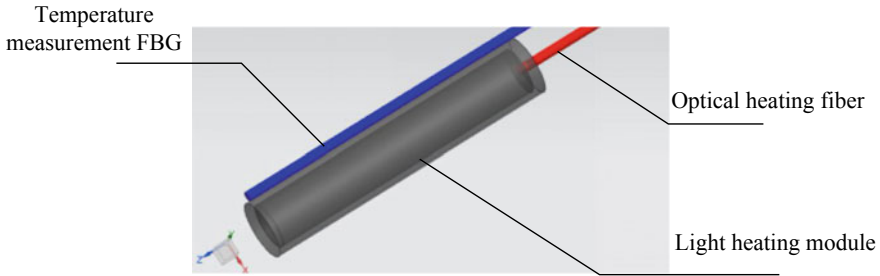
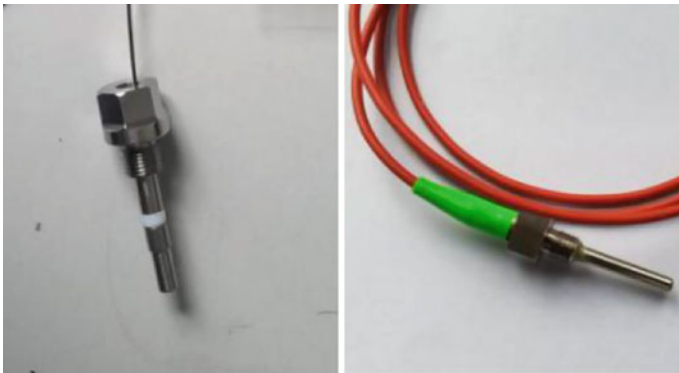


Fig. 2 Overall design of optical thermal gas flow sensor

The flow sensor designed in this paper uses laser heating module and FBG temperature measuring module to replace heating and temperature measuring resistance wire to prevent gas explosion caused by electric spark. As a transmission carrier of optical energy, the optical fiber is coupled into the laser heating module through a certain structural design, and the light is absorbed by the material on the inner surface of the module and converted into thermal energy. The laser heating module selects the light absorbing film as the light heating material and uses the ductility of the base material to make the light absorbing coating inward into a hollow black-like structure. The top of the laser heating module has a small diameter hole for the light-transmitting fiber to enter the structure. For the temperature of the laser heating module, the FBG temperature measurement module is used for measurement. As shown in Fig. 3, in order to ensure the heating rate of the module and the heat balance with the gas, the volume of the module should not be too large. FBG is a stress-free package. The metal tube package temperature measurement FBG can prevent the FBG from being affected by the vibration and pressure in the pipeline, and the stainless steel has high-temperature sensitivity and good heat transfer performance. In actual processing, the diameter of the fiber core is slightly smaller than the inner diameter of the thin metal tube, ensuring that the metal tube does not affect the temperature sensitivity of the FBG. The light heating unit and the temperature sensing unit are packaged in a stainless steel tube, and Fig. 4 shows a physical diagram of sensor processing.



**Fig. 3** Light heating and temperature sensing head



**Fig. 4** Large-sized cantilever beam simulation

## 4 Sensor Experiment and Analysis

In order to verify the linearity of the temperature sensing unit, the FBG temperature sensing unit 1 and the FBG temperature sensing unit 2 are, respectively, calibrated and tested. The equipment mainly includes a cryostat and an FBG wavelength demodulation device.

The calibration relationship between the wavelength drift amount and the temperature is shown in Fig. 5. The temperature calibration range of the FBG temperature sensing unit 1 is 10–80 °C, and the temperature change interval is 5 °C. The Bragg wavelength reflected by FBG in this temperature range increased from 1531.091 to 1531.785 nm, the wavelength change amount was 0.694 nm, and the temperature sensitivity coefficient was 9.9 pm/°C. The wavelength data of the FGB temperature measurement module is linearly fitted with the temperature data. The linear correlation coefficient of the fitting result is 0.99661, and the linearity is good, which meets the experimental requirements.

The FBG temperature sensing unit 2 was subjected to a calibration test in the same manner. The calibration test data of the sensor is shown in Fig. 6. The temperature calibration range of the FBG gas temperature sensor is still 10–80 °C, and the Bragg

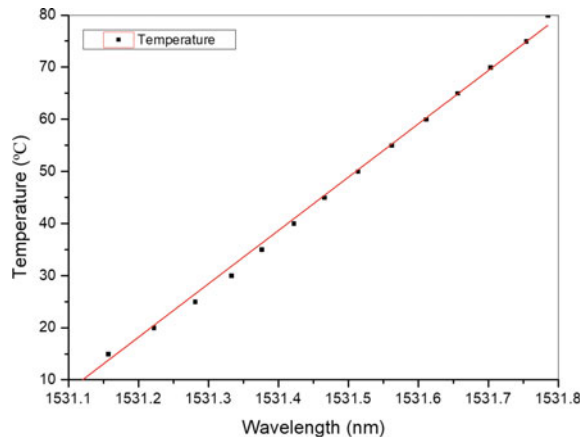


**Fig. 5** Sensor calibration data fitting curve

wavelength range of FBG is 1546.013–1546.573 nm, and the wavelength variation is 0.56 nm. Linear fitting of the wavelength and temperature data, the linear correlation coefficient of the fitting result is 0.99542, and the linearity is good.

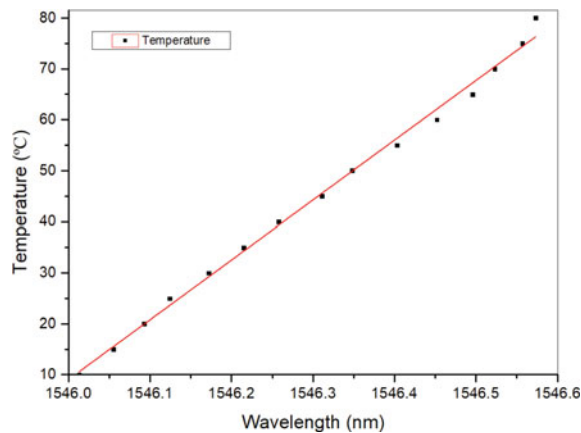


**Fig. 6** Sensor calibration data fitting curve

The calibration test scheme adopted in this paper is the way to compare the flowmeter to be calibrated with the standard flowmeter sensor. The flowmeter to be calibrated and the standard flow sensor are placed in the same gas pipeline with uniform gas flow, so that the two devices are as close as possible to reduce the flow error between the two. The simulation experiment uses air instead of gas for flow measurement. The equipment for providing gas source includes screw air compressor and vertical gas storage tank, see Fig. 7. The 980 nm laser is used to heat the light heating module, and the temperature sensing signal of the FBG is demodulated by the

FBG demodulation device. Demodulation through the wavelength selection characteristic of the Fabry-Perot (F-P) cavity. The narrowband spectrum reflected by the sensing grating enters the F-P filter through the coupler. When the spectrum reflected by the inductive grating coincides with the transmission spectrum of the filter, the output optical power of the filter is the largest. The transmission spectrum of the F-P cavity is related to its spacing, and the spacing of the F-P cavity is controlled by the piezoelectric scanning voltage. Therefore, the reflected light wavelength demodulation can be realized by detecting the scanning voltage corresponding to the maximum light intensity value [8]. The parameters of the demodulation equipment and the 980 nm laser are shown in Tables 1 and 2.

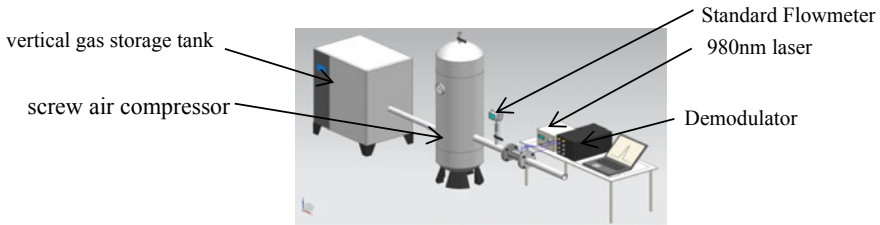


**Fig. 7** Diagram of the test system

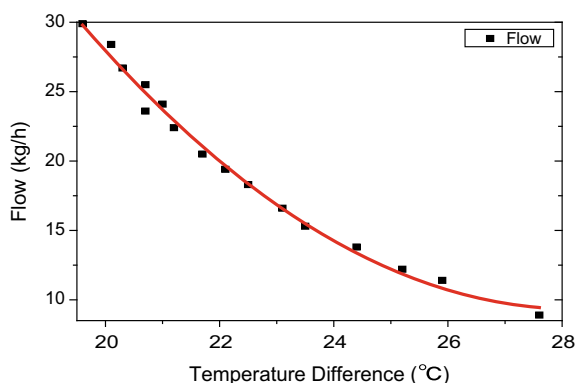
The relationship between the flow rate and the temperature difference of the central wavelength shift reaction of the two FBG temperature measuring units was tested to obtain a relationship between the temperature difference  $\Delta T$  and the flow rate  $q$ , as shown in Fig. 8. It can be seen from the curve that the relationship between the flow rate  $qm$  and the temperature difference  $\Delta T$  is in good agreement with the theoretical prediction. It should be noted that in the low flow range in the curve, the temperature difference for the measurement resolution is sufficiently large, and in the high flow region, the temperature difference becomes small, which may cause the measurement sensitivity to decrease. In practical measurement applications, this problem should be solved by increasing the heating optical power, and the following factors that may affect the measurement reliability need to be considered: the resolution of the FBG demodulation device, the bandwidth of the FBG, and the accuracy of the calibration flow meter, and the volatility of the flow. When the temperature difference drops by 1 °C, the average flow value changes by 0.72 g/s, and the resolution of the FBG demodulation device is 1 pm, that is, 0.1 °C, the average mass flow resolution of the system is 0.072 g/s.

**Table 1** Parameters of FBG demodulation instrument

Parameters	Value
Wavelength range	1525–1565 nm
Resolution	1 pm

**Table 2** Parameters of 980 nm laser

Parameters (25 °C)	Value
Peak power	1.14 W
Central wavelength	980 nm
Center wavelength shift	$\pm 3$ nm
3 dB width	$< 3$ nm
Threshold current	0.4A
Operating current	$< 1.4$ A
Operating voltage	2.2 V

**Fig. 8** The fitting curve of flow temperature difference

## 5 Conclusion

To sum up, this paper presents a thermal gas flow sensor based on FBG, which has the advantages of strong electromagnetic anti-jamming ability and reliable structure. The experimental results show good agreement with the theoretical analysis. The sensor probe based on light heating can ensure the explosion-proof safety characteristics in gas flow measurement, which is of practical significance to the flow measurement in flammable and explosive gas environment. The method of further improving the accuracy of flow measurement is discussed. Through the calibration of the calibration platform, the thermal response of the thermal gas flow sensor based on fiber grating is sensitive, and the correspondence between temperature and flow is clear. The fiber-optic grating thermal flow measurement method is feasible and has broad application prospects in the flammable and explosive occasions of gas metering.



## References

1. Viswanathan, M.: Design and development of thermal mass flowmeters for high pressure applications. *Flow Meas. Instrum.* **13**(3), 95–102 (2002)
2. Baker, R.C., Gimson, C.: The effects of manufacturing methods on the precision of insertion and in-line thermal mass flow meters. *Flow Meas. Instrum.* **12**(2), 113–121 (2001)
3. Huijsing, J.H., Van Dorp, A.L.C.: Thermal mass-flow meter. *J. Phys. E Sci. Instrum.* **21**(10), 994 (1994)
4. Liu, Y., Zhang, J.: Model study of the influence of ambient temperature and installation types on surface temperature measurement by using a fiber Bragg grating sensor. *Sensors* **16**, 975 (2016)
5. King, L.V.: On the convection of heat from small cylinders in a stream of fluid determination of the convection constants of small platinum wires with application to hot wires anemometry. *Proceedings of the Royal Society of London. Series A* (90), 563–570 (1914)
6. Jiang, X., Wang, K., Li, J.: Optical sensor of thermal gas flow based on fiber Bragg grating. *Sensors* **17**(2), 374 (2017)
7. Pospori, A., Marques, C.A.F., Bang, O.: Polymer optical fiber Bragg grating inscription with a single UV laser pulse. *Opt. Express* **25**(8), 9028–9038 (2017)
8. Wu, J., Wu, H., Huang, J.: Research progress in signal demodulation technology of fiber Bragg grating sensors. *Chinese Optics* **7**(4), 519–531 (2014)



# Policy-Based Comparison-Triggered Defragmentation Mechanism for Elastic Optical Networks

Lingqi Luo, Xiaoling Liu, Jingwen Zhang, Cong Yu,  
and Jianhua Shen<sup>(✉)</sup>

School of Communications and Information Engineering, Nanjing University  
of Posts and Telecommunications (NJUPT), Nanjing, China  
shenjha@njupt.edu.cn

**Abstract.** Spectrum fragment is one of the most important issues in elastic optical networks (EONs). To solve the shortcomings of traditional defragmentation mechanisms, a policy-based comparison-triggered defragmentation mechanism (P-CTD) is proposed. The improved mechanism will analyze the arrived traffic request and current spectrum resource situation firstly, then compare and judge whether to trigger spectrum defragmentation according to preset policy. Theoretical analysis and numerical simulation results show that compared with the traditional mechanisms, the proposed P-CTD mechanism can reduce the bandwidth blocking probability (BBP) as 8.73% and improve the resource utilization ratio as 15.26%, respectively.

**Keywords:** Elastic optical networks (EONs) · Spectrum defragmentation · P-CTD · Bandwidth blocking probability (BBP) · Network utilization

## 1 Introduction

With the rapid development of many new services and applications such as big data, cloud computing and artificial intelligence, the differences between customer traffic requirements and network resource have been increasing, which raised continuous growing requirements for flexibility, scalability, openness, etc. Compared with the traditional wavelength-division multiplexing (WDM) technology, elastic optical networks (EONs) can provide many new features including more flexible network architecture and finer spectrum granularity, which makes EON as one of the promising technologies for the future Internet. EONs have been proved its flexible frequency allocation for the dynamic bandwidth requirements environment which can improve the network resource utilization and effectively reduces the blocking probability, respectively [1, 2]. However, in the future complex network environment, some serious spectrum fragmentation problems may occur due to the spectrum resources are continuously allocated and released, which will lead to spectrum fragments and affect the resource allocation for subsequent coming traffic. Furthermore, the issue of fragments may reduce the spectrum utilization and even cause network congestion [3]. Defragmentation is widely accepted as effective ways to reduce or eliminate spectrum

fragmentation while when to trigger the defragmentation mechanism and how to select the suitable defragmentation mechanism is very important for EON.

Recently, many researchers have proposed some solutions. Wang R et al. suggested to classify the spectrum defragmentation mechanism into two categories: active and passive modes [4]. Further, Wang C et al. defined two defragmentation mechanisms including batch defragmentation (BD) [5] and defragmentation upon blocking (BTD) [6], respectively. The BD mechanism will implement spectrum defragmentation regularly, and the BTD mechanism performs defragmentation only when the service requirement on prime optical path is blocked. Unfortunately, the former BD mechanism has little relationship with actual traffic requirement, which may lead to poor network resource utilization. The BTD mechanism only triggers defragmentation when the traffic is blocked, which may lead to higher bandwidth blocking probability (BBP). Then, Cugini et al. proposed a push-pull defragmentation mechanism, which will immediately allocate resource to the existing service once suitable spectrum resources appearing [7]. It can also be classified as an active defragmentation mechanism depending on the definition proposed by Wang R [4]. Although the proposed solution in [7] can optimize traffic allocation, some shortcomings cannot be ignored such as the high complexity and network resources wasting. In general, most traditional triggered defragmentation mechanisms have obvious shortcomings, i.e., the active triggered mechanism lacks corresponding relationship with traffic requirements, which may lead to poor network resource utilization. On the contrary, the passive triggered mechanism will suffer from poor bandwidth blocking performance, etc.

In this paper, we proposed a policy-based comparison-triggered defragmentation mechanism (P-CTD). The proposed P-CTD mechanism will judge whether to implement triggered defragmentation procedure by comparing the current spectrum status with the arriving traffic requirements, by which it can overcome the shortcomings of the traditional triggered mechanism. The rest of this paper is organized as follows. Section 2 presents the principles of the proposed triggered defragmentation mechanism. Section 3 gives the numerical simulations and results analysis. Section 4 summarized our conclusions.

## 2 Principle of P-CTD Mechanism

### 2.1 Policy-Based Comparison-Triggered Defragmentation Mechanism (P-CTD)

Due to the implementation of flexible network nodes such as bandwidth variable transceiver (BVT), EONs has good flexibility to transmit differentiated traffics [8]. However, considering the future complex network environment, the frequency spectrum may be allocated and released frequently. Thus more and more spectrum fragments will appear. At this time, there will be difficult to allocate available spectrum for arriving service requirements considering the frequency spectrum consistency and continuity constraints in EON.

To solve this problem, the proposed P-CTD will implement comparison procedure before triggering defragmentation. Firstly, the spectrum availability before defragmentation

$(a_{bd})$  and traffic requirement ( $r_{ii}$ ) will be calculated. Then these two values will be compared to judge which value is bigger. Then the spectrum availability after defragmentation ( $a_{ad}$ ) should be calculated if the value of  $r_{ii}$  is bigger than  $a_{bd}$ . After that, the value of  $r_{ii}$  and  $a_{ad}$  will be compared. Only can the defragmentation be triggered when  $r_{ii}$  is larger than  $a_{bd}$  but less than or equal to  $a_{ad}$ . The detailed implementation procedure of P-CTD mechanism is shown in Fig. 1.

Considering most commercial optical network equipment ports in current telecom network are mainly 100 and 40 G, which will combine with the standard forward error correction (FEC) scheme, the redundancy overhead is defined as about 25% at most. Therefore, the minimum frequency slot unit in EONs can be set to 12.5 GHz, by which we can calculate that the number of frequency slots required for a single traffic is generally not more than 10 [9]. It is assumed that the traffic arrives within a fixed time window and conform to the Poisson distribution and the number of frequency slots ( $f_i$ ) required by the  $i$ th traffic is from 1 to 10.

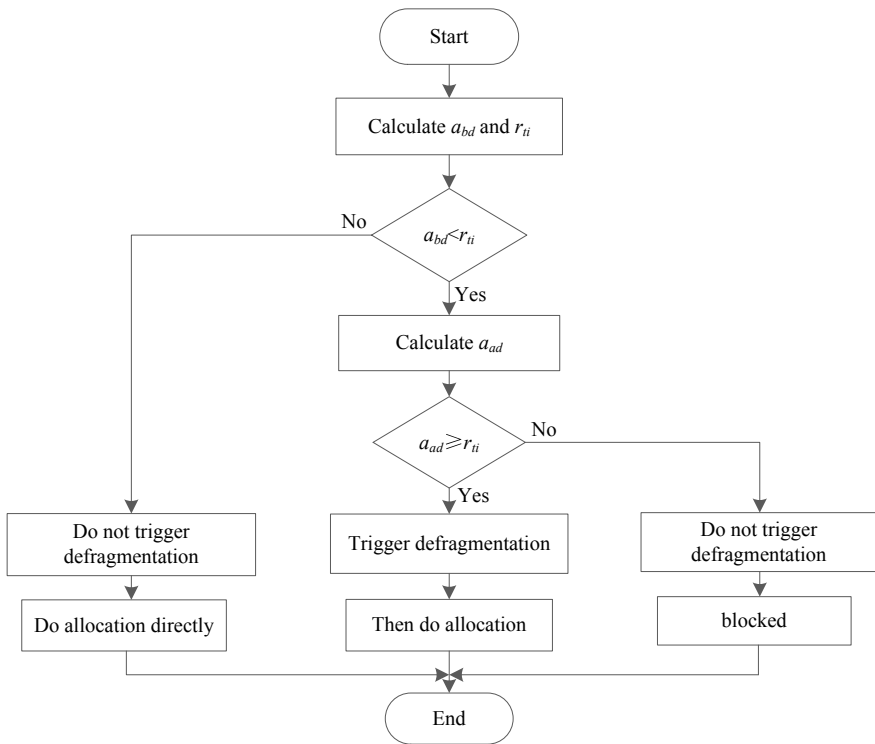


Fig. 1 Flowchart of P-CTD

The three important parameters denoted in Fig. 1,  $a_{bd}$ ,  $a_{ad}$ , and  $r_{ti}$ , are defined as follows

$$a_{bd} = \frac{1}{L} \cdot \sum_{i=1}^n \left( b_i \cdot \frac{b_i}{\sum_{i=1}^n b_i} \right) \tag{1}$$

$$r_{ti} = \frac{f_i}{L} \tag{2}$$

$$a_{ad} = \frac{1}{L} \cdot \sum_{i=1}^n b_i \tag{3}$$

Here  $b_i$  indicates the number of frequency slots in the  $i$ th frequency block with free frequency slots,  $n$  is the total number of frequency blocks with free frequency slots,  $f_i$  is the number of frequency slots required by the corresponding traffic, respectively.

### 2.2 Implementation Example of P-CTD, BD and BTD

Figure 2 shows an implementation example of two traditional triggered mechanisms (BD and BTD) and proposed P-CTD mechanism.

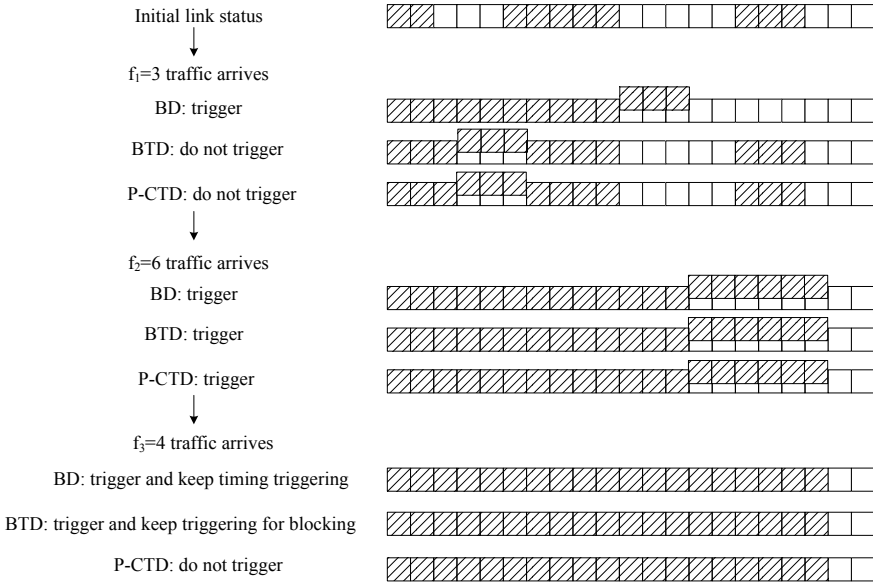


**Fig. 2** An example of the three triggered mechanisms

The dashed area of Fig. 2 indicates that the frequency slot has been already occupied while the blank area indicates that the frequency slot is free. Assumed there are totally 21 frequency slots on the link with 10 slots be occupied initially. The remaining three free blocks have frequency slots with number of 3, 5 and 3, respectively. In this paper, the default spectrum allocation mode is first fit (FF). Without loss of generality, assuming that there are three traffic services arriving in a certain time interval with bandwidth requirements of 3, 6 and 4 frequency slots, respectively. The time interval between each request is the same and equal to the period of BD. Firstly, the traffic with bandwidth request of 3 frequency slots arrives, the defragmentation will be triggered under BD mechanism while there is no defragmentation under BTD for no blocking is detected. According to the steps of P-CTD described in Fig. 1, we can calculate that  $a_{bd} = 0.160$  and  $r_{t1} = 0.143$ , and  $a_{bd} \geq r_{t1}$  which shows there is no need to trigger defragmentation. The traffic with request of 3 frequency slots is then allocated in this spectrum. Secondly, the traffic with bandwidth request of 6 frequency slots arrives, it still has to perform defragmentation under BD mechanism. And this time, the network detects the blocking event, so it also triggers defragmentation under BTD. As for P-CTD mechanism, we can know that  $a_{bd} = 0.202 < r_{t2} = 0.286$  by calculation. Then we can calculate out  $a_{ad}$  and  $a_{ad} = 0.381 \geq r_{t2}$ , which indicates that it is necessary to perform defragmentation now. After defragmentation, the traffic with request of 6 frequency slots can be allocated in this spectrum. Finally, the traffic with bandwidth request of 4 frequency slots arrives. Defragmentation still be performed under BD mechanism and will continue over time. The BTD mechanism will also trigger defragmentation all the time for the current spectrum resource obviously cannot provide service to the traffic. Although we cannot change current situation at once, we will not trigger the defragmentation under P-CTD because of  $a_{ad} = a_{bd} = 0.095 < r_{t3} = 0.190$ , which can save some network resources. Then we marked this traffic blocked.

It can be seen that the improved triggered defragmentation mechanism fully considers both the current spectrum resources and the arrival traffic requests and maximizes the utilization ratio of the current spectrum resources by analyzing the requests, so that the limited spectrum can accommodate as much traffic as possible, and unnecessary defragmentation as well as the overall bandwidth blocking probability are reduced.

### 3 Simulation and Discussion

In order to verify the performance of proposed P-CTD mechanism, numerical simulation method is used to compare with different schemes, i.e., without defragmentation (W/O D), BD mechanism, and BTD mechanism, respectively. The network topology used in the simulation is the NSFNET network with 14 nodes and 21 links. Assumes that there is only one fiber pair on each link and the total spectrum bandwidth of each fiber is set as 4 THz. The selected frequency slot is 12.5 GHz and the number of frequency slots is 320, respectively [10].

As mentioned above, P-CTD mechanism aims to reduce bandwidth blocking probability (BBP), thus can optimize network resources utilization and provide resource for subsequent coming traffic as much as possible. Therefore, the main

performance evaluation for simulation is BBP and resource utilization ratio [11]. And BBP is defined as follows.

$$BBP = \frac{BW_b}{BW_a} \tag{4}$$

Here  $BW_b$  is the blocked traffic bandwidth and  $BW_a$  is the total bandwidth of the traffic. Resource utilization ratio is defined as follows.

$$UR = \frac{N_{ed}}{N_{ad}} \tag{5}$$

Here  $N_{ed}$  is the effective number of defragmentation and  $N_{ad}$  is the total number of defragmentation. Figures 3 and 4 show the simulation results of performance comparison of BBP and resource utilization ratio, respectively.

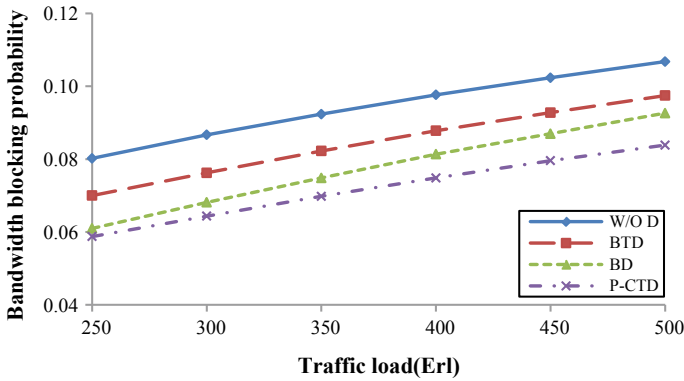


Fig. 3 Comparison of BBP

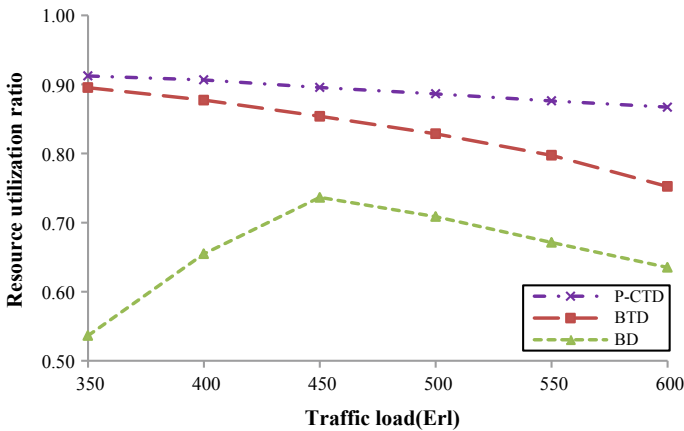


Fig. 4 Comparison of resource utilization ratio

It can be seen in Fig. 3 that the BBP performance of all the four mechanisms decreases with the traffic load increasing, while P-CTD mechanism can achieve the optimal performance. When traffic load is 500 Erl, the BBP for P-CTD is 8.32%, i.e., about 8.73% lower than that of BD, which provides the best performance among the other three mechanisms. In Fig. 4, we can see that with the continuous increase of the traffic load, P-CTD has maintained a high resource utilization ratio at about 90%, which has a significant improvement compared with the performance under BTD and BD scenarios. When the traffic load is 600 Erl, the resource utilization ratio of P-CTD is 86.71%, which makes about 15.26% higher than that of BTD. BD has been performing spectrum defragmentation at a fixed frequency, so as the traffic load continues to increase, the resource utilization ratio for BD mechanism arises firstly and then gradually decreases after reaching the peak. When the traffic load is 450 Erl, the maximum improvement of P-CTD compared to BD is about 21.6%. In general, P-CTD mechanism has an exceeding improvement in BBP compared to the traditional triggered defragmentation mechanism, which will in turn greatly save network resources.

## 4 Conclusion

Fragment is an urgent issue in EON which will influence network performance seriously. Traditional frequency spectrum defragmentation triggered mechanism suffered from poor bandwidth blocking probability (BBP) and network resource utilization performance. A policy-based comparison-triggered defragmentation mechanism (P-CTD) is proposed to solve this problem, which judges whether to trigger defragmentation by analyzing and comparing the coming traffic requirement and current frequency spectrum status. Theoretical analysis and simulation results show that proposed P-CTD can effectively reduce the network's BBP and optimize the use of network resources.

## References

1. Chatterjee, B.C., Sarma, N., Oki, E.: Routing and spectrum allocation in elastic optical networks: A tutorial. *IEEE Commu. Surv. Tutorials* **17**(3), 1776–1800 (2015)
2. Hsu, C.F., Chang, Y.C., Sie, S.C.: Graph-model-based dynamic routing and spectrum assignment in elastic optical networks. *IEEE/OSA J. Opt. Commun. Networking* **8**(7), 507–520 (2016)
3. Shen, J.H., Chen, J., Sun, Y.: Fragmentation aware routing and spectrum assignment algorithm for elastic optical networks. In: 2015 IEEE Region 10 Conference (TENCON), pp. 1–4 (2015)
4. Wang, R., Mukherjee, B.: Provisioning in elastic optical networks with non-disruptive defragmentation. *IEEE J. Lightwave Technol.* **31**(15), 2491–2499 (2013)
5. Wang, C., Shen, G., Chen, B.: Protection path-based hitless spectrum defragmentation in elastic optical networks: shared backup path protection. In: Optical Fiber Communication Conference. pp. W11.7. Optical Society of America (2015)



6. Wang, C., Shen, G., Peng, L.: Protection path-based hitless spectrum defragmentation for elastic optical networks: 1 + 1 path protection. In: Communications and Photonics Conference and Exhibition, 2014. ACP. Asia. IEEE. pp. AF3E.3 (2014)
7. Cugini, F., Paolucci, F., Meloni, G.: Push-pull defragmentation without traffic disruption in flexible grid optical networks. *IEEE J. Lightwave Technol.* **31**(1), 125–133 (2013)
8. Zhong, Z., Li, J., Hua, N.: On QoS-assured degraded provisioning in service-differentiated multi-layer elastic optical networks. In: IEEE Global Communications Conference 2016 (GLOBECOM2016), pp. 4–8. Washington DC, USA. Piscataway (2016)
9. Yin, Y., Zhang, M., Zhu, Z.: Fragmentation-aware routing, modulation and spectrum assignment algorithms in elastic optical networks. In: Optical Fiber Communication Conference and Exposition and the National Fiber Optic Engineers Conference. pp. 1–3. IEEE (2013)
10. Jiang, R., Feng, M., Shen, J.: An defragmentation scheme for extending the maximal unoccupied spectrum block in elastic optical networks. In: International Conference on Optical Communications and Networks. pp. 1–3. IEEE (2017)
11. Ba, S., Chatterjee, B.C., Oki, E.: Defragmentation scheme based on exchanging primary and backup paths in 1 + 1 path protected elastic optical networks. *IEEE/ACM Trans. Networking* **25**(3), 1717–1731 (2017)



# Fabry-Perot Cavity-Based Optical Fiber Pressure Sensor

Hui Li<sup>(✉)</sup>, Qingchao Zhao, Jiasheng Ni, Long Ma, Faxiang Zhang, and Chang Wang

Laser Institute of Shandong Academy of Sciences, Qilu University of Technology, Jinan 250103, China  
hui10622@163.com

**Abstract.** An optical fiber sensor based on Fabry-Perot cavity is introduced; the Fabry-Perot cavity was fabricated by two collimated fibers with smooth end surfaces. The reflection spectrum of the Fabry-Perot cavity can be changed with the ambient pressure, and the reflection spectrum can be transferred into cavity length; thus, the cavity length can be measured to achieve the sensing of the ambient pressure. For the multi-beam interference of the Fabry-Perot cavity, the reflection spectrum was uniform waves with distinctive peaks and valleys. After the Fabry-Perot cavity was well encapsulated with metal structures, the fiber sensor can withstand high temperature of 150 °C and measure the pressure because the cavity length can be linearly varied with the surrounding pressure and the linear coefficient can be 0.99999. When the Fabry-Perot cavity-based sensor was suffered from the upward and downward pressure from 0 to 71 MPa, the cavity lengths of upward and downward were varied within 15 nm which was equivalent of 0.04 MPa. The repeatability and return difference of the sensor have also been studied and the parameters both verified the good property of this kind of sensor. An optical fiber sensor based on Fabry-Perot cavity is introduced, and the response of the cavity length to the ambient pressure, the repeatability, and return difference of the sensor have been studied.

**Keywords:** FP cavity · Pressure sensing · Cavity length · Repeatability · Return difference

## 1 Introduction

Research on optical fiber sensors has drawn more and more attention in recent years especially in harsh environments such as high voltage transformers, nuclear radiation environment, and coal and oil fields, where electronic sensors were prone to be affected [1–3]. However, optical fibers are insensitive to electromagnetic interference, and optical fiber sensors have been applied in the fields of resource exploration, electric power system, defense safety monitoring, and so on. In optical fiber sensors, fiber Bragg gratings (FBGs), Fabry-Perot (FP) cavity, and distributed sensing are typical components. Among them, FP cavity can provide high accuracy and resolution and dynamic measurement. In optical fiber sensors, FP cavities always made up of two collimated fibers and the demodulation system is based on polarized light interference [4–7].

In this article, a FP cavity-based optical fiber sensor for pressure sensing is designed and its spectrum was recorded. In order to judge its property, the cavity length response to pressure, the variation of the cavity length for different experiments, and the return difference in the pressure range of 0–71 MPa were discussed in detail.

## 2 Structure and Spectrum of the Sensor

The FP cavity fiber sensor had two high reflective fiber end faces in a quartz capillary, and the fibers were melted by hydrogen-oxygen flame or a CO<sub>2</sub> laser and combined with the capillary closely. When the FP cavity was formed, it was packaged with metal shell and used in oil wells. Once the ambient pressure is changed, the capillary will expand or shrink and thus the cavity lengths also change, resulting the altering of the spectrum, and subsequently, the demodulation program will calculate the pressure according to the response of the FP cavity length to the pressure [8–10].

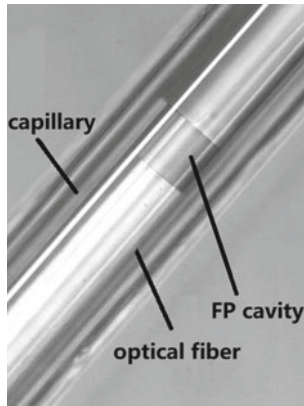


**Fig. 1** Structure of a typical FP cavity under electron microscopy

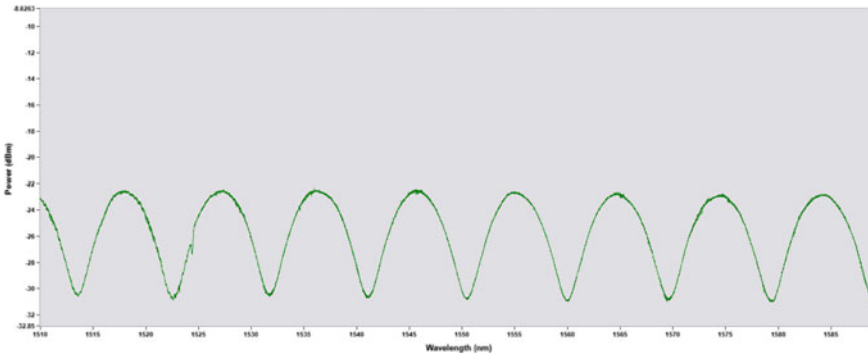


**Fig. 2** Spectrum of a typical FP cavity

## 2.1 Structure of the FP Cavity

The structure of a typical FP cavity fabricated with hydrogen-oxygen flame was shown in Fig. 1; it is apparent that two collimated fibers with smooth end faces formed the FP cavity, and the distance between the two end faces is defined as the FP cavity length  $d$ .

## 2.2 Spectrum of the FP Cavity

As shown in Fig. 2, the reflection light from the FP cavity experienced multiple beam interference between the two fiber end faces and FP cavity length can be demodulated from the wave peaks or valleys. In this article, the original FP cavity length in the air was 128.9  $\mu\text{m}$  at room temperature and the pressure in the following was the relative value to a standard atmospheric pressure (1 atm). The property of a FP cavity can be judged from the spectrum, and a good FP cavity must have spectrum with a loss of peak to peak less than 0.5 dB and peak to valley larger than 7 dB.

## 3 Results and Discussions

When pressure was applied to the FP cavity-based fiber sensor, the capillary would expand or shrink and the cavity length could change with the changing of the ambient pressure. That is to say, the ambient pressure can be reflected by the FP cavity length. Therefore, the response of the FP cavity length to the ambient pressure and the variation of the FP cavity length during pressure upward and downward were studied in detail. In the following, the FP cavity-based fiber sensor was located at the temperature of 150  $^{\circ}\text{C}$ ; because of thermal expansion, the original cavity length was a little larger than that at room temperature. The results are shown in Figs. 3, 4, and 5.

### 3.1 Response of the FP Cavity Length to Ambient Pressure

The response of the FP cavity length to the ambient pressure is shown in Fig. 3. The ambient pressure was changed with a step of 10 MPa from 1 to 71 MPa and the FP cavity length changed linearly. The response curve can be fitted by (1):

$$d = -284.6P + 129038.2 \quad (1)$$

In (1),  $d$  refers to the FP cavity length with a unit of nanometer and  $P$  corresponds to the ambient pressure with a unit of megapascal and (1) has a linear relative coefficient of 0.99999. Since the FP cavity length  $d$  can be demodulated by the reflection spectrum, using (1), the ambient pressure  $P$  can be sensed.

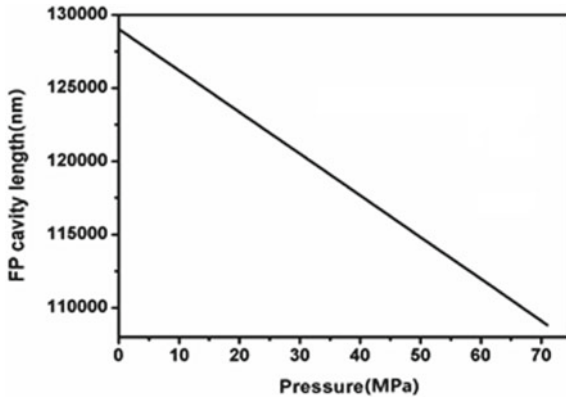


Fig. 3 Response curve of the FP cavity length to ambient pressure at the temperature of 150 °C

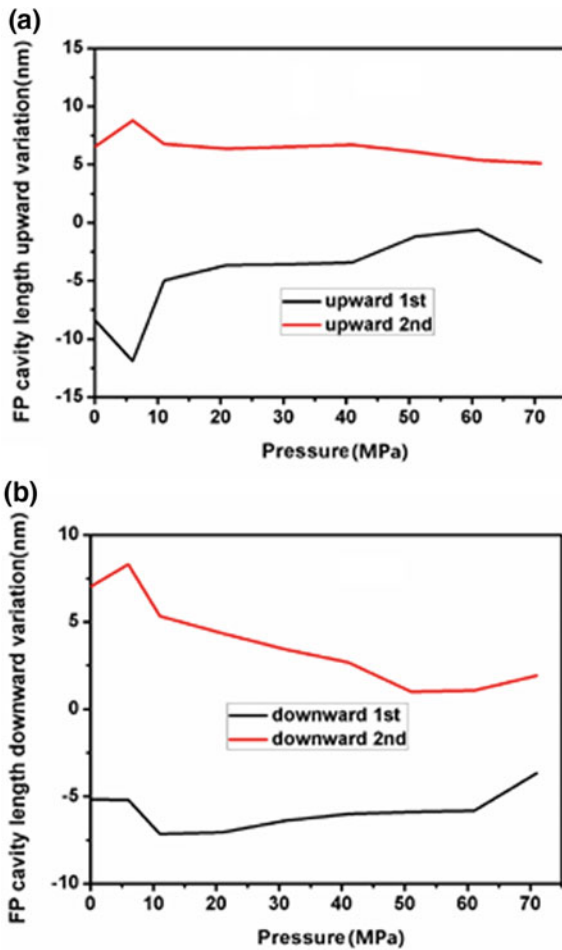


Fig. 4 Variation curves of the FP cavity length during pressure a upward and b downward at the temperature of 150 °C

### 3.2 Variation of the FP Cavity Length During Pressure Upward and Downward

In order to value the property of a FP cavity-based fiber sensor, measurement of the response of the FP cavity length to ambient pressure was carried out for several times; Figs. 4 and 5 display measured results of two typical experiments at different days.

As can be seen from Fig. 4, the FP cavity length shows minor variations during the ambient pressure going upward and downward for two different days and the variations of the cavity length are entirely in the range of 15 nm with the altering of the pressure. Despite the variation at the pressure of 6 and 11 MPa, other variations are all within 5 nm, which means the FP cavity has excellent stability. Changing the variation of the cavity length into pressure, the maximum pressure variation is only 0.04 MPa and it's about 0.5‰ F. S. (full scale).

Therefore, variation curves of the FP cavity length during the ambient pressure upward and downward in Fig. 4 demonstrate that the FP cavity-based fiber sensor has favorable stability in the pressure range of 0–71 MPa.

### 3.3 Repeatability and Return Difference of the FP Cavity Sensor

The repeatability and return difference curves of the FP cavity-based fiber sensors at the temperature of 150 °C were exhibited in Fig. 5. Repeatability refers to the maximum cavity length difference value during the ambient pressure upward or downward, and return difference means the maximum cavity length difference value between the pressure-upward cavity length and the pressure-downward one in different experiments. Therefore, the repeatability and return difference can characterize the properties of a sensor [11, 12].

Apparently, the whole tendency of the repeatability and return difference of the sensor is relatively smooth, and only when the pressure was set at 6 MPa, the value had a little fluctuation. The repeatability and return difference were within 20 and 7 nm, respectively, changing the length values into pressure, they correspond to 0.07 and 0.02 MPa which are 1 and 0.3‰ F.S. The results of repeatability and return difference indicate that the FP cavity-based fiber sensor has excellent property and this fiber sensor can find its applications in the oil fields to predict the petroleum content at the exploration stage and monitor the safe production during the exploitation stage.

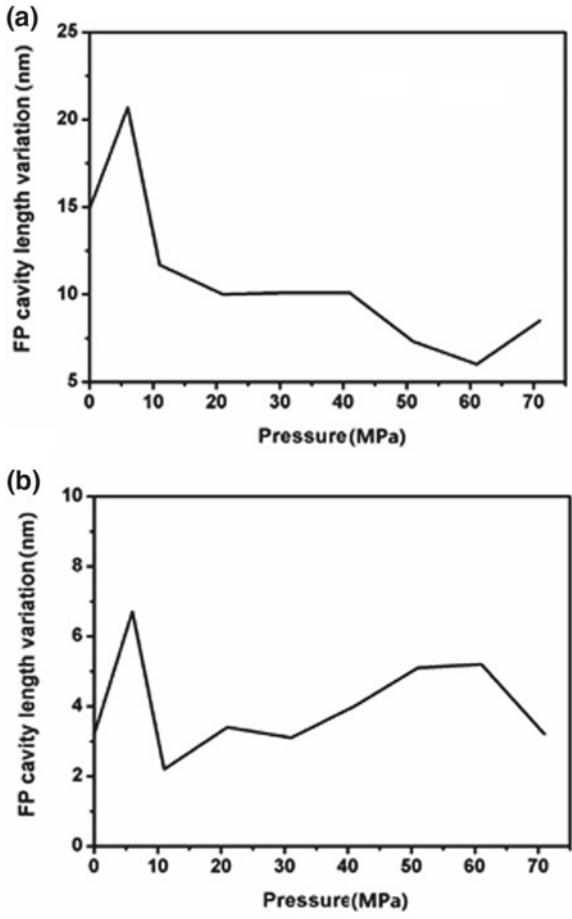


**Fig. 5** **a** Repeatability and **b** return difference curves of the FP cavity sensor at the temperature of 150 °C

### 4 Conclusion

Fabry-Perot cavity-based optical fiber sensors were designed and manufactured for pressure sensing. The FP cavity was formed by two collimated optical fibers in a capillary by hydrogen-oxygen flame or a CO<sub>2</sub> laser with cavity length of 128.9 μm. The FP cavity length could be calculated from the reflection spectrum, and the ambient pressure could be demodulated from the cavity length; thus, in this way, the fiber sensor can be used as pressure sensor in harsh environment. At the temperature of 150 °C, the FP cavity sensor can endure a pressure high up to 71 MPa, and when the ambient pressure was changed, the cavity length varied linearly with pressure and the linear coefficient was up to 0.99999. The FP cavity-based sensor shows excellent features in stability, repeatability, and return difference which are within 0.5, 1, and 0.3% F.S., respectively. Considering the superior characteristics, this kind of fiber sensors can be applied in oil fields to measure the pressure under oil wells.

**Acknowledgements.** The work was conducted with the help of Pro. Gangding Peng from University of New South Wales, Australia.

## References

1. Zhou, X., Peng, W., Yu, Q.: Carbon-coated fiber Fabry-Perot sensor for harsh environments. In: 22nd International Conference on Optical Fiber Sensors, pp. 8421AB. International Society for Optics and Photonics (2012)
2. Eom, J., Park, C., Lee, B., Lee, J., Kwon, I., Chung, E.: Fiber optic Fabry-Perot pressure sensor based on lensed fiber and polymeric diaphragm. *Sens. Actuators A* **225**(15), 25–32 (2015)
3. Liu, G., Han, M., Hou, W.: High-resolution and fast-response fiber-optic temperature sensor using silicon Fabry-Pérot cavity. *Opt. Express* **23**, 7237–7247 (2015)
4. Lee, B., Kim, Y., Park, K., Eom, J., Kim, M., Rho, B., Choi, H.: Interfero-metric fiber optic sensors. *Sensors* **12**, 2467–2486 (2012)
5. Delft, K., Eijkel, J., Mijatovic, D., Druzhinina, T., Rathgen, H., Tas, N., Berg, A., Mugele, F.: Micromachned Fabry-Perot interferometer with embedded nanochannels for nanoscale fluid dynamics. *Nano Lett.* **7**, 345–350 (2007)
6. Pevec, S., Donlagic, D.: All-fiber, long-active-length Fabry-Perot strain sensor. *Opt. Express* **19**, 15641–15651 (2011)
7. Park, K., Kim, Y., Eom, J., Park, S., Park, M., Jang, J., Lee, B.: Compact and multiplexible hydrogen gas sensor assisted by self-referencing technique. *Opt. Express* **19**, 18190–18198 (2011)
8. Zhao, Q., Liu, X., Ma, L., Zhao, W., Wang, H.: Design of fiber optic FP cavity pressure sensor based on corrugated diaphragm. In: AOPC 2017: Fiber Optic Sensing and Optical Communications, pp. 104641. International Society for Optics and Photonics (2017)
9. Zhao, Q., Liu, X., Ma, L., Zhao, W., Wang, H.: Optical fiber pressure sensor based on FP cavity in the oil and gas well. In: IOP Conference Series: Earth and Environmental Science, pp. 012007. IOP (2017)
10. Wang, Y., Wang, C., Zhao, Q., Liu, X.: Research of carbon coating on optical fiber sensor. In: 16th International Conference on Optical Communications and Networks (ICOON), pp. 1–3 (2017)
11. Zhou, X., Yu, Q.: Wide-range displacement sensor based on fiber-optic Fabry-Perot interferometer for subnanometer measurement. *IEEE Sens. J.* **11**, 1602–1606 (2011)
12. Zhou, X., Chen, K., Mao, X., Yu, Q.: A reflective fiber-optic refractive index sensor based on multimode interference in a coreless silica fiber. *Opt. Commun.* **340**, 50–55 (2015)





# Modeling Method of Sunlight Interference Signal

Hao Guo<sup>(✉)</sup>, Na Ma, and Weiwei Liang

Luoyang Electronic Equipment Test Center, Luoyang 471003, China  
whatbeam@163.com

**Abstract.** In view of the requirements for the evaluation of the adaptability of the photoelectric system to the complex environment, the sun AC interference signals under various ground background are measured, and the normal analysis of the test data shows that the intensity of the sunlight interference signal conforms to the normal distribution. This paper presents a method for the modeling of the sun AC interference signal, which simulates the characteristics of the number of interference signals, the intensity of the signal, the position of the signal, the relative timing, and the law of change. Finally, the simulation example of the interference signal under the weak, medium, and strong jamming environment is given by synthesizing the various characteristics of the sunlight AC jamming signal. The method presented in this paper can provide technical reference and support for the modeling of sunlight AC interference signal and the evaluation of photoelectric system adaptability under different sunlight and background.

**Keywords:** Signal detection · Sunlight interference · Signal modeling · Simulation

## 1 Introduction

Optoelectronic systems working in the field are generally affected by the optoelectronic environment, such as sunlight, humidity, temperature, pressure, visibility, and other factors, which may affect the actual performance of the photoelectric system [1–3]. When evaluating the performance of the photoelectric system, it is necessary to place the photoelectric system in a typical field working environment to evaluate its impact and extent. However, it is difficult to use a large number of field measurement methods under the conditions of experimental cost and technology. At this time, the main interference factors can be modeled by the means of simulation, and they are input into the model of the photoelectric system. According to the degree of change of the photoelectric system performance, the influence of the interference factors is evaluated. Through a large number of simulation experiments, the statistical law of interference can be found out, and then, field experiments under typical conditions can be carried out to verify the credibility of the simulation. After several iterations, we can use the simulation method to better evaluate the anti-jamming performance of the photoelectric system.

Aiming at the evaluation requirements of some photoelectric systems, this paper mainly discusses the modeling method of sunlight interference signals.

## 2 Analysis of the Measured Data of Sun AC Interference Signals

Since some optoelectronic systems can only extract the pulse light signal and have no direct response to the DC sunlight signal, this paper uses the pulse light signal measuring equipment to measure the AC sunlight signals in various ground objects, aiming at analyzing the characteristics of the sunlight signal and modeling for the sunlight interference signal.

### 2.1 Test Method

As shown in Fig. 1, the plane of ground object can be seen as an approximately uniform quasi horizontal plane. The test point is the original point  $O$ , and the space right angle coordinate system  $O$ - $xyz$  is set up. The sun's zenith angle of the sun relative to the original point is beta, the azimuth angle is theta, the azimuth angle of the photo detector relative to the test point is alpha, and the azimuth angle is phi.

The photoelectric detector is turned on to measure the sunlight AC interference signal appearing in its field of view. In a certain period of time,  $n$  groups of measurement data are measured. The photoelectric detector is moved to the other background, and the measurement data of sunlight AC interference signal under the other background are obtained.

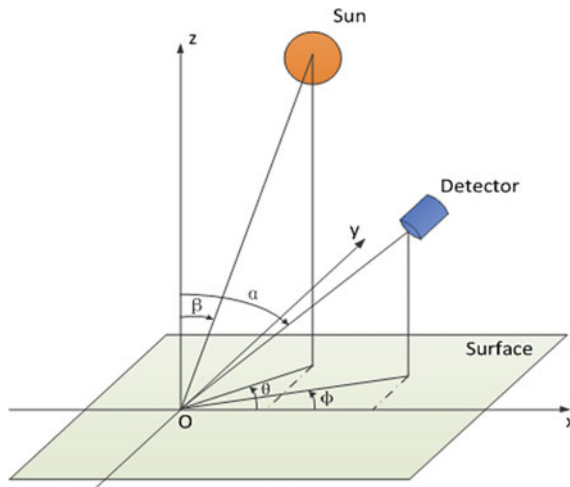


Fig. 1 Schematic diagram of test

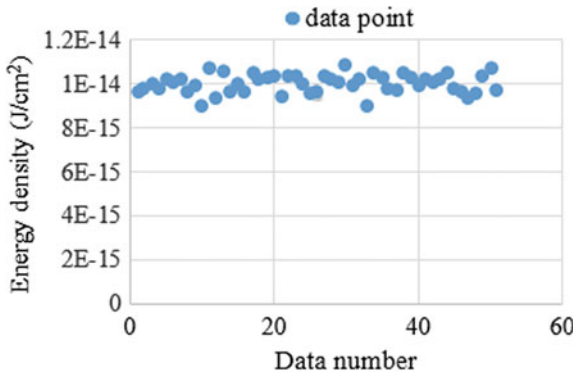


Fig. 2 Test results of gravel

### 2.2 Test Layout

The sunlight AC interference signal data of shallow grassland, sandy land, and urban buildings are measured, as shown in Figs. 2, 3 and 4.

According to the histogram of measured data, the data may be normal distribution. Under the assumption that the overall parameters are unknown, the population mean and standard deviation are usually replaced by the mean and standard deviation of the sample.

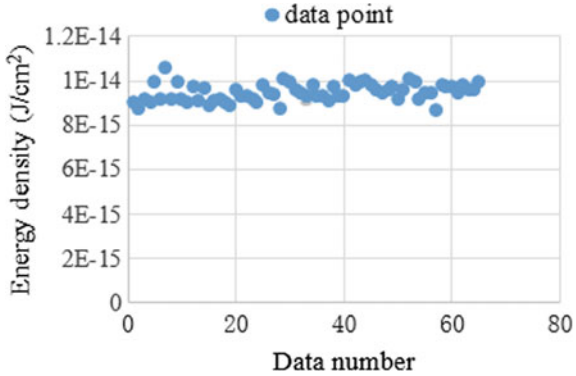
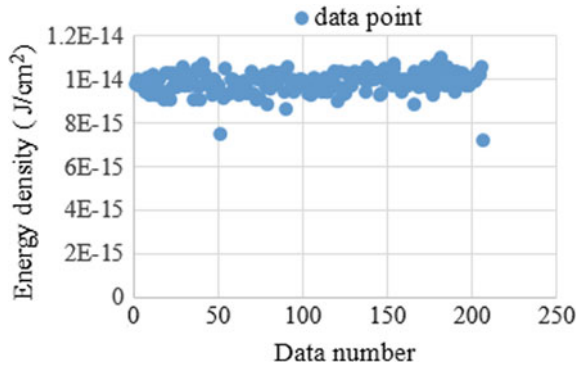


Fig. 3 Test results of grassland



**Fig. 4** Test results of buildings

The Lilliefors test method [4, 5] is used to normality test for the results. The upper bound KS is the difference between empirical cumulative probability and cumulative probability of target distribution.

$$KS = \max_x |SCDF(x) - CDF(x)| \quad (1)$$

where SCDF is the empirical cdf estimated from the sample and CDF is the normal cdf with mean and standard deviation equal to the mean and standard deviation of the sample. If the original hypothesis is true, KS should be very small. If it is large, the original hypothesis is not valid.

The test results show that the 4 sets of data are subject to normal distribution, and

**Table 1** Table of test results

Parameter	Gravel	Shallow grassland	Urban buildings
Mean	1.003e-14	9.486e-15	8.906e-15
Variance	4.269e-16	3.996e-16	5.326e-16

the parameters are shown in Table 1.

### 3 Introduction Modeling Method of Sunlight Interference Signal

The characteristics of the interference signal are mainly reflected in the number of interference signals, the energy density of the signal, the position of the signal (the relative position on the detector), the relative timing (relative to the guiding signal), and

the law of the change of the signal parameters. These aspects are emphasized in the modeling of interference signals.

### 3.1 Modeling of Sunlight Interference Signal Quantity and Distribution Law

Assuming that the background is homogeneous and single background, it is considered that the generation of AC interference signals at a certain time is in a uniform distribution. The presence and absence of four channel signals are considered to be independent of  $U(a, b)$ . Its distribution density expression is

$$p_u(x) = \begin{cases} \frac{1}{b-a}, & a \leq x \leq b \\ 0, & x < a \text{ or } x > b \end{cases} \quad (2)$$

$$-\infty < a < b < \infty$$

The expression of the mean  $E\xi$  and the variance  $D\xi$  is

$$E\xi = \frac{a+b}{2}, D\xi = \frac{(b-a)^2}{12} \quad (3)$$

Under different sunlight and background, the number of interference signals varies. According to the difference of sunlight irradiation intensity and background type, the interference signals are divided into three kinds of strong, medium, and weak interference intensity, and the number of interference signals in the three kinds of interference intensity decreases in turn. The number of interference signals can be adjusted in the following ways.

The uniformly distributed random sequence  $X$  is regarded as an independent variable, and the function is transformed by linear function.

$$Y = aX - b \quad (4)$$

The parameters  $a$  and  $b$  have their bound as  $0 < a < 1$ ,  $b > 0$ . By adjusting the size of  $a$  and  $b$ , the number of interference signals, namely  $Y$ , can be controlled. The smaller the  $A$ , the larger the  $B$ , and  $Y$  is smaller as  $a$  is smaller and  $b$  is larger.

In the simulation, the number of guide pulses that can be received during the whole work process is recorded as  $m$ , and the number of interference signals is  $Y$ , and then, the ratio of interference and guide signals is recorded as  $k$ .

$$k = \frac{Y}{m} \times 100\% \quad (5)$$

Here, the environmental intensity of different sunlight alternating interference signals is defined as follows.

$$\text{environmental intensity} \begin{cases} \text{strong:} & k \geq 30\% \\ \text{medium:} & 10\% < k < 30\% \\ \text{weak:} & k \leq 10\% \end{cases} \quad (6)$$

The classification standard of the AC sunlight interference environment is primarily defined according to the influence of the interference signal on the simulation results. The strong interference environment can make the performance more deviant, and the weak interference has little effect on the performance deviation, and the medium interference is between the two.

### 3.2 Modeling of the Energy Density Distribution of Sun Interference Signals

#### Modeling of sunlight alternating signals caused by scintillation of ground objects

According to the results of the measured data analysis, the intensity of the interference signals obeys the normal distribution  $N(\mu, \sigma^2)$ , and the size of the four signal is considered to be independent of the normal distribution. Its distribution density expression is

$$p_N(x) = \frac{1}{\sqrt{2\pi}\sigma} e^{-\frac{(x-\mu)^2}{2\sigma^2}} \quad (7)$$

$$-\infty < x < \infty, -\infty < \mu < \infty, \sigma > 0$$

The expression of the mean  $E\xi$  and the variance  $D\xi$  is

$$\begin{aligned} E\xi &= \mu \\ D\xi &= \sigma^2 \end{aligned} \quad (8)$$

Under different sunlight and background, the intensity of jamming signal varies. The magnitude of signal intensity can be adjusted by adjusting mean and variance. For strong interference environment, the mean value is  $E1 = 20$ , the variance  $D1 = 1.5$ , the medium interference environment, the mean value  $E2 = 10$ , the variance  $D2 = 1$ , the weak interference environment,  $E3 = 6$ ,  $D3 = 0.5$ .

#### Modeling of AC signals caused by the movement of photoelectric system

According to the Bang–Bang control principle of the optoelectronic system, we can simplify it to a sinusoidal modulation, and the amplitude  $A$  is the ratio of the maximum reflectivity to the minimum reflectivity in the direction of the ground background, and the typical  $A = 4$ .  $A$  can also be adjusted by the variation of object background. The frequency  $\omega$  is proportional to the frequency of the Bang–Bang control transformation of the photoelectric system, where the typical  $\omega = 0.25$  rad/s, the initial phase  $\varphi = 0$ ,  $y_0$  as the initial amplitude,  $y_0 > A$ .

Therefore, the simulation modulation model of the AC signal in a typical case caused by the motion of the photoelectric system can be obtained.

$$y(x) = A \cos(\omega x + \phi) + y_0 = 4 \cos(0.25x) + y_0 \quad (9)$$

$$+ y_0 \quad 0 < x < \infty$$

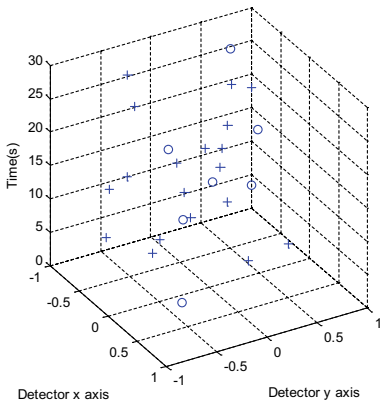
The interference effect caused by atmospheric turbulence is not considered at present.

**Time Sequence Modeling of Sunlight Interference Signal**

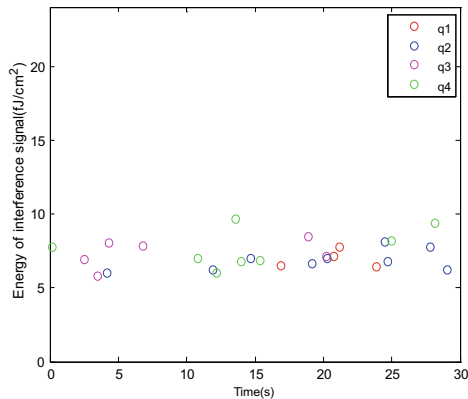
The timing of the sun interference signal is also random. The preliminary analysis shows that the timing of the interference signal is obeying the uniform distribution  $U(a, b)$ , and the time series of the four channel interference signals is considered to be independent of the uniform distribution. Its distribution density expression is same as (2).

The intensity and the relative timing of the interference signal is independent. The relative timing of the interference and the guided signal can be adjusted by changing the maximum value  $b$  of the uniform distribution.

**Position Modeling of Sunlight Alternating Interference Signal on Detector**



(a) Spatial distribution map  
 \* +: less than P1 in magnitude, o: greater than P1 and less than P2,  
 ∅: larger than P2; the same below.



(b) Amplitude distribution map  
 \*q1~q4: the four regions of the detector, the same below.

**Fig. 5** Simulation results of weak sunlight interference AC signals

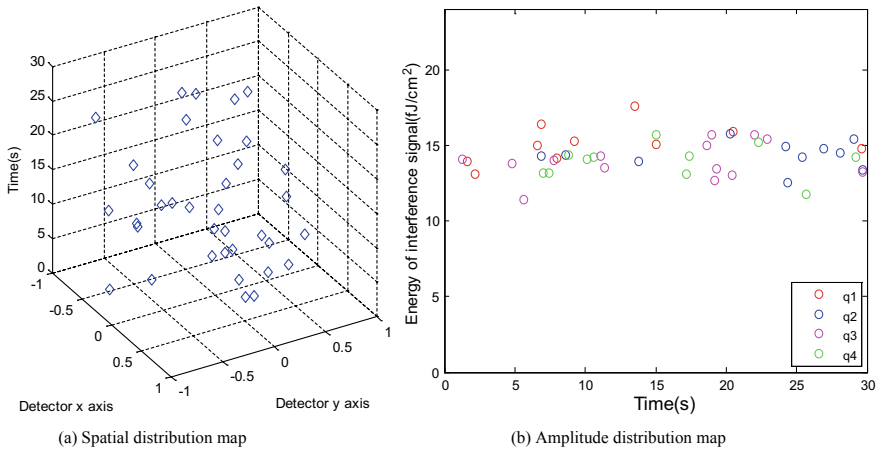


**Fig. 6** Simulation results of medium sunlight interference AC signals

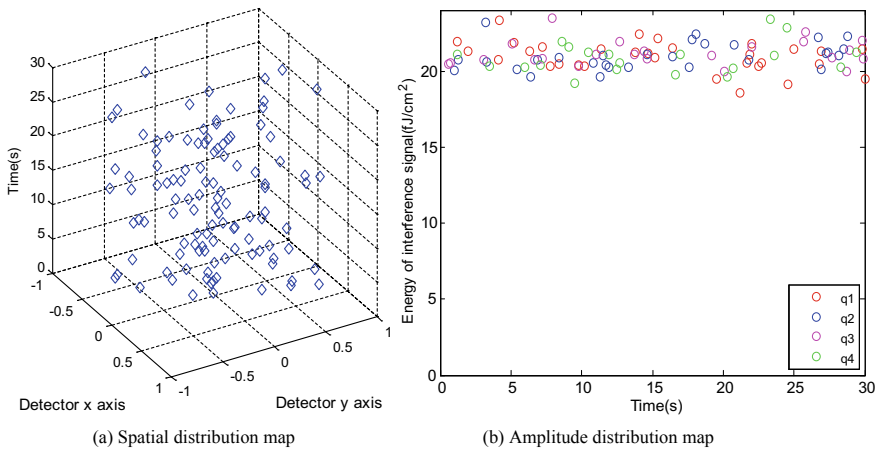


**Fig. 7** Simulation results of strong sunlight interference AC signals

The position of the ground reflected sunlight interference signal on the detector is also random. The preliminary analysis suggests that the position of the interference signal on the detector obeys the uniform distribution  $U(a, b)$ . The location of the four signals is considered to be independent of each other. The distribution density expression is the same as (2).

Because the detector is a four-element detector, the output of the signal on the detector is only related to which quadrant, and has nothing to do with the specific position on the quadrant. Therefore, it is considered that the position can be measured by the angle, which can be divided into four angle ranges:  $0^\circ\text{--}90^\circ$ ,  $90^\circ\text{--}180^\circ$ ,  $180^\circ\text{--}270^\circ$ ,  $270^\circ\text{--}360^\circ$ . It is considered that the probability of interference occurring at a certain location of the detector is independent of the intensity of the interference signal.



### Simulation Results

Considering the number, intensity, time series, and position of the interference signal of the sun, three kinds of weak, medium, and strong interference signals are simulated, respectively. The typical results are shown in Figs. 5, 6 and 7.

## 4 Conclusion

The characteristics of the sunlight interference signal are related to many factors. In this paper, a method of modeling the sun interference AC signal is presented, which is mainly applied to the jamming signal simulation of the fixed reception angle under the quasi uniform and single background. In the complex background, the dynamic simulation of the sun interference signal can be combined with the background distribution and its reflection characteristics, as well as the optical and motion characteristics of the photoelectric system. When all the factors are integrated in the simulation, the relatively realistic and reliable sunlight interference signal is finally obtained, which can be used to support the adaptability evaluation of the photoelectric system under the complex optoelectronic environment.

## References

1. Bie, H.G., Li, K.J.: Effects of solar radiation on the receiver of imaging LADAR. *Infrared and Laser Eng.* **38**, 325–328 (2009)
2. Guo, W.R., Li, P.: Interference from scattered sunlight on photodetector posed in different angles. *J. Detect Control* **31**(1), 41–45 (2009)
3. Shen, C.F., Zhang, X.G.: Research on detection performance of small caliber laser fuze under the sunlight. *J. Ordnance Equip. Eng.* **37**(12), 145–149 (2016)
4. Chen, M., Zheng, C.Y.: *Matlab function and case Handbook*, 1st edn. People's post and Telecommunications Press, Beijing (2014)
5. Liu, Z.J.: *Matlab scientific computing treasure*, 1st edn. Electronics Industry Press, Beijing (2012)



# High-Efficiency Automatic Discovery of Optical Communication Device Based on MDNS

Yuhua Zhang<sup>(✉)</sup>, Xueguang Yuan, Yang'an Zhang, Qin Liu,  
and Yalei Chu

State Key Laboratory of Information Photonics and Optical Communications,  
Beijing University of Posts and Telecommunications, Beijing 100876, China  
Zyh265@qq.com

**Abstract.** This paper comes from the management needs of optical network equipment. Large-scale optical networks require efficient network management software for management. The automatic discovery of network equipment is the key to implement the intelligent network management system and is the basis of the network management software. The traditional automatic discovery method for network devices is mainly based on the ICMP protocol. When ping the IP address on the network one by one, the detection period is too long and the network load is too heavy, so it is not suitable for real-time device discovery. This paper proposes an automatic discovery method based on MDNS protocol. This paper proves that this method can greatly shorten the automatic discovery time of communication equipment and IP services.

**Keywords:** Optical NMS · ICMP · MDNS · Automatic discovery · Optical communication device

## 1 Introduction

This paper is derived from the management needs of recent optical network equipment. Large-scale optical networks require efficient network management software for management. Optical network management is to manage the network in a certain way, so that the network can run normally and efficiently [1]. It maintains the efficient operation of the network system. Since the 1990s, some scholars and experts have studied the network topology discovery technology and proposed corresponding technologies and theories [2]. At the same time, many manufacturers have released some commercial software products, and the automatic discovery of devices has been realized to varying degrees.

Network topology is a method for indicating the relationship between logical connections and physical connections of network devices [3]. Through it, network administrators can intuitively grasp the current running status of network devices, accurately locate fault points in the network, and accurately analyze the network. The problems in the middle provide the basic data to optimize the network and improve the

performance of the network. It can be said that the automatic discovery of network devices is the technical key to realize the intelligent network management system and is the basis of the network management software.

Automatic discovery method for network devices is mainly based on the ICMP protocol [4]. ICMP (Internet Control Message Protocol) is a protocol for connection-less. It is a sub-protocol of the TCP/IP protocol family and belongs to the network layer protocol for IP. The control message is transmitted between the host and the router (the network is unreachable, the host is reachable, the route is available, etc.). ICMP messages are automatically sent when IP data cannot be accessed and the IP router cannot forward packets at the current transmission rate. Although these control messages do not transmit user data, they play an important role in the transfer of user data. Ping uses the ICMP protocol packet to detect if another host is reachable. The principle is to send a request with ICMP with type code 0, and the host with the request responds with ICMP with type code 8. Ping the program to calculate the interval and calculate how many packets are delivered. When pinging the IP address on the network one by one in this way, the detection period is long and the network load is large, so it is not suitable for real-time device discovery.

In summary, we propose an automatic discovery method based on the MDNS protocol. This paper proves that this method can greatly shorten the automatic discovery time of communication equipment and IP services.

## 2 The Principle of Experimental Design

A novel framework based on the traditional INET Framework is proposed. In this paper, we present an extension about MDNS to the INET Framework.

MDNS (Multicast DNS) [5] mainly enables hosts in the LAN to discover and communicate with each other without a traditional DNS server. The port used is 5353, which complies with the DNS protocol and uses the existing DNS information structure, name syntax, and resource record type. And no new action code or response code is specified.

In a local area network, devices and devices need to know each other's IP address before communicating with each other. In most cases, the device's ip is not a static IP address, but an ip address dynamically assigned through the DHCP protocol. In this case, you need to use MDNS to discover the device. The multicast address used by MDNS is 224.0.0.251 and the port is 5353. MDNS is used inside the LAN. Each host that enters the LAN will open to the LAN if the MDNS service is enabled. All hosts multicast a message, who I am (domain name), and what my IP address is. Then other hosts with MDNS service will respond and will tell you who it is (domain name) and what its IP address is. When the device needs to be serviced, the MDNS is used to query the corresponding IP address of the domain name [6]. After receiving the packet, the corresponding device also responds by multicast. At this time, other host devices can also receive the response packet, and other hosts also receive the response packet. The domain name and ip, ttl, etc. are recorded, and the cache is updated.

Objective Modular Network Testbed in C++ (OMNet++) is a component-based modular open network simulation platform that has become popular in science and

industry in recent years. Can be used to solve problems in the following areas: wireless communication network and wired communication network modeling, protocol simulation modeling, queuing network modeling, multiprocessor and distributed hardware system modeling, hardware architecture verification and evaluating multifaceted performance of complex software systems.

In general, it can be used for any system simulation and modeling using discrete time methods, and it can be easily mapped to entities that rely on communication for exchange of information. OMNet++ provides basic tools and mechanisms for writing simulation code, but it does not provide any components specifically for computer network simulation, system architecture simulation, and any other field; specific simulations are made up of simulation models and frameworks such as the Mobility Framework or INET Framework to support.

Before the experiment started, we first expanded the implementation of the MDNS protocol in the original framework and made the corresponding module. In the experiment, we first add this module layer to each optical communication device to realize automatic discovery feature of the optical device.

### 3 Simulation and Results

This network consists of four switches (etherSwitch1..etherSwitch4) and six endpoints: two source hosts (source1, source2), two destination hosts (destination1, destination2) and two other hosts (host1, host2) which are inactive in this simulation (Fig. 1).

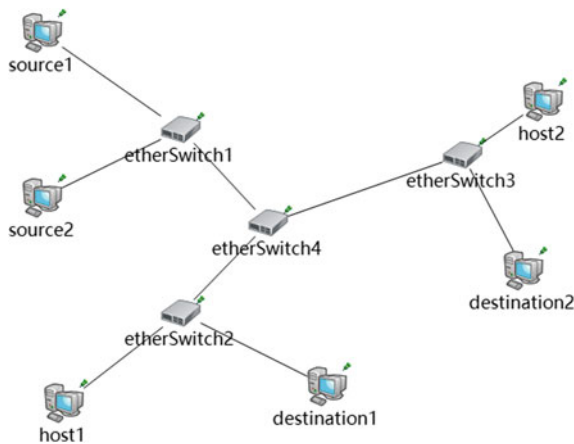


**Fig. 1** The network created by this experiment

This experiment consists of two parts. The first step, pinging the IP address of destination1 with 32 bytes of data by source1, and pinging the IP address of destination2 with 32 bytes of data by source2, and then record the time, respectively, and

repeat 20 times. In the second step, repeat step 1 by using the MDNS-based discovery method instead of using ping and record the time in the same way.

The results are shown in the graph. And Fig. 2a is the result of step 1. Figure 2b is the result of step 2.

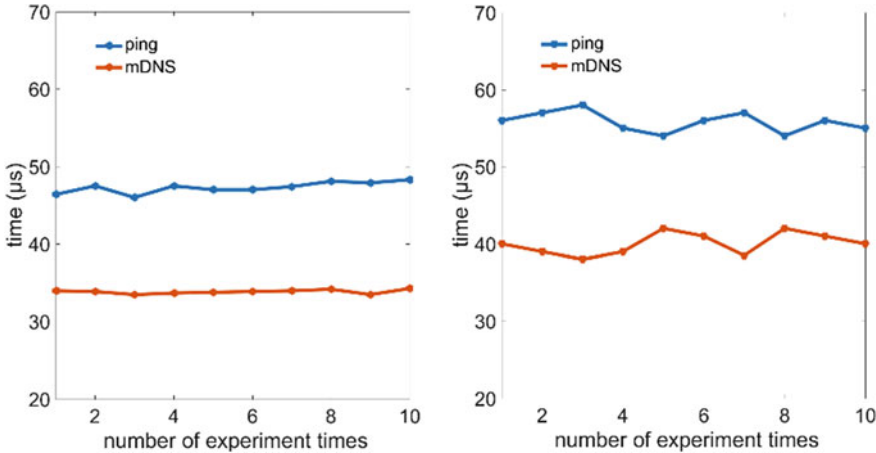


**Fig. 2** Result of this experiment

From the chart results, it is not difficult to see that in each experiment, the time taken by MDNS auto-discovery is less than the time of ping, and the average time saved almost 28% is calculated. Through this experiment, we have shown that using the MDNS method is more efficient than the traditional ping way for automatic discovery.

## 4 Conclusion

The experimental results show that the proposed use of MDNS to achieve automatic discovery of optical network equipment does save more time than the traditional ICMP-based ping method in automatic discovery, saving almost 28% of the time. Therefore, the MDNS-based automatic discovery optical network device method truly optimizes device discovery time and improves NMS efficiency.

## References

1. Ma, J., Zhang, L., Zhang, S., Yao, X.: Vulnerability analysis of the optical network NMS. In: 2012 Second International Conference on Instrumentation, Measurement, Computer, Communication and Control (IMCCC) (2012)
2. Raheja, A., Singh, A.: Network analysis of ICMP ping flood DoS attack in WiMAX and wireless LAN (2016)

3. Lee, D.H, Jeon, W.: Detecting the presence or absence of a user (US20170025861) (2017)
4. Primerano, D., Saporoff, N.W.: Automated discovery and procurement of management information bases (MIBs) (US8914490) (2014)
5. Stolikj, M., Cuijpers, P.J.L., Lukkien, J.J. et al.: Context based service discovery in unmanaged networks using MDNS/DNS-SD. In: IEEE International Conference on Consumer Electronics, pp. 163–165. IEEE (2016)
6. Ishvarchandra, F.B.: Communicating service denials back to client during MDNS service discovery (US20150100700) (2015)



# Adaptive Phase Estimation in the Presence of Nonlinear Phase Noise for Carrier Phase Recovery of PM-QPSK Signals in Coherent Optical Receivers

Faith Kwaku Deynu<sup>1,2</sup>(✉), Bo Xu<sup>1</sup>, and Evans Wilson Akpari<sup>2</sup>

<sup>1</sup> University of Electronic Science and Technology of China,  
Chengdu 611731, China

faithdeynu@yahoo.com

<sup>2</sup> Ho Technical University, P.O. Box HP 217, Ho, Ghana

**Abstract.** There are a number of architectural choices to improving feedback and feedforward carrier phase recovery (CPR) algorithms: filter length, filter shape, error signal, etc. The optimal choice depends on the relative strengths of phase noise and additive noise. On the other hand, the optimal average length of CPE used for filtering the phase noise estimate is quite subjective. In principle, a short average length enables fast carrier phase tracking, and a longer average length enables large ASE noise tolerance. Consequently, the optimal average length becomes relatively so short in the presence of fiber nonlinearities when phase noise is large to prevent any symbol with occurring large ASE noise from severely distorting the CPE process. This may affect the stability of CPE performance and subsequently causing performance degradation. For the steady performance of CPE in the presence of large phase noise, this paper proposes adaptive filtering technique to detect and isolate symbols with significantly large ASE noise from the filtering process to improve stability and performance of CPE algorithms. The results showed that the proposed adaptive filtering CPE technique combined with normalization processing in CPE provides about 1.0 dB Q-factor performance improvement over the conventional CPE method in mitigating the combined effects of laser linewidth and fiber nonlinearity for coherent phase-modulated optical signals. The technique automatically identifies and eliminates symbols with significantly large noise from the filtering process to improve stability and estimation accuracy of the carrier phase estimators. The complexity of additional hardware required to implement the scheme is quite simple.

**Keywords:** Coherent optical fiber communication · Phase noise · Adaptive carrier phase recovery

## 1 Introduction

Due to Kerr effect, interaction of signal and amplified spontaneous emission (ASE) gives rise to Gordon–Mollenauer (GM) effect, a fiber transmission nonlinearity that manifests itself as phase modulation [i.e., nonlinear phase noise (NLPN)] that adds

up to the intrinsic phase noise generated due to the finite linewidth of the free-running lasers used at both the transmitter and receiver, the latter acting as a phase reference for the former. The impact of this combined phase noise is distortion and random rotation of received signal constellation points, which leads to performance degradation when phase-modulated formats [1] are employed in coherent optical fiber transmission networks. As a result, efficient carrier phase estimation (CPE) algorithm with better phase noise tolerance is a prerequisite of digital coherent receivers to track and compensate the carrier phase noise using digital signal processing (DSP) to ensure successful detection of phase-modulated signal formats. There is evidence that the average length is a key parameter that can be optimized in CPR algorithms to influence the performance of digital coherent receivers in wavelength-division multiplexing (WDM) systems [2]. This can improve performance in low-nonlinearity systems or in the absence of ASE noise but this benefit of CPE degrades in the presence of high-nonlinearity. There are a number of architectural choices to improve the average length: filter length, filter shape, error signal. The optimal choice depends on the relative strengths of phase noise and additive noise. Thus, the optimal average length is a balance between phase tracking and suppression of additive noise. In principle, a short average length enables fast carrier phase tracking, and a longer average length enables large ASE noise tolerance. In the presence of fiber nonlinearities where phase noise is large, the optimal average length consequently becomes relatively so short to prevent any symbol with large occurring ASE noise from severely distorting the CPE process. This may affect the stability of CPE performance and subsequently causing performance degradation. For the steady performance of CPE in the presence of large phase noise, combined with normalization processing in CPE, we propose adaptive phase estimation technique to automatically detect and eliminate such signals with large ASE noise from the averaging process.

## 2 Proposed Adaptive Filtering Technique

In order to minimize computation resources required for real-time implementation of digital of CPR algorithms, most existing feedback and feedforward CPE algorithms [3] demonstrated so far perform phase estimation in two chronological steps. The effect of data modulation is first removed to derive a phase reference (PR) signal masked by ASE noise. A block of neighboring PR signals is summed up to filter out this additive noise distortion while tracking the varying phase. But the length of block used to filter the PR signal is quite subjective: The faster the phase noise variation, the smaller the average length, and vice versa. For high fiber launch power or longer fiber transmission length beyond 1000 km in coherent optical communication systems, the optimum average length therefore becomes inevitably small when phase noise is large during fiber nonlinearity, such that it may be unable or challenging to average out any occurring large ASE noise signal. This can meaningfully tilt the carrier phase away from the actual value, causing performance degradation. It is therefore reasonable to get rid of such large ASE noise signals from the averaging process to improve stability of the phase estimation algorithm. Note that in the presence of fiber nonlinearity where OSNR or fiber launch power is assumed to be high, since ASE noise is circularly



Gaussian and independently and identically distributed with zero mean, medium-to-low ASE noise occurs frequently than large ASE noise.

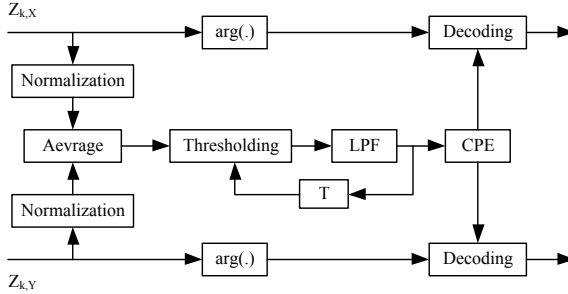


**Fig. 1** Block diagram of proposed adaptive filtering CPE

In principle, the proposed adaptive filtering technique first transformed the complex input signal to the CPE unit into polar coordinates with magnitude and phase using the basic Viterbi-Viterbi carrier phase estimator (V-V CPE) [4]. This is followed by normalization processing to generate a modulation-free phase reference (PR) signal [5]. This yields a normalized input signal with reduced noise distortions and avoids the use of complex multipliers in M-th power nonlinearity approach for modulation removal [6]. Next, the PR signal is digitally low-pass filtered by summing up a block of consecutive PR symbols. Since the two orthogonally polarized signals are affected by same phase noise from same transceiver lasers used for transmitting and detecting both polarization-demultiplexed signals, we adopt joint-polarization CPE algorithm [7] so that the normalized complex phasors of both polarization branches are combined using arithmetic mean to produce a single value before being passed through the low-pass filter. This improves the SNR of the CPR by 3 dB and relaxes laser linewidth requirements for the transceiver lasers (thereby reducing the system costs). Finally, the proposed scheme localizes (detect and isolate) symbols with large ASE noise signals by comparing the phase difference between the current PR signal and the previous output of the low-pass filter (LPF) with a pre-defined threshold, and those found to be exceeding the bound are assumed to be too noisy and discarded by setting the matching PR signal to zero. Thus, the proposed adaptive technique measures the phase difference between and the output of the LPF with a unit delay, and those exceed the pre-defined threshold are considered too noisy and abandoned by setting the corresponding PR signal to zero. Mathematically, the proposed adaptive filtering scheme can be summarized as:

$$\theta_k = 0 \text{ if } |\varphi_{k-1} \cdot \theta_k| > \delta \Delta_{\max} \tag{1}$$

where  $\theta_k$  is the normalized PR signal,  $\varphi_k$  is the averaged (filtered) signal, and  $\Delta_{\max}$  is the maximum conceivable phase variation between a signal with and without ASE noise controlled by a threshold factor  $0 \leq \delta \leq 1$ . Figure 1 shows the principle of operation of the proposed CPE scheme incorporating the adaptive filtering technique where the final joint-polarization phase estimate for both blockwise and sliding averaging can thus respectively be expressed as:

$$\hat{\theta}_k = \text{PU} \left[ \frac{1}{M} \arg \left\{ \sum_{n=1}^L \sum_{i=1}^C \theta_{i,k-n} \right\} \right] \quad (2)$$

$$\hat{\theta}_k = \text{PU} \left[ \frac{1}{M} \arg \left\{ \frac{1}{2L+1} \sum_{n=-L}^L \sum_{i=1}^C \theta_{i,k-n} \right\} \right] \quad (3)$$

where PU refers to phase unwrapping function applied to remove the fourfold phase ambiguity of the wrapped estimated phase,  $L$  is the average length, and  $C$  is the channel index which is 2 here (treating the polarization-multiplexed (PM) system implemented here as a phase-coherent multi-channel transmission). Note that the running average uses precursor and postcursor  $L$  symbols with block length as against  $L$  postcursor symbols for blockwise average. The block length  $L$  is optimized for each averaging method, while the threshold factor  $\delta$  is optimized for adaptive scheme and the phase estimate is updated in each symbol period when using a running average or every symbol period when using blockwise averaging.

### 3 Performance Evaluation

We assessed the performance of the proposed adaptive CPE scheme as detailed in Fig. 1 using both sliding [4] and blockwise [6] equal-weighted averaging V-V CPE. The system for a canonical PM coherent optical fiber wavelength-division multiplexing (WDM) transmission system spans seven CW channels between 1554.9 and 1550.1 nm on a 100 GHz grid [8]. The fiber link is made up of a recirculating loop modeling several 80-km spans of an uncompensated standard single-mode fiber (SSMF), where the fiber spans are assumed identical and the span loss was compensated by EDFA only modeled with a gain of 16 dB and noise figure of 4 dB. The amplified spontaneous emission (ASE) noise is added inline to guarantee that interaction between signal and noise is acceptably captured. After transmission, the center channel at 1552.5 nm is extracted and processed to compensate effects of CD and the average fixed nonlinear phase shift simultaneously using DBP and polarization derotation using CMA, all these impairments stemming from fiber transmission [8]. The optimized value of  $L$  (for both cases of averaging) and the threshold factor  $\delta$  were respectively found to be 3 and 0.8 in all instances. This is followed by carrier phase estimation using the proposed adaptive scheme. In this setup, OSNR values do not offer intuitive insight into signal quality. As such, we adopt the Q-factor as the signal quality metric. Figures 2 and 3 show both the BER and Q-factor as functions of launch power after 1200 km fiber transmission. The advantage of the adaptive approach can be seen to grow bigger as phase noise becomes strong, especially for the blockwise averaging. The obvious performance difference between block and sliding averaging method may be because the former shares a common phase within a block, and thus, it is more sensitive to any phase inaccuracy. Another reason could be that the optimal averaging length for the block averaging method is typically smaller than that of the sliding window method.

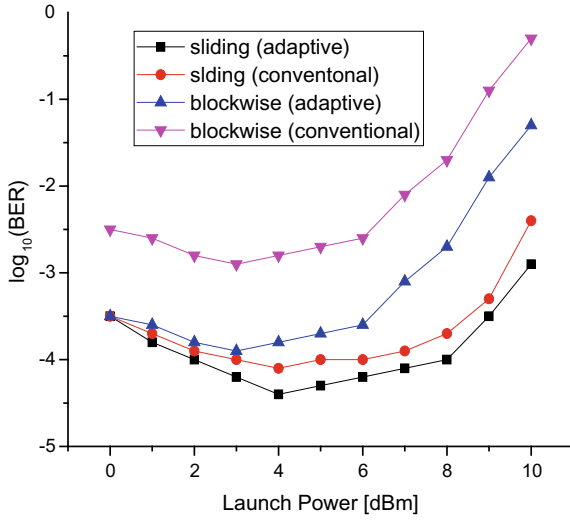


Fig. 2 BER as a function of fiber launch power

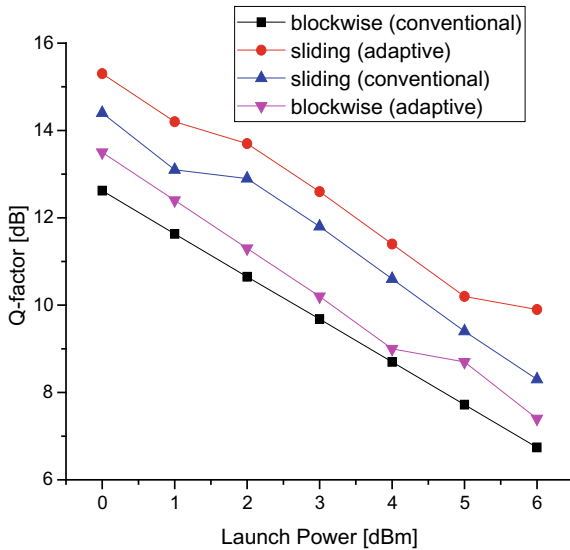
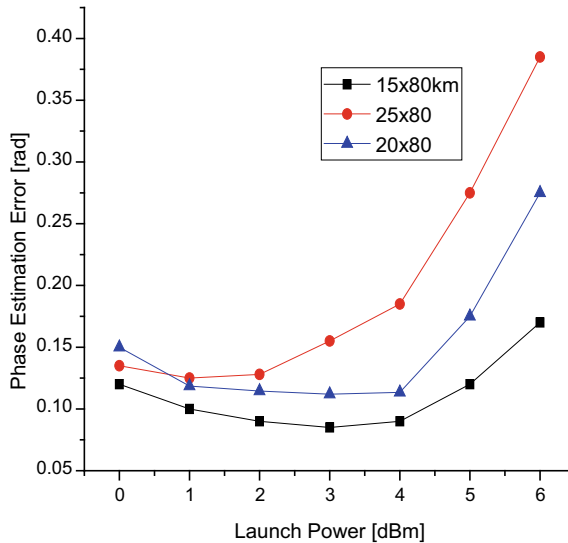


Fig. 3 Q-factor as a function of fiber launch power

Furthermore, the performance of most CPE algorithms is usually measured by their tolerance toward high phase noise values using SNR, BER, Q-factor, etc., as functions of the strength of the phase noise. The mean square error (MSE) metric [6], calculated as difference between the actual phase noise and the estimated phase noise, is also an efficient benchmark to assess the performance of CPE algorithms. The better the

performance, the lower will be MSE value of the CPE algorithm. We analyze the performance of the proposed adaptive CPE algorithm using this MSE metric. Figure 4 shows the result of such assessment implemented using only sliding averaging which validates our prediction using the proposed adaptive CPE. For different fiber transmission lengths, the scheme shows similar performance no matter the value of the launch power, even though there are fluctuations.



**Fig. 4** Phase estimation error as a function of fiber launch power

## 4 Conclusion

From the preceding results, we can conclude that the proposed adaptive filtering CPE technique provides about 1.0 dB Q-factor performance improvement on the conventional CPE method in mitigating the combined effects of laser linewidth and fiber nonlinearity for coherent phase-modulated optical signals. The technique identifies and eliminates symbols with significantly large noise from the filtering process to improve stability and estimation accuracy of the carrier phase estimators. The complexity of additional hardware required to implement the scheme is quite simple.

**Acknowledgements.** This work is supported by the National Natural Science Foundation of China (#61471088).

## References

1. Gordon, P., Mollenauer, L.F.: Phase noise in photonic communications systems using linear amplifiers. *Opt. Lett.* **15**(23), 1351–1353 (1990)
2. Taylor, M.G.: Phase estimation methods detection using digital signal processing. *J. Light Technol.* **27**(7), 901–914 (2009)
3. Ip, E., Kahn, J.M.: Feedforward carrier recovery for coherent optical communications. *J. Light Technol.* **25**(9), 2675–2692 (2007)
4. Viterbi, A.J., Viterbi, A.M.: Nonlinear estimation of PSK-modulated carrier phase with application to burst digital transmission. *IEEE Trans. Inf. Theory* **29**(4), 543–551 (1983)
5. Noé, R., Hoffmann, S., Pfau, T., Adamczyk, O., Herath, V.: Realtime digital polarization and carrier recovery in a polarization-multiplexed optical QPSK transmission. *IEEE-LEOS Summer Topical Meetings*, paper MC2.1, IEEE, Acapulco Mexico (2008)
6. Goldfarb, G., Li, G.: BER estimation of QPSK homodyne detection with carrier phase estimation using digital signal processing. *Opt. Express* **14**(18), 8043–8053 (2006)
7. Garcia, F., Mello, D.A.A., Waldman, H.: Feedforward carrier recovery for polarization demultiplexed signals with unequal signal to noise ratios *Opt. Express* **17**(10), 7958–7969 (2009)
8. Ip, E.: Nonlinear compensation using backpropagation for polarization-multiplexed transmission. *J. Light Technol.* **28**(6), 939–951 (2010)



# The Plasmon in Square Quantum-Dot System with Few Atoms

Renglai Wu<sup>(✉)</sup>, Jun Quan, and Jiangli Song

College of Physics Science and Technology, Lingnan Normal University,  
Zhanjiang, China  
wurenglai@sohu.com

**Abstract.** Based on the eigen-equation method, the eigenfunction is produced to seek plasmon modes in square quantum dots with few atoms. Besides the eigenfunction, charge-resonance peaks are also used to find plasmon. In the process of finding plasmon modes, it is found that only parts of the plasmon modes can be found by charge-resonance peaks, and all the plasmon modes can be found by eigen-equation method. Furthermore, the influence of various parameters on the plasmon shows that: the frequency of the plasmon shifts red with the increase of the quantum-dots size and shifts blue with the increase of the electron number. Moreover, the frequency of plasmon increases with the increase of the on-site and the nearest-neighbor Coulomb interaction due to that the excitation of plasmon needs higher energy under stronger Coulomb interaction.

**Keywords:** Quantum dot · Plasmon modes · Eigen-equation method

## 1 Introduction

The researches of quantum dots have attracted much attention due to the excellent and stable photoelectric properties [1, 2]. Now quantum dots are widely used to fabricate ultra-high resolution microprobe [3, 4], bioluminescent probe [5–7], and micro-laser device [8, 9]. The plasmon produced by the coupling of the external electromagnetic field with the quantum-dot system plays an important role in the study of the photoelectric properties of quantum dots. The capable of plasmon such as local field enhancement and beyond the diffraction limit can bring technical breakthroughs in the fields of microscopic detection, biosensor, and laser. In the future, the exploration of new plasmon modes will go on providing guidance for the photoelectric characteristics of quantum dots and providing the possibility for the discovery and regulation of new light fields. With the miniaturization of quantum-dot devices, the quantum effect of plasmon is very important in the process of finding the plasmon mode and studying their excitation properties. To accurately describe the quantum effect of plasmon, the existing research is mainly based on the quantum response theory [10–13]. However, the results calculated by the quantum response theory depend on the external field, so it is difficult to find all the plasmon modes under one type of external field, e.g., the perturbation theory shows that dark-mode plasmons can only be found in symmetrical plasma metals, but in the experimental, dark-mode plasmons are also found in

symmetrically broken terahertz supermaterials [10]; Refs. [11, 12] reported that the transverse electric field can only excite the transverse mode of plasmon, and the longitudinal electric field can only excite the longitudinal mode of plasmon; Refs. [13, 14] reported that dipole plasmon cannot be excited by antisymmetric electric field and quadrupole plasmon cannot be excited by uniform electric field. So the solution of plasmon mode is not complete enough under one type of external field. To fully explore all the models of the plasmon, it is necessary to develop the eigen-equation method to find the plasmon modes due that the obtained results are not affected by the applied electric field [15–17]. By using the eigen-equation method and the tight-binding approximation, we have explored the plasmon modes in square quantum dots and made a discussion about the influence of the quantum-dots size and electron number on the plasmon.

## 2 Model and Theory

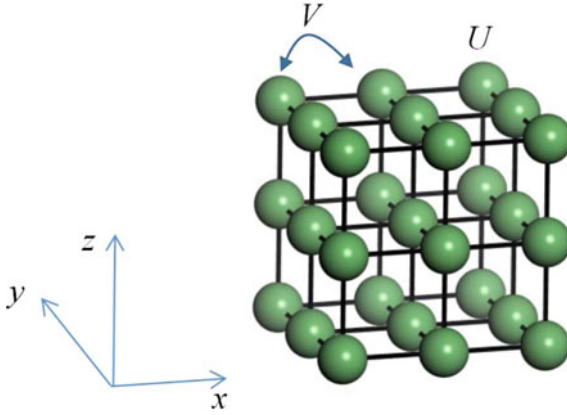


**Fig. 1** The model of square quantum dot with few atoms

The model of square quantum dot is shown in Fig. 1. Here  $U$  is the on-site Coulomb interaction, and  $V$  is the nearest-neighbor Coulomb interactions.  $N_x$ ,  $N_y$  and  $N_z$  are adopted to describe the lattice numbers in the  $x$ ,  $y$ , and  $z$  directions, respectively.

Based on the tight-binding approximation and the linear response theory, in the case of external field  $V^{\text{ex}}(\mathbf{l}, \omega)e^{-i\omega t}$ , the collective charge oscillations of the quantum dot are calculated by:

$$\sum_{\mathbf{l}'} \left[ \delta_{\mathbf{l}\mathbf{l}'} - \sum_{\mathbf{l}''} \Pi(\mathbf{l}, \mathbf{l}'', \omega) v_{\mathbf{l}\mathbf{l}''} \right] Q(\mathbf{l}', \omega) = e^2 \sum_{\mathbf{l}'} \Pi(\mathbf{l}, \mathbf{l}', \omega) V^{\text{ex}}(\mathbf{l}', \omega) \quad (1)$$

where  $v_{\mathbf{l}\mathbf{l}'}$  is the interactions between lattices  $\mathbf{l}''$  and  $\mathbf{l}'$

$$v_{\mathbf{l}'\mathbf{l}''} = \begin{cases} U, & |\mathbf{l}' - \mathbf{l}''| = 0 \\ V, & |\mathbf{l}' - \mathbf{l}''| = 1 \\ 0, & \text{else} \end{cases} \quad (2)$$

Here,  $U$  is the on-site Coulomb interaction, and only nearest-neighbor Coulomb interactions  $V$  is considered.  $\Pi(\mathbf{l}, \mathbf{l}', \omega)$  is the Lindhard function

$$\Pi(\mathbf{l}, \mathbf{l}', \omega) = 2 \sum_{mn} \frac{f(E_m) - f(E_n)}{E_m - E_n - \hbar\omega - i\eta} \psi_m^*(\mathbf{l}) \psi_n(\mathbf{l}) \psi_n^*(\mathbf{l}') \psi_m(\mathbf{l}') \quad (3)$$

where  $\eta$  is the scattering rate,  $f(E_n)$  is the Fermi function,  $E_n$  and  $\psi_n(\mathbf{l})$  are the eigen energy and eigen wave vector, respectively,

$$\begin{cases} \psi_m(\mathbf{l}) = \sqrt{\frac{4}{L_x L_y}} \sin\left(\frac{m_x \pi}{L_x} l_x\right) \sin\left(\frac{m_y \pi}{L_y} l_y\right) \sin\left(\frac{m_z \pi}{L_z} l_z\right) \\ E_m = -2\gamma \cos\left(\frac{m_x \pi}{L_x}\right) - 2\gamma \cos\left(\frac{m_y \pi}{L_y}\right) - 2\gamma \cos\left(\frac{m_z \pi}{L_z}\right) \end{cases} \quad (4)$$

where  $L_x = N_x + 1$ ,  $L_y = N_y + 1$  and  $L_z = N_z + 1$  are, respectively, the length, width, and height of the quantum dots. And  $m_x = 1, 2, 3 \dots N_x$ ,  $m_y = 1, 2, 3 \dots N_y$ ,  $m_z = 1, 2, 3 \dots N_z$ . According to the Eq. (1), the plasmon frequency can be obtained by the collective oscillation peaks of  $Q(\omega) = \sum_{\mathbf{l}} Q(\mathbf{l}, \omega)$  in present of  $V^{\text{ex}}(\mathbf{l}, \omega)$ ; however, it is difficult to find all the plasmon modes under one type of external field, only parts of the plasmon modes can be found through Eq. (1). So we make  $V^{\text{ex}}(\mathbf{l}', \omega) = 0$  and get the eigen equation:

$$\sum_{\mathbf{l}'} \left[ \delta_{\mathbf{l}\mathbf{l}'} - \sum_{\mathbf{l}''} \Pi(\mathbf{l}, \mathbf{l}'', \omega) v_{\mathbf{l}''\mathbf{l}'} \right] Q(\mathbf{l}', \omega) = 0 \quad (5)$$

To get nonzero solutions of  $Q(\mathbf{l}', \omega)$ , the coefficient matrix of Eq. (5) has to satisfy

$$B(\omega) = \det[\delta_{\mathbf{l}\mathbf{l}'} - \sum_{\mathbf{l}''} \Pi(\mathbf{l}, \mathbf{l}'', \omega) v_{\mathbf{l}''\mathbf{l}'}] = 0 \quad (6)$$

Here,  $B(\omega)$  is the determinant of coefficient matrix of Eq. (5), which is a frequency dependent function named as eigenfunction. And the value of  $B(\omega)$  will be zero at the plasmon frequency. Due to the finite scattering rate  $\eta$  in Eq. (3), the eigenfunction  $B(\omega)$  is a plural value, so the eigen plasmon frequency is generally found by  $\text{Re}[B(\omega)] = 0$  with  $\text{Im}[B(\omega)] \approx 0$ , it also implies that  $\text{Im}[1/B(\omega)]$  will show a peak at plasmon frequency. Thus, we can find plasmon both through the peaks of  $\text{Im}[1/B(\omega)]$  and the zero point of  $\text{Re}[B(\omega)]$ . And all the eigen plasmon frequency can be solved by the zero point of  $\text{Re}[B(\omega)]$  since its value is independent on the external field.



### 3 Results and Discussions

In all the calculations, if it is not noticed, the parameters are  $U = 3.0$  eV,  $V = 1.0$  eV,  $\eta = 0.005$  eV. The unit of frequency is  $2\pi\gamma/h$ , with  $h$  the Planck constant. Arbitrary units are applied for the values of the energy absorption and the charge. The system size is described by  $N_x \times N_y \times N_z$ .

In Fig. 2, we show the plasmon by the eigenfunction and show the response of charge to different types of external fields. The results in Fig. 2a1, a2 show that, in the frequency range 1.55–1.65, the zero point of  $\text{Re}[B(\omega)]$  and the peak of  $\text{Im}[1/B(\omega)]$  appear at the same frequency, which can be determined as the plasmon frequency. Moreover, Fig. 2a3, a5 show the peaks of charge resonance at the plasmon frequency, respectively, which implies that the plasmon in the frequency region 1.55–1.65 are

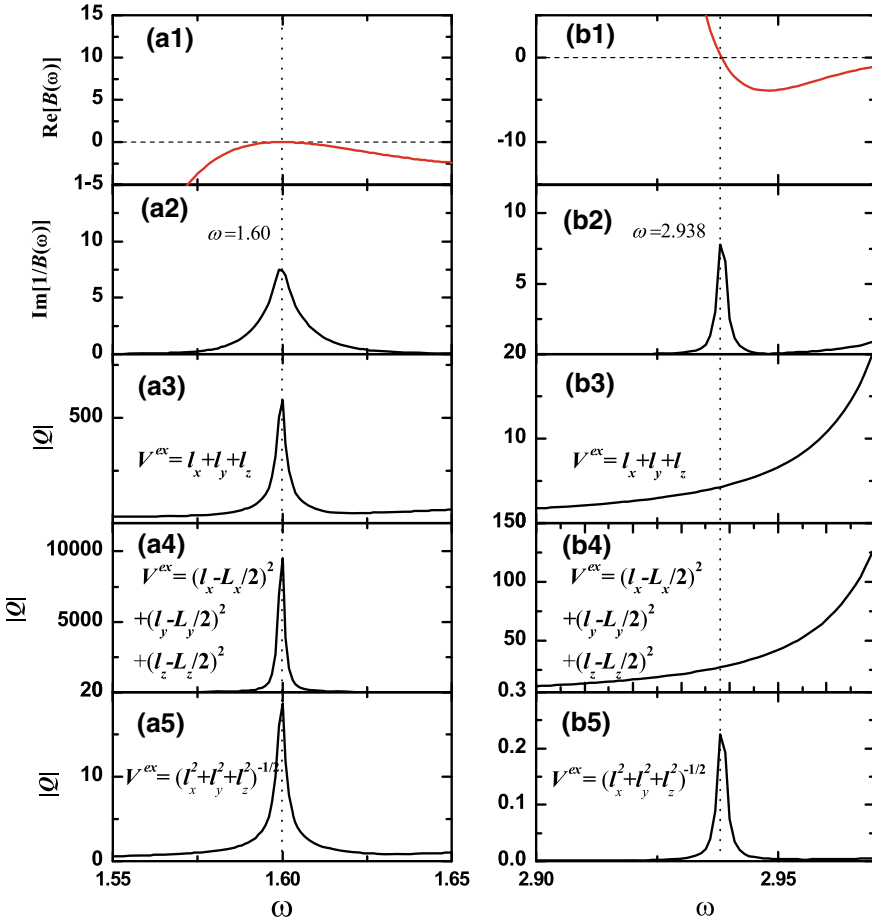


**Fig. 2** a1 and b1  $\text{Re}[B(\omega)]$  varies with the frequency; a2 and b2  $\text{Im}[1/B(\omega)]$  varies with the frequency; a3–a5 and b3–b5 The charge response  $|Q|$  varies with the frequency of external fields. Where the system size is  $3 \times 3 \times 3$ , and  $L_x = L_y = L_z = 4$ ,  $N_e = 2$

excited in the case of external potential  $V^{\text{ex}} = l_x + l_y + l_z$ ,  $V^{\text{ex}} = (l_x - L_x/2)^2 + (l_y - L_y/2)^2 + (l_z - L_z/2)^2$ , and  $V^{\text{ex}} = (l_x^2 + l_y^2 + l_z^2)^{-1/2}$ . Figures 2b1, b2 also show a plasmon mode in the frequency range 2.90–2.97. However, there are no charge-resonance peaks in Fig. 2b3, b4, which implies that, the plasmon in the frequency region 2.90–2.97 are not excited by external potential  $V^{\text{ex}} = l_x + l_y + l_z$  and  $V^{\text{ex}} = (l_x - L_x/2)^2 + (l_y - L_y/2)^2 + (l_z - L_z/2)^2$ . So it is not reliable to find plasmons based on charge resonance, because some plasmon modes may not be excited by an external field. In contrast, it is feasible to find plasmon modes by the eigen-equation method, and all plasmon modes can be found completely.

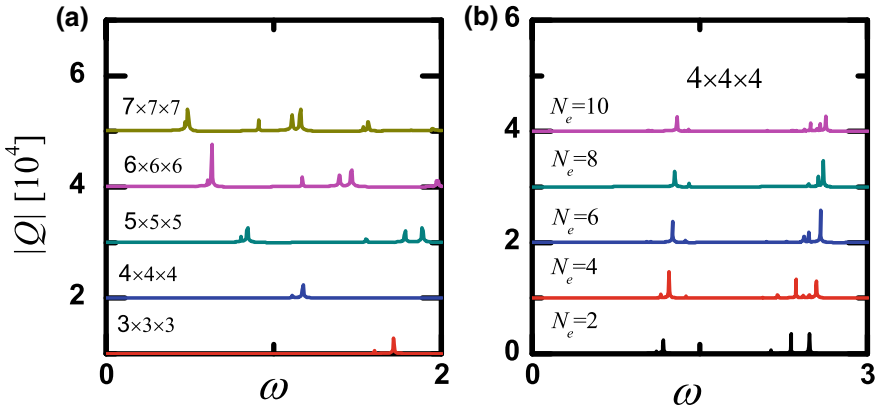


**Fig. 3** The charge response varies with the frequency of external potential  $V^{\text{ex}} = l_x + l_y + l_z$ , where, **a** for a fixed electron number  $N_e = 2$ , and the system sizes are  $3 \times 3 \times 3$  to  $7 \times 7 \times 7$  from bottom the top; **b** for a fixed system size is  $4 \times 4 \times 4$ , the electron number are  $N_e = 2$  to  $N_e = 10$  from bottom the top

In Fig. 3a, the evolution of plasmon with system size shows that, from the bottom to the top of the figure, the frequency of the leftest peaks shift red with the increase of the system size, which mainly caused by the decrease of energy level in large size system. Moreover, more peaks appear in system with larger size, which represents more high order plasmons caused by the splitting of energy levels. In Fig. 3b, the evolution of plasmon with electron number shows that, from the bottom to the top of the figure, the frequency of the leftest peak shifts blue with the increase of the electron number, which mainly caused by the increase of the energy level and fermi energy in large size system.

In Fig. 4a, from the bottom to the top of the figure, the peaks of all the plasmons slightly shift blue with the increase of the on-site Coulomb interaction  $U$ , which implies that the on-site Coulomb interaction gives rise to a blue-shift in charge response. In Fig. 4b, the peaks of all the plasmons shift blue with the increase of the nearest-neighbor Coulomb interactions  $V$ . The results in Fig. 4a, b can be explained by that the excitation of plasmon needs higher energy due to the increase of the Coulomb interaction.

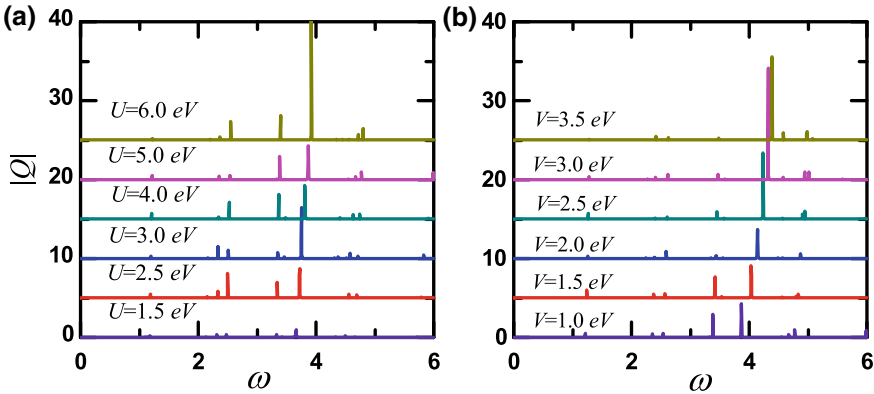


**Fig. 4** The dependence of the charge response on **a** the on-site Coulomb interaction  $U$ , and **b** the nearest-neighbor Coulomb interactions  $V$ . Where all the lines are plotted for the same system size  $4 \times 4 \times 4$  and electron number  $N_e = 2$ . The external potential is  $V^{ex} = l_x + l_y + l_z$

## 4 Conclusions

On the basis of the eigen-equation method and the collective excitation of charges under external fields, the plasmon in square quantum-dot system is observed. Through the comparison of plasmons, respectively, found by the eigen function and charge response, it is found that all plasmon modes can be found by the eigen equation completely; however, some plasmon modes may not be found by the charge resonance due to they are not be excited by some types of electric field. Furthermore, we have studied the influence of various parameters on the plasmon and found that: the frequency of the plasmon shifts red with the increase of the quantum dots size and shifts blue with the increase of the electron number, and the frequency of plasmon shifts blue with the increase of the on-site and the nearest-neighbor Coulomb interaction.

**Acknowledgements.** The work is supported by the National Natural Science Foundation of China (Grant No: 11647156, 11304276, 61674073, 91436102, 11374353) and the Natural Science Foundation of Guangdong Province, China (Grant No.: 2017A030313022).

## References

1. Gan, Z., Xu, H., Hao, Y.: Mechanism for excitation-dependent photoluminescence from graphene quantum dots and other graphene oxide derivatives: consensus, debates and challenges. *Nanoscale* **8**(15), 7794–7807 (2016)
2. Jeong, K.S., Guyot-Sionnest, P.: Mid-infrared photoluminescence of CdS and CdSe colloidal quantum dots. *ACS Nano* **10**(2), 2225–2231 (2016)
3. Xing, Y., Rao, J.: Quantum dot bioconjugates for in vitro diagnostics & in vivo imaging. *Cancer Biomarkers* **4**(6), 307–319 (2008)
4. Xing, Y., Xia, Z., Rao, J.: Semiconductor quantum dots for biosensing and in vivo imaging. *IEEE Trans. Nanobiosci.* **8**, 4–12 (2009)

5. Fei, X., Sun, W., Cao, L., Jiao, X., Lin, D., Jia, G.: Design and preparation of quantum dots fluorescent probes for in situ identification of *Microthrix parvicella* in bulking sludge. *Appl. Microbiol. Biotechnol.* **100**(2), 961–968 (2016)
6. Nakamura, H., Kohmoto, S., Ishikawa, T.: Novel nano-scale site-controlled InAs quantum dot assisted by scanning tunneling microscope probe. *Physica E* **7**(3), 331–336 (2000)
7. Wei, H., Zhang, S., Tian, X., Xu, H.: Highly tunable propagating surface plasmons on supported silver nanowires. *Proc. Natl. Acad. Sci. U.S.A.* **110**(12), 4494–4499 (2013)
8. Chen, S., Liao, M., Tang, M.: Electrically pumped continuous-wave 1.3  $\mu\text{m}$  InAs/GaAs quantum dot lasers monolithically grown on on-axis Si (001) substrates. *Optoelectron. IET* **8**(2), 20–24(2017)
9. Wan, Y., Norman, J., Li, Q., Kennedy, M., Liang, D., Bowers, J. E.: 1.3  $\mu\text{m}$  submilliamp threshold quantum dot micro-lasers on Si. *Optica* **4**(8), 940–994 (2017)
10. Chen, F., Alemu, N., Johnston, R. L.: Collective plasmon modes in a compositionally asymmetric nanoparticle dimer. *AIP Adv.* **1**(3), 032134-1-16 (2011)
11. Yuan, Z., Gao, S.: Plasmon resonances in linear atomic chains: free-electron behavior and anisotropic screening of d electrons. *Phys. Rev. B* **78**(23), 1879–1882 (2008)
12. Yan, J., Yuan, Z., Gao, S.: End and central plasmon resonances in linear atomic chains. *Phys. Rev. Lett.* **98**(21), 216602–216605 (2007)
13. Wu, R., Xue, H., Yu, Y., Hu, H., Liu, Q.: Quadrupole plasmon excitations in confined one-dimensional systems. *EPL* **108**(2), 27001 (2014)
14. Wu, R., Xue, H., Yu, Y., Hu, H.: Dipole and quadrupole plasmon in confined quasi-one-dimensional electron gas systems. *Phys. Lett. A* **378**(40), 2995–3000 (2014)
15. Toyoda, T., Dawson, K.A., Indekeu, J.O.: Self-consistent linear response approximation for quantum many-body systems. *Phys. A* **253**, 498–506 (1998)
16. Uchida, T., Hiraiwa, N., Yamada, K., Fujita, M., Toyoda, T.: Magnetic induction dependence of the dispersion of magnetoplasmon in a two-dimensional electron gas with finite layer thickness. *Int. J. Mod. Phys. B* **28**, 1450044 (2014)
17. Xin, W., Wu, R., Xue, H.: Plasmonic excitations in mesoscopic-sized atomic chains: a tight-binding model. *Acta Phys. Sin.* **62**(22), 177301 (2013)



# Electrophysiological and Phototactic Behavior Studies of *Musca domestica*

Wei-Wei Xu<sup>1</sup>(✉), Shun Kamada<sup>2</sup>, Takanori Kozai<sup>1</sup>, Tao Zheng<sup>1</sup>,  
Takeshi Fujihara<sup>1</sup>, Tomoya Konishi<sup>1</sup>, and Masaru Kamano<sup>1</sup>

<sup>1</sup> National Institute of Technology, Anan College, 265 Aoki Minobayashi,  
Anan, Tokushima 7740017, Japan

kamano@anan-nct.ac.jp

<sup>2</sup> Tokushima University, 2-1 Minamijosanjima, Tokushima 7708506, Japan

**Abstract.** Lighting technologies change the life of human beings and bring various applications in illumination and biological engineering. One case is the phototaxis research by light controlling the spread of insects. Optical methods by phototaxis of ultraviolet light have attracted much attention for capturing and killing *Musca domestica*. However, the development of an effective and environmentally acceptable light traps is still challenging due to the complex responses of insects to wavelength and intensity. Herein, we developed the LED light source for selectively attracting *Musca domestica* by investigating spectral sensitivity of their compound eyes through electroretinograms (ERG) signal and the phototactic behavior to different LEDs. The spectral sensitivity of the compound eyes showed that both female and male had a primary peak at 360 nm and a secondary peak at 520 nm. The attraction efficiency of LEDs was compared with different colors (wavelengths), which revealed that purple LED (415 nm) attracted the most of *Musca domestica*s and will broaden the applications of purple LED in the insect pest control.

**Keywords:** LEDs applications · Phototaxis · Electroretinograms

## 1 Introduction

The phototaxis research to control the spread of insects [1, 2] has been known and studied for decades [3, 4]. One application is the optical control of the most common insect on the planet—*Musca domestica*, which are not only nuisance pests buzzing around homes, carrying potential disease, but also transferring more than 100 different pathogens harmful to both humans and pets [5–7]. The short lifespans but strong reproductive capacity of *Musca domestica* make it one of the knottiest problems. Therefore, lots of methods have been developed to fight against with *Musca domestica* [8, 9]. However, the mushrooming of insecticides for *Musca domestica* succeeded in controlling the quantities at first but later greatly increased environmental pollution and insecticide resistance [10, 11]. Another method of biological method by natural enemies reduced the efficiency and would become another disaster if breaking the balance in the biological chain [12]. Besides, a sticky cylinder trap cannot eliminate the

housefly populations either [13]. The optical phototaxis method of capturing and killing *Musca domestica* with ultraviolet lights has attracted attention [14]. However, the irresistible attraction to many insects disobeys the protection of the biological chain. The exposure of UV will damage human eyes and bare skin in homelife [15]. To develop a selective and visible light source, controlling *Musca domestica* becomes necessary. The response of *Musca domestica* to light are attributed by the two forms of central rhabdomeres of retinula cells in each ommatidium with four photoreceptors.

LED lighting technology has changed the life of human beings and brought various applications for illumination, display and even biological engineering for promoting integrated pest management [16–18]. Herein, based on electroretinographic (ERG) signals, phototaxis response of *Musca domestica* to LEDs has been researched to develop a method of LED light control of *Musca domestica*. ERG signals of compound eyes were recorded monochromatic stimuli ranging from 300 to 700 nm. Meanwhile, to understand the visual responses of the *Musca domestica* to light, the absorption spectra of the visual pigment was obtained by dissolving compound eyes into chemical solutions. In the ERG signals, a peak falling in the ultraviolet region of 360 nm was observed while another peak was in the green region (peak at 520 nm). The spectral sensitivity curve was considered well matching to the absorption spectra of the visual pigment. In phototactic behavior experiments, the attraction efficiency of *Musca domestica* to light-emitting diodes (LEDs) with different central wavelengths (415, 456, 520, 600 and 636 nm) was studied under the same photon flux density. The results revealed *Musca domestica*s preferred shorter wavelength light—the purple LED (415 nm) attracted the most while the red attracted the least.

## 2 Materials and Methods

### 2.1 Insect Offspring

*Musca domestica* were obtained from Applied Biology Center of Sumika Techno Service Company. The offspring reproduction of the *Musca domestica*s was maintained in the thermostatic chamber (C-007-50L, MRT, W425, D525, H435 mm) of National Institute of Technology, Anan College. The *Musca domestica* used in the experiment were obtained from laboratory breeding after eclosion for more than 10 days. The *Musca domestica* only reared on horn sugar and distilled water were placed in a thermostatic chamber at 25 °C under a photoperiod of 12 h:12 h (light period 6:00–18:00).

The images of *Musca domestica* classified as female and male were shown on the left and right side in Fig. 1a, respectively. Scanning electron microscope (SEM) images of the *Musca domestica* compound eye at different magnifications were shown in Fig. 1b, c. Each eye consisted of thousands of ommatidia which were hexagonal lens of 10–20  $\mu\text{m}$  width and 5–10  $\mu\text{m}$  high. The compound eye was the main photoreceptor of *Musca domestica* which would be recorded by ERG signals. When light stimulated the cell (photoreceptor) in the retina inside the ommatidia, electrons were excited and would generate a potential difference referred to the state without light. This voltage was usually defined as ERG signal (shown in Fig. 1d).

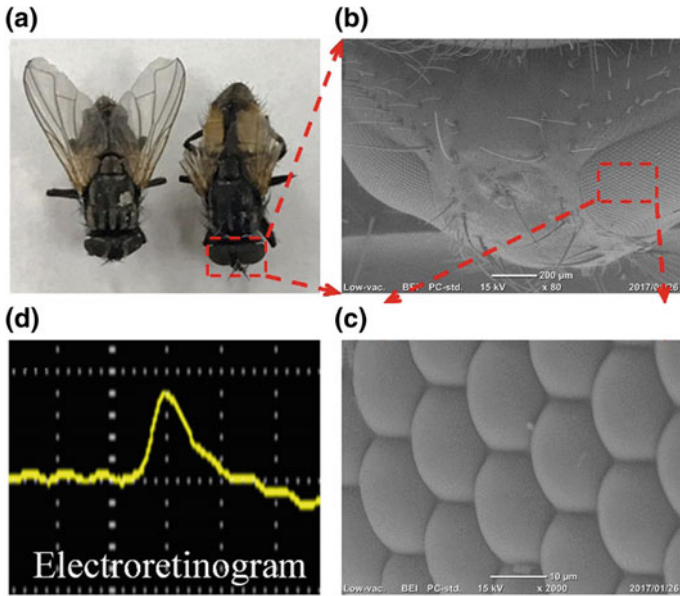


**Fig. 1** *Musca domestica* compound eye morphology and electroretinogram. **a** An example of female and male *Musca domestica* shown on the left and right sides. **b**, **c** SEM images of *Musca domestica* compound eye. **d** Electretinogram (ERG) response of *Musca domestica* compound eye to light-stimulation for typically 1 s

## 2.2 Spectral Sensitivity of the Compound Eye

The measurement of ERG was briefly shown in Fig. 2. First, the reared adult *Musca domestica*s in the laboratory were classified as female and male. Then five individuals of each sex were used to measure the ERG response. An anesthetized *Musca domestica* was fixed on a glass piece with bees' wax and mounted in the dark shield box. Two tungsten needles (7P-010, Micro supporter) with diameter of about 10 μm were inserted into the retina of the compound eye and abdomen to be the positive and negative electrode, respectively. ERG responses were recorded by a preamplifier (ADA400A, Tektronix) which was connected to an oscilloscope (TDS2014B, Tektronix). The monochromatic stimuli were provided by a 500 W xenon arc lamp (C7535, Hamamatsu) and an optical splitter (M10-k1, Spectrometer Co., Ltd.) ranging from 300 to 700 nm with a 20 nm interval. The light was placed right on the compound eye through an optical fiber (MC2000B, Thorlabs Inc.). The quantum flux of each monochromatic stimuli was measured and adjusted to the same photon flux density by using a photometer (Multichannel Voltage Recorder, MCR-4V) and an optical filter. After keeping the *Musca domestica* in the dark shield box for 20 min, the compound eye was irradiated with a series of monochromatic flashes of 100 ms duration. After 60 s recovering, the wavelength was changed from short to long wavelength and then in the reverse direction to record ERG responses. Based on the response-stimulus intensity function recorded by a 4-log-unit intensity, the spectral

sensitivity curve of the compound eyes was calculated, as well as the relationship between wavelength and ERG responses. Here the inset SEM image Fig. 2(iii) showed the damaged eye by the needles.

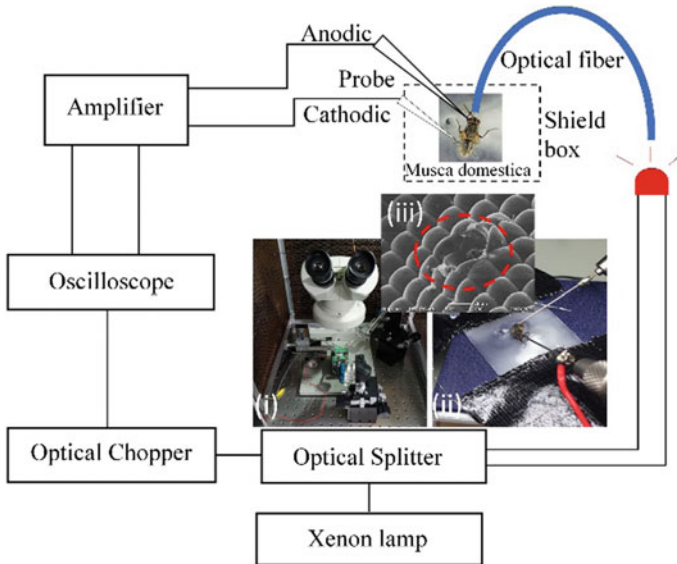


**Fig. 2** Measurement system for ERG signal. The inset (i) is the whole setup. (ii) denotes close sight. (iii) SEM image showed the *Musca domestica* eye after removing the needles

### 2.3 Behavioral Experiments

The phototactic behaviors of adult *Musca domestica* were evaluated based on the attraction to LEDs at various wavelengths through the dynamic tracking video in the laboratory (shown in Fig. 3). The experiments were conducted in a dark room by building a round basin with bottom and top diameter of 450 and 500 mm, two acrylic plates (450 mm) placed in the middle of the round basin, and an acrylic plate of height 20 mm to form a closed behavioral space. A monitor wireless camera (WHC7M, Masprc Electric Works) was fixed at the top of the round bowl to record the moving route range of *Musca domestica*. A hole for LEDs was punched in the surrounding side of the round basin. The area of the attraction range was counted in a arc area of radius 40 mm in the centre of the optical fiber. The LED was connected to the function generator to illuminate the target area.

The light intensity at 4 cm far from the top of the fiber of each light source was measured by a photometer and changed into number of photons ( $4 \mu\text{mol}/\text{m}^2/\text{s}$ ). The LEDs with central wavelength of purple 415 nm, blue 456 nm, white, green 520 nm, yellow 600 nm and red 636 nm (Nichia Corp, Tokushima, Japan) were used in the experiment (shown in the Fig. 3). The anesthetized *Musca domestica*s were taken out of the thermostatic chamber, placed in the middle area of the round basin and



covered with a black curtain keeping out other light. The monitor wireless camera started capturing 5 min later after the *Musca domestica* resumed consciousness and freely flying. The wavelength preference characteristics were evaluated based on the time of *Musca domestica* staying near the light source in the 40 mm radius to the LED light source. After 2 h of dynamic tracking video, the attraction ratio of the *Musca domestica*s to different LEDs was analyzed by two-dimensional animation measurement software (MoveTr2D, Library company). All the experiments were conducted at 25 °C after 18:00 in the evening and repeated three times.

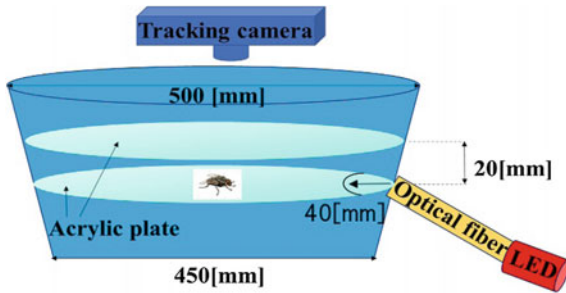


Fig. 3 Measurement setup for the phototactic behaviors to LEDs

### 3 Results and Discussions

#### 3.1 Spectral Sensitivity of Compound Eyes

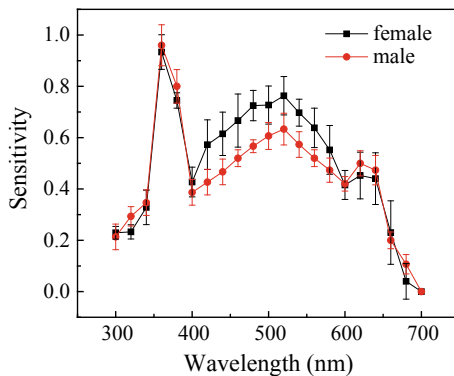


Fig. 4 Average spectral sensitivity of females (black squares) and males (red circles) measured by ERG method

Figure 4 showed the average sensitivity of five females (black squares) and five males (red circles). The data of each wavelength were measured by the average response-energy curve from visual cells. The primary peak was found at 360 nm in the curves of

both female and male. Besides, there was a secondary peak at 520 nm for both female and male which was maybe due to the high sensitivity of photoreceptor in ultraviolet and green wavelengths. The sensitivity of female and male *Musca domestica* at 520 nm was about 66% and 77% of 360 nm, respectively. There was another peak around 630–640 nm. The sensitivity became weaker when the wavelength was more than 640 nm. The slightly stronger sensitivity of females than males revealed sexual differences in the visible wavelength.

### 3.2 Absorption and Light Transporting Inside the Ommatidium

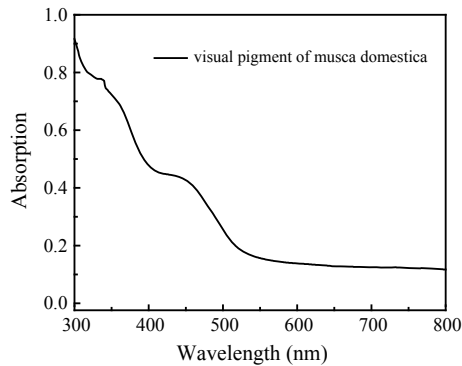
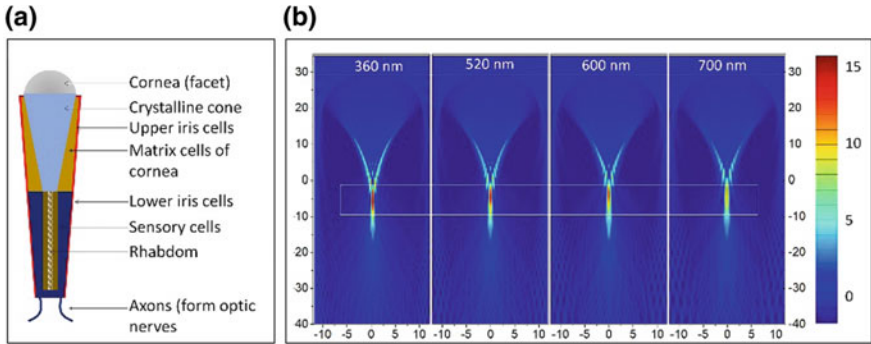


Fig. 5 Absorption spectra of the visual pigments

The absorption spectra of the visual pigments from *Musca domestica* were measured by ultraviolet visible spectrophotometer (shown in Fig. 5). The response of *Musca domestica* to light was attributed by the two forms of central rhabdomeres of reticular cells in each ommatidium with four photoreceptors. They were sensitive to different wavelength, in other words, color vision [19]. There were three optical components in *Musca domestica* compound eye determining the angular of photoreceptors: the light diffracting facet lens, the wave-guiding rhabdomere and the light-absorbing visual pigment in the rhabdomere [20]. The light absorption of visual pigments decreased from 300 to 600 nm with two absorption peaks around 360 and 450 nm. The light absorption became much weaker when the wavelength was more than 600 nm. These absorption spectra of the visual pigments showed a good matching to the spectral sensitivity curve especially at the peaks of 360 and 520 nm. It was inferred that the UV and green-absorbing visual pigments expressed in the photoreceptor cells of *Musca domestica* absorbed the light, excited electrons and generated the potentials for the ERG signals.

The transmittance of LED lights inside an ommatidium of the compound eye was simulated as shown in Fig. 6. The model was designed based on the SEM images of the ommatidium structure shown in Fig. 1. The diameter of the cornea was 20  $\mu\text{m}$  with depth 10  $\mu\text{m}$  as shown in Fig. 7a. A finite-difference time-domain (FDTD) method was used to estimate the different wavelength (360, 520, 600 and 700 nm) by an

ommatidium, as shown in Fig. 7b. The light focus was gradually shifted upward and the intensity of light absorption was gradually decreased as the wavelength becomes longer. In this case, if purple light was right focused inside the sensory cell, obviously the longer wavelength would lose the focus at the same position. This could be one reason why the red light was not sensitive. Another reason was the less absorption of materials at longer wavelength would make the sensitivity worse.



**Fig. 6** Transmittance of light inside the ommatidium. **a** The general structure of a *Musca domestica* ommatidium. **b** FDTD simulation of light transporting at various wavelengths in an ommatidium eye

### 3.3 Attraction Rate by Different LED Colors

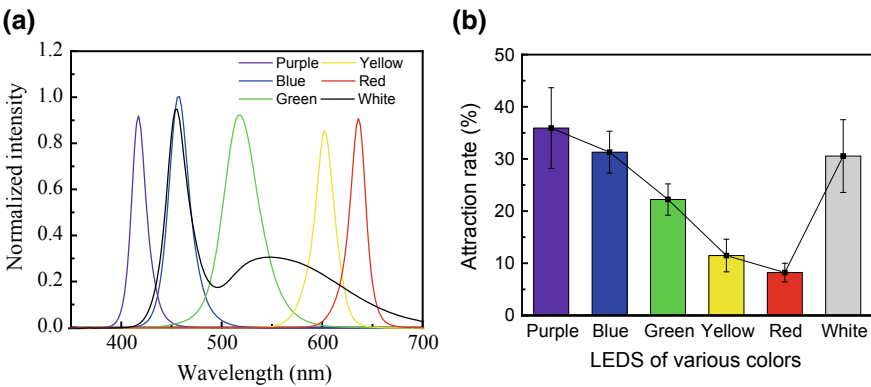


**Fig. 7** **a** Spectrum of different LEDs. **b** Spectral preference of *Musca domestica* for LEDs at six different wavelengths of light

The attraction rate of *Musca domestica* to LEDs of different colors was shown in Fig. 7. Most of the *Musca domestica* moved to the LEDs light source after 10 s, staying near the edge of the light source and moving back and forth around the light

source. In the case of different LEDs light, purple LED (415 nm) was the most attractive color to *Musca domestica*s than other LEDs, about 35% ratio in 2 h staying 4 cm from the light source. The more next attractive LED color was blue LED (456 nm) light with a probability of 30%. The third one was the white LED light. The rate was similar to blue LED but higher than others due to the specific spectrum range of the white LED including two peak wavelengths at 456 and 550 nm. Although the secondary peak of the spectral sensitivity was 520 nm, *Musca domestica*s were much less attracted to the green LED (520 nm) than purple and blue LED light. Orange and red LEDs light were the least attractive light source to *Musca domestica*s at the same level, which was reasonable from the spectrum or absorption curve (Fig. 7a).

## 4 Conclusions

Based on ERG measurement, the sensitive spectrum of *Musca domestica*s to light has been found a primary peak in the violet (360 nm), a secondary peak in the green (520 nm) region and a third peak around 620 nm. The spectrum between male and female revealed a little sexual difference. Absorption of the pigments has been measured showing well matching to spectrum sensitivity. Also, FDTD simulations were conducted to show the light transporting inside ommatidia. Based on these analyses, significant differences between different LEDs for the attraction rate of *Musca domestica* have been found. The shorter wavelength tended to be most attractive while the longer wavelength was the least, in which purple LEDs were the best while the red LEDs were the worst. Therefore, red LED is recommended for illumination inside food factories and store houses while a purple LED could be used at the gate to attract *Musca domestica* out. Based on these results, a new method by combining different light source for *Musca domestica* control could be established which will broaden the applications of purple LED in the insect pest control.

**Acknowledgements.** This work is supported by Tokushima Government Budget for scientific research of LED with insect repellent effect.

## References

1. Shimoda, M., Ken-ichiro, H.: Insect reactions to light and its applications to pest management. *Appl. Entomol. Zool.* **48**(4), 413–421 (2013)
2. Boda, P., Horváth, G., Kriska, G., Blahó, M., Csabai, Z.: Phototaxis and polarotaxis hand in hand: night dispersal flight of aquatic insects distracted synergistically by light intensity and reflection polarization. *Naturwissenschaften* **101**(5), 385–395 (2014)
3. Kessler, M.E., Chabora, P.C.: Light intensity and phototaxis in the house fly: photonegativity in a yellow-eyed mutant. *Behav. Genet.* **7**(2), 129–137 (1977)
4. Meyer, H.: Phototaxis in the walking male and female fly (*Calliphora erythrocephala* Meig.). *J. Comp. Physiol.* **123**(4), 307–314 (1978)
5. Fotedar, R.: Vector potential of houseflies (*Musca domestica*) in the transmission of *Vibrio cholerae* in India. *Acta Trop.* **78**(1), 31–34 (2001)

6. Butler, J.F., Maruniak, A.G., Meek, F., Maraniak, J.E.: Wild Florida house flies (*Musca domestica*) as carriers of pathogenic bacteria. *Florida Entomol.* **93**(2), 218–223 (2010)
7. Cirillo, V.J.: “Winged sponges”: houseflies as carriers of typhoid fever in 19th-and early 20th-century military camps. *Perspect. Biol. Med.* **49**(1), 52–63 (2006)
8. Malik, A., Singh, N., Satya, S.: House fly (*Musca domestica*): a review of control strategies for a challenging pest. *J. Environ. Sci. Health Part B* **42**(4), 453–469 (2007)
9. Axtell, R.C.: Fly management in poultry production: cultural, biological, and chemical. *Poult. Sci.* **65**(4), 657–667 (1986)
10. Malik, A., Singh, N., Satya, S.: House fly (*Musca domestica*): a review of control strategies for a challenging pest. *J. Environ. Sci. Health Part B* **42**(4), 453–469 (2007)
11. Walsh, S.B., Dolden, T.A., Moores, G.D., Kristensen, M., Lewis, T., Devonshire, A.L., Williamson, M.S.: Identification and characterization of mutations in housefly (*Musca domestica*) acetylcholinesterase involved in insecticide resistance. *Biochem. J.* **359**(1), 175–181 (2001)
12. Henrik, S., Nachman, G.: Biological control of house flies *Musca domestica* and stable flies *Stomoxys calcitrans* (Diptera: Muscidae) by means of inundative releases of *Spalangia cameroni* (Hymenoptera: Pteromalidae). *Bull. Entomol. Res.* **94**(6), 555–567 (2004)
13. Geden, C.J.: Visual targets for capture and management of house flies, *Musca domestica* L. *J. Vector Ecol.* **31**(1), 152–157 (2006)
14. Smallegange, R.C.: Attractiveness of Different Light Wavelengths, Flicker Frequencies and Odours to the Housefly (*Musca domestica* L.). Rijksuniversiteit Groningen, Groningen, The Netherlands (2003)
15. Van Kuijk, F.J.: Effects of ultraviolet light on the eye: role of protective glasses. *Environ. Health Perspect.* **96**, 177–184 (1991)
16. Wakefield, A., Broyles, M.E.J., Stone, E., Jones, G., Harris, S.: Experimentally comparing the attractiveness of domestic lights to insects: do LEDs attract fewer insects than conventional light types? *Ecol. Evol.* **6**(22), 8028–8036 (2016)
17. Held, G.: Introduction to Light Emitting Diode Technology and Applications. Auerbach Publications, New York (2009)
18. Katsuki, M., Arikawa, K., Wakakuwa, M., Omae, Y., Okada, K., Sasaki, R., Shinoda, K., Miyatake, T.: Which wavelength does the cigarette beetle, *Lasioderma serricorne* (Coleoptera: Anobiidae), prefer? Electrophysiological and behavioral studies using light-emitting diodes (LEDs). *Appl. Entomol. Zool.* **48**(4), 547–551 (2013)
19. Lunau, K.: Visual ecology of flies with particular reference to colour vision and colour preferences. *J. Comp. Physiol. A* **200**(6), 497–512 (2014)
20. Diclaro, J.W., Cohnstaedt, L.W., Pereira, R.M., Allan, S.A., Koehler, P.G.: Behavioral and physiological response of *Musca domestica* to colored visual targets. *J. Med. Entomol.* **49**(1), 94–100 (2012)



# High Temperature Sensor Based on Regenerative Fiber Bragg Grating

Guohui Lyu<sup>1</sup>(✉), Yu Sun<sup>1</sup>, Yan Zhang<sup>1</sup>, Chaozheng Wang<sup>1</sup>, Xiaohang Liu<sup>1</sup>, and Xu Jiang<sup>2</sup>

<sup>1</sup> Research Center for Fiber, Optic Sensing Technology National Local Joint Engineering, and the College of Electronic Engineering, Heilongjiang University, Harbin, China

lvguohui@hlju.edu.cn

<sup>2</sup> College of Data Science and Technology, Heilongjiang University, Harbin, China

**Abstract.** In this paper, two kinds of gratings are used to represent seed gratings of different intensities, which are obtained by conventional writing ( $R \geq 70\%$ ) and saturation writing ( $R \geq 99\%$ ) on low-cost SMF-28 fibers respectively. After same high-temperature annealing process, the performance of the grating with saturation writing is more stable, and it is suitable for making a high temperature sensor. By means of calibration tests, the wavelength of the regenerative grating drifted by 15.3 nm during the temperature rise to 1100 °C, and its full-scale temperature resolution was 0.073 °C/pm. In combination with the engineering needs, the high temperature resistant capillary ceramic tube and corundum tube are used to encapsulate the grating; therefore, the high temperature resistance of the regenerative fiber grating is used to fabricate the ceramic packaged fiber grating high temperature sensor. Sensing targets with the temperature range from 0 to 1000 °C and an accuracy of 1 °C are implemented ultimately.

**Keywords:** Fiber Bragg grating · Fiber grating thermal degradation · Regenerative fiber grating · High temperature sensor

## 1 Introduction

In aerospace, metallurgy, petrochemical and other industrial fields, high temperatures around 1000 °C are often needed to be measured. Thermocouple sensors are currently widely used. However, the traditional thermocouple sensor is mostly made of precious metals such as platinum and rhodium, and the internal metal of which will gradually melt and evaporate in the high temperature environment, resulting in a decrease in measurement accuracy. Therefore, it needs to be replaced frequently, which increases the cost of use.

Fiber Bragg grating (FBG) sensors have advantages such as anti-electromagnetic interference, easy to form distributed sensing arrays, small size, light weight, etc. Yet the FBG produced by the common process unable to realize sensing due to the gradual erasure when the temperature is higher than 300 °C. A. Martinez et al. wrote a grating

point by point by employing a femtosecond laser on general communication SMF-28 fiber, which can work stably at temperatures below 900 °C; M. Forkine incorporated fluorine and germanium elements into the fiber and wrote the grating with UV light; then, through a specific high temperature, annealing procedure the “chemical composition grating” that can withstand temperatures above 1000 °C was finally obtained; S. J. Mihailov et al. also wrote a grating by a high-power femtosecond laser and a phase mask on an SMF-28 fiber, which can work stably at temperatures below 1050 °C [1–3].

In this paper, a regenerative fiber grating high temperature sensor is designed based on the actual needs of industrial high temperature measurement. The high temperature annealing hydrogen-loaded grating is used to regenerate a new grating on the basis of erasing the original grating, and the regenerated grating can withstand at a high temperature of about 1000 °C [4–6]. Experiments have shown that it can achieve temperature sensing in the range from 0 to 1000 °C.

## 2 Principle

### 2.1 Thermal Erasing Principle of Fiber Grating

The central reflection wavelength of the FBG is given as follows:

$$\lambda_B = 2 \cdot n_{\text{eff}} \cdot A \quad (1)$$

where  $\lambda_B$ ,  $n_{\text{eff}}$  and  $A$  represent the central reflection wavelength, the effective refractive index and grating period of the FBG, respectively. Changes in parameters such as ambient temperature, the effective refractive index  $n_{\text{eff}}$  and the grating period  $A$  will alter the central reflection wavelength of the FBG. However, as the external temperature gradually increases, the grating parameters will be erased and cannot be restored. This phenomenon in which the periodic refractive index distribution gradually disappears and the temperature sensing characteristics gradually decay is called the thermal decline effect of FBG. Theoretical model of capture state is generally considered to be the formation mechanism of thermal decline effect. According to this theory, as seen in Fig. 1, in the process of writing a grating with a UV laser, carriers in the fiber core material are excited and transitioned. Transition from a low energy level to a higher energy level and trapped in a continuously distributed energy trap, thereby forming a metastable FBG. This metastable structure is not permanent and the energy trap depth of which is related to the heat release rate of the carriers. When the grating is heated to a certain extent, carriers will overflow from the energy trap, resulting in the thermal decline effect of the grating [7].

### 2.2 Regeneration Mechanism of Fiber Grating

The formation mechanism of regenerative grating mainly includes the principle of periodic diffusion of chemical substances and the theory of stress relaxation. According to the principle of periodic diffusion of chemical substances, the gratings are regenerated due to the oxygen modulation in water molecules. The large bond energy of

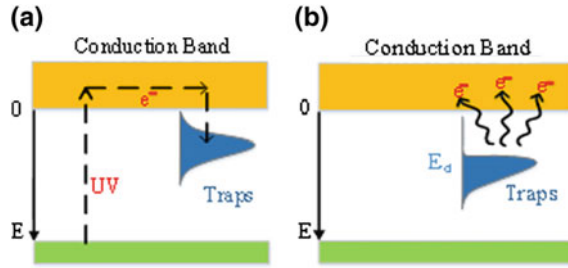


**Fig. 1** Theoretical model of high temperature capture state: **a** UV excited carriers are confined to potential trap. **b** Heat release of carriers

water molecules makes it difficult to decompose and the dispersion of water molecules from a high concentration region to a low region is very slow, which result the regenerative grating has better high temperature stability than the ordinary grating. According to the principle of stress relaxation model, the initial grating will form a periodic stress distribution inside due to the intensity distribution of the irradiated laser, which will result the difference of stress relaxation inside the fiber, and hydrogen loading will strengthen this difference. Regenerative grating is more stable due to the soft transition of quartz glass to another amorphous phase.

### 3 Fabrication Experiment of Regenerated Fiber Bragg Grating

#### 3.1 Fiber Grating Regeneration Experiment Process

The fabrication method of regenerated fiber gratings is to treat ordinary fiber gratings at high temperature to erase the original gratings, and then maintain constant temperature or elevate temperature to regenerate new gratings. The specific operation steps are as follows: Firstly, the original grating is pretreated, remove the coating of the fiber grating and cover with the high temperature resistance zirconia ceramic tube and put them in the thermocouple verification furnace. The grating portion is located in the middle of the high temperature furnace. Start the verification furnace and open the control software to set some parameters. Set the temperature to 850 °C and start heating. After one hour of heating, maintain the temperature at 850 °C about 3 h. When the regenerated grating is observed saturated then raise the temperature to 1100 °C to perform post-annealing, and maintain at this temperature for 20 min, then close the verification furnace and let it cool down to the room temperature.

#### 3.2 Experimental Platform and Device for Fiber Bragg Grating Regeneration Experiment

For the above experiment process, the experimental platform is set up as shown in Fig. 2. The fiber grating, encapsulated into the high-temperature resistant ceramic tube,



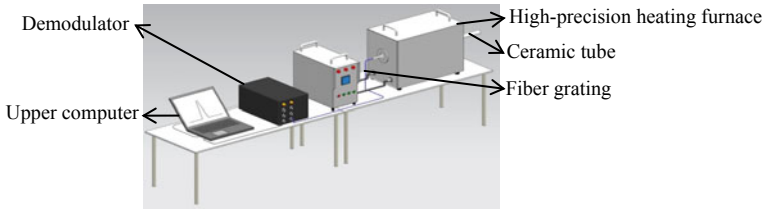


**Fig. 2** Experimental platform for grating regeneration

was inserted into the high-precision heating furnace and the other end of the fiber was connected to the demodulator, then make the demodulator connected to the upper computer.

Two kinds of fiber gratings are used in the experiment, one of which is a conventional low reflectivity fiber grating with its reflectivity  $\geq 70\%$ , and the other is a high reflectivity fiber grating, whose reflectivity is  $\geq 99\%$ . The pressure of hydrogen loading is 120 standard atmospheres and the time of hydrogen loading is 7–10 days.

## 4 Experimental Results and Analysis

### 4.1 Experimental Results and Analysis of Regenerated Fiber Bragg Gratings

In this paper, the low reflectivity FBG is tested and the variation process of the FBG's central reflection wavelength and reflected power with temperature is obtained, as shown in Figs. 3 and 4.

From the experimental results, it can be seen that the low reflectivity FBG, which is written by conventional method, regenerated saturation reflected light intensity is about 10% of the original reflection intensity and the central reflection wavelength drift 20.0981 nm. The regenerated grating is gradually erased in the process of high temperature annealing. The variation process of the center reflected wavelength and reflected power of the high reflectivity FBG with the temperature is obtained, as shown in Figs. 5 and 6.

From the experimental results, it can be seen that the high reflectivity fiber grating, which is written by high-power laser, regenerated saturation reflected light intensity is about 40% of the original reflection intensity and the central reflection wavelength drift 15.3 nm. The variation of the spectrum of reflected light with the corresponding temperature during the regeneration process is shown in Fig. 7.

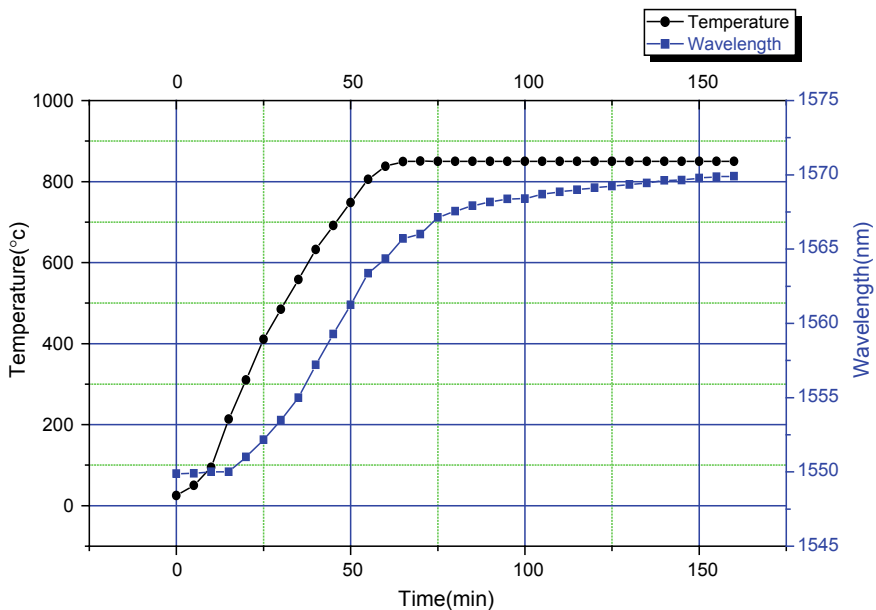


**Fig. 3** The variation process of the central reflection wavelength with temperature of low reflectivity fiber grating

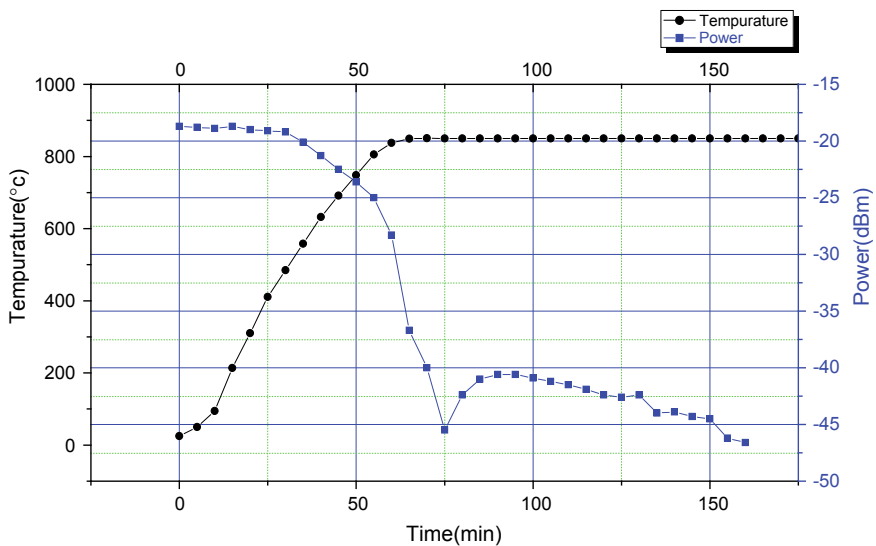


**Fig. 4** The variation process of the central reflection light intensity with temperature of low reflectivity fiber grating

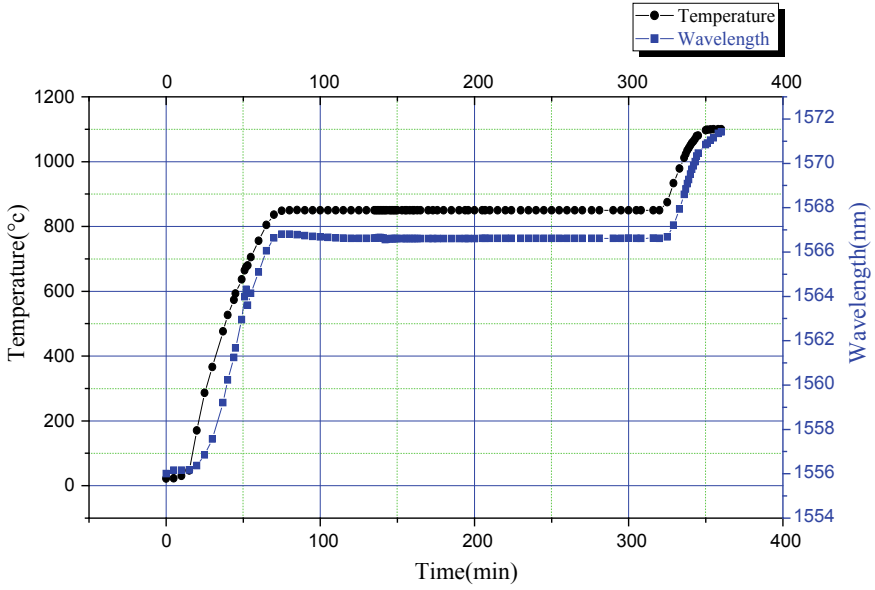


Fig. 5 The variation process of the central reflection wavelength with temperature of high reflectivity fiber grating

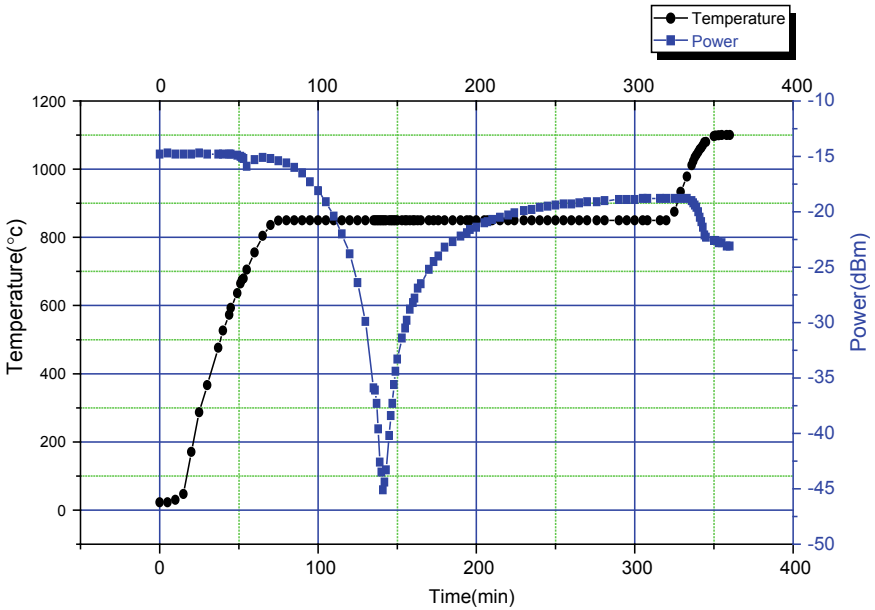


Fig. 6 The variation process of the central reflection light intensity with temperature of high reflectivity fiber grating

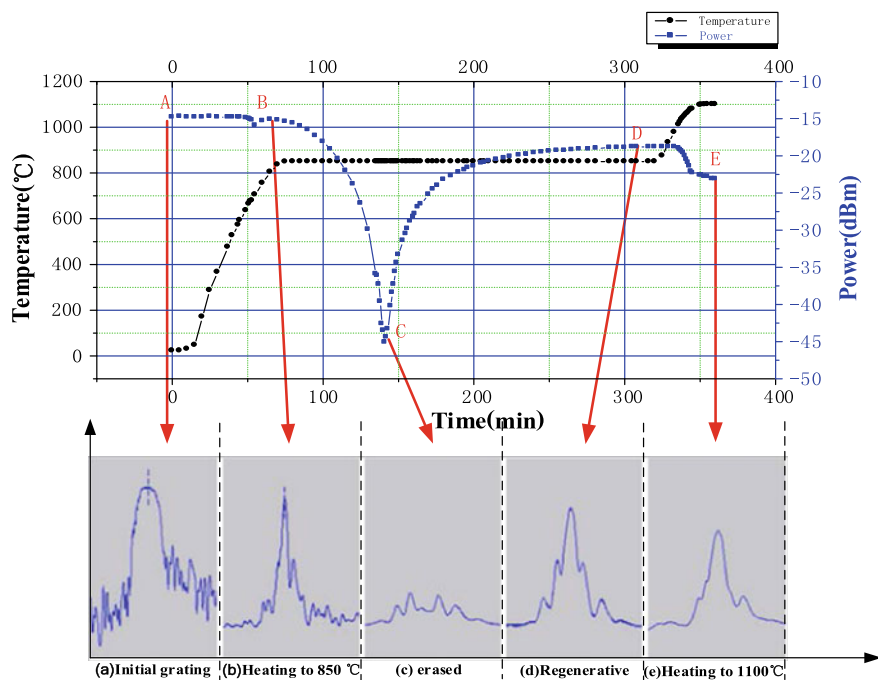


Fig. 7 The variation process of the central reflection light intensity with temperature of high reflectivity fiber grating

## 5 Calibration Results and Analysis of Regenerated Fiber Bragg Gratings

The calibration test of regenerated fiber Bragg grating (FBG) is carried out. The calibrated experimental instrument and platform are the same as those used in the fabrication of regenerated grating. The regenerated grating is put into the high temperature verification furnace, because the calibrating temperature range of the thermocouple verification furnace is 300–1200 °C. Therefore, the wavelength values of the nine temperature points of 300 °C/400 °C/500 °C/600 °C/700 °C/800 °C/900 °C/1000 °C/1100 °C are recorded, the curves of the variation of wavelength with temperature as shown in Fig. 8. Since there may be other factors affecting the spacing or effective refractive index of fiber gratings during heating, the variation of temperature with wavelength is quadratic fitted, and the curve of the relationship between temperature and wavelength is shown in Fig. 9. The fitting curve shows the fitting formula and fitting degree, and the fitting degree is 0.9987, which shows that the fitting curve can well reflect the relationship between temperature and wavelength, and the change of temperature can be obtained by detecting the change of wavelength.

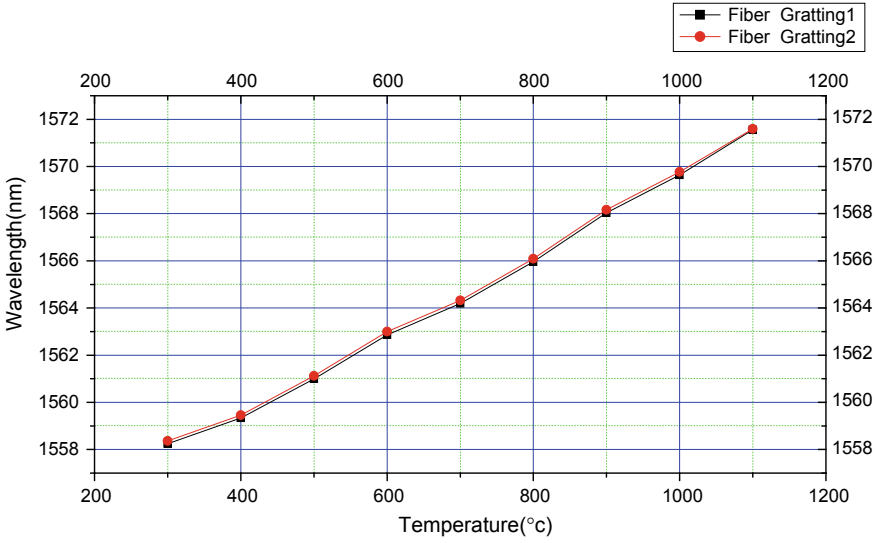


Fig. 8 Calibration curve of two high reflectivity fiber gratings

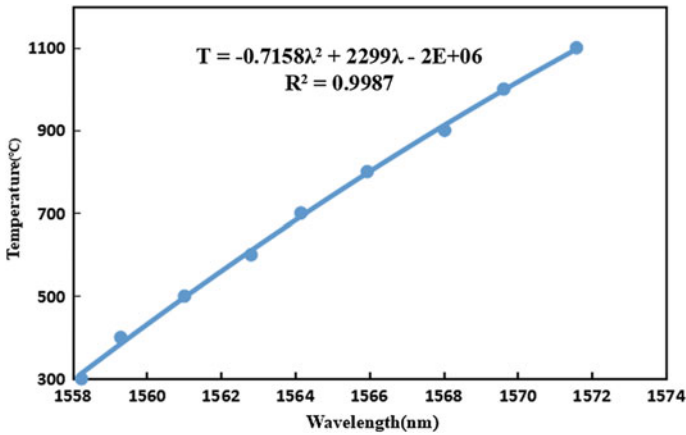


Fig. 9 Quadratic fitting curve of temperature and wavelength of regenerated grating

## 6 Packaging Design of Regenerated Fiber Bragg Grating

Because the high temperature can make the optical fiber surface to produce microcrack and the mechanical properties are greatly reduced, it needs to be packaged and protected. The regenerated grating is packaged by ceramic tube and alloy steel. Contrast the thermo-optical response characteristics of regenerated fiber gratings with or without packaging. The response characteristics of the package and unpackaged regenerated fiber Bragg grating are found to be very similar, that is, the package does not affect the sensing characteristics of the grating.

## 7 Conclusion

In summary, comparing the two experiments of FBG with different reflectivity, a regenerative FBG high-temperature sensor capable of sensing temperature range from 0 to 1000 °C is fabricated, and it has broad application prospects at high temperature measurement applications.

## References

1. Lindner, E., Chojetzki, C., Brückner, S., Becker, M., Rothhardt, M., Bartelt, H.: Thermal regeneration of fiber Bragg gratings in photosensitive fibers. *Opt. Express* **17**, 12523–12531 (2009)
2. Quintela, A.: Fiber Bragg grating regeneration temperature in standard fibers. In: *International Conference on Optical Fibre Sensors (2015)*
3. Bandyopadhyay, S., Canning, J., Biswas, P.: A study of regenerated gratings produced in germanosilicate fibers by high temperature annealing. *Opt. Express* **19**(2), 1198 (2011)
4. Zhang, B., Kahrizi, M.: High-temperature resistance fiber Bragg grating temperature sensor fabrication. *IEEE Sens. J.* **7**(4), 586–591 (2007)
5. Kumar, J., Prakash, O., Mahakud, R.: Studies on the stability of regenerated fiber Bragg gratings at 1100 °C. In: *The Workshop on Recent Advances in Photonics*, pp. 1–4. *IEEE* (2017)
6. Smelser, C.W., Dan, G., Mihailov, S.J.: Study of high temperature stable fiber Bragg gratings fabricated in silica based fiber. In: *Photonics North. International Society for Optics and Photonics*, pp. 77500J–77500J-6 (2010)
7. Erdogan, T., Mizrahi, V., Lemaire, P.J.: Decay of ultraviolet-induced fiber Bragg gratings. *J. Appl. Phys.* **76**(1), 73–80 (1994)



# Tunable NIR Filter with High $Q$ -Factor Realized by Using TiN as Plasmonic Layer

Lingli Wang<sup>1</sup>, Jun Tan<sup>1</sup>, Yongming Shan<sup>2</sup>, Guojun Jin<sup>1</sup>,  
Yuying Wang<sup>3</sup>, Limin Hu<sup>4</sup>, Kai Xu<sup>1</sup>, and Yanlong Meng<sup>1</sup>✉

<sup>1</sup> College of Optical and Electronic Technology, China Jilianglinag University,  
Hangzhou 310018, Zhejiang, People's Republic of China

myl@cjlu.edu.cn

<sup>2</sup> Physics and Information Engineering, Jiaxing University, Jiaxing 310018,  
Zhejiang, People's Republic of China

<sup>3</sup> College of Life and Environmental Science, Hangzhou Normal University,  
Hangzhou 310018, Zhejiang, People's Republic of China

<sup>4</sup> Huapu Yongming Optoelectronics Co., Hangzhou 310018, Zhejiang,  
People's Republic of China

**Abstract.** Surface plasmon filters have a wide range of applications in nano-integrated optics because of simple structure and easy integration. Traditional noble metals used for surface plasmon filters are expensive. In this paper, we propose an infrared filter by using TiN. By adjusting the thickness of the metal replacement layer TiN and the photoresist waveguide layer, a pure 2  $\mu\text{m}$  infrared filter is obtained. The full width at half maximum reaches 21.26 nm. Furthermore, the wavelength of peak of filter can be adjusted conveniently from 0.8 to 2.5  $\mu\text{m}$  by modulating the period. Our study provides a theoretical basis for finding cheap alternatives to the materials used in plasma filters.

**Keywords:** Filter · Surface plasmon · TiN film · FDTD · SPP

## 1 Introduction

An optical filter is a device that has a wavelength selective character in a certain wavelength of an electromagnetic wave; for example, a filter having a wavelength selective character in a near-infrared light band can selectively absorb and reflect a part of infrared light. The surface plasmon effect can greatly down the size of the device, making it ideal for using such filters in integrated and miniaturized display devices. It also can manipulate the intensity, phase, and polarization of the scattered light effectively for excellent optical response and wide color adjustability [1–5]. Although plasmonic nanostructures have so many advantages and great potentials in their applications, they must be cut on a large scale if they are to be used in commercial applications [6–8]. We have proposed the replacement of noble metal materials in optical filters with relatively inexpensive titanium nitride materials. TiN is a transition metal nitride composed of a mixture of metal bonds, ionic bonds, and covalent bonds [9, 10]. The TiN film is translucent in the visible region and highly reflective in the infrared region, which makes it possible to replace precious metals [11–13].

In the study of surface plasmon-based components, the resolution processed based on Maxwell's equations needs high accuracy in consideration of the difference in geometrical dimensions and dielectric parameters of metal microstructures. As a result, the time domain finite difference method (FDTD) is used in this paper for it is the most simple and intuitive, less approximate and high precision micro/nano-optical device simulation method.

In this paper, an NIR optical filter using TiN is simulated. By modulating the structure period, the peak wavelength of the filter can be adjusted from 0.8 to 2.5  $\mu\text{m}$ . The thickness of the TiN and the photoresist waveguide layer of the adjusted metal were obtained by FDTD simulation calculation, and a pure 2  $\mu\text{m}$  infrared filter was obtained, of which full width at half maximum of the spectrum reaches 21.26 nm.

## 2 Simulation Structure and Method

The structure of NIR optical filter used in simulation is shown in Fig. 1. The simple structure is composed of a  $\text{SiO}_2$  substrate, thin TiN layer with periodic slits, and a capping layer of optical adhesive, which is on the top to TiN. Periodic sub-wavelength slits on TiN form a grating structure. Here, the thicknesses of optical adhesive on top of TiN thin layer, TiN thin layer, and  $\text{SiO}_2$  substrate are set to  $T_1$ ,  $T_2$ , and  $T_3$ . The period of grating is  $p$ , and the width of slit is  $w$ . The simulation is carried out by a commercial FDTD software of Lumerical Corp.

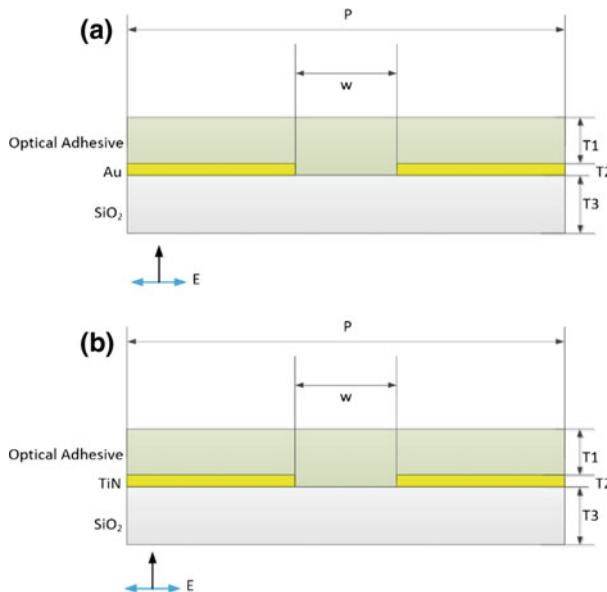


**Fig. 1** **a** Schematic of a plasmonic metallic grating filter. For geometrical parameters,  $T_2$  is the gold layer thickness,  $w$  is the gold slit width,  $T_1$  is the waveguide layer thickness, and  $P$  is the grating period. **b** Substituting TiN for Au



In the simulation, a plane electromagnetic wave with transverse magnetic field polarization is used as light source. The wavelength range is from 1200 to 2500 nm. The light is incident from the bottom of substrate and propagates along the forward direction of  $z$ -axis. The boundary conditions of simulation area at  $x$ -axis and  $y$ -axis are periodic. In order to completely absorb the scattered light and prevent it from returning to the position of the structure, which causes errors in the simulation results, we have used the perfect matching layer boundary condition (PML) at  $z$ -direction.

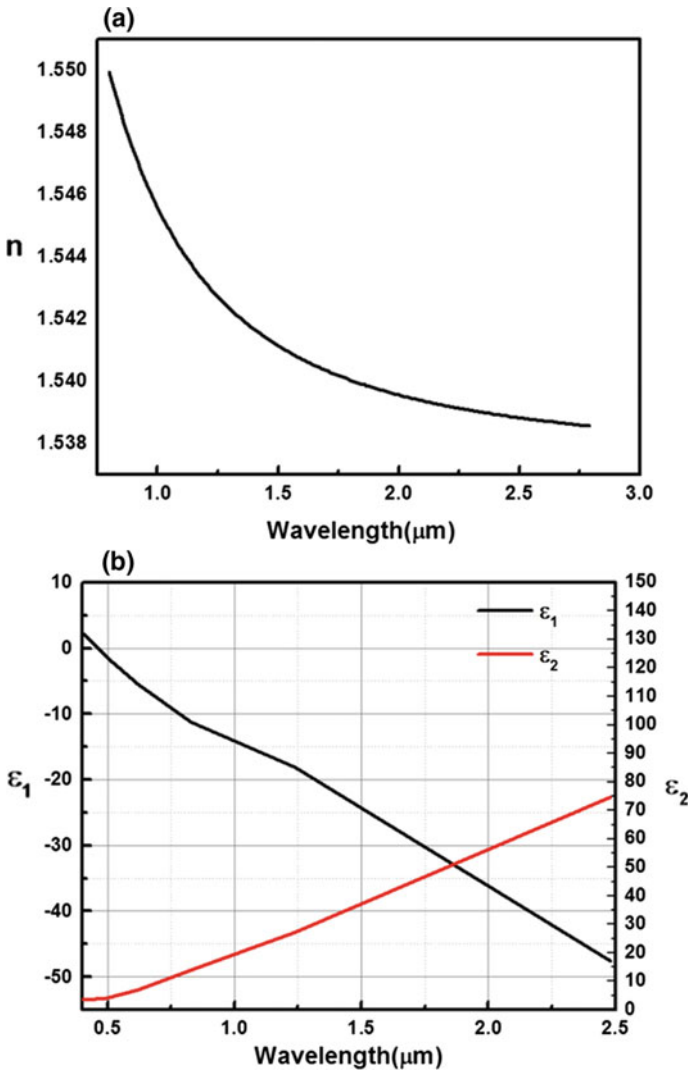


**Fig. 2** **a** Refractive index of optical adhesive. **b** The real and imaginary parts of complex permittivity of TiN

The refractive index of optical adhesive is shown in Fig. 2a. The extinction coefficient of optical adhesive in the studied wavelength range is zero. The real and imaginary parts of the complex permittivity of TiN film are shown in Fig. 2b. It is straightforward that the real part of the TiN permittivity remains negative in the wavelength range from 500 to 2500 nm. It is well known that the negative real part of complex permittivity of material indicates the material will possess metallic characteristic. That is also a necessary condition for the plasma wave excitation on the surface of metallic TiN layer.

### 3 Results and Discussion

In order to investigate the relation between those parameters of devices' structure and wavelength selective characteristic, the four structural parameters of  $T_1$ ,  $T_2$ ,  $W$ , and  $P$  are adjusted sequentially. At first,  $T_2$ ,  $W$ , and  $P$  are set to 40 nm, 300 nm, and 1  $\mu\text{m}$ , respectively. Then, the thickness of the optical adhesive layer on top of TiN is adjusted from 0 nm to 1  $\mu\text{m}$ . The transmittance evolution of the filter is shown in Fig. 3a.

It can be seen from the figure that narrow band with high transmittance emerges at 1.45  $\mu\text{m}$  as the thickness of optical adhesive layer exceeds 0.6  $\mu\text{m}$ . When  $T_1$  is 800 nm, the transmittance at 1.45  $\mu\text{m}$  reaches maximum. As  $T_1$  keeps on increasing, there is a slight shift in the position of peak which means a weak effect of thickness of optical adhesive on the wavelength selection of filter.

Similar to the Fabry-Perot (FP) resonance, the resonance in the cavity composed of the two metal ends of slit plays an extremely important role in the enhanced transmission of subwavelength metal grating structures, which has been reported in the work [14, 15]. In the sub-wavelength range, when light is incident on the surface of the metal grating, the metal slit can be regarded as a miniature FP cavity, unlike the micro-structured FP cavity. The TiN material can still be considered as two mirrors with a certain reflectivity. The height of the grating is the cavity length, which constitutes a structure similar to the FP cavity. When the FP cavity matching condition is satisfied, resonance enhancement occurs, and the transmittance is reluctant. We fixed the thickness of the waveguide layer  $T_1$  to 800 nm and optimized the thickness of the TiN layer with metal characteristics. The scanning result is shown in Fig. 3b. The numerical simulation results show that as the height of the grating increases, the maximum transmission value will gradually decrease, because the higher the height of the metal grating, the longer the propagating distance of the light in the metal, resulting in a greater loss of light energy.

Since the thickness of the waveguide layer and TiN is fixed, the effect of the width of the metal slit on the transmission spectrum of the structure is investigated further. Figure 4a depicts the transmission spectrum as a function of incident wavelength at different slit widths. As can be seen from the figure, when the slit width  $w = 100\text{--}400$  nm, the filtering performance is better.

For the metal grating structure, the SPP resonance excitation of the upper and lower surfaces of the metal medium satisfies the following condition [16, 17]:

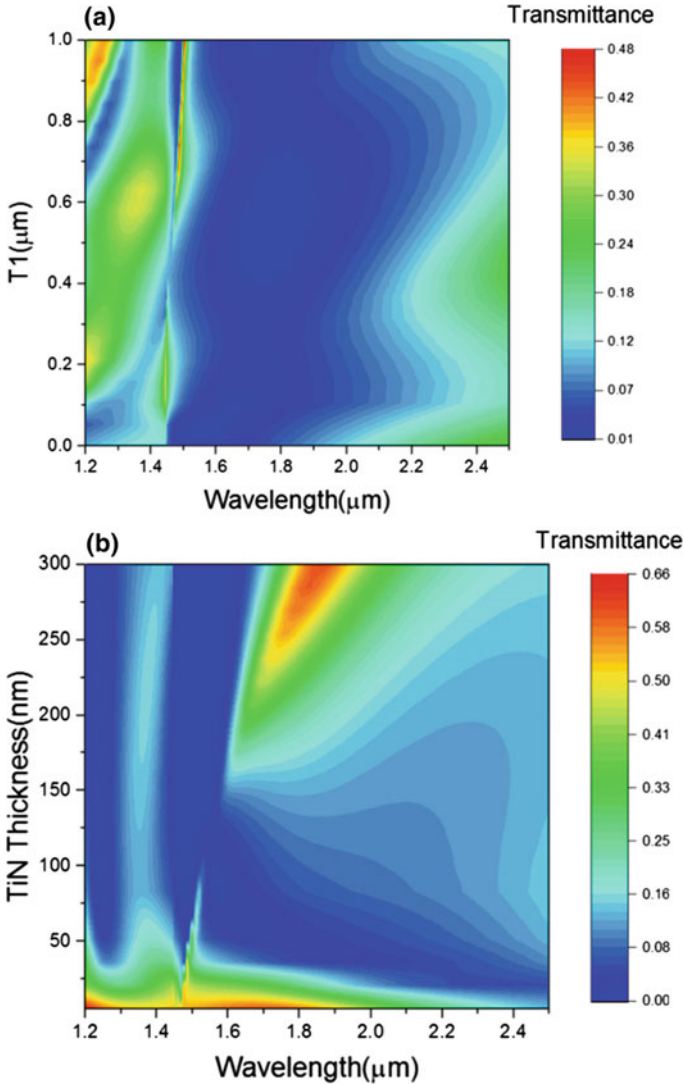


**Fig. 3** **a** Schematic diagram of the change in transmittance of the filter under variations in optical adhesive thickness and wavelength. **b** Schematic representation of the change in transmittance of the filter as a function of thickness and wavelength of the TiN material layer

$$\frac{2\pi}{\lambda_0} \sin \theta + \frac{m2\pi}{P} = -\frac{2\pi}{\lambda_0} \sqrt{\frac{\epsilon_2 \epsilon_1}{\epsilon_1 + \epsilon_2}} = K_{\text{SPP}} \quad m = \pm 1, \pm 2, \dots \quad (1)$$

where  $P$ ,  $m$ , and  $K_{\text{SPP}}$  are the grating period, the grating level, and the wave vector of the SPP mode. Under this resonant condition, the incident light transfers energy to the SPP waves propagating along the upper and lower surfaces of the metal grating. Figure 4b discusses the effect of grating period on transmittance. When the period of the structure varies from 50 to 2000 nm, there are three transmission maximum bands

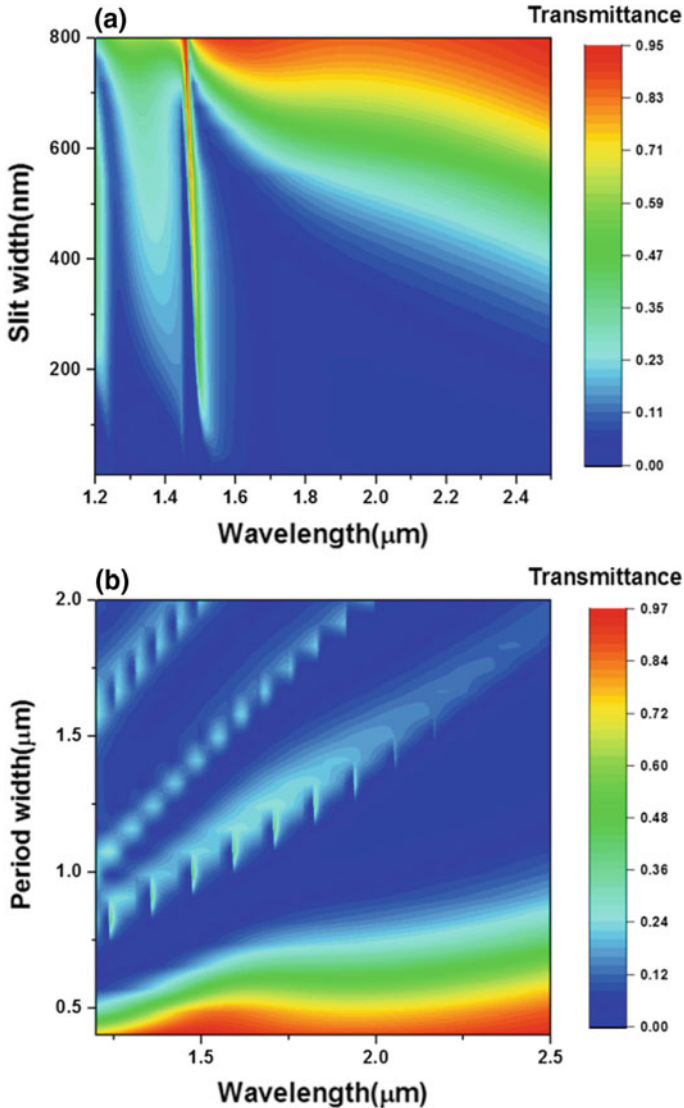


**Fig. 4** **a** Schematic diagram of the change in transmittance of the filter under slit width and wavelength variation. **b** Schematic diagram of the change in transmittance of the filter over the period width and wavelength

when the grating period is greater than 700 nm. According to the formula, they are derived from the excitation of the SPP mode on the metal surface, corresponding to the SPP mode with the order of  $m = 1, 2, 3$ . Based on the above analysis, we can conclude that the transmission maximum in the metal grating structure is formed by the excitation of different levels of the SPP mode on the surface of the metal grating. We also analyzed the electric field distribution of the structure, as shown in Fig. 5, showing the coupling between the surface plasmons at the interface of the metallic material and the waveguide layer and the narrow-slit waveguide mode.

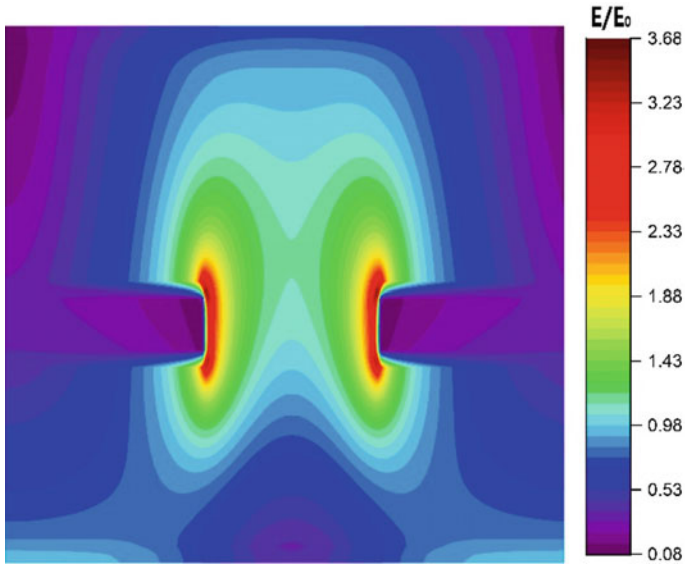


**Fig. 5** Hybrid electric field distribution of the simulation structural model

We choose the grating period  $P = 1350$  nm, the grating metal slit width  $w = 420$  nm, the thickness of the metal replacement layer TiN material  $T2 = 46$  nm, and the waveguide layer photoresist thickness  $T1 = 1140$  nm as the optimal combination of parameters, as shown in Fig. 6. A pure infrared filter at  $2 \mu\text{m}$  was obtained

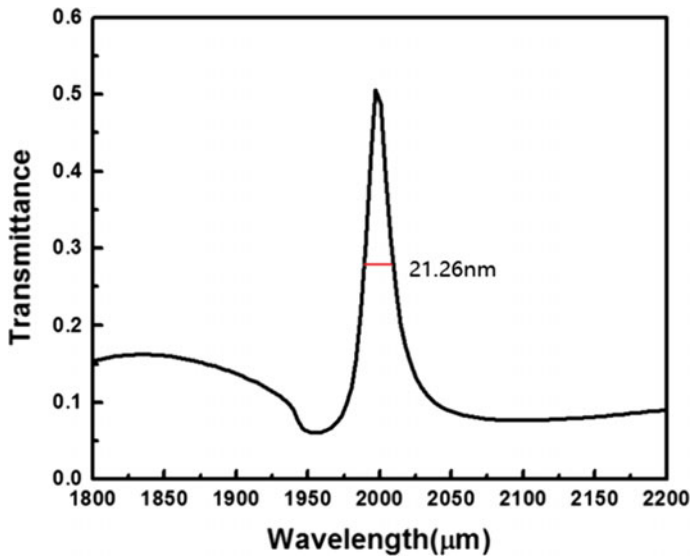


**Fig. 6** Transmitted spectrum of device with FWHM of 21.26 nm, the wavelength of peak is 2000 nm

with a full width at half maximum (FWHM) of 21.26 nm. At last, the very narrow FWHM gives rise to a quality factor ( $Q$ -factor) as high as  $\sim 94$  ( $Q = (\lambda/\Delta\lambda)$ ).

## 4 Conclusion

In summary, a simple near-infrared optical filter using TiN is demonstrated theoretically. By simulating, a continuous shift of peak from 0.8 to 2.5  $\mu\text{m}$  is obtained. The filter presents a favorable selectivity of wavelength. The half-width of the spectrum at 2  $\mu\text{m}$  can reach 21.26 nm. Our study provides a new way to realize NIR optical filter without any noble metals. Such simple structure is also helpful for practical utilization of NIR optical filter.

**Acknowledgements.** Thanks for the support of National Key Research and Development Program (No. 2017YFB0403501), Zhejiang Provincial Natural Science Foundation (No. LQ15F040004), the Open Fund of the State Key Laboratory of Integrated Optoelectronics (No. IOSKL2015KF28), and the Talent Development Project in Photoelectric Detection of Top Priority Construction Subject of Instrument Science and Technology of Zhejiang Province (No. JL150540).

## References

1. Meng, L., Zhao, D., Li, Q.: Polarization-sensitive perfect absorbers at near-infrared wavelengths. *Opt. Express* **21**(S1), A111–A122 (2013)
2. Yu, N., Aieta, F., Genevet, P.: A broadband, background-free quarter-wave plate based on plasmonic metasurfaces. *Nano Lett.* **12**(12), 6328 (2012)
3. Yu, Y., When, L., Song, S.: Transmissive/reflective structural color filters: theory and applications. *J. Nanomater.* **2014**(8), 6 (2014)
4. Naik, G.V., Shalaev, V.M., Boltasseva, A.: Alternative plasmonic materials: beyond gold and silver. *Adv. Mater.* **25**(24), 3264–3294 (2013)
5. Xu, T., Shi, H., Wu, Y.K.: Structural colors: from plasmonic to carbon nanostructures. *Small* **7**(22), 3128–3136 (2011)
6. Cheng, W.T., Yang, K.Y., Wang, C.M.: High-efficiency broadband meta-hologram with polarization-controlled dual images. *Nano Lett.* **14**(1), 225 (2014)
7. Chong, X.Y., Li, E., Squire, K., Wang, A.: On-chip near-infrared spectroscopy of CO<sub>2</sub> using high resolution plasmonic filter array. *Appl. Phys. Lett.* **108** (2016)
8. Yebo, N., Bogaerts, W., Hens, Z., Baets, R.: On-chip arrayed waveguide grating interrogated silicon-on-insulator microring resonator-based gas sensor. *IEEE Photon. Technol. Lett.* **23**, 20 (2011)
9. Zheng, B.Y., Wang, Y., Nordlander, P.: Color-selective and CMOS-compatible photodetection based on aluminum plasmonics. *Adv. Mater.* **26**(36), 6318–6323 (2014)
10. Popović, M., Novaković, M., Mitrić, M.: Structural optical and electrical properties of argon implanted TiN thin films. *Int. J. Refract. Metals Hard Mater.* **48**(48), 318–323 (2015)
11. Siesler, H.W., Ozaki, Y., Kawata, S., Heise, H.M.: Near-infrared spectroscopy: principles, instruments, applications. Wiley, London (2008)

12. Xia, Z., Eftekhari, A.A., Soltani, M., Momeni, B., Li, Q., Chamanzar, M., Yegnanarayanan, S., Adibi, A.: High resolution on-chip spectroscopy based on miniaturized microdonut resonators. *Opt. Express* **19**, 13 (2011)
13. Liang, Y.Z., Peng, W.: Theoretical study of transmission of Sub-wavelength Nano-structured metallic grating. *Applied Spectroscopy* **67**(1), 49–53 (2013)
14. Mazulquim, D.B., Lee, K.J., Yoon, J.W., Muniz, L.V., Borges, B.H., Neto, L.G., Magnusson, R.: Efficient band-pass color filters enabled by resonant modes and plasmons near the Rayleigh anomaly. *Opt. Express* **22**, 25 (2014)
15. Maier, S.A.: *Plasmonics: fundamentals and applications*. Springer, New York (2007)
16. Raether, H.: *Surface plasmons on smooth and rough surfaces and on gratings*. Springer, Berlin, Germany (1988)
17. Liang, Y.Z., Peng, W., Hu, R.: Symmetry reduced double layer metallic grating structure for dual-wavelength spectral filtering. *Opt. Express* **22**(10), 11633–11645 (2014)



# Research on Cascade Inner Microcavity-Based Fiber Sensor

Huifang Chen<sup>(✉)</sup>, Hai Wang, Kezhen Rong, and Tiantian Chen

China Jiliang University, Hangzhou 310018, China  
chenhf@cjlu.edu.cn

**Abstract.** A multimode interference-based fiber cavity sensor was proposed. It was a single-mode–multimode–single-mode cascaded structure with an inner air cavity. The sensitivities of microcavity-based fiber sensor were theoretically analyzed. The sensitivities of temperature and axial strain were formula derived. A microcavity model was established with COMSOL software to study the sensitivities affecting factors. The transmission modes in cavity wall were analyzed, and the effective refractive indexes of them were simulated. With these simulation results, a conclusion could be obtained that the effective refractive indexes were depended on the mode order and the cavity diameter. The temperature and axial strain sensitivities were decided by the effective refractive indexes, and the size of the cavity was the key factor. The larger the size of the microcavity and the higher of the transmission modes, the higher the sensitivity of the sensor could be obtained. It can be a theoretical guidance to design and fabricate fiber cavity sensors.

**Keywords:** Fiber optic sensing · Cascade structure · Microcavity · Sensitivity

## 1 Introduction

In recent years, fiber optic sensors have been widely used in the measurement of temperature [1–3], strain [4–6], refractive index [7] due to their high sensitivity, strong anti-electromagnetic interference capability and low cost. Temperature and strain are important parameters needing monitor in industrial production, environmental monitoring and food testing. To date, there are many fiber structures could be applied in temperature and strain measurement. Among them, the microcavity structure in optical fiber is widely used with the advantages of simple structure, strong adaptability and high mechanical strength. Jauregui-Vazquez et al. [8] fabricated a spherical air microcavity sensor with air-core photonic crystal fiber (PCF) and got temperature sensitivity of 3.66 pm/°C. Wang et al. formed an ellipsoidal air cavity by cascading single mode fiber and PCF for temperature measurement [9], the sensitivity was 1.67 pm/°C. Men et al. [10] fabricated a fiber sandwich structure with two microcavities to realize temperature and strain measurement simultaneously. The sensitivity of temperature and strain were 98.8 pm/°C and  $-1.2$  pm/ $\mu\epsilon$ , respectively. From these research reports, it can be found that the temperature sensitivities were on the level of dozens of picometer per centigrade and the strain sensitivities were on the level of



several picometers per microstrain. However, the main factors to the sensitivities were not studied. The application was limited by the lack of theoretical research.

In this manuscript, the sensitivities of microcavity-based fiber sensor were theoretically analyzed. A microcavity model was established with COMSOL software. The transmission modes in cavity wall were analyzed, and the effective refractive indexes of them were simulated. They would be a theoretical guidance of such kind of microcavity fiber sensors.

## 2 Principles

A cascaded air cavity fiber sensor is shown in Fig. 1. The cascaded structure is made with single mode fiber (SMF) and multimode fiber (MMF), and the sphere air cavity is located in at the center of MMF.

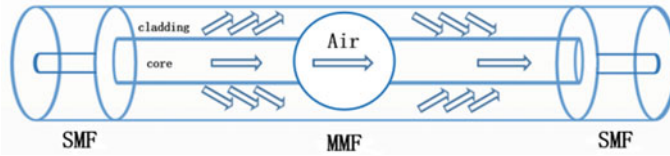


**Fig. 1** Optical fiber sensor structure

The incident light from a broadband source travels in the core of SMF. When arriving at the facet of SMF and MMF, the light scatters in the core of MMF. At the facet of MMF and air cavity, the light scatters again. Part of light travels in the air cavity, the others travel in the cavity wall. At the end of the air cavity, the light recombines in the core of MMF and is recorded by an optical spectrum analyzer. The optical path difference induced by the transmission modes in air cavity and cavity wall results in a mode interferometer. The interference intensity can be expressed as:

$$I = I_1 + I_2 + 2\sqrt{I_1 I_2} \cos \left[ \frac{2\pi \Delta L}{\lambda} \right] \quad (1)$$

where  $I_1$  and  $I_2$  represent the intensity of light beam passing through the inner air cavity and traveling along cavity wall,  $\lambda$  is the incident light wavelength,  $L$  is the cavity length,  $\Delta n = n_{cl} - n_{co}$  denotes the effective RI difference between the air cavity mode and the wall mode,  $n_{co}$  and  $n_{cl}$  are the effective RI of the core mode and the cladding mode, respectively. When the phase term satisfies the condition  $2\pi L \Delta n / \lambda = (2m + 1)\pi$ , where  $m$  is an integer, the intensity dip appears at the wavelength of

$$\delta \lambda_{\text{dip}} \approx \frac{\lambda^2}{\Delta n L} \quad (2)$$

The cascade fiber structure could be used as a temperature and axial strain sensor by monitoring the dip wavelength. The dip wavelength shift could be obtained by differentiating (2):

$$\frac{\delta\lambda_{\text{dip}}}{\lambda_{\text{dip}}} = \left( \frac{1}{\Delta n} \frac{\partial \Delta n}{\partial T} + \alpha \right) \Delta T + \left( 1 + \frac{1}{\Delta n} \frac{\partial \Delta n}{\partial \varepsilon} \right) \varepsilon \quad (3)$$

Here,  $\Delta T$  represents the change of temperature;  $\partial L/\partial T$  is the variation of inner air cavity length induced by thermal expansion of the material;  $\alpha$  is the thermo-expansion coefficient ( $\alpha = \partial L/L\partial T$ ) which is  $\sim 5 \times 10^{-7}/^\circ\text{C}$  for pure silica;  $\varepsilon$  is the axial strain applied on the fiber device and defined as  $\varepsilon = \Delta L/L$ ;  $\Delta L$  is the extended length due to tensile strain. According to Eq. (3), the sensitivity of temperature and strain at  $\lambda_{\text{dip}}$  can be expressed as

$$S_T = \frac{\delta\lambda_{\text{dip}}}{\Delta T} = \left[ \frac{1}{\Delta n} \frac{\partial \Delta n}{\partial T} + \alpha \right] \lambda_{\text{dip}} \quad (4)$$

$$S_\varepsilon = \frac{\delta\lambda_{\text{dip}}}{\varepsilon} = \left[ 1 + \frac{1}{\Delta n} \frac{\partial \Delta n}{\partial \varepsilon} \right] \lambda_{\text{dip}} \quad (5)$$

It can be seen from (4) and (5) that there are three factors affecting on the sensitivities: the RI difference ( $\Delta n$ ) the gradient of RI difference ( $\partial \Delta n/L\partial T$  or  $\partial \Delta n/L\partial \varepsilon$ ) and the dip wavelength ( $\lambda_{\text{dip}}$ ).

### 3 Simulation Results and Discussions

To study the sensitivities affecting factors, a simulation model was build with COM-SOL at the cavity plane. The cavity was filled with air with RI of 1, the cavity wall was set as pure silica with RI of 1.444, the outside RI was 1. The diameters of the microcavity were 35, 50, 65 and 80  $\mu\text{m}$ , respectively. In the simulation results, there were several kinds of transmission modes in the cavity wall. Depending on the number of intensity rings, the transmission modes could be defined as fundamental modes and high order modes, as shown in Figs. 2 and 3. The effective RI of these modes was plot in Fig. 4. It could be concluded that the effective RI was decided by the cavity size and the order of modes. A cascade fiber with small cavity has thick cavity wall, the RI of modes are higher than those of bigger cavities. As the simulation wavelength becomes longer, the effective refractive index of the cavity wall mode decreases, that is, the dispersion slope is negative, and the larger the diameter of the microcavity, the higher the mode of the cavity wall transmission mode, the faster the effective refractive index declines.

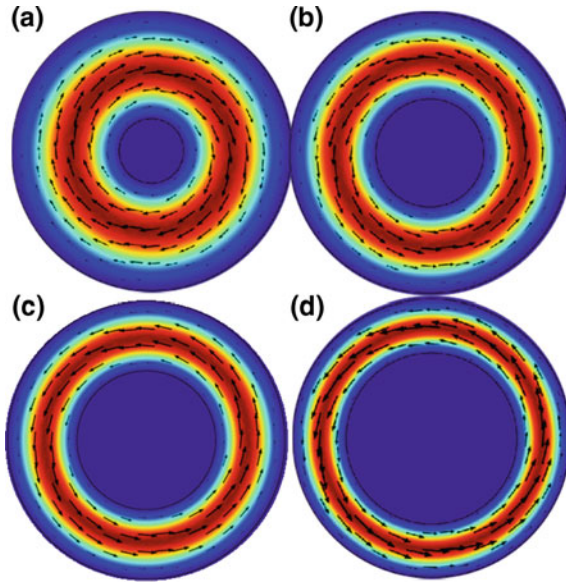


**Fig. 2** Fundamental modes in cavity wall with different cavity diameters: **a** 35  $\mu\text{m}$ , **b** 50  $\mu\text{m}$ , **c** 65  $\mu\text{m}$ , **d** 80  $\mu\text{m}$

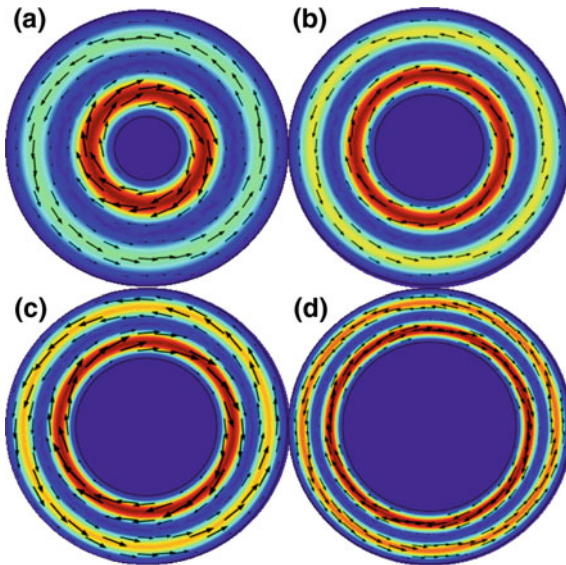


**Fig. 3** High order modes in cavity wall with different cavity diameters: **a** 35  $\mu\text{m}$ , **b** 50  $\mu\text{m}$ , **c** 65  $\mu\text{m}$ , **d** 80  $\mu\text{m}$

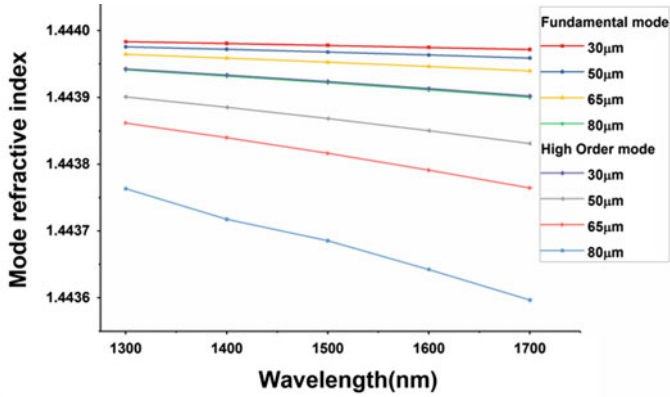


Fig. 4 Effective RI of transmission modes in microcavity walls

When the temperature changing or applying axial strain on the fiber device, the RI of air in the cavity would not change, the sensing sensitivity is decided by the RI difference ( $\Delta n$ ) and the changing ratio of  $\Delta n$  ( $\partial\Delta n/L\partial T$  or  $\partial\Delta n/L\partial\varepsilon$ ). To study the changing ratio of  $\Delta n$ , a temperature change and strain change were applied to the simulation modal. The simulated temperature range is 0–75 °C, and the strain range is 0–800 μm. The effective RI of these modes was shown in Figs. 5 and 6.

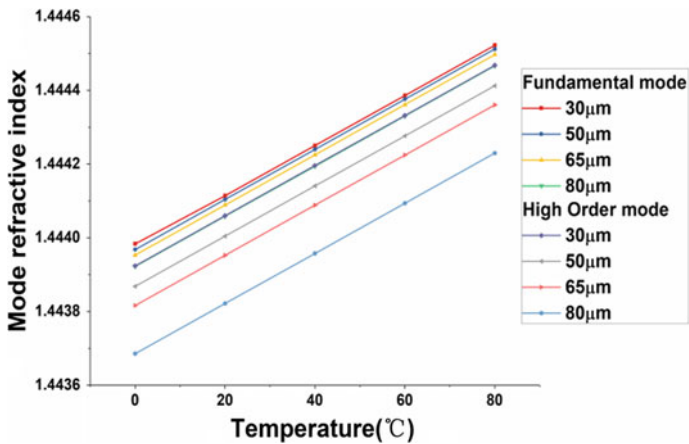


Fig. 5 Effective RI evolution with changing temperature

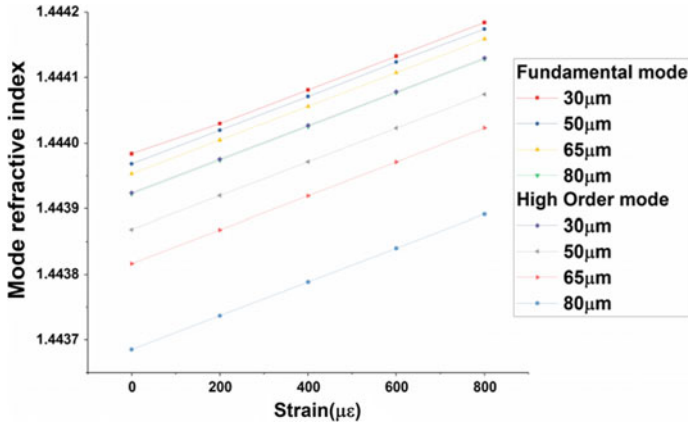


Fig. 6 Effective RI evolution with changing strain

Figure 5 reveals thermal change of the difference between the mode indices. It can be seen from that both the mode refractive index increase linearly with temperature increase. The changing rate of effective RI to temperature ( $\partial\Delta n/\partial\Delta T$ ) will not change with the transmission modes or the size of microcavity changes. Therefore, we can draw conclusions from Fig. 5 that  $\partial\Delta n/\partial\Delta T$  will not change with the temperature change. The temperature sensitivity of the fiber microcavity sensor is only related to the effective RI difference between the core mode and the cladding mode  $\Delta n$ .

Figure 6 reveals strain change of the difference between the mode indices. It can be seen from this figure that the effective RI increases linearly with strain change. And the changing rate of effective RI value to strain ( $\partial\Delta n/\partial\varepsilon$ ) will not change as the mode or size of the microcavity changes. Therefore, we can draw conclusions from Fig. 6 that  $\partial\Delta n/\partial\varepsilon$  will not change with the strain change. The strain sensitivity of the fiber microcavity sensor is only related to the effective RI difference between the core mode and the cladding mode  $\Delta n$ .

According to the simulation results, we can conclude that the temperature and the strain sensitivity of the cascade inner microcavity-based fiber sensor are only related to the effective RI difference between the air cavity mode and the cavity wall mode  $\Delta n$ . The temperature and strain sensitivities become larger as the size of the microcavity increases and the higher order of the transmission modes.

## 4 Conclusions

In this manuscript, we simulated a multimode interference-based fiber sensor which was proposed. It was a single mode-multimode-single mode cascaded structure with an inner air cavity. The transmission modes were analyzed with simulations. The effective refractive indexes were depended on the mode order and the cavity diameter. The sensing sensitivities of temperature and axial strain were formula derived. With these simulation results, a conclusion could be obtained that the temperature and axial strain

sensitivities were decided by the effective refractive indexes, and the size of the cavity was the key factor. The larger the size of the microcavity, the higher of the transmission modes, the higher the sensitivity of the sensor. It can be a theoretical guidance to design and fabricate fiber cavity sensors.

## References

1. Shroeder, K., Ecke, W., Mueller, R., Willsch, R., Andreev, A.: A fiber Bragg grating refractometer. *Meas. Sci. Technol.* **12**, 757–764 (2001)
2. Liang, W., Huang, Y., Xu, Y., Lee, R.K., Yariv, A.: Highly sensitive fiber Bragg grating refractive index sensors. *Appl. Phys. Lett.* **86**, 151122 (2005)
3. Zhou, K., Lai, Y., Chen, X., Sugden, K., Zhang, L., Bennion, I.: A refractometer based on a micro-slot in a fiber Bragg grating formed by chemically assisted femtosecond laser processing. *Opt. Express* **15**, 15848–15853 (2007)
4. Bhatia, V., Vengsarkar, A.M.: Optical fiber long-period grating sensors. *Opt. Lett.* **21**, 692–694 (1996)
5. Kin, D.W., Zhang, Y., Cooper, K.L., Wang, A.: In-fiber reflection mode interferometer based on a long-period grating for external refractive-index measurement. *Appl. Opt.* **44**, 5368–5373 (2005)
6. Kim, D.W., Shen, F., Chen, X., Wang, A.: Simultaneous measurement of refractive index and temperature based on a reflection-mode long-period grating and an intrinsic Fabry-Perot interferometer sensor. *Opt. Lett.* **30**, 3000–3002 (2005)
7. Fan, X., White, I.M., Shopova, S.I., Zhu, H., Suter, J.D., Sun, Y.: Sensitive optical biosensors for unlabeled targets: a review. *Anal. Chim. Acta* **620**, 8–26 (2008)
8. Jauregui-Vazquez, D., Lopez-Dieguez, Y., Sierra-Hernandez, J.M.: Modified all-fiber Fabry-Perot interferometer and its refractive index, load, and temperature analyses. *IEEE Photonics J.* **7**(3), 1–9 (2017)
9. Wang, T., Ge, Y., Chang, J.: Wavelength-interrogation Fabry-Perot refractive index sensor based on a sealed in-fiber cavity. *IEEE Photonics Technol. Lett.* **28**(1), 3–6 (2015)
10. Men, L., Lu, P., Chen, Q.: Femtosecond laser trimmed fiber taper for simultaneous measurement of axial strain and temperature. *IEEE Photonics Technol. Lett.* **23**(5), 320–322 (2011)



# Optical Fiber Sensor for Steady Micro-flow Rate Measurement

Zhicheng Zhu, Juan Kang<sup>(✉)</sup>, Qian Zhang, Yi Li, and Chunliu Zhao

Institute of Optoelectronic Technology, China Jiliang University, Hangzhou, Zhejiang, China  
243410386@qq.com

**Abstract.** A fiber sensor with simply a section of SMF inserted in a syringe head for steady micro-flow rate measurement has been proposed and experimentally demonstrated. The end face of the SMF and the measured steady micro-flow is formed as an F-P cavity. The length of the formed F-P cavity is easily be modulated by the fluctuation of the steady micro-flow rate. The experimental results show that the highest sensitivities of steady micro-flow rate is 0.020 nm/( $\mu\text{L}/\text{min}$ ) and obtained by saline water under 10% concentration at the rate of 100  $\mu\text{L}/\text{min}$ .

**Keywords:** Rate measurement · Steady micro-flow · Optical fiber

## 1 Introduction

Flow rate measurement, especially micro-flow rate measurement, is widely demanded in the field such as blood vessels, microfluidics preparation, tissue fluid extraction, and so on. In medical research, flow rate sensors have been used in ventilated patients, such as hot wire anemometers and ultrasonic flow meters [1, 2]. In industry fields, differential pressure flow meters, for instance, thermal mass flow meter and soft sensor based on LSSVR [3] have been extensively applied. The former existing conventional flow rate sensors own quite a few disadvantages such as complicated structure, low sensitivity, and weak performance to electromagnetic interference [4]. Although there have also had many mature techniques such as LDV (Laser Doppler Velocimetry) [5], PIV (Particle Image Velocimetry) [6, 7], and thermal flow sensors [8] in detecting flow rate of micro-flow channel, but all these methods are operated complicatedly and their experimental conditions are relatively prepared with rigor. With the development of fiber sensor technology, fiber-optics-based flow rate sensors have been designed with the ability of high sensitivity and electromagnetic immunity. Many related researches have been reported in recent years. A microfluidic flow sensor utilizing the principle of flow-induced vibration on an optical cantilever has been applied in flow rate measurement [9]. An optical fiber-based humidity sensor is applied to solve the problem of breathing diagnostics [10]. All the researched methods let the fiber-optics-based sensors boom in flow rate measurement.

In this paper, a low-cost optical fiber sensor for steady micro-flow rate measurement is proposed. The sensor is simply composed by a section of SMF inserted parallel in the syringe needle. The SMF inserted in the syringe needle is fixed with the syringe needle by Vaseline and can be easily moved to adjust the end face between the SMF and the syringe needle. The proposed sensor is mainly based on F-P interference, in which the end face between the SMF and the syringe needle is formed as the F-P cavity. The output interference spectrum is changed by the fluctuation of the steady micro-flow rate and is used for micro-flow rate monitoring. The proposed sensor can provide a reference for steady micro-flow rate measuring fields in narrow channels.

## 2 Operation Principles

The proposed sensor is shown in Fig. 1. It just consists of a SMF and a syringe head. One section of cleaved SMF is inserted inside the syringe head. The distance between the end face of the SMF (M1) and the end face of the syringe head is  $80\ \mu\text{m}$ . The diameter of the SMF is  $125\ \mu\text{m}$  and the inner diameter of the syringe head is  $150\ \mu\text{m}$ . The gap between the SMF and syringe head is sealed by Vaseline. When the sensor is inserted to a microchannel, the end face of the syringe head is sealed by the measured micro-flow. Then the F-P cavity is formed by the measured micro-flow and the proposed sensor head. Vaseline used in sensor can not only tactfully avoid the capillarity but also make SMF move easily to change the length of the F-P cavity.

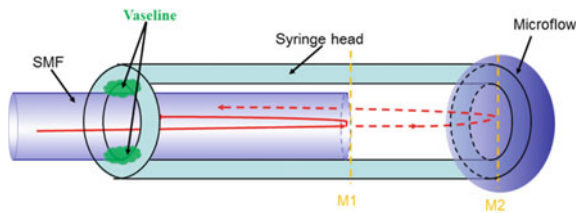


**Fig. 1** Structure of the proposed sensor

When the light transmits through the SMF and arrives at M1, a portion light is reflected by M1, another portion still transmits straightly and finally reflected by the micro-flow surface (M2). As a result, two portions of light are encountered and interfered with each other. The output interference spectrum is shown in Fig. 2 The whole process of light propagating follows the principle of F-P interferometer which is used in the following experiments.



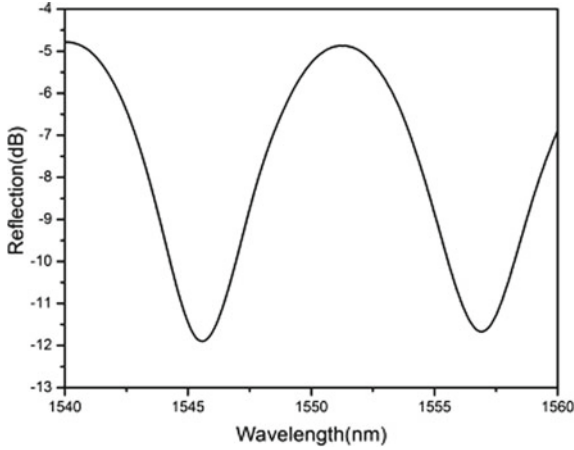


**Fig. 2** Output interference spectrum with the cavity length of 80  $\mu\text{m}$

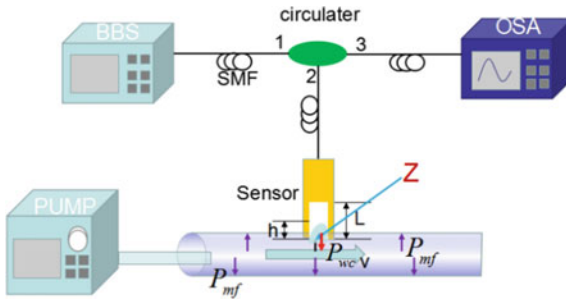


**Fig. 3** Setup of the measuring system

During the measurement, a polytetrafluoroethylene (PTFE) tube is used for steady micro-flow channel. The proposed sensor is vertically inserted to the PTFE tube. The whole setup of the steady micro-flow rate measurement is shown in Fig. 3. Light from the BBS is transmitted from the port 1 of optic circulator into port 2. F-P-based interference phenomenon then occurs by the proposed sensor. Finally, the interference light is outputted from port 3 and monitored by OSA. Specifically, the measured steady micro-flows with different rates are pumped by single channel syringe pump modeled WHSP01.

When the steady micro-flow is passed through the PTFE tube, it exerts a static press ( $P_{mf}$ ) on the side of the PTFE Tube. The static press obeys the Bernoulli's equation and can be expressed as [11]:

$$P_{mf} = C - \frac{\rho v^2}{2} \tag{1}$$

where  $C$  is a constant,  $\rho$  is the liquid density,  $v$  is the velocity of the liquid. When the micro-flow is passing through the connection of the sensor and the PTFE tube at the position  $Z$  in Fig. 3, it will be pressed to form a section of water column at point  $Z$ . The water column also imposes a pressure  $P_{wc}$  which can be expressed as [11]:

$$P_{wc} = \rho gh \quad (2)$$

where  $g$  is the acceleration of gravity,  $h$  is height of water column in sensor. When  $P_{mf} = P_{wc}$ , the height of the water column will reach the transient stability and can be deduced as:

$$h = \frac{C}{\rho g} - \frac{\rho v^2}{2\rho g} \quad (3)$$

When the velocity of the steady micro-flow fluctuates, the balance between  $P_{mf}$  and  $P_{wc}$  is broken and the height of water column  $h$  is changed accordingly. The change of  $h$  can be obtained as follows by differentiating Eq. (3):

$$\Delta h = -\frac{v}{g} \Delta v \quad (4)$$

According to the formula of flow rate which is expressed as  $Q = vS$ , where  $S$  is the cross-sectional area of the microchannel, the relationship between the change of  $h$  and the fluctuation of  $Q$  is as follows:

$$\Delta h = -\frac{Q}{gS^2} \Delta Q \quad (5)$$

According to the principle of F-P cavity, the relationship between shift of the output interference wavelength and length change of the F-P cavity is known as follows [12]:

$$\Delta \lambda = \frac{\Delta h}{h_a} \lambda_0 \quad (6)$$

where  $\lambda_0$  is the transmission peak wavelength,  $h_a$  is the original length of the F-P cavity. Combined Eq. (6) with Eq. (5), the relationship between cavity length change and rate is obtained as:

$$\Delta \lambda = \frac{-\lambda_0 Q}{h_a g S^2} \Delta Q \quad (7)$$

It can be seen that the shifting of the wavelength is caused by fluctuation of the micro-flow rate. Therefore the micro-flow rate can be measured by monitor the output spectrum change of the F-P interferometer.

### 3 Experimental Results and Discussions

In the experiment, all measurements are performed at standard environment with the temperature of 27 °C, air pressure of 1 bar and the humidity of 45% in order to avoid the impacts brought by the environment. Saline water with different concentrations of 0, 10 and 20% is prepared for steady micro-flow rate measurement. Three different concentrations with the rate from 0 to 500 μL/min by the step of 100 μL/min are injected to the PTFE tube to monitor the output spectral change. When the steady micro-flow is selected as pure water, that is to say the concentration is at 0%, the output wavelength is shifted from 1545.58 to 1543.92 nm by the rate changing from 0 to 500 μL/min. The output spectra are shown in Fig. 4a. When the steady micro-flow is replaced by the saline water with the concentration of 20%, the output wavelength is shifted from 1548.92 to 1543.52 nm, which are shown in Fig. 4b. It can be seen different concentrations of saline water at 0 μL/min result in different original peak wavelength. The phenomenon is caused by different surface tension owned by different liquid, which causes the micro-change of the length of the original F-P cavity. Therefore, relative wavelength shift is used for fitting of steady micro-flow rate. Figure 5 shows change of the relative output spectra shift under different steady micro-flow concentrations with different rates.

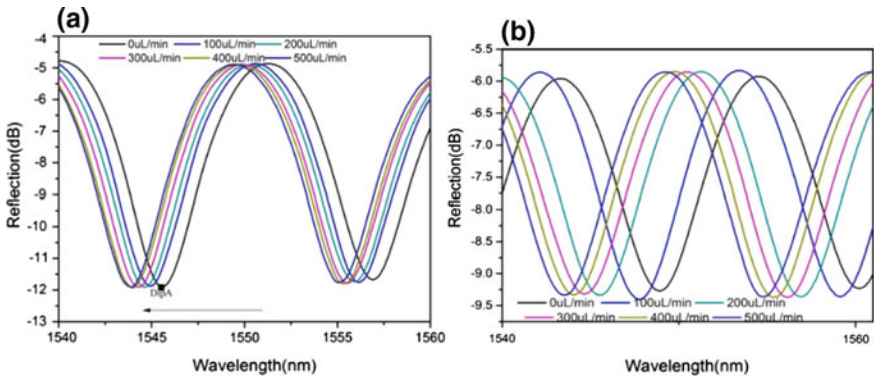


Fig. 4 Output spectra with different micro-flow rate at concentrations of 0 and 20%

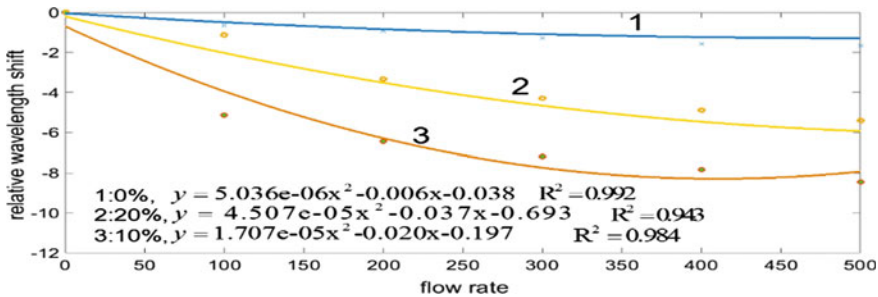


Fig. 5 Relationship between relative wavelength shift and micro-flow rate under different concentrations

From the fitting curve, the highest rate sensitivity is  $0.020 \text{ nm}/(\mu\text{L}/\text{min})$  and obtained by saline water under 10% concentration at rate of  $100 \mu\text{L}/\text{min}$ . Samples of different concentration are only three and cannot be deduced for further regularity. It is a defect and should be avoided in further experiment.

## 4 Conclusions

In this paper, a fiber sensor with a section of SMF inserted in a syringe head for steady micro-flow rate measurement has been experimentally demonstrated. Three different concentrations of saline water at 0, 10, 20% have been matched for steady micro-flow rate measurement. Experimental results show that the highest sensitivities of steady micro-flow rate is  $0.020 \text{ nm}/(\mu\text{L}/\text{min})$  and obtained by saline water under 10% concentration at the rate of  $100 \mu\text{L}/\text{min}$ . Compared with the existing optical fiber methods, the proposed sensor is capable of steady micro-flow rate measurement with simple fabrication, low-cost and robust structure. It can be widely used in the field of narrow channel such as blood vessels and microfluidics chip design.

**Acknowledgements.** This work was supported by the National Natural Science Foundation of China under Grants 61505194.

## References

1. Baker, R.C.: Flow Measurement Handbook: Industrial Designs Operating Principles Performance and Applications. Cambridge University Press (2000)
2. Branca, F.P.: Clinical engineering fundamentals. In: Original Foreign-Language Citation: Fondamenti di ingegneria clinica, vol. 1. Springer (2000)
3. Yang, Y.Q., Wang, S.H. Lin, Y.F.: Soft sensor for coal mill primary air flow based on LSSVR. In: 2012 International Conference on Machine Learning and Cybernetics, Xian, pp. 434–439 (2012)
4. Battista, L., Sciuto, S.A. Scorza, A.: Preliminary evaluation of a fiber-optic sensor for flow measurements in pulmonary ventilators. In: 2011 IEEE International Symposium on Medical Measurements and Applications, Bari, pp. 29–34 (2011)
5. Ishida, H.: Blood flow velocity imaging of malignant melanoma by micro multipoint laser Doppler Velocimetry. *Appl. Phys. Lett.* **97** (2010)
6. Lindken, R.: Micro-particle image velocimetry (mu PIV): recent developments applications and guidelines. *Lab Chip* **9**, 2551–2567 (2009)
7. Wereley, S.T., Meinhart, C.D.: Recent advances in micro-particle image velocimetry. *Annu. Rev. Fluid Mech.* **42**, 557–576 (2010)
8. Kikutani, Y.: Flowing thermal lens micro-flow velocimeter. *Sens. Actuators B-Chem.* **133**, 91–96 (2008)
9. Ju, P., Tsai, C., Fu, L., Lin, C.: Microfluidic flow meter and viscometer utilizing flow-induced vibration on an optic fiber cantilever. In: 2011 16th International Solid-State Sensors, Actuators and Microsystems Conference, Beijing, pp. 1428–1431 (2011)
10. Chen, Q., Claus, R.O., Spillman, W.B., Arregui, F.J., Matias, I.R., Cooper, K.L.: Optical fiber sensors for breathing diagnostics. In: 2002 15th Optical Fiber Sensors Conference

Technical Digest. OFS 2002 (Cat. No. 02EX533), Portland, OR, USA, vol. 1, pp. 273–276 (2002)

11. Wu, M.Y.: Principle of Bernoulli equation and its application. *Inf. Rec. Mater.* **19**(9), 115–117 (2018)
12. Xu, F., Ren, D., Shi, X.: High-sensitivity Fabry–Perot interferometric pressure sensor based on a nanothick silver diaphragm. *Opt. Lett.* **37**(2), 133–135 (2012)

**Part II**  
**LEDs, OLEDs and Related Materials**



# An Ultrathin Tandem Organic Light-Emitting Diodes with Very Low Driving Voltage and High Efficiency

Yanhong Deng<sup>1</sup>(✉), Jinjiang Wang<sup>1</sup>, Liezun Chen<sup>1</sup>, Xiangyu Jiang<sup>1</sup>,  
Ke Xie<sup>1</sup>, Yuqi Peng<sup>1</sup>, and Yanqing Li<sup>2</sup>(✉)

<sup>1</sup> College of Physics and Electronics Engineering, Hengyang Normal University,  
Hengyang 421002, China  
2006318dyh@hynu.edu.cn

<sup>2</sup> Institute of Functional Nano and Soft Materials (FUNSOM), Soochow  
University, Suzhou 215123, China  
yqli@suda.edu.cn

**Abstract.** Low driving voltage, high luminance, and high efficiency are the important parameters of organic light-emitting diodes (OLEDs) for their application of display and lighting. Usually, synthesis of new materials, doping technique and designing suitable device structures were the main methods to use for realizing the aim of the wide application of OLEDs. In this paper, we try to obtain a high efficiency and low driving voltage tandem OLED with ultrathin films through optimizing the thickness of hole transporting layer (HTL), electron transport layer (ETL), emission layer (EML), and charge generation layer (CGL). As a result, we got the ultrathin tandem OLED with a very low driving voltage of 7.44 V, the luminance of 16,080 cd/m<sup>2</sup>, the current efficiency of 16.08 cd/A, and power efficiency of 6.28 lm/W, respectively. This research not only saves the cost and improves the power efficiency, which may supply a theoretical basis for the development of OLEDs in the lighting field.

**Keywords:** Driving voltage · Tandem Organic Light-Emitting Diodes (OLEDs) · Efficiency

## 1 Introduction

In tandem organic light-emitting diodes (OLEDs), the luminance and current efficiency are multi-fold growth with the increasing number of electroluminescence (EL) unit, but also the multi-fold growth of driving voltage, which means that the power efficiency of tandem OLED is not improved, and not conducive to its practical application, especially in lighting field. So, reduction in the driving voltage of OLEDs is a key issue to improve the power efficiency in the application of flat panel displays and solid-state lighting [1]. Usually, there are several methods to reduce the driving voltage of OLEDs. One of the most powerful solutions is to use doping concept in the carrier transporting or injection layer [1–11]. From the electrical doping mechanism of organic semiconductor, the doping process can be regarded as a charge transfer process, which is the host material to obtain hole or electron from acceptor or donor, and realize p- or

n-doped. For example, p-doped occurs through the charge transfer from the highest occupied molecular orbital (HOMO) of the host material to the lowest unoccupied molecular orbital (LUMO) of the dopant material [12], while n-doped occurs through the charge transfer from the HOMO of the dopant material to the LUMO of the host material. As we know, p- and n-type doping is widely used to improve or change the device electrical characteristics. If using the proper doped systems, it can be increased the conductivity of film with several orders of magnitude and can also realize ohmic contact between the electrode and the organic layer, reduce the injection barrier at the electrode/organic interface, and provide excellent hole or electron injection from electrode to organic layer [13]. Inserting a buffer layer with suitable thickness like MoOx [14], SiO<sub>2</sub> [15], CFx [16], LiF [17], Ag<sub>2</sub>O [18], TCNQ [19] can improve balance of the hole and electron injections. And synthesis of organic materials with high mobility and proper energy level [20–24] can conducive to achieve good charge balance and confine excitons in the EML [23–26].

In this work, we try to realize an ultrathin tandem OLED with low driving voltage, high brightness, and high efficiency through optimizing the thickness of organic layers. Basing on our early works [10, 27, 28], we firstly design several single devices (given in Table 1) and then fabricate serial tandem devices with different thickness of function layers. As a result, we obtained the ultrathin tandem OLED with a very low driving voltage of 7.44 V and high power efficiency of 6.28 lm/W.

**Table 1** Structures of single-EL-unit devices with different thickness of organic layers

Devices	Layer structure
A	ITO/NPB(20 nm)/C545T:Alq <sub>3</sub> (1 wt%, 10 nm)/BPhen(20 nm)/LiF(0.5 nm)/Al (100 nm)
B	ITO/NPB(20 nm)/C545T:Alq <sub>3</sub> (1 wt%, 10 nm)/BPhen(30 nm)/LiF(0.5 nm)/Al (100 nm)
C	ITO/NPB(20 nm)/C545T:Alq <sub>3</sub> (1 wt%, 20 nm)/BPhen(20 nm)/LiF(0.5 nm)/Al (100 nm)
D	ITO/NPB(20 nm)/C545T:Alq <sub>3</sub> (1 wt%, 20 nm)/BPhen(30 nm)/LiF(0.5 nm)/Al (100 nm)

## 2 Experimental Methods

In this work, all organic devices were fabricated on the indium-tin-oxide (ITO) coated glass with a sheet resistance of 20 Ω/sq by evaporation method without breaking the vacuum ( $<2 \times 10^{-6}$  Torr). The ITO surface was cleaned with ultrapurified water and organic solvents, dry-cleaned for 30 min, and treated by UV–ozone for 15 min before put into high-vacuum thermal evaporation system. A shadow mask was used to define the Al cathode to form an emissive area of 10 mm<sup>2</sup>. The evaporation rates of all organic layers were 2 Å/s, LiF layer was 0.1 Å/s, and Al cathode was 5 Å/s, respectively.

The fabricated devices were encapsulated immediately by using epoxy resin and glass lids prior to the measurement. The current density–voltage–luminance, current efficiency–current density–power efficiency characteristics, and EL spectra were recorded on a computer-controlled programmable Keithley model 2400 power source with a Photo Research 655 spectrometer.



### 3 Results and Discussion

To get the low driving voltage of tandem OLEDs, firstly, four single-unit OLEDs with different thickness of organic layers were fabricated. The structures of single-unit devices are listed in Table 1, the corresponding performance is displayed in Fig. 1, and more detailed performance parameters are shown in Table 2. It is known that the driving voltage and luminance increased with the thickness of organic layers, which appears that the thinnest device A has the lowest driving voltage, and the thickest device D has the best luminance. With the aim to realize the device with low driving

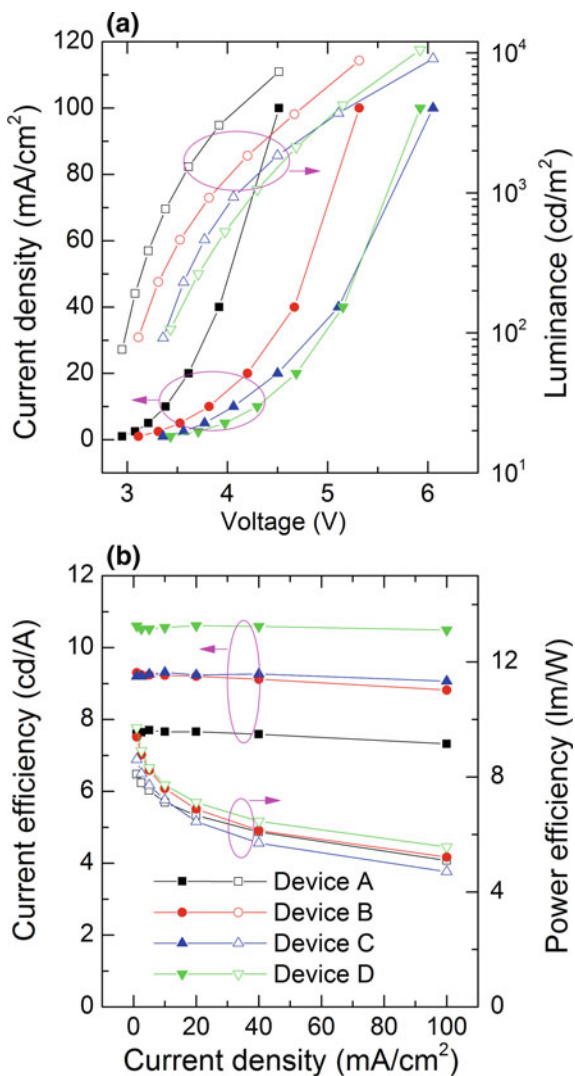


**Fig. 1** a Current density–voltage–luminance and b current efficiency–current density–power characteristics of devices listed in Table 1

voltage and high efficiency, we chose the thinner EL unit for further research and designed a serial structure of tandem devices based on these kinds of EL unit through changing the thickness of hole transporting layers (HTL), electron transporting layers (ETL), emission layers (EML), and charge generation layer (CGL), respectively.

**Table 2** Performances of devices A–D.  $V_d$  is driving voltage at  $J = 1 \text{ mA/cm}^2$ ,  $L$ ,  $\eta_c$ , and  $\eta_p$  are the maximum luminance, current efficiency, and power efficiency, respectively

Devices	$V_d$ (V)	$L$ ( $\text{cd/m}^2$ )	$\eta_c$ ( $\text{cd/A}$ )	$\eta_p$ ( $\text{lm/W}$ )	EL peak (nm)
A	2.95	7323	7.7	8.09	520
B	3.11	8818	9.3	9.39	520
C	3.35	9066	9.31	8.60	520
D	3.43	10,490	10.61	9.70	520

### 3.1 Optimizing the Thickness of HTL

First of all, we try to changing the thickness of HTL on the second EL unit with the structure of ITO/NPB(20 nm)/C545T:Alq<sub>3</sub>(1 wt%, 10 nm)/BPhen(20 nm)/Mg:BPhen(10 wt%, 10 nm)/MoO<sub>3</sub>(5 nm)/NPB(x nm)/C545T:Alq<sub>3</sub>(1 wt%, 20 nm)/BPhen(40 nm)/LiF(0.5 nm)/Al(100 nm). Here, x is 20 nm for device E and 40 nm for device F. The current density–voltage–luminance and current efficiency–current density–power efficiency characteristics of devices E–F are shown in Fig. 2. According to Fig. 2, we can know that the thickness of HTL on the second EL unit plays an important role in driving voltage and device efficiencies. With a thickness difference of 20 nm in NPB layer, the device performance exhibits a large difference. The driving voltage of devices E and F is 7.44 and 8.09 V at  $J = 1 \text{ mA/cm}^2$ , and their luminance is 14,950 and 16,340  $\text{cd/m}^2$  at the current density of 100  $\text{mA/cm}^2$ . But the driving voltage is still very high, and the efficiency is not as perfect as we anticipated.

### 3.2 Optimizing the Thickness of EML

In this part, we modify the thickness of EML for further research and design this kind of device: ITO/NPB(20 nm)/C545T:Alq<sub>3</sub>(1 wt%, y nm)/BPhen(20 nm)/Mg:BPhen(10 wt%, 10 nm)/MoO<sub>3</sub>(3 nm)/NPB(20 nm)/C545T:Alq<sub>3</sub>(1 wt%, z nm)/BPhen(20 nm)/LiF(0.5 nm)/Al(100 nm), y and z are 10 and 10 nm for device G, 10 and 20 nm for device H, and 20 and 20 nm for device I, respectively. It is shown in Fig. 3 that device H has the largest luminance and efficiency, which are 15230  $\text{cd/m}^2$  and 15.23  $\text{cd/A}$  at  $J = 100 \text{ mA/cm}^2$ , while the driving voltage is a bit higher than device G, which are 7.10 and 6.71 V at  $J = 1 \text{ mA/cm}^2$ .

### 3.3 Optimizing the Thickness of ETL

Then, we attempt to get the device with low driving voltage by optimizing the thickness of ETL, and use device structure: ITO/NPB(20 nm)/C545T:Alq<sub>3</sub>(1 wt%, 10 nm)/BPhen(m nm)/Mg:BPhen(10 wt%, 10 nm)/MoO<sub>3</sub>(3 nm)/NPB(20 nm)/C545T:

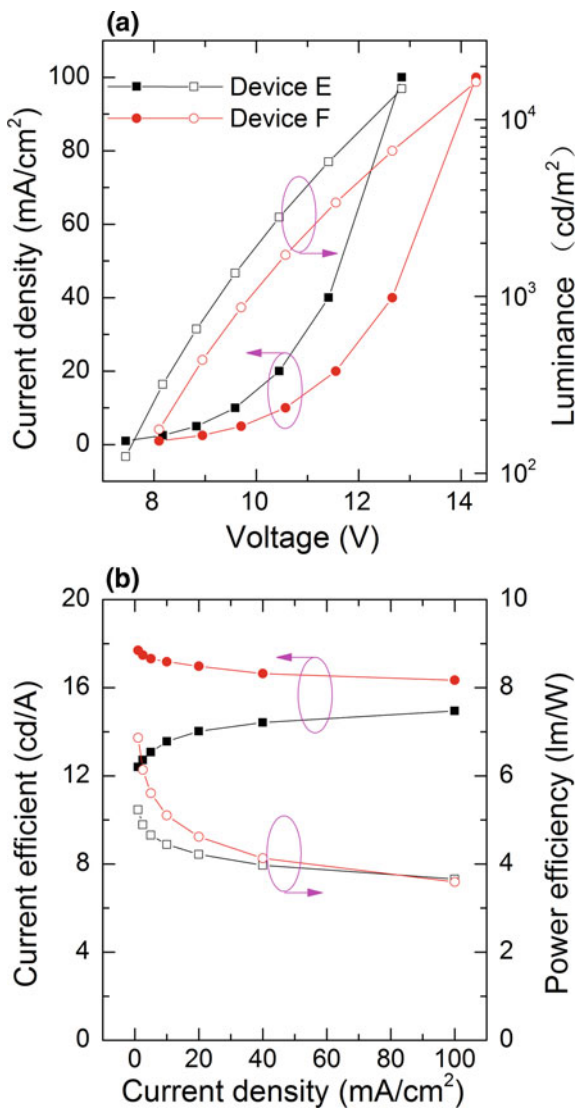


**Fig. 2** Performance of tandem devices E-F with 20 nm thick difference in the HTL of the second EL unit

Alq<sub>3</sub>(1 wt%, 20 nm)/BPhen(n nm)/LiF(0.5 nm)/Al(100 nm). Here, m and n are 20 and 20 nm for device H, 20 and 30 nm for device J, 30 and 30 nm for device K, respectively. Figure 4 compares the electrical and luminescent properties of devices H, J, and K, they show the same variation trend as a comparison of devices G-I, the thinnest device has the lowest driving voltage, and the device with middle thickness has the highest current efficiency and power efficiency, and a bit higher driving voltage than the thinnest device. This phenomenon may be due to the suitable energy level of this

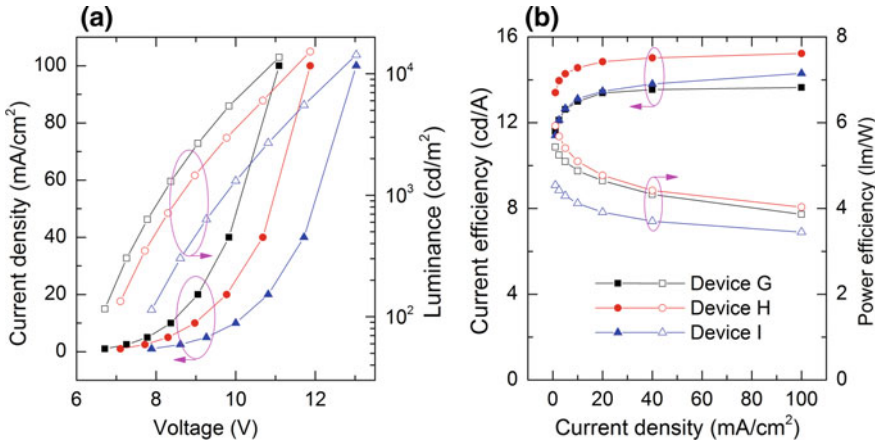


**Fig. 3** **a** Current density–voltage–luminance and **b** current efficiency–current density–power efficiency curves of tandem devices G–I with different thickness of EML

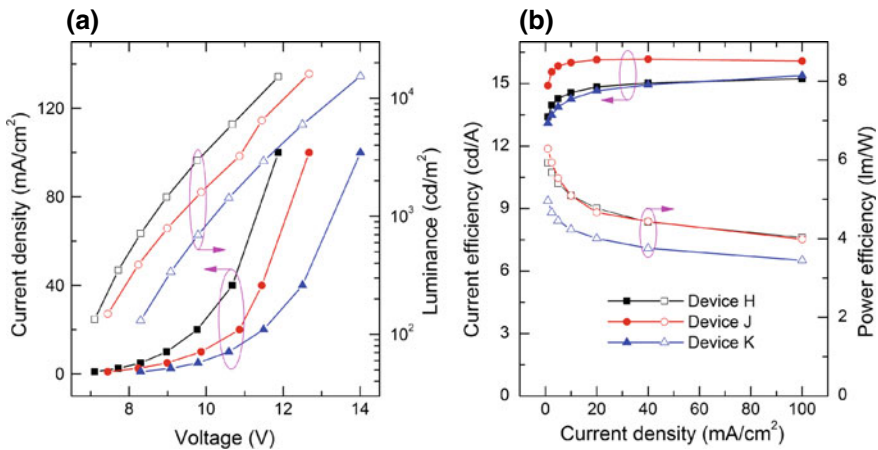


**Fig. 4** **a** Current density–voltage–luminance and **b** current efficiency–current density–power efficiency characteristics of tandem devices with different thickness of ETL

kind of organic layers and its adjacent layers, which is convenient for carriers transporting and promote the effective combination of charge within the device.

### 3.4 Optimizing the Thickness of CGL

It is reported that the device performance may be affected by the thickness of the charge generation layer [29]. And how the thickness of CGL affects the device performance still needs study. In this part, several devices were designed to make clear of this problem, which are: (H) ITO/NPB(20 nm)/C545T:Alq<sub>3</sub>(1 wt%, 10 nm)/BPhen(20 nm)/

Mg:BPhen(10 wt%, 10 nm)/MoO<sub>3</sub>(3 nm)/NPB(20 nm)/C545T:Alq<sub>3</sub>(1 wt%, 20 nm)/BPhen(20 nm)/LiF(0.5 nm)/Al(100 nm); (L)ITO/NPB(20 nm)/C545T:Alq<sub>3</sub> (1 wt%, 10 nm)/BPhen(20 nm)/Mg:BPhen(10 wt%, 5 nm)/MoO<sub>3</sub>(1 nm)/NPB(20 nm)/C545T:Alq<sub>3</sub>(1 wt%, 20 nm)/BPhen(20 nm)/LiF(0.5 nm)/Al(100 nm); (M) ITO/NPB(20 nm)/C545T:Alq<sub>3</sub>(1 wt%, 10 nm)/BPhen(20 nm)/Mg:BPhen(10 wt%, 5 nm)/MoO<sub>3</sub>(3 nm)/NPB(20 nm)/C545T:Alq<sub>3</sub>(1 wt%, 20 nm)/BPhen(20 nm)/LiF(0.5 nm)/Al(100 nm); (N) ITO/NPB(20 nm)/C545T:Alq<sub>3</sub>(1 wt%, 10 nm)/BPhen(20 nm)/Mg:BPhen(10 wt%, 10 nm)/MoO<sub>3</sub>(1 nm)/NPB(20 nm)/C545T:Alq<sub>3</sub>(1 wt%, 20 nm)/BPhen(20 nm)/LiF(0.5 nm)/Al(100 nm). As shown in Fig. 5, device H shows the largest efficiencies and the lowest driving voltage. Comparing the devices H and N, which is different in thickness of MoO<sub>3</sub>, the thicker of MoO<sub>3</sub>, the better of device performance, the same phenomenon can be seen in the comparison of devices L and M. It seems like that 5-nm and 10-nm-thick Mg:BPhen layer displays very little effect on the luminance and current efficiency, but large effect on the driving voltage and power efficiency of devices H and M. There appears the same worse performances of devices L and N, though they are different in thickness of Mg:BPhen layer, which may be due to 1-nm-thick MoO<sub>3</sub> film is very thin, its evaporation is too little and cannot form a continuous film, and finally exhibit a great impact on the generation and transmission capacity of carriers.

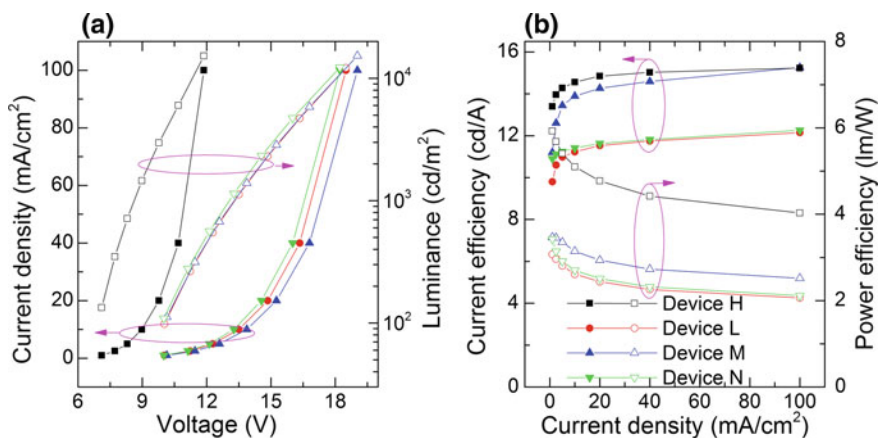


**Fig. 5** a Current density–voltage–luminance and b current efficiency–current density–power efficiency curves of tandem devices H, L, M, and N

### 3.5 Comparison of Two Tandem OLEDs

Figure 6 compares the performances of the optimized device J and reference device O. Here, the thickness and structure of the reference device are we usually used, which is ITO/NPB(40 nm)/C545T:Alq<sub>3</sub>(1 wt%, 20 nm)/BPhen(40 nm)/Mg:BPhen(10 wt%, 10 nm)/MoO<sub>3</sub>(5 nm)/NPB(40 nm)/C545T:Alq<sub>3</sub>(1 wt%, 20 nm)/BPhen(40 nm)/LiF(0.5 nm)/Al(100 nm). From Fig. 6, we can know that with a total difference of 80 nm thick in organic layers, the driving voltage of devices J and O is 7.44 and 10.21 V at the current density of 1 mA/cm<sup>2</sup>, the maxim current efficiency is 16.08 and 19.64 cd/A,

and the maxim power efficiency is 6.28 and 5.28 lm/W. It is obvious that the driving voltage is reduced and the power efficiency is increased after optimizing, this is a good phenomenon that we see, but there is still a long way to realize a lower driving voltage and higher power efficiency device, and need that we make more efforts.

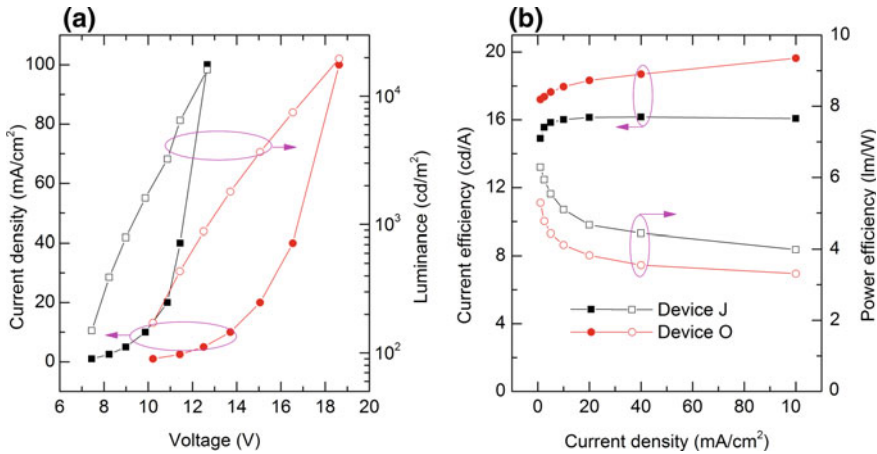


**Fig. 6** Electroluminescence properties of devices J and O

## 4 Summary

We fabricated an ultrathin tandem device with a driving voltage of 7.44 V and power efficiency of 6.28 lm/W. This is implemented to reduce cost and enhance the efficiency of the device. We believe that further optimization of device parameters will more ascension the device performance, and hope this study can provide a train of thought for the OLED application.

**Acknowledgements.** The authors gratefully acknowledge the Hunan Provincial Natural Science Foundation of China (No. 2018JJ3010, 2017JJ2009), Scientific Research Fund of Hunan Provincial Education Department (No. 15B033), the Hunan Provincial Applied Basic Research Base of Optoelectronic Information Technology (GD18K05), Science and Technology Plan Project of Hunan Province (No. 2016TP1020), Open fund project of Hunan Provincial Key Laboratory of Intelligent Information Processing and Application for Hengyang normal university (No. 2017IPAYB02), the Science and Technology Development Plan Project in Hengyang City (No. 2017KJ159), the Excellent Talents Program of HYNU, and the college students inquiry learning and innovative experimental project of Hengyang Normal University (No. CX1754).

## References

1. Pfeiffer, M., Forrest, S.R., Leo, K., Thompson, M. E.: Electrophosphorescent p-i-n organic light emitting devices for Very-High-Efficiency Flat-Panel displays. *Adv. Mater.* (Weinheim, Ger.) **14**, 1633 (2002)
2. Zhou, X., Blochwitz, J., Pfeiffer, M., Nollau, A., Fritz, T., Leo, K.: Enhanced hole injection into amorphous hole-transport layers of organic light emitting diodes using controlled p-type doping. *Adv. Funct. Mater.* **11**, 310 (2001)
3. Qasim, K., Wang, B.P., Zhang, Y.P., Li, P.F., Wang, Y.S., Li, S.J., Lee, S. T., Liao, L.S., Lei, W., Bao, Q.L.: Solution-processed extremely efficient multicolor perovskite light emitting diodes utilizing doped electron transport layer. *Adv. Funct. Mater.* **27**(21), 1606874 (2017)
4. Huang, J., Pfeiffer, M., Werner, A., Blochwitz, J., Leo, K., Liu, S.: Low-voltage organic electroluminescent devices using pin structures. *Appl. Phys. Lett.* **80**, 139 (2002)
5. Soman, A., Manuraj, M., Unni, K.N.N.: Addressing the efficiency roll-off in a fluorescent OLED by facile electron transport layer doping and carrier confinement. *Opt. Mater.* **79**, 413–419 (2018)
6. Walzer, K., Maennig, B., Pfeiffer, M., Leo, K.: Highly efficient organic devices based on electrically doped transport layers. *Chem. Rev.* **107**, 1233 (2007)
7. Chang, C.C., Hsieh, M.T., Chen, J.F., Hwang, S.W., Chen, C.H.: Highly power efficient organic light emitting diodes with a doping layer. *Appl. Phys. Lett.* **89**, 253504 (2006)
8. Ikeda, H., Sakata, J., Hayakawa, M., Aoyama, T., Kawakami, T., Kamata, K., Iwaki, Y., Seo, S., Noda, Y., Nomura, R., Yamazaki, S.: Low-Drive-Voltage OLEDs with a buffer layer having molybdenum oxide. *SID Int. Symp. Digest Tech. Papers* **37**, 923 (2006)
9. Chen, D.C., Liu, K.K., Gan, L., Liu, M., Gao, K., Xie, G.Z., Ma, Y.G., Shi, Y.C., Su, J.: Modulation of exciton generation in organic active planar p-n heterojunction: toward low driving voltage and high-efficiency OLEDs employing conventional and thermally activated delayed fluorescent emitters. *Adv. Mater.* **28**(31), 6758–6765 (2016)
10. Deng, Y.H., Li, Y.Q., Ou, Q.D., Wang, Q.K., Sun, F.Z., Chen, X.Y., Tang, J.X.: The doping effect of cesium-based compounds on carrier transport and operational stability in organic light-emitting diodes. *Org. Electron.* **15**, 1215–1221 (2014)
11. Chiba, T., Pu, Y.J., Ide, T., Ohisa, S., Fukuda, H., Hikichi, T., Takashima, D., Takahashi, T., Kawata, S., Kido, J.: Addition of Lithium 8-Quinolate into polyethylenimine electron-injection layer in OLEDs: not only reducing driving voltage but also improving device lifetime. *ACS Appl. Mater. Interfaces.* **9**(21), 18113–18119 (2017)
12. Gao, W., Kahn, A.: Controlled p-doping of zinc phthalocyanine by coevaporation with tetrafluorotetracyanoquinodimethane: a direct and inverse photoemission study. *Appl. Phys. Lett.* **79**, 4040 (2001)
13. Walzer, K., Maennig, B., Pfeiffer, M., Leo, K.: Highly efficient organic devices based on electrically doped transport layers. *Chem. Rev.* **107**(4), 1233 (2007)
14. Zhou, Y., Fuentes-Hernandez, C., Shim, J., Meyer, J., Giordano, A.J., Li, H., Winget, P., Papadopoulos, T., Cheun, H., Kim, J., Fenoll, M., Dindar, A., Haske, W., Najafabadi, E., Khan, T.M., Sojoudi, H., Barlow, S., Graham, S., Brédas, J. L., Marder, S.R., Kahn, A., Kippelen, B.: A universal method to produce low-work function electrodes for organic electronics. *Science* **336**, 327 (2012)
15. Deng, Z.B., Ding, X.M., Lee, S.T., Gambling, W.A.: Enhanced brightness and efficiency in organic electroluminescent devices using SiO<sub>2</sub> buffer layers. *Appl. Phys. Lett.* **74**, 2227 (1999)

16. Tong, S.W., Lee, C.S., Lifshitz, Y., Gao, D.Q., Lee, S.T.: Conducting fluorocarbon coatings for organic light-emitting diodes. *Appl. Phys. Lett.* **84**, 4032 (2004)
17. Zhao, J.M., Zhang, S.T., Wang, X.J., Zhang, Y.Q., Wang, X.Z., Zhong, G.Y., Wang, Z.J., Ding, W., Huang, X.M., Hou, X.Y.: Dual role of LiF as a hole-injection buffer in organic light-emitting diodes. *Appl. Phys. Lett.* **84**, 2913 (2003)
18. Wang, C.T., Ting, C.C., Kao, P.C., Li, S.R., Chu, S.Y.: Improvement of OLED performance by tuning of silver oxide buffer layer composition on silver grid surface using UV-ozone treatment. *Appl. Phys. Lett.* **113**, 051602 (2018)
19. Zhang, J., Xin, L.W., Gao, J., Liu, Y., Rui, H.S., Lin, X., Hua, Y.L., Wu, X.M., Yin, S.G.: Improving the performance of organic light-emitting devices by incorporating non-doped TCNQ as electron buffer layer. *J. Mater. Sci.: Mater. Electron.* **28**(17), 12761–12767 (2017)
20. Han, C., Xie, G., Xu, H., Zhang, Z., Yu, D., Zhao, Y., Yan, P., Deng, Z., Li, Q., Liu, S.: Towards highly efficient blue-phosphorescent organic light-emitting diodes with low operating voltage and excellent efficiency stability. *Chem. Eur. J.* **17**, 445 (2011)
21. Gong, S., Chang, Y.L., Wu, K., White, R., Lu, Z.H., Song, D., Yang, C.: High-power-efficiency blue electrophosphorescence enabled by the synergistic combination of phosphine-oxide-based host and electron-transporting materials. *Chem. Mater.* **26**, 1463 (2014)
22. Sasabe, H., Gonmori, E., Chiba, T., Li, Y.J., Tanaka, D., Su, S.J., Takeda, T., Pu, Y.J., Nakayama, K.I., Kido, J.: Wide-energy-gap electron-transport materials containing 3, 5-dipyridylphenyl moieties for an ultra high efficiency blue organic light-emitting device. *Chem. Mater.* **20**, 5951 (2008)
23. Xiao, L., Su, S.J., Agata, Y., Lan, H., Kido, J.: Nearly 100% internal quantum efficiency in an organic Blue-Light electrophosphorescent device using a weak electron transporting material with a wide energy gap. *Adv. Mater.* **21**, 1271 (2009)
24. Ye, H., Chen, D., Liu, M., Su, S.J., Wang, Y.F., Lo, C.C., Lien, A., Kido, J.: Pyridine-Containing Electron-Transport materials for highly efficient blue phosphorescent OLEDs with ultralow operating voltage and reduced efficiency roll-off. *Adv. Funct. Mater.* **24**, 3268 (2014)
25. Jeon, S.O., Jang, S.E., Son, H.S., Lee, J.Y.: External quantum efficiency above 20% in deep blue phosphorescent organic light-emitting diodes. *Adv. Mater.* **23**, 1436 (2011)
26. Kim, C.Y., Ha, D.G., Kang, H.H., Yun, H.J., Kwon, S.K., Kim, J.J., Kim, Y.H.: Synthesis and characterization of new blue light emitting iridium complexes containing a trimethylsilyl group. *J. Mater. Chem.* **22**, 22721 (2012)
27. Deng, Y.H., Ou, Q.D., Wang, Q.K., Wei, H.X., Li, Y.Q., Lee, S.T., Tang, J.X.: The role of charge generation layers in the operational stability of tandem organic light-emitting diodes. *J. Mater. Chem. C* **2**, 1982–1989 (2014)
28. Deng, Y.H., Wang, J.J., Ou, Q.D., Zhang, D.Y., Chen, L.Z., Li, Y.Q., Tang, J.X.: The electro-optic performance and photovoltaic effect of organic devices based on cesium carbonate/Al/molybdenum trioxide intermediate connector. *Org. Electron.* **51**, 452–457 (2017)
29. Fung, M.K., Li, Y.Q., Liao, L.S.: Lead-free inverted planar Formamidinium Tin Triiodide Perovskite solar cells achieving power conversion efficiencies up to 6.22%. *Adv. Mater.* **28**(42), 1–28 (2016)





# The Study of Working Mechanism of Organic Heterojunction Charge Generation Layer

Feiping Lu<sup>(✉)</sup>, Yuxiang Zhao, Yinglong Shi, Qing Liu, Xiaobin Liu, and Weijun Ling

Department of Physics, Tianshui Normal University, Tianshui, People's Republic of China  
lufp\_sysu@163.com

**Abstract.** The tandem organic light-emitting diodes (tandem OLEDs), which having two or more electroluminescence (EL) units vertically stacked in series through charge generation layer (CGL), were widely used in flat-panel displays and solid state lighting because of their advantages of enhanced current efficiency and luminance at low current densities, as well as their prolonged lifetime as compared to the conventional single-unit devices. In a tandem OLEDs, the CGLs play an important role, serving as the charge generation layer, and it is critical for the performance of tandem OLEDs. It is the basis of fabrication high-efficiency tandem OLEDs to deeply understand the working mechanism of CGL. Organic heterojunctions (OHJs) layers are frequently used as CGLs in the construction of high-efficiency tandem OLEDs. In order to understand the working mechanism of organic heterojunctions CGLs, the device with the structure of glass/ITO/tris (8-hydroxyquinoline) aluminium (Alq<sub>3</sub>) (60 nm)/C<sub>60</sub>(x nm)/pentacene((40-x) nm)/N,N'-bis(naphthalen-1-yl)-N,N'-bis(phenyl)-benzidine (NPB) (40 nm)/Al (100 nm) were successfully fabricated, here the organic heterojunction C<sub>60</sub>/pentacene was used as CGL. The experiment results demonstrated that the organic heterojunction CGL with the structure of C<sub>60</sub> (15 nm)/pentacene (25 nm) with the most effective charge generation ability. By analyzing the carrier transport characteristics in device, the device current can be attributed to the organic heterojunction CGL. Finally, by numerically analyzing the current-voltage (J-V) characteristics of devices, the results showed the charge generation mechanism of organic heterojunction was in accord with quantum tunneling process. The obtained results can help ones deeply understand the working mechanism of organic heterojunction CGLs and fabricate high-efficiency OLEDs.

**Keywords:** Tandem organic light-emitting diodes · Charge generation layer · Working mechanism · Organic heterojunctions layer

## 1 Introduction

Organic light-emitting diodes (OLEDs) have been widely used in flat-panel displays and solid state lighting due to their advantages resulting from surface emitting, the ease of manufacturing large areas, the possibility for flexible and transparent applications, and the vast number of available materials for specific demands. In general, a long operating lifetime and high efficiency must be ensured before mass-production of OLEDs for practical use. In order to obtain the higher brightness, one should increase the device current density; however, experiment results have indicated that the operating lifetime of OLEDs is inversely proportional to the device current density, so there is a conflict between the high-luminance and long operating lifetime [1]. Many methods have been used to solve this issues, among them, tandem OLEDs having two or more electroluminescence units vertically stacked in series through charge generation layers (CGLs) can meet this requirement, because they have the advantages of enhanced current efficiency and luminance at a relative low current density, the lifetime of devices can be prolonged as compared to conventional single-unit devices [2–15]. In tandem OLEDs, the CGLs play a crucial role in determining the effectiveness of the stacked EL units. Up to now, many high-performance CGLs have been developed and successfully used in tandem OLEDs. Usually, the CGLs used in tandem OLEDs have a bilayer structure, which can be formed by a metal–metal (or metal oxide) bilayer [2, 3], an organic–metal (or metal oxide) bilayer [4, 5], an organic–organic bilayer [6, 7], a bulk heterojunction [8], or a hybrid interconnector layer [9, 10]. In those CGLs, organic heterojunction (OHJ) CGLs were widely used in tandem OLEDs for their good light transmittance and technological compatibility with OLEDs. To deeply understand the working mechanism of CGLs, the Ultraviolet photoelectron spectroscopy (UPS) and X-ray photoelectron spectroscopy (XPS) technology were used to analyze the working mechanism of CGLs, on the other hand, many theoretical models were proposed to explain the working mechanism of CGLs. Such as the thermally assisted charge generation mode was used to express the working mechanism of transition metal oxides (TMOs) CGLs [11]. Fowler–Nordheim model has been introduced to explain the tunneling process for charge generation in the organic heterojunction CGLs [12]. Kleemann et al. introduced the Zener tunneling model to simulate the I–V characteristics of a homojunction under reverse voltage [13]. Sun et al. used the same model to explain the charge generation process of the HAT-CN/m-MTDATA heterojunction under reverse bias [14]. In this paper, we designed a series of devices and obtained the devices current density generated by the OHLs CGLs. By numerical analysis methods, we found the working mechanism of OHJs charge generation layers is in accord with quantum tunneling; the results obtained in this work can help us to deeply understand the working mechanism of OHC layer.

## 2 Experiments

The OHJs always are made up of two kinds of organic thin film, one is p-typed organic materials, and another is n-typed organic materials, such as F16CuPc/CuPc, C<sub>60</sub>/Pentacene, C<sub>60</sub>/ZnPc, C<sub>60</sub>/H2Pc, and C<sub>60</sub>/Thiophenes. In order to indicate the OHJ layer

can effectively generate current and obtain the current density only generated by the OHJ layers, several devices were fabricated, as shown in Fig. 1. All materials used in this work have purity higher than 99% and the active area of each device is  $0.09 \text{ cm}^2$  ( $3 \text{ mm} \times 3 \text{ mm}$ ). All devices were grown on clean glass substrates with a 100 nm thick layer of ITO with a sheet resistance of 10 per square, and a thermally deposited Al film was used as the cathode. ITO substrates were ultrasonically cleaned in acetone, ethanol, and deionized water successively, then treated by  $\text{O}_2$  plasma at the pressure 42 Pa for 10 min, at last, directly placed into vacuum chamber without exposing air. All the films were thermally evaporated in a UHV growth chamber without breaking vacuum. Organic thin films were thermally evaporated in a UHV growth chamber at a base pressure of around  $1.5 \sim 1.9 \times 10^{-7}$  Torr. The cathode Al film was thermally evaporated at a base pressure of around  $2 \times 10^{-6}$  Torr. The evaporation rate was controlled with a quartz thickness monitor. For organic and Al materials are  $1 \sim 1.3 \text{ A/s}$  and  $3 \text{ A/s}$ , respectively. The current density–voltage characteristics of the devices were measured using a Keithley 2450 source measure unit at room temperature in air after the device fabrication immediately.

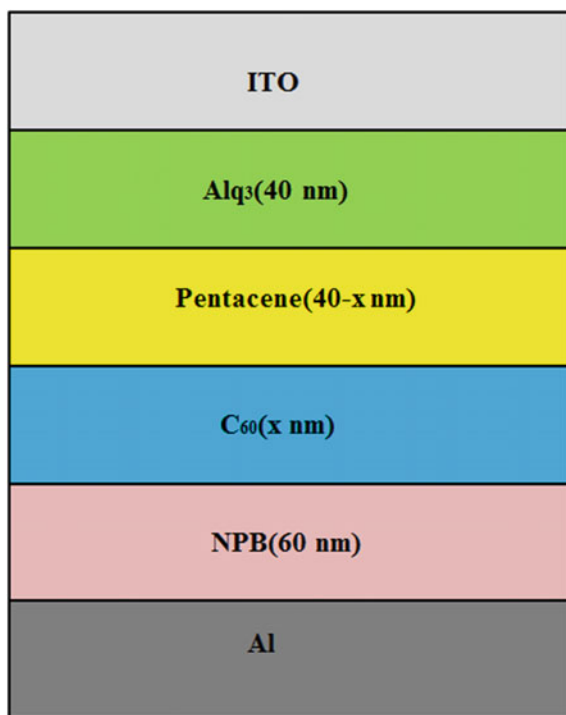


**Fig. 1** Structure of devices

### 3 Results and Discussion

Figure 2 is the J–V characteristic of devices. Table 1 shows the parameters of all organic materials used in this work. We can see from Table 1 that the electron mobility is higher than the hole mobility in Alq<sub>3</sub>, and the hole mobility is higher than electron mobility in NPB, so the Alq<sub>3</sub> and NPB are considered as electron transport and hole transport materials, respectively. On the other hand, when upon applying the voltage, the holes need overcome a barrier about 0.5 eV when injected from anode ITO into Alq<sub>3</sub>, and the electrons need overcome a barrier about 0.8 eV when injected from cathode Al into NPB, so due to the high-injection barrier (holes injected from anode into Alq<sub>3</sub> thin film layer and electrons injected into NPB thin film layer) and very low carrier mobility (hole transport in Alq<sub>3</sub> thin film and electron transport in NPB thin film), the device with the structure of ITO/Alq<sub>3</sub>/NPB/Al (device 1) has very little current density under an applied voltage even approached to 20 V. When inserting an organic thin film (C<sub>60</sub> or Pentacene (device 2 and device 3, respectively)) with the thickness of 40 nm into the interface of NPB/Alq<sub>3</sub>, the device current density is almost same with above device 1. This situation was changed when inserting a OHJ layer (C<sub>60</sub> (15 nm)/Pentacene (25 nm)) into the interface of NPB/Alq<sub>3</sub> (device 4), the current density can be greatly improved compared with device 1, device 2 and device 3. Those results show that OHJ layer (C<sub>60</sub> (15 nm)/Pentacene (25 nm)) thin film is an essential to the charge generation and separation process in device. According to above analysis, we can deduce that the devices current density of device 4 can be attributed to the OHC layer.

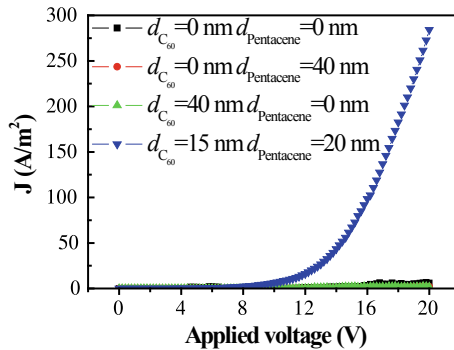
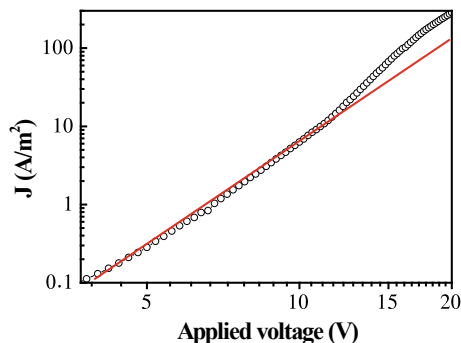


Fig. 2 J–V characteristic of devices

Figure 3 shows the J–V characteristics of device 4 in the double logarithmic coordinate plot, we can see the relationship between device current density and applied voltage is nearly linear when the applied voltage lower than 12 V, and deviated linear relationship when applied voltage over 12 V, the reason of deviated can be attributed to that, which is a strong hint that the charge generation and injection process is a



**Fig. 3** J–V curves of device 2 in the double logarithmic coordinates

tunneling process. The Fowler–Nordheim (F–N) tunneling model proposed by Fowler and Nordheim [15] was used to express this mechanism:

$$I \propto E^2 \exp\left(\frac{k}{E}\right) \tag{1}$$

**Table 1** Parameters of materials

Material	Electron mobility (cm <sup>2</sup> V <sup>-1</sup> s <sup>-1</sup> )	Hole mobility (cm <sup>2</sup> V <sup>-1</sup> s <sup>-1</sup> )	HOMO (eV)	LUMO (eV)
NPB	6.1 × 10 <sup>-6</sup>	6.1 × 10 <sup>-4</sup>	5.5	2.4
Alq <sub>3</sub>	1.0 × 10 <sup>-6</sup>	2.0 × 10 <sup>-8</sup>	5.7	3.1
C <sub>60</sub>	8.5 × 10 <sup>-2</sup>		6.42	4.12
CuPc		2.4 × 10 <sup>-4</sup>	4.81	2.92

where  $I$  is the current,  $E$  is the electric field intensity,  $k$  is a constant which is related to the height of the tunneling barrier. We can obtain the following relation according to Eq. (1),

$$\ln\left(\frac{J}{E^2}\right) \propto \ln\left(\frac{1}{E}\right) \tag{2}$$

We can see from Eq. (2) that the relationship between  $\ln(J/E^2)$  and  $\ln(1/E^2)$  is linear. Figure 4 shows the experimental results of  $\ln(J/E^2)$  and  $\ln(1/E^2)$ , which is in line with the Eq. (2), it demonstrated that the working mechanism of organic heterojunction CGL is in line with Fowler–Nordheim (F–N) tunneling.

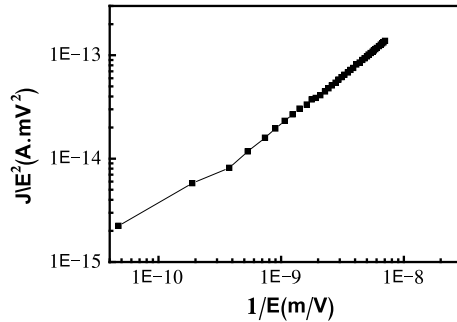


Fig. 4  $J/E^2$ – $1/E$  curves of device 2 in the double logarithmic coordinates plot

## 4 Conclusions

By design series of devices, we found that the OHJ layer with the structure of  $C_{60}$  (15 nm)/Pentacene (25 nm) can effectively generate charges, and the device current density of device 4 can be attributed to the OHC layer ( $C_{60}$  (15 nm)/Pentacene (25 nm)). By numerically analyzing the current–voltage ( $J$ – $V$ ) characteristics of devices, the results showed the charge generation mechanism of organic heterojunction was in accord with quantum tunneling process. The obtained results can help ones deeply understand the working mechanism of organic heterojunction charge generation layer and fabricate high-efficiency OLEDs.

**Acknowledgements.** This work was supported by the National Natural Science Foundation of China (61665010, 11464040, 11764035, 61461046, 61465012), the National Natural Science Foundation of Gansu Province (18JR3RE242) and the ‘QinLan’ Talent Engineering Fund by Tianshui Normal University.

## References

1. Van Slyke, S.A., Chen, C.H., Tang, C.W.: Organic electroluminescent devices with improved stability. *Appl. Phys. Lett.* **69**(15), 2160–2162 (1996)
2. Chang, C.C., Hwang, S.W., Chen, C.H.: High-efficiency organic electroluminescent device with multiple emitting units. *Jpn. J. Appl. Phys.* **43**, 6418 (2004)
3. Chang, C.C., Chen, J.F., Hwang, S.W.: Highly efficient white organic electroluminescent devices based on tandem architecture. *Applied Physics Letters* **87**(25), 253501–253501-3 (2005)
4. Chang, C.C., Hwang, S.W., Chen, C.H.: High-efficiency organic electroluminescent device with multiple emitting units. *Jpn. J. Appl. Phys.* **43**, 6418 (2004)
5. Zhang, H., Dai, Y., Ma, D.: High efficiency tandem organic light-emitting devices with  $Al/WO_3/Au$  interconnecting layer. *Appl. Phys. Lett.* **91**(12), 123504–123504-3 (2007)
6. Kang, S.J., Yi, Y., Kim, C.Y.: Energy level diagrams of  $C_{60}$ /pentacene/Au and pentacene/ $C_{60}$ /Au. *Synth. Met.* **156**(1), 32–37 (2006)
7. Guo, F., Ma, D.: White organic light-emitting diodes based on tandem structures. *Appl. Phys. Lett.* **87**(17), 173510–173510-3 (2005)

8. Chen, Y., Chen, J., Ma, D.: High power efficiency tandem organic light-emitting diodes based on bulk heterojunction organic bipolar charge generation layer. *Appl. Phys. Lett.* **98** (24), 243309-243309-3 (2011)
9. Xiao, J., Wang, X.X., Zhu, H.: Efficiency enhancement utilizing hybrid charge generation layer in tandem organic light-emitting diodes. *Appl. Phys. Lett.* **101**(1), 013301-013301-4 (2012)
10. Yang, J.P., Bao, Q.Y., Xiao, Y.: Hybrid intermediate connector for tandem OLEDs with the combination of MoO<sub>3</sub>-based interlayer and p-type doping. *Org. Electron.* **13**, 2243–2249 (2012)
11. Qi, X., Li, N., Forrest, S.R.: Analysis of metal-oxide-based charge generation layers used in stacked organic light-emitting diodes. *J. Appl. Phys.* **107**(1), 014514-014514-8 (2010)
12. Kröger, M., Hamwi, S., Meyer, J.: Temperature-independent field-induced charge separation at doped organic/organic interfaces: experimental modeling of electrical properties. *Phys. Rev. B* **75**(23), 235321 (2007)
13. Kleemann, H., Gutierrez, R., Lindner, F.: Organic Zener diodes: tunneling across the gap in organic semiconductor materials. *Nano Lett.* **10**(12), 4929–4934 (2010)
14. Sun, H., Guo, Q., Yang, D.: High efficiency tandem organic light emitting diode using an organic heterojunction as the charge generation layer: an investigation into the charge generation model and device performance. *ACS Photonics* **2**(2), 271–279 (2015)
15. Guo, Q., Sun, H., Wang, J.: Charge generation mechanism of tandem organic light emitting diodes with pentacene/C70 organic 15 heterojunction as the connecting layer. *J. Mater. Chem. C* **4**(2), 376–382 (2016)



# Experimental Research and Theoretical Study of Cesium, Oxygen Activation on Defect AlGaN (0001) Surface

Zesen Liu, Liang Chen<sup>(✉)</sup>, Shuqin Zhang, Qingyang Meng, Zhenhuan Gu, and Jing Hua

College of Optical and Electronic Technology, China Jiliang University,  
Hangzhou, People's Republic of China  
lzs15957134979@163.com

**Abstract.** We carry out the Cs, O activation experiment of AlGaN photocathodes and find the photocurrent is different from that of AlGaAs in the Cs, O coadsorption stage of activation. This is mainly due to there are dimers and trenches on the surfaces of AlGaAs photocathodes, and they provide enough position for Cs, O atoms to attach. Then pure surface model and the other two defect surface models with Ga or N vacancy are built. The result shows that the work function on the defect surface will have a significant decline at the stage of O adsorption. Thus, the photocurrent of AlGaN with defect surface will increase obviously at the second activation stage which is consistent with our experiment.

**Keywords:** Activation experiment · Defect AlGaN photocathodes · Work function

## 1 Introduction

There are many studies of alkali-metal adsorption on solid surfaces have been reported over the last decade. The AlGaN-based photocathodes are currently attracting great interest due to their potential application in ultraviolet regions [1]. Cs, O coadsorption is the most popular method for activation of III-V semiconductor photocathodes to obtain negative electron affinity (NEA) [2–4]. Many experimental researches show that Cs, O coadsorption on AlGaN surfaces will result in a lower work function and a higher photocurrent when the Cs source and the O source enter in the correct order. Yo-Yo activation method was widely applied, in which the activation procedure consists of two stages. The first stage is Cs-only activation, and the second stage is Cs, O coadsorption [5]. Many Cs activations show that there will appear a phenomenon called ‘Cs-kill’ when the surface is over-cesiated [6, 7]. However, this will not appear in the Cs activation experiments of GaAs and AlGaAs photocathodes.



It is known that GaAs and AlGaAs have a zinc blende structure while GaN and AlGaN are wurtzite structure. There are many studies on the surface morphology of GaAs and AlGaAs [8, 9], so we can find that there are dimers and trenches on the surfaces of GaAs and AlGaAs photocathodes. The surfaces of GaN and AlGaN are smooth, which cannot provide enough space for Cs, O atoms to attach. Previous study [10] have reported that the photocurrent increases 4–5 times at the second activation stage for GaAs and AlGaAs photocathodes, while it rises slightly for GaN and AlGaN photocathodes. In order to make an effective Cs activation experiment, firstly, we conducted a Cs, O activation comparison experiment between AlGaN photocathode and AlGaAs photocathode. Secondly,  $\text{Al}_{0.25}\text{Ga}_{0.75}\text{N}$  (0001) surface models with Ga and N vacancy defects were built. Then, we make a comparison of Cs, O coadsorption between clean  $\text{Al}_{0.25}\text{Ga}_{0.75}\text{N}$  (0001) surface models and surface models with vacancy defects.

## 2 Cs/O Coadsorption Activation Experiments

We have carried out the Cs, O coadsorption on AlGaN photocathode experiment. For this activation experiment, the samples were grown by metal organic chemical vapor deposition (MOCVD) on sapphire substrates. In order to decrease the lattice mismatch, a 150 nm AlN buffer layer was added. For the AlGaN emission layer, the best Al component is 0.25, while the final Al component of the sample is 0.24 because of the error in the process of epitaxial growth. And the thickness of  $\text{Al}_{0.24}\text{Ga}_{0.76}\text{N}$  emission layer is 150 nm. To keep high symmetry and simplify the calculation, the Al component in theoretical models is set as 0.25, which is close to the experiment sample.

The AlGaN photocathodes activation and evaluation system is established, the diagrammatic sketch is shown in Fig. 1. The ultra-high vacuum activating unit is used for Cs, O coadsorption activation experiment, and the NEA AlGaN photocathode was obtained. Photocurrent and spectral response are detected by multi-information online monitoring system. The quadruple mass spectrometer (QMS) system is used to analyze the composition of residual gas after activation experiment. The surface analysis system is composed of XPS [11] and UPS, which aim to detect the surface information.

In this article, we adopt the standard activation method called ‘yo-yo’ activation method to perform the experiment. The experimental process is as follows: reaction of Cs source with AlGaN sample at room temperature until a maximum photocurrent is obtained. Cs atoms deposition continues under a constant Cs source, and O source is not admitted into the chamber until the photocurrent stops increasing. When the photocurrent gets a new peak, re-enter the Cs source and close the O source, and the photocurrent drops again in Cs atmosphere, then the O source is opened again. When there is no significant increase between the present photocurrent peak and the previous one, the activation experiment is ended, while the activation experiment usually ends with a short time of exposure to Cs vapor.

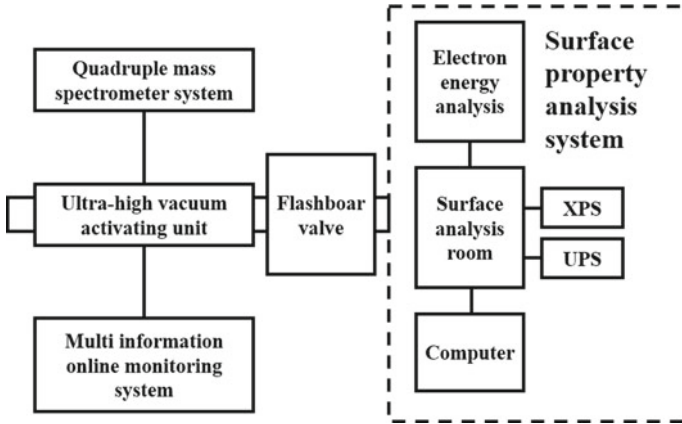


**Fig. 1** AlGaIn photocathodes activation and evaluation system

The photocurrent detected by multi-information online monitoring system is shown as Fig. 2a. And the photocurrent of AlGaAs photocathode prepared by Chen et al. [2] was shown in Fig. 2b. At Cs-only activation stage, it can be found the photocurrent increases with the increase of Cs activation time for both photocathodes. And the AlGaIn photocurrent peak (631.83 nA) appears at 27 min while the AlGaAs photocurrent peak (579.52 nA) appears at 22 min. For Cs, O alternate activation stage, the photocurrent of AlGaAs photocathode has a significant increase when compared with AlGaIn photocathode. By contrast experiments, we get that both AlGaIn and AlGaAs photocathodes have a consistent activation efficiency at Cs-only activation stage. While the activation efficiency of AlGaIn photocathode at the second stage is much lower than that of AlGaAs photocathodes.

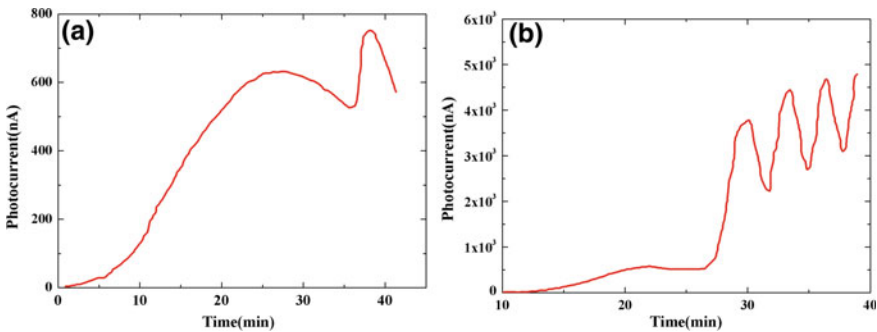


**Fig. 2** Photocurrents as function of activation time. **a** AlGaIn photocathode, **b** AlGaAs photocathode

### 3 Models and Methods

In this paper, all calculation methods are implemented from the software package Cambridge sequential total energy package (CASTEP). Density functional theory-general gradient approximate (DFT-GGA) [12] framework with the pseudopotential plane wave method was used in the calculations. Geometry optimizations were undergone using Broyden–Fletcher–Goldfarb–Shanno (BFGS) algorithm before total energy calculations. After a series of convergence tests, the plane wave cut-off energy was taken as 700 eV; a  $7 \times 7 \times 1$  Monkhorst-Pack  $k$  point grid was used to sample the Brillouin zone (BZ) of the surface. Ultrasoft pseudopotentials (USP) [13] were used for all atomic species, and nonlinear core corrections (NLCC) [14] were adopted for Ga atoms.

Three surface models were built based on optimized bulk supercells (shown as Fig. 3), consisting of cleaning surface model (Fig. 3a), Ga vacancy (Fig. 3b) and N vacancy (Fig. 3c). The defective surface was obtained by removing a Ga/N atom from the clean AlGaN (0001) surface. The clean surface and surfaces with defects were all simulated with periodically repeating supercells of eight AlGaN slab layers separated by vacuum regions. Nitrogen dangling bonds were saturated with a layer of fractionally charged pseudohydrogen.

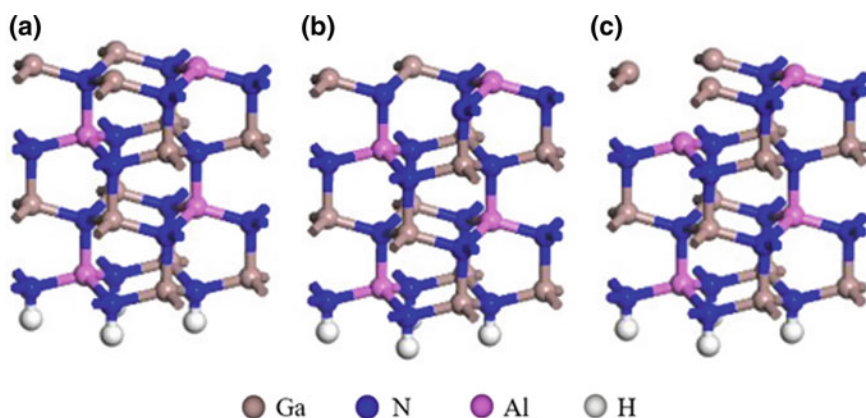


**Fig. 3** **a** Clean AlGaN (0001) surface model, **b** Ga-defect surface model, **c** N-defect surface model

### 4 Work Function and Dipole Moment

The photoemission of NEA photocathodes performed to follow a ‘three-step-model’ proposed by Spicer et al. [15], including photon adsorption, electrons heating and escape into the vacuum. The QE of photocathodes is closely related to the escape probability of photoelectron, and the work function is the minimum energy that electrons need to escape into the vacuum. Therefore, the lower work function is necessary for AlGaN photocathodes materials. The work function can be expressed as [16]:

$$\phi = E_{\text{vac}} - E_{\text{F}} \quad (1)$$

where  $E_{\text{vac}}$  and  $E_{\text{F}}$  represent the vacuum level and the surface Fermi level, respectively. Figure 4 shows the work function values of  $\text{Al}_{0.25}\text{Ga}_{0.75}\text{N}$  photocathode with different  $\theta_{\text{Cs}}$ . The results indicating that the clean  $\text{Al}_{0.25}\text{Ga}_{0.75}\text{N}$  (0001) surface obtains the lowest work function (1.855 eV) when the  $\theta_{\text{Cs}}$  is 0.5 ML, but with the further increase of  $\theta_{\text{Cs}}$ , the work function will increase slightly. This ‘Cs-kill’ phenomenon is mainly because the adjacent Cs atoms share electrons more easily than transfer electrons to surface.

In order to study the effect of Cs, O coadsorption activation on defect  $\text{Al}_{0.25}\text{Ga}_{0.75}\text{N}$  (0001) surface, we have set up three sets of control experiments. They are ‘1 ML Cs adatoms’, ‘1 ML Cs and 0.25 ML O adatoms’ and ‘1 ML Cs and 0.5 ML O adatoms’,

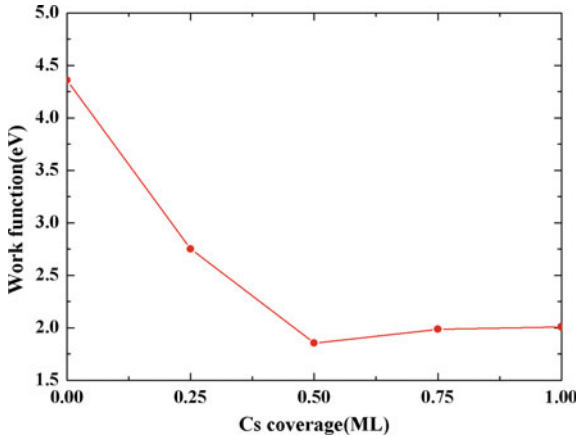


**Fig. 4** Work function of Cs adsorption on clean AlGaN (0001) surface with different  $\theta_{\text{Cs}}$

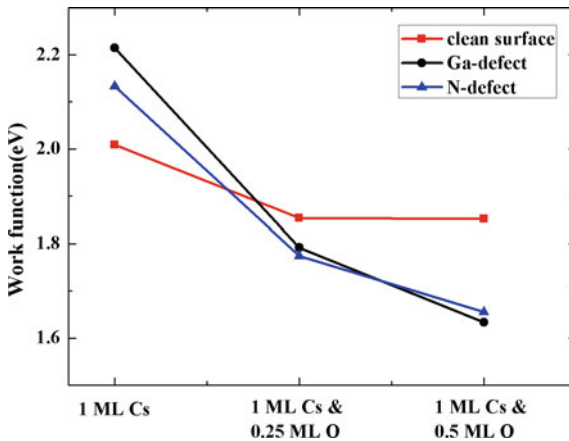


**Fig. 5** Work function of 1 ML Cs, 1 ML Cs and 0.25 ML O adatoms and 1 ML Cs and 0.5 ML O adatoms adsorption on clean and defect  $\text{Al}_{0.25}\text{Ga}_{0.75}\text{N}$  (0001) surface

respectively. The result is shown in Fig. 5. It can be found that it has a significant influence on lowering work function when O atoms adsorption on over-cesiated  $\text{Al}_{0.25}\text{Ga}_{0.75}\text{N}$  (0001) surface. For clean  $\text{Al}_{0.25}\text{Ga}_{0.75}\text{N}$  (0001) surface, the decrease trend of work function becomes slower with the increase of  $\theta_{\text{O}}$ . But for defect surface, the decrease of work function is still obvious with the increase of  $\theta_{\text{O}}$ . And this difference between clean surface and defect surface can be explained by Cs-O dipole moments.

The schematic diagram of Cs induced single dipole moment and Cs, O induced double dipole moments is shown in Fig. 6.

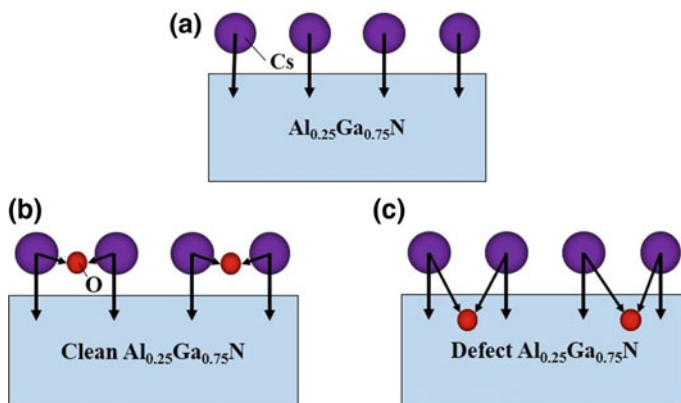


**Fig. 6** Schematic diagram of Cs induced single dipole moment (a) and Cs, O induced double dipole moments (b, c)

From Fig. 6a, Cs induced single dipole moment Cs- $\text{Al}_{0.25}\text{Ga}_{0.75}\text{N}$  is perpendicular to  $\text{Al}_{0.25}\text{Ga}_{0.75}\text{N}$  (0001) surface and it is oriented to substrate, so Cs- $\text{Al}_{0.25}\text{Ga}_{0.75}\text{N}$  dipoles are helpful for lowering work function. From Fig. 6b, it can be found that the Cs-O dipoles are almost parallel to clean  $\text{Al}_{0.25}\text{Ga}_{0.75}\text{N}$  (0001) surface, and they will be neutralized because they are oriented to every direction along the surface. So, O adsorption on clean  $\text{Al}_{0.25}\text{Ga}_{0.75}\text{N}$  (0001) surface just makes a little change on the work function of the surface. But for defect  $\text{Al}_{0.25}\text{Ga}_{0.75}\text{N}$  (0001) surface, there is a position for O adatom to locate. So O adatom is below Cs atom, and Cs-O dipole is oriented to substrate. The difference of lowering work function at the stage of O adsorption is mainly due to the Ga or N vacancy defect on  $\text{Al}_{0.25}\text{Ga}_{0.75}\text{N}$  (0001) surface.

## 5 Conclusion

In this paper, the Cs, O activation experiment for AlGaN photocathodes was carried out. We get that both AlGaN and AlGaAs photocathodes have a consistent activation efficiency at Cs-only activation stage. While the activation efficiency of AlGaN photocathode at Cs, O coadsorption activation stage is much lower than that of AlGaAs photocathode. Besides, the first principle calculations of Cs, O coadsorption on clean and defect  $\text{Al}_{0.25}\text{Ga}_{0.75}\text{N}$  (0001) surfaces were performed. For Cs-only activation stage,

the calculated work function decreases when  $\theta_{\text{Cs}}$  is from 0 to 0.5 ML, while it has a slight increase when  $\theta_{\text{Cs}}$  reaches 0.75 ML. For Cs, O coadsorption activation stage, O adsorption on the clean surface has less influence on work function than defect surface. This is mainly because the Cs-O dipole is parallel to clean  $\text{Al}_{0.25}\text{Ga}_{0.75}\text{N}$  (0001) surface, which is ineffective to lower work function. However, there exist vacancy positions on defect surface, so O atom will locate the position and form Cs-O *dipoles* which are perpendicular to the defect  $\text{Al}_{0.25}\text{Ga}_{0.75}\text{N}$  (0001) surface. While the work function on the defect surface will have a significant decline at the stage of O adsorption, and the photocurrent will increase obviously at the second activation stage. We can prepare defective AlGaN surface structure, and it will be an important issue to improve the quantum efficiency of AlGaN photocathodes.

**Acknowledgements.** This work was supported by the National Natural Science Foundation of China under Grant Nos. 61775203, 61308089 and 6144005, the National Key Research and Development Program of China under Grant No. 2017YFF0210800. The work was also supported in part by the National Science Foundation of the United States under Grant ECCS-1254902. We particularly appreciated Meishan Wang of School of Information and Electrical Engineering, Ludong University for first principle calculations.

## References

1. Muth, J.F., Brown, J.D., Johnson, M.A.L., Yu, Z., Kolbas, R.M., Cook, J.W., Schetzina J.F.: Absorption coefficient and refractive index of GaN, AlN and AlGaN alloys. *MRS Proc.* **537**, G5.2 (1998)
2. Chen, X., Hao, G., Chang, B., Zhang, Y., Jin, M.: Stability of negative electron affinity  $\text{Ga}_{0.37}\text{Al}_{0.63}\text{As}$  photocathodes in an ultrahigh vacuum system. *Appl. Opt.* **52**(25) (2013)
3. Wang, X., Chang, B., Ren, L., Gao, P.: Influence of the p-type doping concentration on reflection-mode GaN photocathode. *Appl. Phys. Lett.* **98**(8), 082109 (2011)
4. Chen, X., Jin, M., Zeng, Y., Hao, G., Cheng, H.: Effect of Cs adsorption on the photoemission performance of GaAlAs photocathode. *Appl. Opt.* **53**(32), 7709–7715 (2014)
5. Turnbull, A.A., & Evans, G.B.: Photoemission from GaAs-Cs-O. *J. Phys. D Appl. Phys.* (1968)
6. Hao, G., Yang, M., Chang, B., Chen, X., Zhang, J., Fu, X.: Attenuation performance of reflection-mode AlGaN photocathode under different preparation methods. *Appl. Opt.* **52** (23), 5671 (2013)
7. Rodway, D.C., Allenson, M.B.: In situ surface study of the activating layer on GaAs (Cs, O) photocathodes. *J. Phys. D Appl. Phys.* **19**(7), 1353–1371 (1986)
8. Labella, V.P., Yang, H., Bullock, D.W., Thibado, P.M., Kratzer, P., Scheffler, M.: Atomic structure of the GaAs (001)-(2 × 4) surface resolved using scanning tunneling microscopy and first-principles theory. *Phys. Rev. Lett.* **83**(15), 2989–2992 (1999)
9. Hashizume, T., Xue, Q.K., Zhou, J., Ichimiya, A., Sakurai, T.: Structures of As-rich GaAs (001)-(2 × 4) reconstructions. (1994)
10. Yi Jun, Z., Ji Jun, Z., Xiao Hui, W., Ben Kang, C., Yun Sheng, Q., Jun Ju, Z., Pin, G.: Comparison of the photoemission behaviour between negative electron affinity GaAs and GaN photocathodes. *Chin. Phys. B* **20**(4), 048501 (2011)
11. Kočan, M., Rizzi, A., Lüth, H., Keller, S., Mishra, U.K.: Surface potential at as-grown GaN (0001) MBE layers. *physica status solidi (b)* **234**(3), 5 (2002)

12. Hammer, B., Morikawa, Y., Nørskov, J.K.: CO chemisorption at metal surfaces and overlayers. *Phys. Rev. Lett.* **76**(12), 2141–2144 (1996)
13. Kresse, G.J., Joubert, D.P.: From ultrasoft pseudopotentials to the projector augmented-wave method. *Phys. Rev. B* **59**(3), 1758–1775 (1999)
14. Louie, S.G., Froyen, S., Cohen, M.L.: Nonlinear ionic pseudopotentials in spin-density-functional calculations. *Phys. Rev. B* **26**(4), 1738–1742 (1982)
15. Spicer, William E., HerreraGomez, Alberto: Modern theory and applications of photocathodes. *Proc. SPIE-Int. Soc. Opt. Eng.* **18**(3), 245–246 (1993)
16. Rosa, A.L., Neugebauer, J.: First-principles calculations of the structural and electronic properties of clean GaN (0001), surfaces. *Phys. Rev. B* **73**(20), 591–596 (2006)



# Preparation of Er<sup>3+</sup>-Doped NaYF<sub>4</sub> and Its First-Principles Analysis

Qingyang Meng, Shuqin Zhang<sup>(✉)</sup>, Liang Chen, Zhenhuan Gu,  
Zesen Liu, and Jing Hua

College of Optical and Electronic Technology, China Jiliang University,  
Hangzhou, People's Republic of China  
532298184@qq.com

**Abstract.** Successfully prepared Er<sup>3+</sup>-doped NaYF<sub>4</sub> micron crystal by hydrothermal method. The experimental results show that the Er<sup>3+</sup>-doped NaYF<sub>4</sub> exhibits a strong up-conversion fluorescence emission. Er<sup>3+</sup>-doped NaYF<sub>4</sub> micron crystals exhibit strong green emission and can be used in phosphors and micro-optical devices. The energy band structure and electron density of NaYF<sub>4</sub> before and after doping were studied by first principle calculation. It is verified that NaYF<sub>4</sub> is a good up-conversion luminescent material, and the stability of Er<sup>3+</sup> ion is enhanced by doping.

**Keywords:** Glass ceramic · Rare earth ions · First-principles

## 1 Introduction

In recent years, rare-earth ion-doped up-conversion luminescent materials have been widely used in the fields of laser, optical communication, flat panel display and medical imaging and have attracted more and more attention and research. Sodium yttrium fluoride (NaYF<sub>4</sub>) is considered to be one of the most favorable substrates for up-conversion luminescence of rare-earth ions. This is mainly due to its small phonon energy, which is beneficial to the up-conversion luminescence of rare-earth ions [1, 2]. There are two phases in NaYF<sub>4</sub>: cubic phase and hexagonal phase. In cubic phase NaYF<sub>4</sub> ( $\alpha$ -NaYF<sub>4</sub>), Y<sup>3+</sup> ion only corresponds to one crystallographic lattice, while in  $\beta$ -NaYF<sub>4</sub>, Y<sup>3+</sup> ion has three crystallographic sites, so the luminescence intensity is improved effectively. The change of the crystal phase of the rare-earth ion-doped NaYF<sub>4</sub> will have certain influence on the luminescence ability of the material itself, so it is necessary to study the controllability of the crystal phase of the product. In this paper, Er<sup>3+</sup> is doped into NaYF<sub>4</sub>, and the first principle calculation is done on it [3, 4].



## 2 Experimental

### 2.1 Preparation Process

A certain amount of Y<sub>2</sub>O<sub>3</sub>, Er<sub>2</sub>O<sub>3</sub>, NH<sub>4</sub>HF<sub>2</sub> and NaF were sequentially added to the beaker, and then the nitrate solution was added to dissolve it, and the mixture was uniformly stirred. The NH<sub>4</sub>F solution was added to maintain the pH at 8. The prepared solution was placed in a Teflon-lined stainless steel reaction vessel with a filling degree of about 55%. The reaction vessel was placed in an oven and dried at 280 °C for 24 h. After allowing it to cool naturally, it was taken out, washed with deionized water, centrifuged and repeated 4 times. It was dried in an oven for 24 h, naturally cooled, placed in a muffle furnace and annealed at a temperature of 500 °C to obtain a product.

### 2.2 First Principle Calculation

In this paper, the influence of rare-earth ion Er<sup>3+</sup> on the crystal and electronic structure of NaYF<sub>4</sub> is calculated by first principle, adopting Castep Module in Material Studio 6.0 Software of NeoTrident Company.

When the model is established, Na and Y are arranged at intervals on the corresponding random occupancy grid points. Similarly, Na and vacancies are also arranged at intervals on the corresponding random occupancy grid points. The structural model constructed is shown in Fig. 1.

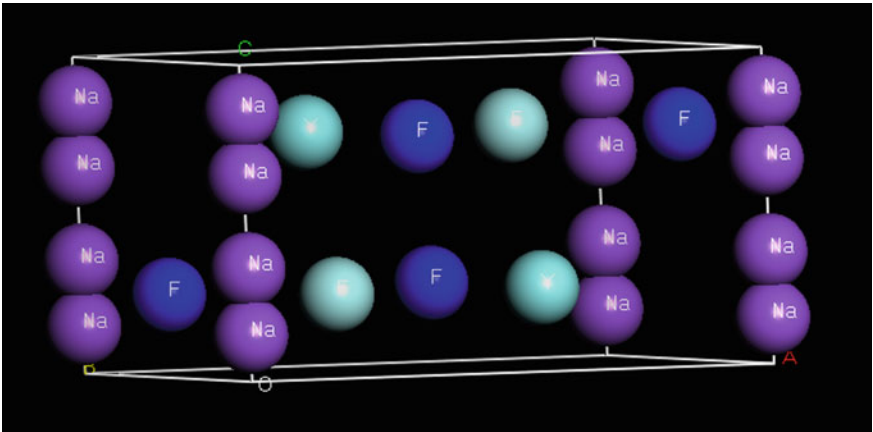


**Fig. 1** NaYF<sub>4</sub> structure model diagram

The interaction potential between electron and electron adopts generalized gradient approximation (GGA). The plane wave energy of the NaYF<sub>4</sub> system is 410 eV; the K point is set to  $5 \times 5 \times 4$ ; the pseudopotential selects the super-soft pseudopotential; the energy convergence criterion of the atom is  $5 \times 10^{-6}$  eV/atom; and the convergence criterion of the interaction force between atoms is 0.01 eV/Å. The internal stress

convergence criterion is 0.02 GPa, and the maximum displacement convergence criterion is  $5 \times 10^{-4}$  Å.

Then, the  $Y^{3+}$  ion doped in the  $NaYF_4$  is replaced with an  $Er^{3+}$  ion. The  $NaYF_4$  structure constructed above is a unit cell and is replaced by a  $2 \times 2 \times 1$  supercell after doping, as shown in Fig. 2.

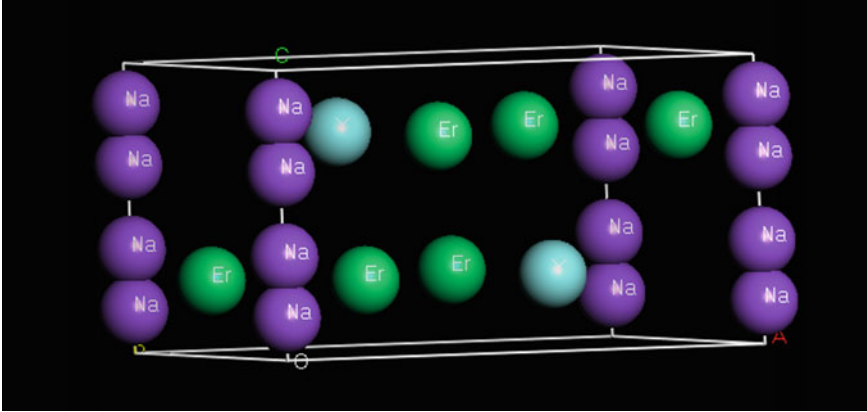


**Fig. 2**  $NaYF_4$  structure model doped with  $Er^{3+}$  ions

The plane wave energy of the  $Er^{3+}$  ion doped in the  $NaYF_4$  system is 410 eV; the K point is set to  $2 \times 2 \times 4$ ; the pseudopotential selects the super-soft pseudopotential; the energy convergence criterion of the atom is  $5 \times 10^{-6}$  eV/atom; and the convergence criterion of the interaction force between atoms is 0.01 eV/Å. The internal stress convergence criterion is 0.02 GPa, and the maximum displacement convergence criterion is  $5 \times 10^{-4}$  Å.

### 3 Results and Discussions

#### 3.1 Band Structure Analysis

After  $Er^{3+}$  doping, the  $Er^{3+}$  impurity level is formed in the forbidden band of  $NaYF_4$ . The valence band top and the conduction band bottom are located in the Brillouin zone, which is a direct bandgap semiconductor. The Fermi level is at the impurity level. After  $Er^{3+}$  doping, the forbidden bandwidth of  $NaYF_4$  is smaller than that of the eigenstate  $NaYF_4$ , as shown in Fig. 3.

#### 3.2 Electron Density Analysis

The electron density of states (PDOS) diagram of the intrinsic state  $NaYF_4$  and  $Er^{3+}$  doped  $NaYF_4$  shows that the valence bands of the two groups are roughly composed of three parts. The undoped ones are the bottom valence band of  $-95$  to  $-92$  eV, the

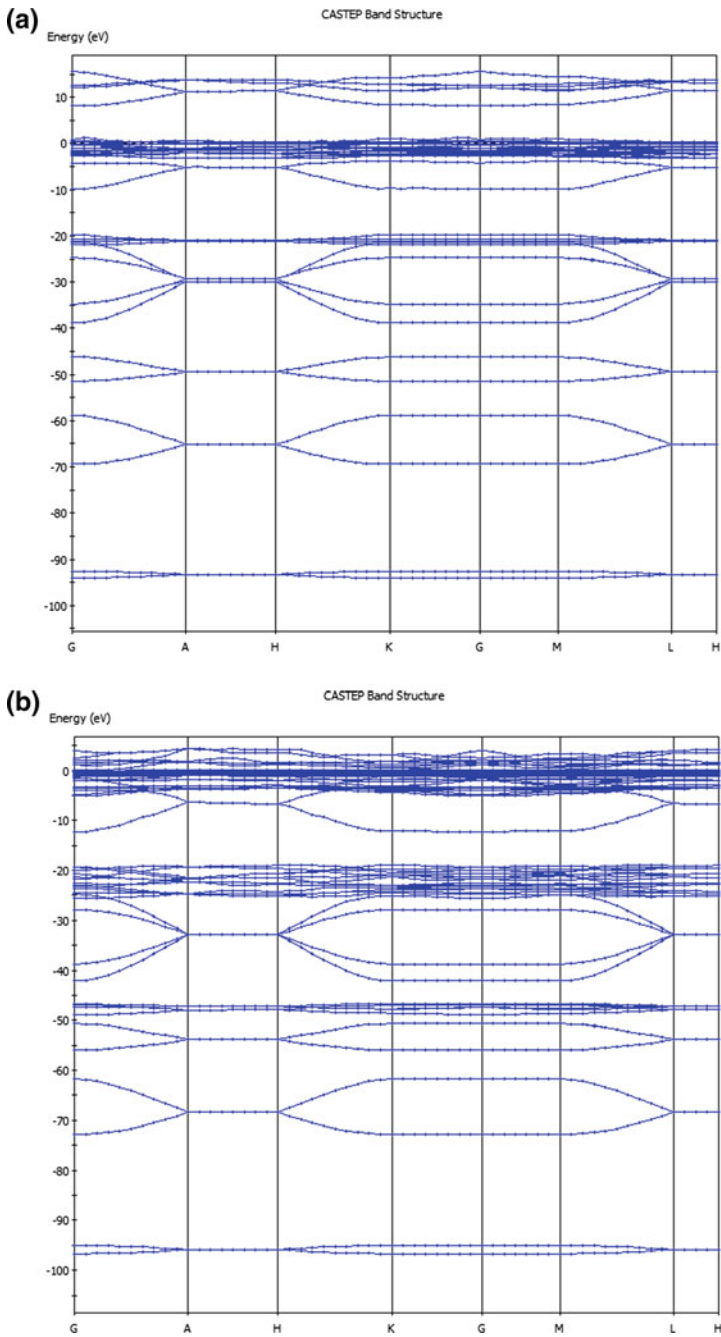


**Fig. 3** **a**  $\text{NaYF}_4$  band structure diagram before  $\text{Er}^{3+}$  doping, **b**  $\text{NaYF}_4$  band structure diagram after  $\text{Er}^{3+}$  doping

lower valence band of  $-70$  to  $-19$  eV and the upper valence band of  $-10$  to  $2$  eV. The  $\text{NaYF}_4$  doped with  $\text{Er}^{3+}$  is the bottom valence band of  $-97$  to  $-94$  eV, the lower valence band of  $-74$  to  $-19$  eV and the upper valence band of  $-12$  to  $4$  eV. The conduction band is in the range of  $7$ – $16$  eV [5]. But there is a big difference between the two in Fermi level, The Fermi level of doped  $\text{NaYF}_4$  is  $25$  eV, while that of doped  $\text{NaYF}_4$  is  $75$  eV, as shown in Fig. 4. After doping with  $\text{Er}^{3+}$ , the band gap of  $\text{NaYF}_4$  decreases, the impurity energy level is formed, and the electron excited transition energy is reduced. Therefore,  $\text{Er}^{3+}$  element can improve the photocatalytic performance of  $\text{NaYF}_4$ .

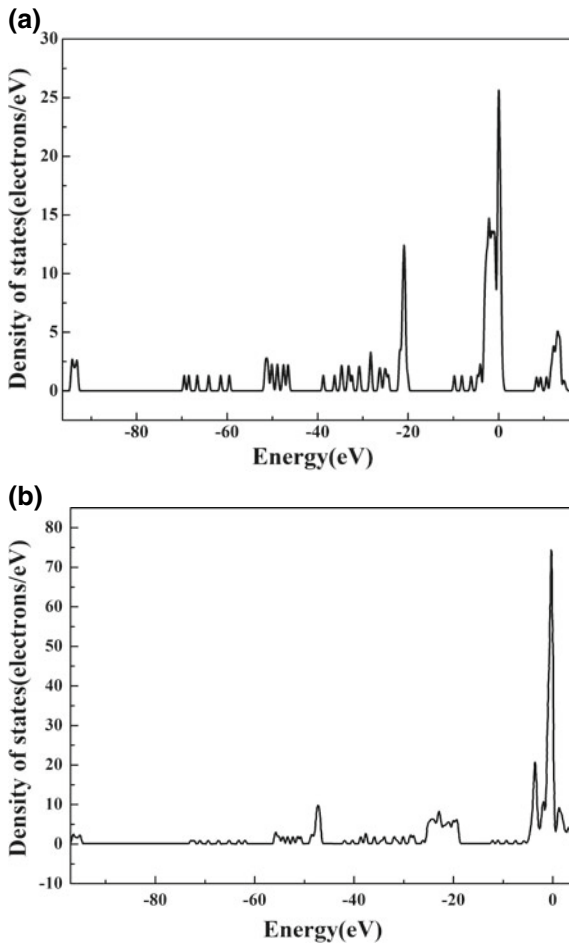


**Fig. 4** **a**  $\text{NaYF}_4$  electron density analysis before  $\text{Er}^{3+}$  doping, **b**  $\text{NaYF}_4$  electron density analysis after  $\text{Er}^{3+}$  doping

The bottom valence band of NaYF<sub>4</sub> is mainly contributed by the 2s orbital electrons of Na. The peak type of the valence band is sharp and the electron localization is strong, and it does not bond with other electrons. Therefore, the influence of this valence band on the overall properties of the material is relatively small. The lower valence band is mainly contributed by the 2s orbital electron of F and the 2p orbital electron of Na, and there is resonance between the 2s orbital of F and the 2p orbital of Na, which indicates that the orbital hybrid effect occurs between the 2s orbital of F and the 2p orbital of Na. The upper valence band is mainly contributed by the 2p orbital electrons of F and the 4d orbital electrons of Y, and the corresponding orbital hybridization effect is also found between them. The 2p orbital of F is widened to some extent, which indicates that it has strong delocalization and important contribution to the bonding of the system.

### 3.3 Cohesive Energy Analysis

Cohesive energy is a parameter that measures the interaction between aggregated substances. It refers to the energy required for condensed matter to eliminate the intermolecular force of gasification. Since the free atomic constituent compound is generally an exothermic process, the cohesive energy is usually a negative value, and the smaller the value, the more stable the material. The calculation method of cohesive energy is  $(EAB - nA \times EA - nB \times EB)/n_{\text{total}}$ , where EAB is the total energy of material AB, EA and EB are the energy of single A atom and B atom respectively, and nA and nB are respectively The number of A atoms and B atoms in the middle, and n<sub>total</sub> is the total number of atoms contained in the system [6].

The cohesive energy of NaYF<sub>4</sub> is -5.65 eV/atom, which is a better material for up-converting the luminescent substrate from the viewpoint of stability. After doping with Er<sup>3+</sup> ions, the cohesive energy of NaYF<sub>4</sub> became -5.69, indicating that Er<sup>3+</sup> enhanced its stability.

### 3.4 Population Analysis

In NaYF<sub>4</sub>, F is -0.54 valence, mainly at 2p orbital. Na loses 0.88 electrons. The number of electrons in each orbit is found to be mainly lost in 3s orbit, and Y is +1.28 valence. Its ability to lose electrons is stronger than that of Na, because it fails to lose all electrons, so it cannot reach +3 valence as shown in Table 1 [7].

**Table 1** Electron population of atoms in NaYF<sub>4</sub>

Atom	s	p	d	Total	Effective charge
F	1.93	5.59	0	7.75	-0.57
Na	2.09	6.01	0	8.15	0.88
Y	0.22	0.30	1.16	1.72	1.27

When NaYF<sub>4</sub> is doped into Er<sup>3+</sup>, the electrons are lost in the 6s orbit, the electrons also appear in the d orbital, and the electrons in the f orbit decrease, which is due to the transition of the 4f orbital in the doping process, as shown in Table 2.

**Table 2** Electron population of Er-doped NaYF<sub>4</sub>

Atom	<i>s</i>	<i>p</i>	<i>d</i>	<i>f</i>	Total	Effective charge
Er	2.28	5.85	1.10	11.09	20.37	1.46

Table 3 shows the overlapping population of NaYF<sub>4</sub>, Na-F is relatively pure, slightly larger than Y-F. The formation of Er-F covalent bond after doping into Er can prove that the stability of NaYF<sub>4</sub> is better than that of NaYF<sub>4</sub> doped with Er element.

**Table 3** Overlapping population of NaYF<sub>4</sub>

Bond	Overlapping population	Bond distance
Na-F	0.02	2.47
Y-F	0.22	2.42
Er-F	0.18	2.281

## 4 Conclusions

Er<sup>3+</sup>-doped NaYF<sub>4</sub> was successfully prepared by hydrothermal method. The energy band structure and electron density of NaYF<sub>4</sub> before and after doping were studied by first principle calculation. It is verified that NaYF<sub>4</sub> is a good up-conversion luminescent material, and the stability of Er ion is enhanced by doping.

## References

- Gusowski, M.A., Swart, H.C., Karlsson, L.S.: NaYF<sub>4</sub>: Pr<sup>3+</sup> nanocrystals displaying photon cascade emission. *Nanoscale* **4**(2), 541 (2012)
- Yao, G.: Semi-empirical and ab initio study of lanthanide and transition metal ions doped in hexagonal beta-NaYF<sub>4</sub>. *Dissertations & Theses—Gradworks* (2015)
- Grzechnik, A., Bouvier, P., Mezouar, M.: Hexagonal Na<sub>1.5</sub>Y<sub>1.5</sub>F<sub>6</sub>, at high pressures. *J. Solid State Chem.* **165**(1), 159–164 (2002)
- Zhang, J.X.: *First-Principle Study on Rare Earth Doped Fluoride Up-Conversion Material and Its Preparation*. Yanshan University (2014)
- Szefczyk, B., Roszak, R., Roszak, S.: Structure of the hexagonal NaYF<sub>4</sub> phase from first-principles molecular dynamics. *Rsc Adv.* **4**(43), 22526–22535 (2014)
- Guangxian, X., Jimei, X.: *New Frontiers in Rare Earth Science and Applications*. Science Press (1985)
- Chen, M., Ma, Y., Li, M.: Facile one-pot synthesis of hydrophilic NaYF<sub>4</sub>:Yb, Er<sup>3+</sup>:NaYF<sub>4</sub>:Yb active-core/active-shell nanoparticles with enhanced up-conversion luminescence. *Mater. Lett.* **114**, 80–83 (2014)



# The Comparative Analysis of the LED and High-Pressure Sodium Lamp as Road Lighting

Jianming Huang<sup>1</sup>(✉), Lei Zhang<sup>1</sup>, Limin Hu<sup>1</sup>, Yanhua Han<sup>1</sup>,  
Mingzhong Xu<sup>1</sup>, Weipeng He<sup>1</sup>, Bin Ru<sup>1</sup>, Haiyong Chen<sup>1</sup>,  
Shaoqin Fu<sup>1</sup>, Yu Xia<sup>1</sup>, Yueming Yu<sup>1</sup>, Zhangwan Wang<sup>1</sup>, Qunjie Wu<sup>1</sup>,  
Yan Shi<sup>1</sup>, and Shiyu Wang<sup>2</sup>

<sup>1</sup> HANGZHOU HPWINNER OPTO CORPORATION, North 2F,  
No. 3 Building, No. 18 Kangzhong Road, Gongshu District, Hangzhou,  
Zhejiang, China  
hlm@hpwin.com

<sup>2</sup> College of Optical and Electronic Technology, China Jiliang University,  
Hangzhou, China

**Abstract.** This paper mainly studies the advantages and disadvantages of LED and high-pressure sodium lamp and further evaluates the development trend of public lighting systems by comparing the color temperature, color rendering index, fog permeability, energy efficiency and economic benefits of the two sources.

**Keywords:** LED · High-pressure sodium lamp · Color temperature · Color rendering index · Fog permeability · Energy efficiency · Economic benefits

## 1 Introduction

The public lighting systems occupy a large part of the total electrical energy. Currently, as two widely used light sources LED and high-pressure sodium lamp (HPS) need to be comprehensively analyzed.

## 2 The Color Temperature and Color Rendering Analysis

### 2.1 Color Temperature Selection

Different light has different color temperature. From the perspective of human vision, the low color temperature makes people warm and stable, while the high color temperature makes people calmness and refreshment.

From Table 1 [1], the color temperature value of the HPS ranges from 1950 to 2250 K, and people will only see the yellow light under the human vision. However, LED can create some light sources with different color temperatures, so it can offer more choice to road lighting.

**Table 1** Color temperature of some common light sources

Light sources	Color temperature (K)	Light sources	Color temperature
Candlelight	2000	Warm fluorescent lamp	2500–3000
High-pressure sodium lamp	1950–2250	High-pressure mercury lamp	3450–3750
Tungsten lamp	2700	Metal halide lamp	4000–4600

**2.2 Color Temperature Selection**

Usually, light source with higher color rendering index has better color reproduction ability. As shown in Fig. 1, it can be seen that unlike the LED, the blue, green and red spectral content of the sodium lamp is low, which also directly leads to the low color rendering index of the high-pressure sodium lamp.

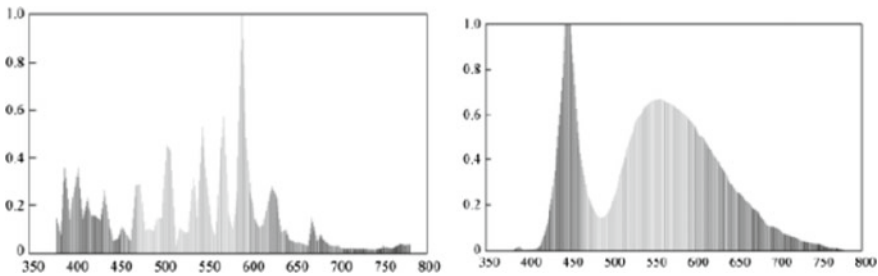


**Fig. 1** Spectral distribution of high-pressure sodium lamps and LED

As can be seen from Table 2 [2], the LED has better color rendering and stronger color reproduction ability. Street lamp with higher color rendering index has richer the spectral content. That is benefit to identify object.

**Table 2** LED and high-pressure sodium lamp parameters comparison

Light source	Power/W	Actual power consumption	Luminous flux/lm	Luminaire efficiency	Effective luminous flux/lm	Ra	Average life/h
HPS	100	120	11,000	0.6	6600	20–30	24,000
LED	99	99	7650	0.85	6502.5	80	60,000



### 3 LED and High-Pressure Sodium Lamp's Performance

#### 3.1 LED and the High-Pressure Sodium Lamp on the Fog Permeability

From the aspect of the capability to penetrate the fog, the fog permeability of light at different wavelengths is different. As shown in Table 3, we can learn that the high-pressure sodium lamp emitting a yellow light wavelength has a higher fog permeability than the white LED in the case of a heavy fog.

**Table 3** Transmittance of various color lights at different fog concentrations

Fog concentration (gear position)	White light (%)	Red light (%)	Yellow light (%)	Green light (%)	Blue light (%)
0	100	100	100	100	100
10	75.90	75.95	96.29	75.76	74.21
12	51.20	54.73	67.17	50.36	50.84
14	22.80	22.88	29.34	19.55	21.75
16	10.10	6.21	9.02	6.70	6.33
18	5.90	3.87	4.29	3.06	2.86

However, as shown in Table 2, high-pressure sodium lamp color rendering index is not high, under the irradiation of high-pressure sodium lamp, most of the objects appear yellow, and some objects appear blue. The objects of green and red may even appear black, that is, when the light of the sodium lamp is irradiated onto the objects of these colors, almost no reflected light emits. Under such lighting, if a person drives in the rainy and foggy night, the driver will can't see the pedestrians in green or red clearly, because these clothes appear black and are easily submerged in the background light, which increase the ratio of the traffic accident. However, if LED lighting is used, because of higher color rendering index, some traffic accident can be avoided. The objects in any color have reflected light in the fog, which is helpful for identifying the object. Therefore, compared with color rendering, white LED street lights are better than high-pressure sodium lamps.

#### 3.2 Comparative Analysis of Energy Efficiency of the LED and the High-Pressure Sodium Lamp

It can be seen from Table 4 that the LED light efficiency is higher than that of the high-pressure sodium lamp under the same lighting time, and the average illuminance of the high-pressure sodium lamp is higher than 160 W LED, but the power consumption is more than twice that of the 160 W LED. It can conclude that the LED consumes less power and is more efficient.

**Table 4** Data statistics for road test

Type of lamp	Total turn-on time (h)	Power consumption per unit time (kWh/h)	Total luminous flux	Lighting effect (lm/W)	Average illumination (lx)
400 W HPS	60	7.14	34,748	82	55.6
160 W LED	60	3.94	16,131	95.4	33.4

## 4 Comparison of Economic Benefits Between the LED and HPS

As shown in Table 5 [3], we use the public lighting system of a certain urban road in Brazil as a reference. From the perspective of social benefits, though the cost of LED is higher, such light sources have longer life, higher stability and less consume power than the high-pressure sodium lamps, and the maintenance costs of high-pressure sodium lamps are extremely high. Sum up, LED can fully achieve the energy saving, emission reduction and low-carbon effects, which are in line with our sustainable development requirements.

**Table 5** Cost comparison between LED and high-pressure sodium lamp

Type of lamp	Total turn-on time (h)	Power consumption (kWh)	Electricity price unit (degree/yuan)	Average life (h)	Total price (yuan)
HPS	3650	15.68*3650	0.9	20,000	51,508.8
LED	3650	6.72*3650	0.9	70,000	22,075.2

## 5 Conclusions

In summary, both LED lights and high-pressure sodium lamps have their own advantages. With the improvement in LED's performance and the breaking in the key technical problems, as well as the reduction of LED tunnel light products' price, LED lighting will not only reflect energy-saving effects better and reduce the initial investment and operating expenses, so achieving good economic benefit.

## References

1. Feng, S.L., Lu, Z.: On the color temperature selection of LED Street lights in urban roads. *Constr. Technol.* **9**, 61–63 (2016)
2. Chen, H.B.: Research on the fogging of street lamps and optimization design. *China Lighting Appliances* **7**, 5–8 (2012)
3. Deng, X., Tu, W.: Comparative analysis of the application of high pressure sodium lamps and LED lamps in highway tunnels. *Road Traffic Technol.* **6**, 114–119 (2012)



# Distribution of Quantum Dots in Quantum Dots Enhancement Films

Yuxue Feng, Zugang Liu<sup>(✉)</sup>, Renshi Chen, Xin Wang, Lei Li,  
and Hong Zhao

China Jiliang University, Hangzhou 310018, China  
zgliu78@cjlu.edu.cn

**Abstract.** Quantum dots (QDs) enhancement film (QDEF) is a QD contained film, used in LCD system to improve display color quality. The uniformity of QD in QDEF directly affects the color rendering ability of quantum dot display devices. Custom-built equipment was set up for investigating the uniformity. The blue light absorption, the green light conversion efficiency and red light conversion efficiency were used as the tools in judging the uniformity of the QD films. The results showed that the QD concentration is higher in the middle region than edge region, and the conversion efficiency of green light is about twice as high as that of red light.

**Keywords:** Quantum dot · QDEF film · Uniformity

## 1 Introduction

Quantum dots (QDs), as a new type of inorganic fluorescent materials, have attracted large attention in both academic and industrious fields recently. Compared with traditional organic phosphors, the QDs possess the advantages of broader absorption spectrum, narrower emission spectrum and better luminescent stability [1–4]. Now, the research of QDs in the field of display technology mainly includes two aspects. One is QD light-emitting diode technology (QLED), and the other is QD backlight unit (QD-BLU) [5–8] in liquid crystal display (LCD). QLEDs cannot be commercialized due to the imperfection of the existing technology, so the QD-BLU technology is applied in the LCD on the market [9, 10]. One of the current technologies for QDs to be applied in QD-BLU exists in the form of optical films, named QDEF. The effect on the color rendering ability of display devices will depend on the quality of QDEF. So the research and analysis of defects in QDEF can be useful for improving the performance and yield of QDEF, which is an effective means to reduce cost. The QDEF is mainly composed of two parts: the quantum dot layer and the protection layer [11]. The demerits of QDEF mainly include the nonuniform thickness of the films, the impurities in the films and the nonuniform distribution of quantum dots in the protection layer. This work focuses on establishing a set of simple testing equipment to test the uniformity of QDs in the film. The blue light absorption and the conversion efficiencies of green light and red light are applied for judging the uniformity of the measured QDEF.

## 2 Experiment

### 2.1 Equipment

A set of equipment was designed and established (Fig. 1). A diffusion film was placed on a blue light source, which is regarded as the excitation light source in order to obtain the uniform emitting light. Then, select a region of  $15\text{ cm} \times 15\text{ cm}$  on the diffusion film, in which 25 spots were marked with an interval of 3 cm. Finally, the USB4000 was connected to the computer, and the spectrum of the sample QDEF can be measured with SpectraSuite software.

### 2.2 Method

The test was divided into two steps. The first step, the dark spectrum was saved and removed. This step mainly aims at eliminating the influence of the spectrometer. The second step, the 25-point spectral data of blue light source without or with QDEF were measured and recorded via setting the parameters in the SpectraSuite software with the integration time to 120 us and the smoothness to 10 (to make the spectral curve smoother). The measured spectral data are plotted into spectral curves, and the integral area of each peak was calculated to represent the number of photons emitted by each peak. There are two methods to evaluate the uniformity of QDEF. One is based on the number of blue photons absorbed, and the other is based on the green light conversion efficiency and red light conversion efficiency.

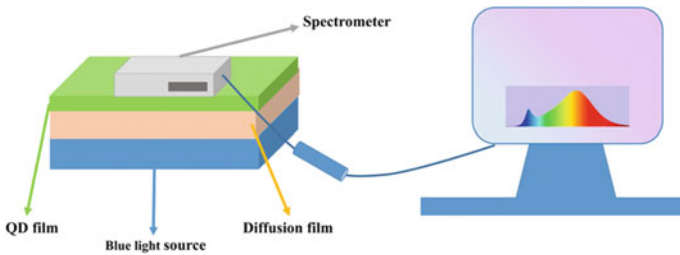


**Fig. 1** Schematic of testing equipment

QDs absorb photons and re-emit photons, so the number of blue photons absorbed represents the number of quantum dots at the measured point. The absorbed number of blue light photons by QDEF can be calculated according to the following (1):

$$N - N_t = N_b \quad (1)$$

where  $N$  is the number of photons emitted by the blue light source,  $N_t$  is the number of blue photons transmitted, and  $N_b$  is the number of blue photons absorbed. The light

conversion efficiency in different regions of the QDEF can be obtained according to the absorbed number of blue photons emitted, green photon emitted and red photon emitted, as shown in (2) and (3).

$$N_g/N_b \times 100\% = \eta_g \quad (2)$$

$$N_r/N_b \times 100\% = \eta_r \quad (3)$$

Among them,  $\eta_g$  and  $\eta_r$  are green light conversion rate and red light conversion rate,  $N_g$  and  $N_r$  are the numbers of green photons and red photons emitted, respectively.

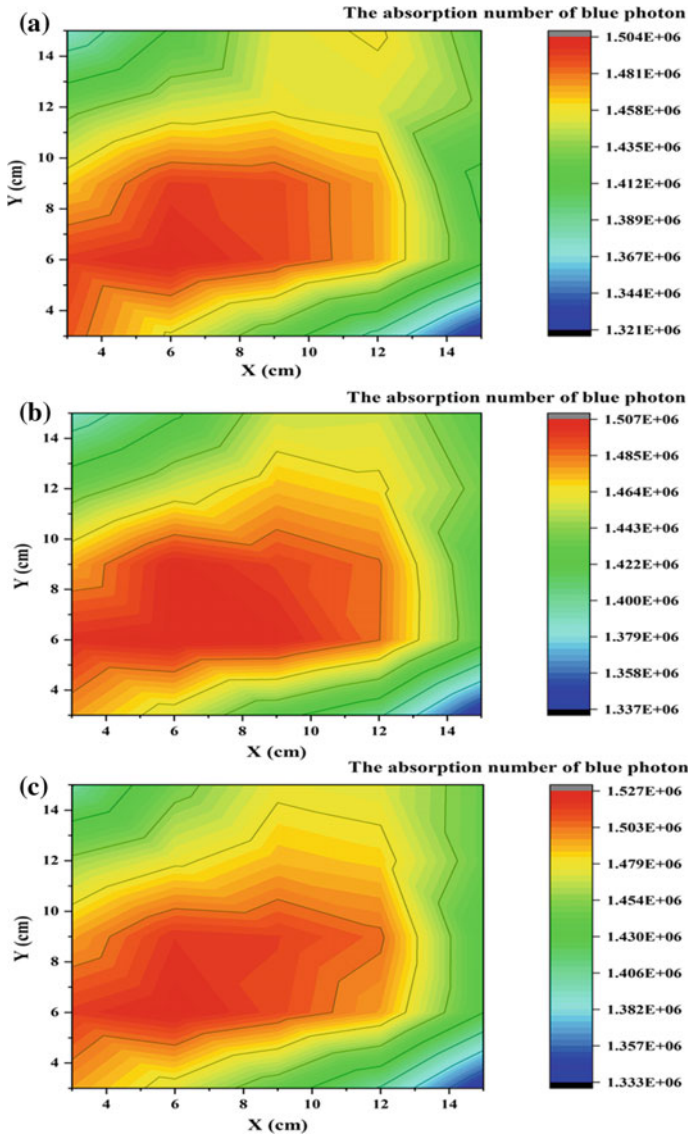
### 3 Discussion

Three QDEF films were used for this experiment and named as B-1, B-2 and B-3. The spectral data of the sample film are measured via the above test equipment and method, and these data are recorded and plotted into spectrograms and are used for calculating the number of photons emitted, ignoring the reabsorption of green emission by red QDs. Then according to the above formula, the absorbed number of blue light photon and the light conversion efficiency included green light and red light conversion rates are calculated. In order to show the concentration difference of QDs at different locations on the same sample and the concentration difference between B-1, B-2 and B-3 samples more clearly, the absorption number of blue photon and the light conversion rate were plotted by origin plotting software. Figure 2 shows the number of blue photons absorbed for B-1, B-2 and B-3, respectively. The red region presents higher absorption of blue photon. As seen from each single graph, the concentration of QDs in different regions of a single quantum dot film is obviously different. The absorbed amount of blue light in the middle region is larger than that in the edge region. This shows that the concentration of QDs in the middle region is higher than that in the edge region.

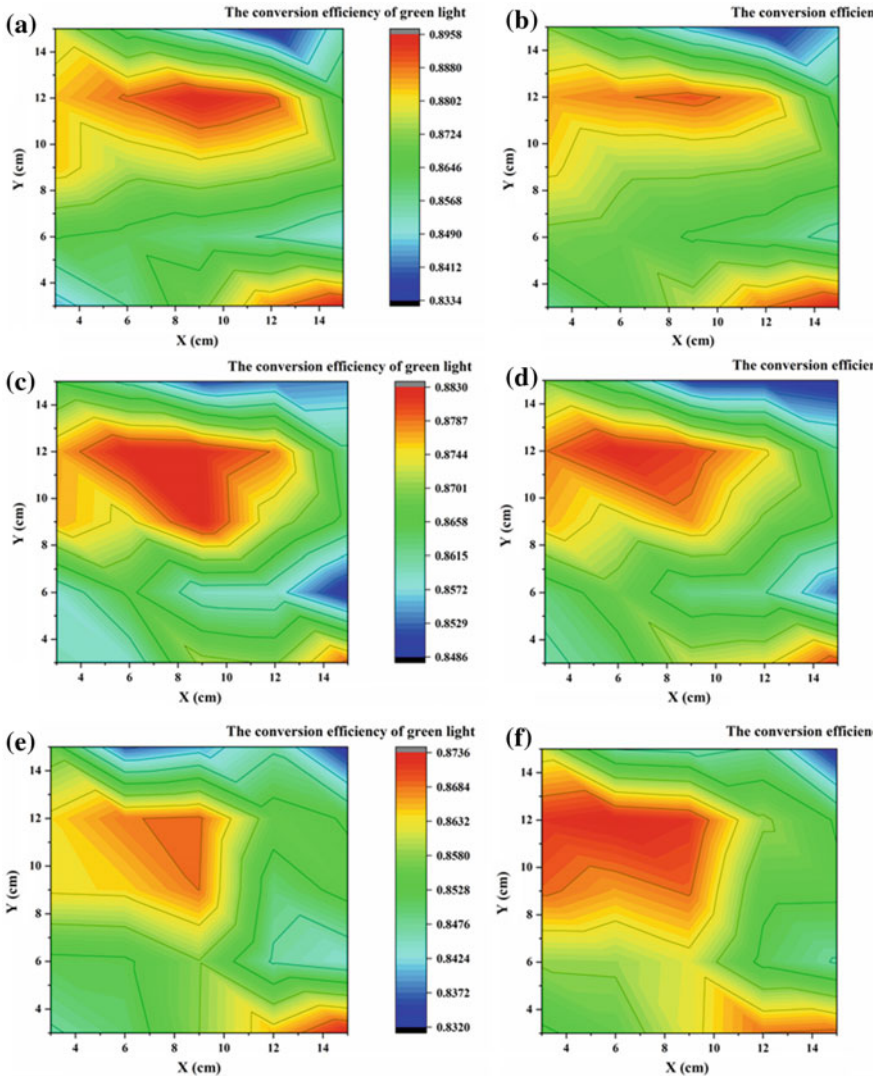
By comparing three graphs, it can be seen that the overall concentration distribution trend of B-1, B-2 and B-3 is approximately the same. The overall concentration distribution and variation trend of B-2 and B-3 are similar. The overall concentration of B-1 is lower than that of B-2 and B-3, and the color variation of B-1 is relatively flat compared to B-2 and B-3. These results suggest that the concentration uniformity of B-1 is better than that of B-2 and B-3.

Figure 3 shows the conversion rate of green light and the conversion rate of red light of B-1, B-2 and B-3, respectively. The red region indicates the high conversion rate. As seen, the conversion rate of green light is much higher than that of red light, which indicates that the concentration of green fluorescent QDs in the sample film is higher than that of red fluorescent QDs.

By comparing the green conversion rate of B-1, B-2 and B-3, it can be seen that the difference of green light conversion rate between different regions of B-2 is the largest, followed by B-1, and B-3 is the smallest. However, from the red light conversion rate of them, the difference between different regions of B-3 is the greatest, followed by B-2, and B-1 is the smallest. So based on the comparison of the above two methods, it comes to a conclusion that the uniformity of QDs in B-1 is better.



**Fig. 2** a Absorption number of blue photon for B-1. b Absorption number of blue photon for B-2. c Absorption number of blue photon for B-3



**Fig. 3** a–b Conversion efficiency of green light and red light for B-1, respectively. c–d Conversion efficiency of green light and red light for B-2, respectively. e–f Conversion efficiency of green light and red light for B-3, respectively

## 4 Conclusion

We have designed a set of simple test equipment for testing the uniformity of QDs distribution in the film. By investigating the three samples of QDEF, it can be seen that the difference in concentration distribution of various QDEF is small, and all samples exhibit a high concentration in the intermediate region, which may be due to the QDs

colloidal mixture ejected from the center of the sprinkler resulting in a lot of accumulation in the process of printing. In addition, the green light conversion efficiency of the samples is much higher than that of the red light (about twice), and the conversion efficiency is not directly related to the concentration of QDs. QDEF is used widely in display technology, and the requirements for QD film quality are in urgent need. At present, the equipment for quality testing of QDEF needs to be designed and developed. The standards for evaluating QDEF based on the blue light absorption, the green light conversion efficiency and red light conversion efficiency need to be established. This paper provides a simple test method in the uniformity of QDEF, and the data and the evaluation criteria of QDEF quality need to be further improved.

**Acknowledgements.** Project 201810356013 supported by National Undergraduate Innovation Project.

## References

1. Jang, E., Jun S., Jang, H., Lim, J., Kim, B., Kim, Y.: White-light-emitting diodes with quantum dot color converters for display backlights. *Adv. Mater.* **22**, 3076 (2010)
2. Shirasaki, Y., Supran, G.J., Bawendi, M.G., Bulović, V.: Emergence of colloidal quantum-dot light-emitting technologies. *Nat. Photonics* **7**, 13–23 (2013)
3. Peng, X.: An essay on synthetic chemistry of colloidal nanocrystals. *Nano Res.* **2**, 425–447 (2009)
4. Amirav, L., Alivisatos, A.P.: Luminescence studies of individual quantum dot photocatalysts. *J. Am. Chem. Soc.* **135**, 13049 (2013)
5. Coe-Sullivan, S., Liu, W., Allen, P., Steckel, J.S.: Quantum dots for LED down conversion in display applications. *Ecs J. Solid State Sci. Technol.* **2**, R3026–R3030 (2013)
6. Choi, Y., Seol, M., Kim, W., Yong, K.: Chemical bath deposition of stoichiometric CdSe quantum dots for efficient quantum-dot-sensitized solar cell application. *J. Phys. Chem. C* **118**, 5664–5670 (2014)
7. Luo, Z., Chen, Y., Wu, S.T.: Wide color gamut LCD with a quantum dot backlight. *Opt. Express* **21**, 26269–26284 (2013)
8. Demir, H.V., Nizamoglu, S., Erdem, T., Mutlugun, E., Gaponik, N., Eychmüller, A.: Quantum dot integrated LEDs using photonic and excitonic color conversion. *Nano Today* **6**, 632–647 (2011)
9. Pu, C., Peng, X.: To battle surface traps on CdSe/CdS core/shell nanocrystals: shell isolation versus surface treatment. *J. Am. Chem. Soc.* **138**, 8134 (2016)
10. Lin, W., Niu, Y., Meng, R., Huang, L., Cao, H., Zhang, Z.: Shell-thickness dependent optical properties of CdSe/CdS core/shell nanocrystals coated with thiol ligands. *Nano Res.* **9**, 260–271 (2016)
11. Bawendi, M.G., Brus, L.E.: The quantum mechanics of larger semiconductor clusters (“quantum dots”). *Annu. Rev. Phys. Chem.* **41**, 477–496 (1990)



**Part III**  
**Photo Detectors and Solar Cells**



# Size Dependent Performances of Organic Photodiode Arrays

Chen Liu<sup>1</sup>, Junkang Zhong<sup>2</sup>, Xinda Chen<sup>1</sup>, and Yingquan Peng<sup>1</sup>(✉)

<sup>1</sup> Institute of Microelectronics, College of Optical and Electronic Technology, China Jiliang University, Xueyuan Street 258#, Hangzhou 310018, China  
yqpeng@cjlju.edu.cn

<sup>2</sup> School of Physical Science and Technology, Lanzhou University, South Tianshui Road 222#, Lanzhou 730000, China

**Abstract.** Organic photodiode array has recently attracted a lot of attention for large-area light detection applications and imaging. In this work, Organic photodiode  $3 \times 2$  (Sample A),  $4 \times 3$  (Sample B),  $5 \times 4$  (Sample C), and  $6 \times 5$  (Sample D) arrays based on copper phthalocyanine (CuPc)/C<sub>60</sub> planar heterojunction in which CuPc used as optical sensitive material were fabricated and characterized. It is found that the dark current density of the device increases as the array increases through experimental data. A circuit model was constructed to analyze the cause of this phenomenon, and an analytical expression between dark current density and array size was obtained.

**Keywords:** OPD · Array · Size

## 1 Introduction

Organic photodiodes (OPDs) have attracted wide attention due to the advantages of large-area fabrication, low-cost, flexibility and light-weighted, in which improving the quantum efficiency has been the research hot spot in organic devices [1–3]. And organic photodiode array has recently attracted a lot of attention for large-area light detection applications and imaging [4–6]. They combine light absorption in the region of the spectrum from ultraviolet to near-infrared effectively with good photogeneration yield, sensitivity, and response time. As organic semiconductor materials have low dielectric constants and rather high exciton binding energies (0.1–1.4 eV), OPDs are preferably based on the concept of heteromorphic planar heterojunction structure [7, 8]. In a typical heteromorphic planar heterojunction, the donor and acceptor organic materials are layered between the two electrodes to form a planar donor–acceptor heterojunction interface. The photogenerated excitons generated in the planar heterojunction diffuse to the interface of the heterojunction and dissociate into free electrons and holes which participate in the conductive transport. So the charge separation efficiency of the planar heterojunction is higher than the single layer. Moreover, the probability of recombination of free charges in the organic layer is also reduced, so the device performance is also higher than that of a single layer device. While the performance of single OPDs can be considered as sufficiently well developed for most

demands, the integration in complex, pixelated detector arrays is significantly less progressed.

Within this contribution, four different scales of array were fabricated to analyze the effects of the array scale on the current density–voltage properties of the organic photodiodes array.

## 2 Experimental

All the organic materials were commercially obtained and used as received. Organic photodiode arrays with the size of  $3 \times 2$  (Sample A),  $4 \times 3$  (Sample B),  $5 \times 4$  (Sample C), and  $6 \times 5$  (Sample D) were fabricated, in which the single device areas are of 6, 4, 2, and  $1.5 \text{ mm}^2$ , respectively. The sample structure is schematically illustrated in Fig. 1. The heterogeneous planar heterojunction consists of fullerene ( $\text{C}_{60}$ ) and copper phthalocyanine (CuPc). CuPc is a p-type organic semiconductor with high optical absorption in the range of 600–800 nm.  $\text{C}_{60}$  is an n-type organic semiconductor material with low LUMO level and widely used as electron acceptor in organic solar cells, OPDs, and photosensitive organic field-effect transistors. Patterned ITO-coated glass substrates with the sheet resistance of  $10 \text{ } \Omega \text{ sq}^{-1}$  were ultrasonically cleaned by acetone, ethanol, and deionized water sequentially. Then, the ITO substrates were dried with  $\text{N}_2$  gas blowing before baked in an oven with a temperature of  $60 \text{ } ^\circ\text{C}$  for 30 min. CuPc (50 nm)/ $\text{C}_{60}$  (50 nm)/BCP (10 nm) were thermally deposited on the ITO substrates under a vacuum of  $2.5 \times 10^{-3} \text{ Pa}$ . The thickness of the organic and metal thin films was monitored by a quartz crystal microbalance which was located in the vicinity of the samples. The change in the resonant frequency of the quartz is proportional to the film thickness. The deposition rate was kept constant at approximately  $0.15 \text{ } \text{Å s}^{-1}$ . The sample fabrication was completed by thermal deposition of 100-nm-thick Al strips perpendicular to ITO strips.

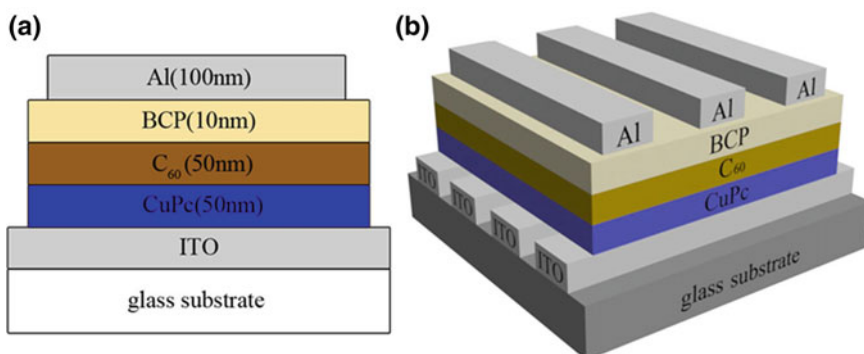


**Fig. 1** **a** Schematic structure of superlattice photodiodes based on CuPc and  $\text{C}_{60}$ , **b** schematic diagram of organic photodiode  $4 \times 3$  array structure

Current–voltage characteristics were measured by a semiconductor characterization system under dark and illumination conditions. By the characterization of optoelectronics performance of sample, a laser diode with the optical intensity of 162 and 424 mW/cm<sup>2</sup> was used. Light is incident from the ITO side into the active layer. All measurements were carried out at pressures less than 10 Pa.

### 3 Result and Discussions

For Organic photodiode array, photoresponsivity ( $R$ ) and photosensitivity ( $P$ ) are two key parameters to evaluate the photosensitive performance, which can be expressed as

$$R = \frac{I_{\text{ph}}}{P_{\text{inc}}A} \quad (1)$$

$$P = \frac{I_{\text{ph}}}{|I_{\text{dark}}|} = \frac{|I_{\text{ill}} - I_{\text{dark}}|}{|I_{\text{dark}}|} \quad (2)$$

where  $P_{\text{inc}}$  is the power of the incident light per unit area (i.e., illumination intensity), and  $A$  is the effective irradiated area of the device;  $I_{\text{ph}}$  is the photocurrent which equals to the difference between the current under illumination ( $I_{\text{ill}}$ ) and in the dark ( $I_{\text{dark}}$ ), characterizing a net enhancement of current induced by illumination. The external quantum efficiency ( $EQE$ ) represents the ability to provide photogenerated carriers per single incident photon, which can be defined as

$$EQE = \frac{hc}{q\lambda} \quad (3)$$

Here,  $q$  is the elementary charge ( $1.602 \times 10^{-19}$  C),  $h$  and  $c$  represent Planck's constant and velocity of light, respectively, and  $\lambda$  stands for the light wavelength.

Figure 2 shows the I–V characteristics of the OPD array with four different scales in the dark and under illumination. As shown in Fig. 2a, b, under illumination with incident optical power density of 162 mW/cm<sup>2</sup>, the device current density under illumination ( $I_{\text{ill}}$ ) of the Samples A and B at  $-10$  V reverse bias were in the range of 16.5–19.0 mA/cm<sup>2</sup>, and 20.0–30.0 mA/cm<sup>2</sup>, respectively. Representative current density–voltage ( $J$ – $V$ ) curves characteristic of the OPDs under a 424 mW/cm<sup>2</sup> illumination are presented in Figs. 2c, d.  $I_{\text{ill}}$  is relatively elevated in  $-10$  V reverse bias, with the range of 55–79 mA/cm<sup>2</sup> and 45–65 mA/cm<sup>2</sup> for Samples C and D. As the scale of the array increases, the Sample C and Sample D have significantly larger photocurrents than Samples A and B. The main reason is that in order to cover a large area, the laser spot size is increased when measuring  $3 \times 2$  and  $4 \times 3$  arrays, resulting in a decrease in light intensity, and accordingly, the corresponding photocurrent is smaller. As seen in Fig. 1, the dark current values are 0.15 ~ 0.41 mA/cm<sup>2</sup> (Sample A), 0.10–0.28 mA/cm<sup>2</sup> (Sample B), 0.23–1.61 mA/cm<sup>2</sup> (Sample C), and 0.59–1.75 mA/cm<sup>2</sup> (Sample D) in  $-10$  V reverse bias, respectively. As summarized in Table 1, as the scale of OPD array increases, the dark density of OPD array also shows the trend of increasing.

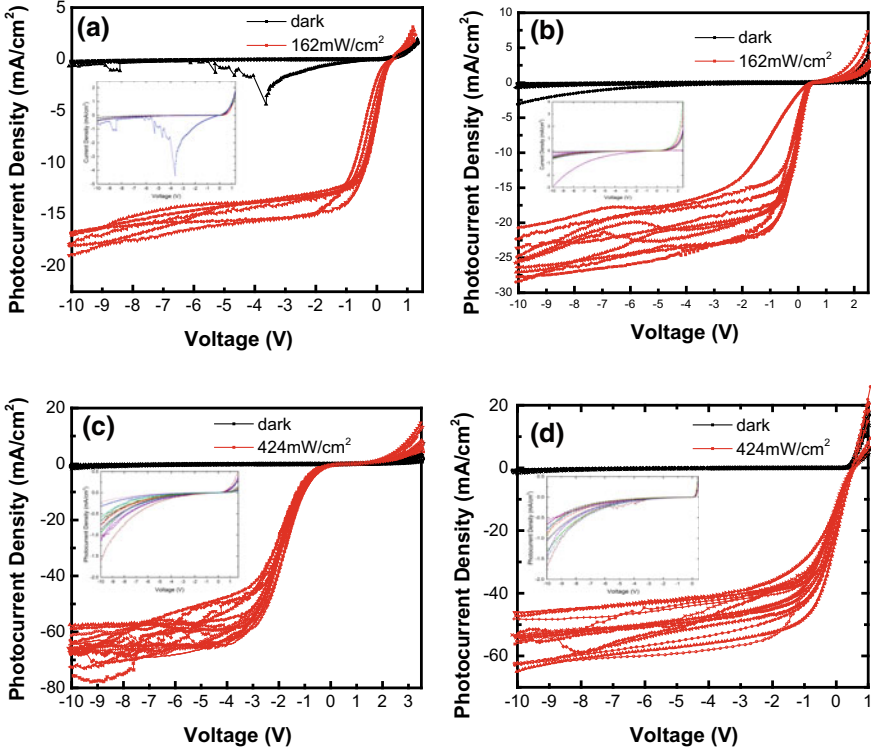


**Fig. 2** Current–voltage characteristics of organic photodiode arrays with the sizes of  $3 \times 2$  (a),  $4 \times 3$  (b),  $5 \times 4$  (c), and  $6 \times 5$  (d) measured both in the dark and under illumination. The light in a, b is  $162 \text{ mW/cm}^2$ , while that in c, d are  $424 \text{ mW/cm}^2$ . The inset in (a), (b), (c), and (d) shows the dark current curve

**Table 1** Summary of device parameter details in the experiment

	$J_{\text{dark}} \text{ (mA/cm}^2\text{)}^{\text{a}}$	$J_{\text{ill}} \text{ (mA/cm}^2\text{)}^{\text{a}}$	$P_{\text{mix}}^{\text{a}}$	$R \text{ (mA/W)}^{\text{a}}$	EQE (%)
Sample A	$0.391 \pm 0.131$	$17.6 \pm 0.8^{\text{b}}$	$45^{\text{b}}$	$106.188^{\text{b}}$	39.22
Sample B	$0.694 \pm 0.720$	$25.2 \pm 2.3^{\text{b}}$	$32^{\text{b}}$	$154.772^{\text{b}}$	25.63
Sample C	$0.900 \pm 0.475$	$65.8 \pm 4.4^{\text{c}}$	$28^{\text{c}}$	$152.93^{\text{c}}$	32.1
Sample D	$1.01 \pm 0.38$	$55.3 \pm 6.0^{\text{c}}$	$39^{\text{c}}$	$128.05^{\text{c}}$	27.4

<sup>a</sup>The bias voltage is  $-10 \text{ V}$

<sup>b</sup> $P_{\text{inc}} = 162 \text{ mW/cm}^2$

<sup>c</sup> $P_{\text{inc}} = 424 \text{ mW/cm}^2$

In the case of the same structure and fabrication process, the dark current of the discrete diode is directly proportional to the effective area of the diode, and the current density should remain unchanged. However, the trends exhibited in the arrays prepared herein are different. From a relatively simple structural analysis, an  $n \times 2$  organic

photodiode array of the size shown in Fig. 3a. The interlace of ITO strip electrode and Al strip electrode are OPDs. Applying a proper negative voltage ( $V$ ) to the intersection (OPD 1.1) of the No. 1 ITO electrode and the No. 1 Al electrode in the array under dark conditions, the parallel circuit has a reverse biased OPD on one of the branches, and the other branches have two reverse biased OPDs in series with the forward biased OPD. The diode in the forward conduction state can be considered as short-circuit state due to its extremely small resistance in the forward bias.

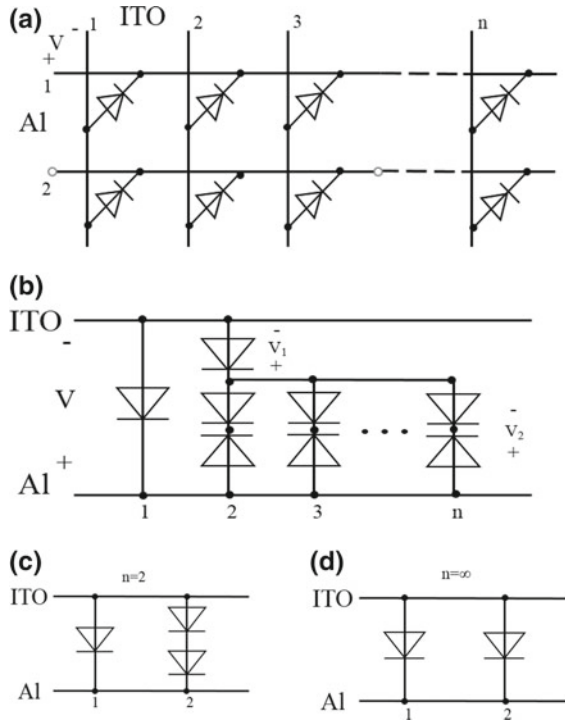


**Fig. 3** Schematic diagram and equivalent circuit diagram of  $n \times 2$  organic photodiode array

From Fig. 3b, measuring dark current density ( $J$ ) can be expressed as

$$J = J_d(V) + J_d(V_1) \tag{4}$$

where

$$J_d(V_1) = (n - 1) \times J_d(V_2) \tag{5}$$

And

$$V_1 + V_2 = V \quad (6)$$

Now assume that the organic photodiode array is  $2 \times 2$ , meaning that is  $n = 2$ . Figure 3c shows the equivalent circuit diagram at this time, from which one obtains

$$J_2 = J_d(V) + J_d(V/2) \quad (7)$$

And Fig. 3d shows the equivalent circuit diagram which  $n$  is close to infinity and one then gets

$$J_n = J_d(V) + J_d(V) = 2 \times J_d(V) \quad (8)$$

For an organic photodiode operating in a reverse bias state,  $J_d(V) > J_d(V/2)$  can be found from its volt–current characteristic curve and, therefore, have  $J_n > J_2$ .

## 4 Conclusion

In conclusion, a series of planar heterojunction-based OPD arrays were fabricated and characterized, and the performance of each device was analyzed in detail. The results show that, with the increase of array size, the dark current of diodes in the array increases correspondingly. A circuit model was constructed to analyze the cause of this phenomenon, and an analytical expression between dark current density and array size was obtained.

**Acknowledgements.** This work was supported by National Key R&D Program of China Grant No.2016YFF0203605, and the Natural Science Foundation of Zhejiang Province Grant No. LY18F050009 and LY18F040007.

## References

1. Ng, T.N., Wong, W.S., Chabinye, M.L.: Flexible image sensor array with bulk heterojunction organic photodiode. *Appl. Phys. Lett.* **92**(21), 211303 (2008)
2. Li, D., Liu, X., Dong, G.: A flexible blue light sensitive organic photodiode with high properties for the applications in low-voltage-control circuit and flexion sensors. *Laser Photonics Rev.* **8**(2), 316–323 (2014)
3. Chen, W.B., Xiang, H.F., Xu, Z.X.: Improving efficiency of organic photovoltaic cells with pentacene-doped CuPc layer. *Appl. Phys. Lett.* **91**(19), 191109 (2007)
4. Nau, S., Wolf, C., Sax, S., List-Kratochvil, E.J.: Organic non-volatile resistive photo-switches for flexible image detector arrays. *Adv. Mater.* **27**(6), 1048–1052 (2015)
5. Deckman, I., Lechène, P.B., Pierre, A.: All-printed full-color pixel organic photodiode array with a single active layer. *Org. Electron.* S156611991830051X (2018)
6. Eckstein, R., Strobel, N., Tobias, R.: Fully digitally printed image sensor based on organic photodiodes. *Adv. Opt. Mater.* **6**(5), 1701108 (2018)

7. Ng, T.N., Wong, W.S., Chabinyc, M.L.: Flexible image sensor array with bulk heterojunction organic photodiode. *Appl. Phys. Lett.* **92**(21), 213303-1–213303-3 (2008)
8. Placencia, D., Wang, W., Shallcross, R. C.: Photovoltaic cells: organic photovoltaic cells based on solvent-annealed, textured titanyl phthalocyanine/C60 heterojunctions. *Adv. Funct. Mater.* **19**(12), NA-NA (2010)





# High Photosensitivity Near-Infrared PhOFETs Based on PbPc:C<sub>60</sub> Bulk Heterojunction

Qinyong Dai<sup>1</sup>, Wenli Lv<sup>1</sup>, Yingquan Peng<sup>1</sup>(✉), Wenli Lv<sup>1</sup>, Sunan Xu<sup>1</sup>, Yi Wei<sup>1</sup>, Lei Sun<sup>1</sup>, and Ying Wang<sup>2</sup>

<sup>1</sup> Institute of Microelectronics, College of Optical and Electronic Technology, China Jiliang University, Xueyuan Street 258#, Hangzhou 310018, China  
yqpeng@cjlu.edu.cn

<sup>2</sup> College of Information Engineering, China Jiliang University, Xueyuan Street 258#, Hangzhou 310016, China

**Abstract.** Near-infrared (NIR) photosensitivity organic field-effect transistors (PhOFETs) have drawn substantial attention due to their applications in the field of industry and science. It is difficult to fabricate the device with high photosensitivity and high photoresponsivity, which greatly limits their development. In this paper, a high photosensitivity (NIR) PhOFETs based on lead phthalocyanine (PbPc):C<sub>60</sub> bulk heterojunction were proposed. For NIR light with a wavelength of 808 nm, the device exhibited a relative high photosensitivity through the applied gate voltage and the maximum photosensitivity as high as 2300, which was attributed to the inherent high exciton dissociation efficiency and the relatively low carrier mobility of the BHJ active layer.

**Keywords:** Photoresponsive · Bulk heterojunction · Photoresponsivity

## 1 Introduction

Optical detection of near-infrared (NIR) regions using organic electronic devices is currently a hot research topic due to wide application of NIR light in industry, agriculture, transportation, and other areas [1–4]. NIR photosensitivity organic field-effect transistors (PhOFETs) are a kind of PhOFETs which contain a sort of organic NIR photosensitive semiconductors. They have received widespread attention in recent years because of their advantages, such as low-cost, lightweight, mechanical flexibility, and large-area fabrication [5].

To characterize the PhOFETs, an important parameter of the phototransistor is photosensitivity  $P$ , which is defined as the ratio of the photocurrent ( $I_{ph}$ ) to the dark current ( $I_{dark}$ ) [6].

$$P = \frac{I_{ph}}{I_{dark}} = \frac{I_{ill} - I_{dark}}{I_{dark}} \quad (1)$$

where  $I_{ill}$  is the drain current under illumination. Another important parameter is photoresponsivity  $R$ , defined as the ratio of the photocurrent to the incident optical power on the channel area of the device  $P_{opt}$

$$R = \frac{I_{\text{ph}}}{P_{\text{opt}}} \quad (2)$$

In an PhOFET, large output current and mobility can be achieved by optimizing the contacts of the source/drain electrodes to the active material. Ohmic or near ohmic contacts are often used due to the significant low overall resistance of the device. However, for a PhOFET, large dark current and mobility will lead to a low photosensitivity. Moreover, photocurrent increases with the increase of the gate voltage, leading to a high photoresponsivity of the PhOFETs at a high gate voltage [8, 9]. As a result, the relatively low photosensitivity value occurs in the condition of the maximum photoresponsivity in most works on PhOFETs [6–8]. For example, Zühal Alpaslan Kösemen et al. fabricated a PhOFET based on a planar heterojunction structure of 3-hexylthiophene-2, 5-diyl, and copper phthalocyanine. The photoresponsivity of the device can reach 497 A/W, but the photosensitivity is only 1.23 at the same condition [10]. Anamika Dey et al. reported a zinc phthalocyanine-based PhOFET with the inorganic aluminium oxide/poly(vinyl alcohol)/organic nonpolar poly(methyl methacrylate) trilayer dielectric configuration. A high photoresponsivity of the device 9689.39 A/W was obtained while the photosensitivity (1.49) is much smaller [11]. Concluding the summary of the recent publications, it is difficult to fabricate PhOFETs with both of the high photosensitivity and photoresponsivity. In order to solve this problem, Y. Peng et al. proposed a PhOFET based on palladium phthalocyanine by using Al as source/drain electrodes. The device exhibited a high photosensitivity and a high photoresponsivity simultaneously due to low dark current which was mainly caused by the Schottky contacts between the Al source/drain electrodes and PbPc [12].

In general, large quantities of studies focused on the improvement of the device performance such as mobility, absorption, and photogenerated exciton dissociation efficiency [13–16]. Among them, active layer structure of PhOFETs includes single layer [13], planar heterojunction [14], bulk heterojunction (BHJ) [15], and hybrid planar-bulk heterojunction [16] were studied to realize high photoresponsivity. In particular, BHJs constituent of photosensitive electron donor and high mobility electron acceptor demonstrate high efficiency in photogenerated exciton dissociation and high internal quantum efficiency [17]. In this paper, a NIR PhOFET based on PbPc:C<sub>60</sub> BHJ which exhibited a high photosensitivity through the applied gate voltage was proposed. The high photosensitivity was attributed to the inherent high exciton dissociation efficiency and the relatively low carrier mobility of the BHJ active layer.

## 2 Experiment Detail

PbPc and C<sub>60</sub> were purchased from Acros, Tci. and Lum. Tech. Ltd., respectively, and used as received. The configuration of bottom-gate top-contact PhOFETs and the chemical structure of PbPc and C<sub>60</sub> are shown in Fig. 1. Heavily n-doped Si substrates with a resistivity of 0.03 Ohm cm acts as the gate electrode with a 1000 nm thermally grown SiO<sub>2</sub> layer (capacitance per unit area, C<sub>ox</sub>= 3.18 nF/cm<sup>2</sup>) as the gate dielectric. The substrate was ultrasonically cleaned with acetone, ethanol, and deionized water for

10 min each and baked in a vacuum oven at 60 °C for 20 min. PbPc:C<sub>60</sub> (weight ratio 1:1) bulk heterojunction (BHJ) was used as the photosensitive layer, depositing on the substrate by vacuum thermal evaporation. After deposition of the organic layer, Au source/drain electrodes were thermally deposited on the top of the sample through a shadow mask which defined a channel length (*L*)/width (*W*) of 25 μm/3 mm. During all materials deposition, the chamber pressure was kept at a value of less than  $8.0 \times 10^{-4}$  Pa and the evaporation rate were maintained in the range of 0.10–0.2 Å/s, monitored by a quartz crystal oscillator.

After device fabrication, the samples were immediately transferred into a vacuum chamber (vacuum level ~10 Pa) and measured by using an organic semiconductor characterization system. For the measurements of photoeffects, a NIR laser diode with a wavelength of 808 nm and a power density of 175 mW/cm<sup>2</sup> were used.

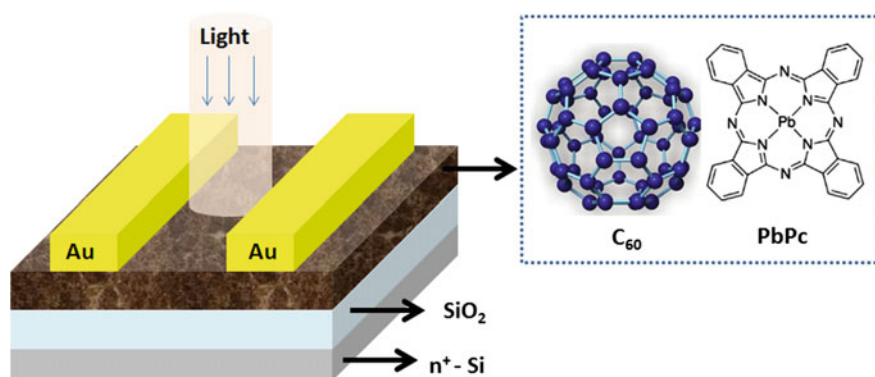


**Fig. 1** Schematic configuration and illustration of as-fabricated PbPc:C<sub>60</sub> bulk heterojunction PhOFET. The insert is the molecular structure of PbPc and C<sub>60</sub>

### 3 Results and Discussion

The output and transfer characteristics of the device in the dark and under illumination were plotted in Fig. 2. The typical n-type unipolar FET characteristics were observed. In the dark, a small saturation drain current ( $I_d$ ) of -6 nA was obtained at a drain voltage ( $V_d$ ) of -50 V and a gate voltage ( $V_g$ ) of -100 V. Under illumination, the saturation drain current increased dramatically and reached 368 nA at the same  $V_g$  and  $V_d$ , which was 61 times larger than that in the dark. From Fig. 3c, the threshold voltage ( $V_{th}$ ) and the electron mobility in the dark were extracted of 37 V and  $2.84 \times 10^{-5}$  cm<sup>2</sup> V<sup>-1</sup> s<sup>-1</sup>, respectively. In addition, with the increased negative  $V_g$ ,  $I_d$  decreased to a very low value less than 0.1 nA and did not show any increasing tendency, which indicated that the electrons in the channel were gradually depleted, and the holes in the channel were not effectively accumulated and transported. When excited by the incident NIR light (Fig. 2d), the threshold voltage reduced to -74 V, and the electron mobility increased to  $1.13 \times 10^{-4}$  cm<sup>2</sup> V<sup>-1</sup> s<sup>-1</sup>, respectively. Under illumination, two effects, i.e., the photovoltaic effect and photoconductive effect were assumed to occur

depending on the gate voltage  $V_g$ . It was suggested that the threshold voltage shift, defined as the difference between the threshold voltage under illumination and that in the dark was caused by the photovoltaic effect resulting from the accumulating or trapping of less mobile carriers in PhOFETs. And the large drain current  $I_d$  of 106 nA at a  $V_d = -50$  V and  $V_g < V_{th}$  was achieved under illumination which was 1020 times larger than that in the dark, attributing to the photoconductive effect.

Figures 3a, b show the dependences of photosensitivity on drain voltages and gate voltages, respectively. With the increased  $V_d$ , the  $P$  increased monotonically. Meanwhile, the  $P$  decreased with the increased  $V_g$ . As a result, the device cannot work at a gate and drain voltages with both high photosensitivity and high photoresponsivity, which is in consistent with that reported in literature [10, 11]. However, the device fabricated in this work exhibited much larger photosensitivity than that of PhOFETs based on single layer, planar heterojunction and hybrid planar-bulk heterojunction active layer [7–11]. The larger  $P$  was due to the following two reasons: (i) the BHJ active layer structure mixed by donor and acceptor materials resulted a very low carrier mobility and output current in the dark; (ii) the inherent high exciton dissociation efficiency in the BHJ active layer resulted a larger photocurrent under illumination.

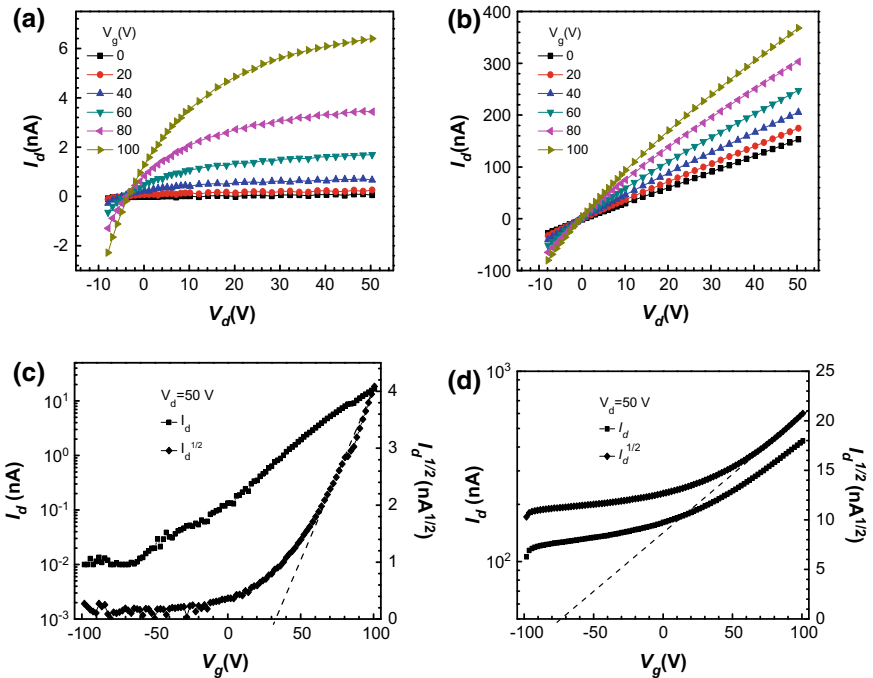


**Fig. 2** Output characteristics of the device **a** in the dark and, **b** under illumination. Transfer characteristics **c** in the dark and, **d** under illumination

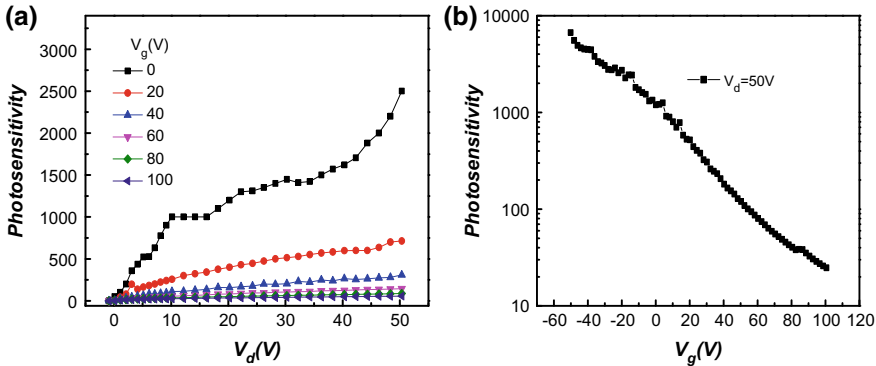


**Fig. 3** The dependences of photosensitivity on **a** drain voltages with different gate voltages and **b** gate voltages at drain voltages of 50 V

## 4 Conclusion

NIR PhOFETs based on PbPc:C<sub>60</sub>, BHJ were fabricated and characterized. For NIR light with a wavelength of 808 nm, the device exhibited a relative high photosensitivity through the applied gate voltage and the maximum photosensitivity was 2300, which was attributed to the inherent high exciton dissociation efficiency and the relatively low carrier mobility of the BHJ active layer.

**Acknowledgements.** This work was supported by National Key R&D Program of China Grant No. 2016YFF0203605, the Natural Science Foundation of Zhejiang Province Grant No. LY18F050009 and LY18F040007.

## References

1. Vogler, D.E., Sigrist, M.W.: Near-infrared laser based cavity ringdown spectroscopy for applications in petrochemical industry. *Appl. Phys. B* **85**(23), 349–354 (2006)
2. Luo, L.B., Chen, J.J., Wang, M.Z., Hu, H., Wu, C.Y., Li, Q., Wang, L., Huang, J.A., Liang, C.F.X.: Near-Infrared light photovoltaic detector based on GaAs nanocone array/monolayer graphene schottky junction. *Adv. Func. Mater.* **24**(19), 2794–2800 (2014)
3. Sun, X., Wang, C., Gao, M., Hu, A., Liu, Z.: Remotely controlled red blood cell carriers for cancer targeting and near-infrared light-triggered drug release in combined photothermal-chemotherapy. *Adv. Func. Mater.* **25**(16), 2386–2394 (2015)
4. Heerlein, J., Kamerman, G.W., Behringer, M., Steinvall, O., Bishop, G.J., Jäger, C., Gonglewski, J.D., Lewis, K.L., Hollins, R.C., Merlet, T.J.: Near-infrared power LED for emerging security and defence applications. *Proc. SPIE* **8186**, 81860 (2011)
5. Chen, D., Yao, B., Fan, G., Lv, W., Gao, P.: Influence of donor-acceptor layer sequence on photoresponsive organic field-effect transistors based on palladium phthalocyanine and C60. *Appl. Phys. Lett.* **102**(16), 163303 (2013)
6. Hamilton, M.C., Martin, S., Kanicki, J.: Thin-film organic polymer phototransistors. *IEEE Trans. Electron Devices* **51**(6), 877–885 (2004)

7. Mukherjee, B., Mukherjee, M., Choi, Y., Pyo, S.: Organic phototransistor with n-type semiconductor channel and polymeric gate dielectric. *J. Phys. Chem. C* **113**, 18870–18873 (2009)
8. Pal, T., Arif, M., Khondaker, S.I.: High performance organic phototransistor based on regioregular poly(3-hexylthiophene). *Nanotechnology* **21**(32), 325201 (2010)
9. Yao, B., Lv, W., Chen, D., Fan, G., Zhou, M.: Photoresponsivity enhancement of pentacene organic phototransistors by introducing C60 buffer layer under source/drain electrodes. *Appl. Phys. Lett.* **101**(16), 163301 (2012)
10. Kösemen, Z.A., Kösemen, A., Öztürk, S., Canımkbey, B., Erkovan, M., Yerli, Y.: Performance improvement in photosensitive organic field effect transistor by using multi-layer structure. *Thin Solid Films* **6090**(18), 30867 (2018)
11. Dey, A., Singh, A., Das, D., Iyer, P.K.: High-performance ZnPc thin film-based photosensitive organic field-effect transistors: influence of multilayer dielectric systems and thin film growth structure. *ACS Omega* **2**(3), 1241–1248 (2017)
12. Peng, Y.Q., Lv, W.L., Yao, B., Xie, J., Yang, T., Fan, G., Chen, D., Gao, P., Zhou, M., Wang, Y.: Improved performance of photosensitive field-effect transistors based on palladium phthalocyanine by utilizing Al as source and drain electrodes. *IEEE Trans. Electron Devices* **60**(3), 1208–1212 (2013)
13. Peng, Y.Q., Gao, P., Lv, W.L., Yao, B., Fan, G., Chen, D., Xie, J., Zhou, M., Li, Y., Wang, Y.: Photo-induced balanced ambipolar charge transport in organic field-effect transistors. *IEEE Photonics Technol. Lett.* **25**(22), 2149–2152 (2013)
14. Ren, Q., Xu, Q., Xia, H., Luo, X., Zhao, F., Sun, L., Li, Y., Lv, W., Du, L., Peng, Y., Zhao, Z.: High performance photoresponsive field-effect transistors based on MoS<sub>2</sub>/pentacene heterojunction. *Org. Electron.* **51**, 142–148 (2017)
15. Peng, Y.Q., Huang, F.B., Zhang, J., Luo, X., Xu, K., Lv, W., Xu, S., Wang, Y., Tang, Y., Wei, Y., Xu, Z., Yang, Y., Lu, F.: Broad spectral response photosensitive organic field-effect transistors realized by the hybrid planar-bulk heterojunction composed of three molecules with complementary optical absorption. *Org. Electron.* **43**, 27–32 (2017)
16. Huang, F., Li, Y., Xia, H., Zhang, J., Xu, K., Peng, Y., Liu, G.: Towards high performance broad spectral response fullerene based photosensitive organic field-effect transistors with tricomponent bulk heterojunctions. *Carbon* **118**, 666–674 (2017)
17. Peng, Y.Q., Lv, W.L., Yao, B., Fan, G., Chen, D., Gao, P., Zhou, M., Wang, Y.: High performance near infrared photosensitive organic field-effect transistors realized by an organic hybrid planar-bulk heterojunction. *Org. Electron.* **14**(4), 1045–1051 (2013)



# Thickness-Dependent Performance of Photosensitive Organic Field-Effect Transistors Based on Palladium Phthalocyanine

Juanjuan Zhou, Wenli Lv<sup>(✉)</sup>, Sunan Xu, and Yingquan Peng

Institute of Microelectronics, College of Optical and Electronic Technology,  
China Jiliang University, Xueyuan Street 258#, Hangzhou 310018, China  
lvwl@cjlu.edu.cn

**Abstract.** In this study, photosensitive organic field-effect transistors (PhOFETs) based on palladium phthalocyanine (PdPc) active layer with different thickness were fabricated and characterized. The photoelectric measurement results demonstrated that the device with 46.7-nm-thick PdPc film exhibited the best photoresponsivity of 1.47 mA/W and the maximum saturation field-effect mobility of  $1.88 \times 10^{-3} \text{ cm}^2/\text{Vs}$  in all devices. In addition, for drain voltage  $V_d = -50 \text{ V}$  and gate voltage  $V_g = -50 \text{ V}$ , the device photosensitivity of 20-nm-thick PdPc film reached a maximum at 5.77 compared with other devices in the same condition. Herein, we assumed that the different characteristics with a series thickness were dependent on the grain size and contact resistances in PdPc films. For which the grain size in PdPc films increased to a certain thickness around 46.7 nm and exhibited improved PhOFETs performances. Hereafter, the performance declined due to increasing contact resistances with thickness.

**Keywords:** Photosensitive organic field-effect transistors (PhOFETs) · Thickness · Palladium phthalocyanine (PdPc)

## 1 Introduction

The organic field-effect transistors (OFETs [1–3]) have made a remarkable contribution to lowering production prices for organic circuitry over the past decades due to their attractive advantages, such as low cost [4], lightweight [5], and large-area fabrication [6]. Among them, the photosensitive organic field-effect transistors (PhOFETs [7]), in which light was used as an additional control quantity to create photo-generated carriers, have drawn substantial attention in academia [8]. Performance of PhOFETs is mainly determined by the ability of channel carrier transport, the capacity of light absorption, and the dissociation efficiency of photo-generated excitons. Thus, to simultaneously achieve high mobility, strong light absorption and high exciton dissociation efficiency in a single-layer-based PhOFETs is an effective way to obtain high performance.

One of the important researches to deal with above-mentioned questions is the dependence of device performance on the organic semiconductor layer thickness [9]. For widely known aspect as, most of the charge is accumulated in few nanometers of the semiconductor near the insulator [10]. Consequently, the saturation field-effect mobility and photoresponsivity under the same bias should be unaffected by the active layer thickness in the devices. However, several studies in OFETs about the dependence of device performance on the active layer thickness have been investigated. For example, Satoshi Hoshino et al. reported the device properties of copper phthalocyanine (CuPc)-based OFETs with various active layer thicknesses [11]. The device with 80-nm-thick CuPc film showed the maximum field-effect mobility of  $3.53 \times 10^{-3} \text{ cm}^2/\text{Vs}$ . They attributed the thickness dependence to a significantly trap-affected carrier transport process in the conduction channel which formed in the vicinity of the gate insulator. Dipti Gupta et al. investigated the dependence of OFETs characteristics with pentacene thickness utilizing two-dimensional drift-diffusion simulation [12]. The atomic force micrographs (AFM) revealed the fact that grain size was a dominant reason for the existence of optimum pentacene thickness ( $\sim 35 \text{ nm}$ ). Paul V. Pesavento et al. described variable temperature contact resistances measurements on pentacene-based OFETs via a gated four-probe technique [13]. And the contact resistances depending on film thickness were approximately  $2 \times 10^3$ – $7 \times 10^6 \text{ } \Omega \text{ cm}$  which was not determined by the barrier at the metal-pentacene interface but the drift/diffusion of carriers near the metal-pentacene interface. However, concluding the summary of the recent publications, there have been very few studies of the performance dependence on active layer thickness in PhOFETs.

In this paper, PhOFETs formed by conventional bottom-gate top-contact geometry with different thickness of PdPc films were fabricated and investigated. It was noted that the photo/dark current ratio ( $P$ ) was decreased with increasing PdPc thickness and showed a small value due to large dark current caused by the low carrier injection barrier at Au/PdPc interface. Furthermore, we observed that the device performance such as photoresponsivity ( $R$ ) and saturation field-effect mobility ( $\mu$ ) all had a maximum value which was depended on the PdPc active layer thickness. For 46.7-nm-thick PdPc film PhOFET, the largest  $R$  and maximum  $\mu$  were 1.47 mA/W and  $1.88 \times 10^{-3} \text{ cm}^2/\text{Vs}$ , respectively. Thus, we proposed that the increasing performance of PhOFETs was attributed to the growing grain size. After reaching a certain size, the performance reduced due to large contact resistances which were affected by active layer thickness.

## 2 Experimental Details

PdPc was synthesized according to procedures detailed in the literature [14]. As shown in Fig. 1a, PdPc-based OFETs with different thickness (denoted as  $x$ ,  $x = 20, 26.7, 33.3, 40, 46.7, 53.3, \text{ and } 60 \text{ nm}$ ) and bottom-gate top-contact geometry were fabricated. A heavily  $n$ -doped Si substrate (the resistivity is  $0.03 \text{ } \Omega \text{ cm}$ ) acts as the gate electrode with a 1000 nm thermally grown  $\text{SiO}_2$  layer (capacitance per unit area,  $C_{\text{ox}} = 3.18 \text{ nF/cm}^2$ ) as the gate dielectric. The substrates were ultrasonically cleaned by acetone, ethanol, and deionized water, then dried with  $\text{N}_2$  gas blowing and baked in the



oven with a temperature of 60 °C for 20 min. PdPc films with different thickness were firstly deposited on the substrates. Subsequently, Au source/drain electrodes were deposited through a shadow mask which defined a channel length ( $L$ )/width ( $W$ ) of 25  $\mu\text{m}$ /3 mm. All the organic active layers and metal electrodes were deposited by vacuum thermal evaporation. During the deposition, the chamber pressure was kept at  $4 \times 10^{-4}$  Pa, and the evaporation rate was kept at 0.10–0.15  $\text{\AA}/\text{s}$  monitored by a quartz crystal oscillator.

After devices fabrication, the samples were immediately transferred into a vacuum chamber (vacuum level  $\sim 10$  Pa) and measured by an organic semiconductor characterization system. For optical absorption measurements, a 20-nm-thick PdPc film was deposited on a cleaned quartz substrate and measured by TU-1901 spectrometer (see Fig. 1b). For the measurements of photo-effects, a red laser diode with a wavelength of 650 nm and a power density of 100  $\text{mW}/\text{cm}^2$  was used.

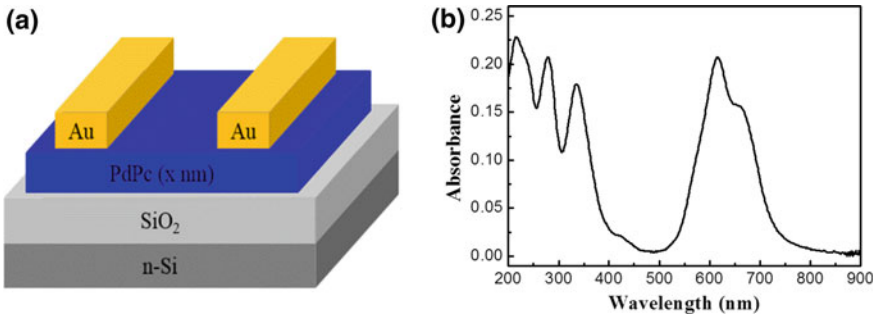


**Fig. 1** **a** Devices structure with different thickness of PdPc films. “ $x$ ” denotes the thickness (20, 26.7, 33.3, 40, 46.7, 53.3, and 60 nm), **b** optical absorption spectrum of a 20-nm-thick PdPc film on a quartz substrate

### 3 Results and Discussion

To characterize a PhOFET, the photo/dark current ratio ( $P$ ), the photoresponsivity ( $R$ ), and the saturation field-effect mobility ( $\mu$ ) are three key performance parameters. Of which, the photo/dark current ratio is expressed as [15]

$$P = \frac{I_{\text{ph}}}{|I_{\text{dark}}|} = \frac{|I_{\text{ill}} - I_{\text{dark}}|}{|I_{\text{dark}}|} \quad (1)$$

Wherein  $I_{\text{ph}}$  is the drain photocurrent, and  $I_{\text{dark}}$  and  $I_{\text{ill}}$  are the drain photocurrent in the dark and illumination. The photoresponsivity is defined as the ratio of drain photocurrent to optical power density [15].

$$R = \frac{I_{\text{ph}}}{P_{\text{inc}}} = \frac{I_{\text{ill}} - I_{\text{dark}}}{P_{\text{opt}}A} \quad (2)$$

Wherein  $P_{\text{inc}}$  and  $P_{\text{opt}}$  are the optical power density and incident optical power, and  $A$  is the device area. The saturation field-effect mobility which in the saturation regime can be extracted from [15]

$$I_{\text{d}} = \frac{W}{2L} \mu C_{\text{ox}} (V_{\text{g}} - V_{\text{Th}})^2 \quad (3)$$

Wherein  $I_{\text{d}}$  is the drain current,  $C_{\text{ox}}$  is the gate dielectric capacitance per unit area, and  $V_{\text{Th}}$  is the saturation threshold voltage.

All the devices exhibited typical  $p$ -type field-effect transistor characteristics. As shown in Fig. 2, the drain current–drain voltage ( $I_{\text{d}}-V_{\text{d}}$ ) output characteristics dependence on various PdPc active layer thickness ( $x = 20, 26.7, 33.3, 40, 46.7, 53.3,$  and  $60$  nm) were observed. In the dark, drain current firstly increased and then decreased with  $x$  growing up. Similarly, the drain current rose continually until PdPc thickness reached to  $46.7$  nm, but over the critical  $46.7$  nm, it rather declined under illumination. At gate voltage  $V_{\text{g}} = -50$  V and  $V_{\text{d}} = -50$  V, the drain current at  $x = 46.7$  nm manifested  $-61.10$  nA which was maximum in the dark, while it increased by a factor of  $\sim 1.8$  times and reached to  $-171.41$  nA under illumination in the same condition.

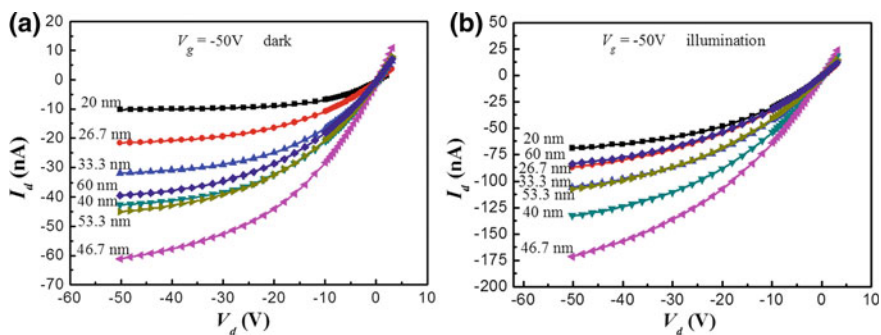


**Fig. 2** Output characteristic ( $V_{\text{g}} = -50$  V) of devices, **a** in the dark and **b** under illumination

Furthermore, the photoresponsivity and saturation field-effect mobility dependence on PdPc thickness had a similar trend to that of drain current (see Fig. 3). Considering the grain size varies with different film thickness, we assumed that the thinner PdPc organic active layer demonstrated a lower  $\mu$  due to discontinuous films. That is, the dispersed islands which formed interfacial scattering centers obstructed channel carriers transport. It was concluded that the grain size in PdPc films rose continually with thickness and reached to maximum at a certain value around  $46.7$  nm. In addition, the photo/dark current ratio was decreased with PdPc thickness changed from  $20$  to  $60$  nm and showed a small value due to large dark current caused by the energy barrier for

holes transport at Au/PdPc interfaces. Just as shown in Fig. 3a, at  $V_g = -50$  V,  $V_d = -50$  V, and  $x = 20$  nm, the photo/dark current ratio was as large as 5.77, while at the same gate and drain voltage it obtained 1.12 in 60-nm-thick PdPc film OFETs.

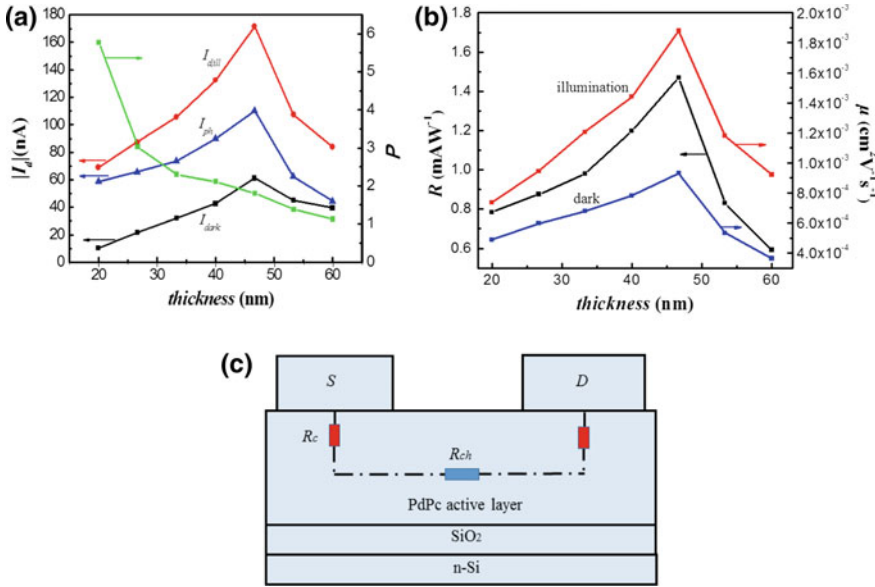


**Fig. 3** a  $I_{ph}$ ,  $I_{dark}$ ,  $I_{ill}$ , and  $P$ , b  $\mu$  and  $R$  dependent on thickness ( $V_g = -50$  V,  $V_d = -50$  V) of devices in the dark and under illumination, c schematic diagram of channel resistance  $R_{ch}$  and contact resistance  $R_C$  in a PhOFET

According to Mott–Schottky [16], the contact of source/drain electrodes with the organic semiconductor is generally considered to be a metal–semiconductor hetero-junction. Simultaneously, it is regarded as an ohmic contact because of the work function of the metal is close to the highest occupied molecule orbital (HOMO) of a  $p$ -type organic semiconductor. In this paper, Au (the work function is  $\sim 5.1$  eV [17]) was used as source/drain electrodes, and PdPc was used as the active layer material. Thus, the contact resistances including two elements were generated. One was produced by the energy level difference between the Fermi level ( $E_F$ ) of Au and PdPc at their interface. The other was induced by the parasitic resistances in the charge accumulation region. For top-contact devices, the carriers are injected into active layer from source electrode, transported a distance in the semiconductor, and extracted from the drain electrode. Thereby, the contact resistances can significantly affect carriers transport. It is assumed that the channel resistance  $R_{ch}$  is in series with the contact resistance  $R_C$  (see Fig. 3c). Thus, the total on-resistance  $R_{ON}$  can be expressed as [18, 19]

$$R_{\text{ON}} = R_{\text{ch}} + R_{\text{C}} = \frac{L}{\mu_{\text{ch}} C_{\text{ox}} W (V_{\text{g}} - V_{\text{Th}})} + R_{\text{C}} \quad (4)$$

Wherein  $\mu_{\text{ch}}$  is the mobility of holes in the channel. Since the channel resistance  $R_{\text{ch}}$  is a function of channel length  $W$ , the total on-resistance  $R_{\text{ON}}$  is almost unaffected by it. Thus, the thickness of the PdPc films will dramatically affect by contact resistance  $R_{\text{C}}$ . As shown in Fig. 3b, the saturation field-effect mobility in the dark and under the illumination of 46.7-nm-thick device was determined to be  $9.31 \times 10^{-4}$  and  $1.88 \times 10^{-3} \text{ cm}^2/\text{Vs}$ , respectively. Moreover, the photoresponsivity manifested a maximum value of 1.47 mA/W at  $x = 46.7 \text{ nm}$  which is  $\sim 2.49$  times of 60-nm-thick device. After that, the decline of them was attributed to the increased contact resistances. Theoretically speaking, the thicker the film was, the longer the carriers will transport in the vertical direction. Thus, the contact resistance increased as the thickness grew up and resulted in a decline of PhOFETs characteristics.

## 4 Conclusions

In this paper, the PhOFETs formed by conventional bottom-gate top-contact geometry with different thickness of PdPc films were fabricated and investigated. The photoelectric characteristics suggested that the 46.7-nm-thick PhOFET exhibited the largest  $R$  of 1.47 mA/W and a maximum  $\mu$  of  $1.88 \times 10^{-3} \text{ cm}^2/\text{Vs}$  in all devices. In addition, at  $V_{\text{g}} = -50 \text{ V}$ ,  $V_{\text{d}} = -50 \text{ V}$ , and  $x = 20 \text{ nm}$ , the photo/dark current ratio was as large as 5.77. For this, we assumed that the grain size in PdPc films had increased continually with thickness and reached to maximum at a certain value around 46.7 nm. After that, the contact resistances grew up with thickness which resulted in the decline of PhOFETs characteristics.

**Acknowledgements.** This work was supported by National Key R&D Program of China Grant No. 2016YFF0203605 and the Natural Science Foundation of Zhejiang Province Grant No. LY18F050009.

## References

1. Lee, W.H., Park, Y.D.: Organic semiconductor/insulator polymer blends for high-performance organic transistors. *Polymers* **6**, 1057–1073 (2014)
2. Scaccabarozzi, A.D., Stingelin, N.: Semiconducting: insulating polymer blends for optoelectronic applications—a review of recent advances. *J. Mater. Chem. A* **2**, 10818–10824 (2014)
3. Arias, A.C.: Vertically segregated polymer blends: Their use in organic electronics. *J. Macromol. Sci.* **46**, 103–125 (2006)
4. Lee, S.H., Kim, D.Y., Noh, Y.Y.: Improved ambipolar charge injection in organic field-effect transistors with low cost metal electrode using polymer sorted semiconducting carbon nanotubes. *Org. Electron.* **46**, 28–34 (2017)

5. Lim, C.J., Li, L., Lei, Y.L., Zhou, F., Wu, B., Liu, X.Y., Zhu, F.R., Ong, B.S., Hu, X., Su, H., Ng, S.C.: Synthesis and characterization of three thienopyridazine-based copolymers and their application in OFET. *Tetrahedron Lett.* **57**, 1523–1527 (2016)
6. Li, Y., Lv, W.L., Luo, X., Sun, L., Zhao, F.Y., Zhang, J.P., Zhong, J.K., Huang, F.B., Peng, Y.Q.: Enhanced performance of PbPc photosensitive organic field effect transistors by inserting different-thickness pentacene inducing layers. *Org. Electron.* **26**, 186–190 (2015)
7. Karimov, K.S., Qazi, I., Tahir, M.M., Khan, T.A., Shafique, U.: Photo organic field effect transistor's properties. *Turk. J. Phys.* **32**, 13–19 (2008)
8. Peng, Y.Q., Lv, W.L., Yao, B., Xie, J.P., Yang, T., Fan, G.Y., Chen, D.Q., Gao, P.J., Zhou, M.Q., Wang, Y.: Improved performance of photosensitive field-effect transistors based on palladium phthalocyanine by utilizing Al as source and drain electrodes. *IEEE Trans. Electron Devices* **60**(3), 1208–1212 (2013)
9. Boudinet, D., Benwadih, M., Altazin, S., Gwoziecki, R., Verilhac, J.M., Coppard, R., Le Blevennec, G., Chartier, I., Horowitz, G.: Influence of the semiconductor layer thickness on electrical performance of staggered n- and p-channel organic thin-film transistors. *Org. Electron.* **11**(2), 291–298 (2010)
10. Hauff, E.V., Johnen, F., Tunc, A.V., Govor, L., Parisi, J.: Detailed investigation of the conducting channel in poly (3-hexylthiophene) field effect transistors. *J. Appl. Phys.* **108**, 063709 (2010)
11. Hoshino, S., Kamata, T., Yase, K.: Effect of active layer thickness on device properties of organic thin-film transistors based on Cu (II) phthalocyanine. *J. Appl. Phys.* **92**(10), 6028–6032 (2002)
12. Gupta, D., Hong, Y.: Understanding the effect of semiconductor thickness on device characteristics in organic thin film transistors by way of two-dimensional simulations. *Org. Electron.* **11**, 127–136 (2010)
13. Pesavento, P.V., Puntambekar, K.P., Frisbie, C.D., McKeen, J.C., Ruden, P.P.: Film and contact resistance in pentacene thin-film transistors: dependence on film thickness, electrode geometry, and correlation with hole mobility. *J. Appl. Phys.* **99**(9), 094504 (2006)
14. Brown, R.J.C., Kucernak, A.R., Long, N.J., Batalla, C.M.: Spectroscopic and electrochemical studies on platinum and palladium phthalocyanines. *New J. Chem.* **28**(6), 676 (2004)
15. Hamilton, M.C., Martin, S., Kanicki, J.: Thin-film organic polymer phototransistors. *IEEE Trans. Electron Devices* **51**(6), 877–885 (2004)
16. Roha, J., Kimb, H., Parka, M., Kwack, J., Lee, C.: Improved electron injection in all-solution-processed n-type organic field-effect transistors with an inkjet-printed ZnO electron injection layer. *Appl. Surf. Sci.* **420**, 100–104 (2017)
17. Michaelson, H.B.: The work function of the elements and its periodicity. *J. Appl. Phys.* **48**, 4729 (1977)
18. Kano, M., Minari, T., Tsukagoshi, K., Maeda, H.: Control of device parameters by active layer thickness in organic field-effect transistors. *Appl. Phys. Lett.* **98**, 073307 (2011)
19. Choi, J.M., Im, S.: Optimum channel thickness of rubrene thin-film transistors. *Appl. Phys. Lett.* **93**, 043309 (2008)



# Channel-Length-Dependent Performances of Planar Photodiodes Based on Perovskite

Guangmeng Liao<sup>1</sup>, Kun Xu<sup>1</sup>, Feiyu Zhao<sup>1</sup>, Fobao Huang<sup>1</sup>,  
Yuanlong Liang<sup>1</sup>, Lan He<sup>1</sup>, Yingquan Peng<sup>1,2</sup>✉,  
and Rongzheng Ding<sup>2</sup>

<sup>1</sup> Institute of Microelectronics, School of Physical Science and Technology,  
Lanzhou University, South Tianshui Road 222#, Lanzhou 730000, China  
yqpeng@cjlu.edu.cn

<sup>2</sup> Institute of Microelectronics, College of Optical and Electronic Technology,  
China Jiliang University, Xueyuan Street 258#, Hangzhou 310018, China

**Abstract.** In this paper, planar photodiodes based on perovskite were fabricated and characterized. We explored the relationship between channel length and photo-generated current. The study demonstrates that the photo-generated current generated by planar photodiode at weak light is hardly affected by the channel length. However, due to the influence of the diffusion mechanism, the photo-generated current gradually increases with the channel length under strong light. Our study provides a reasonable explanation for the diffusion mechanism of photo-generated carriers in horizontal structure.

**Keywords:** Planar structure · Perovskite · Diffusion mechanism

## 1 Introduction

Organic photodetectors have advantages of low cost, large area detection, wide material selection, and flexible device fabrication [1–4]. All of these make organic photodiodes have special research value and broad application prospects in the traditional photoelectricity field. Under the current situation that the comprehensive performance of organic photodetectors is behind of inorganic photodetectors, utilizing the inherent advantages of organic photosensitive materials and improving device structure to optimize device performance are methods for shortening the gap.

As we all know, perovskite has been proven to be a promising photoelectric device material that applying to solar cells [5], light-emitting diodes [6, 7], photodetectors [8–10], and lasers [11], due to their excellent optical and electrical properties with large absorption cross-section, long photo-generated carrier diffusion length, and high charge mobility [12, 13]. In this paper, in order to prove the relationship between channel length and photo-generated current, we fabricated planar photodiodes by using perovskite as light absorber and carriers' transport layer. Finally, our study provides a reasonable explanation for the diffusion mechanism of photo-generated carriers in horizontal structure.

## 2 Experiment

### 2.1 Materials and Device Fabrication

In the experiment, all reagents were of analytical grade. The perovskite was obtained by dissolving  $\text{CH}_3\text{NH}_3\text{I}$  and  $\text{PbCl}_2$  (3:1 molar ratio) in DMF at room temperature. As shown in Fig. 1a, the perovskite film was spin-coated on the cleaned glass substrate and two gold electrodes were deposited as electrodes of planar photodiodes. The glass substrates were firstly cleaned in the order of acetone, alcohol, and deionized water for 10 min each, and then were dried with floating  $\text{N}_2$  gas and baked in a vacuum oven at  $60^\circ\text{C}$  for 20 min. After that, 300-nm-thick perovskite films were spin-coated on clean glass substrates with 1500 rad/min for 40 s, and then baked in a vacuum oven with a temperature of  $100^\circ\text{C}$  for 1 h. Next, 45-nm-thick gold electrodes were vacuum evaporated on perovskite films by using shadow masks to define the channel lengths of 18, 25, 35, 50, and  $130\ \mu\text{m}$ , respectively, and the width of all channels was 3 mm. The chamber pressure during the deposition of gold was maintained at  $2 \times 10^{-3}$  Pa and the evaporation rate was kept at 0.2–0.3  $\text{\AA}/\text{s}$ .

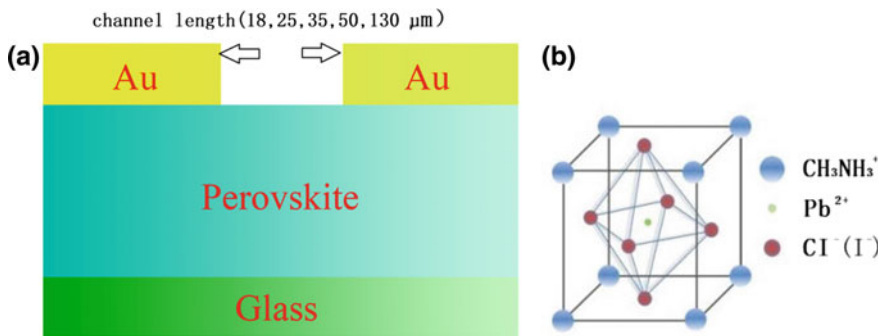


**Fig. 1** a Schematic structure of devices and b perovskite molecular structure

### 2.2 Measurement and Characterizations

The absorption spectra of perovskite film were measured by used TU-1901 spectrometer. All measurements were conducted using a semiconductor characterization system in a dark chamber at room temperature. Laser diodes with wavelengths covered at 405, 532, 655, and 808 nm were used as the light source, and the different optical powers were realized by using neutral density filters.

## 3 Results and Discussion

Figure 2 shows the absorption spectra of a 300-nm-thick perovskite film on quartz glass. It is seen that the perovskite film has a strong light absorption in the visible region from 400 to 700 nm and weak light absorption in the near-infrared region.

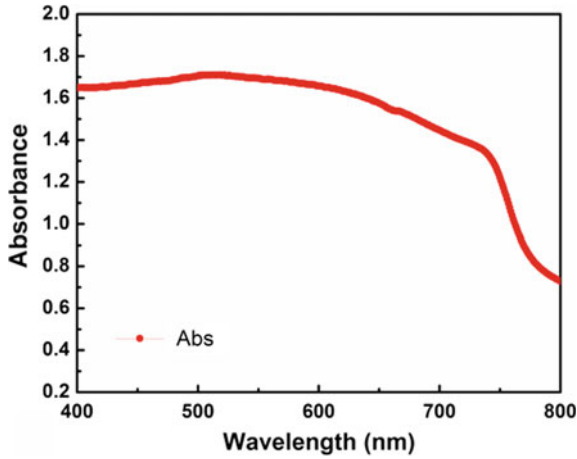


Fig. 2 Absorption spectra of perovskite film on quartz glass

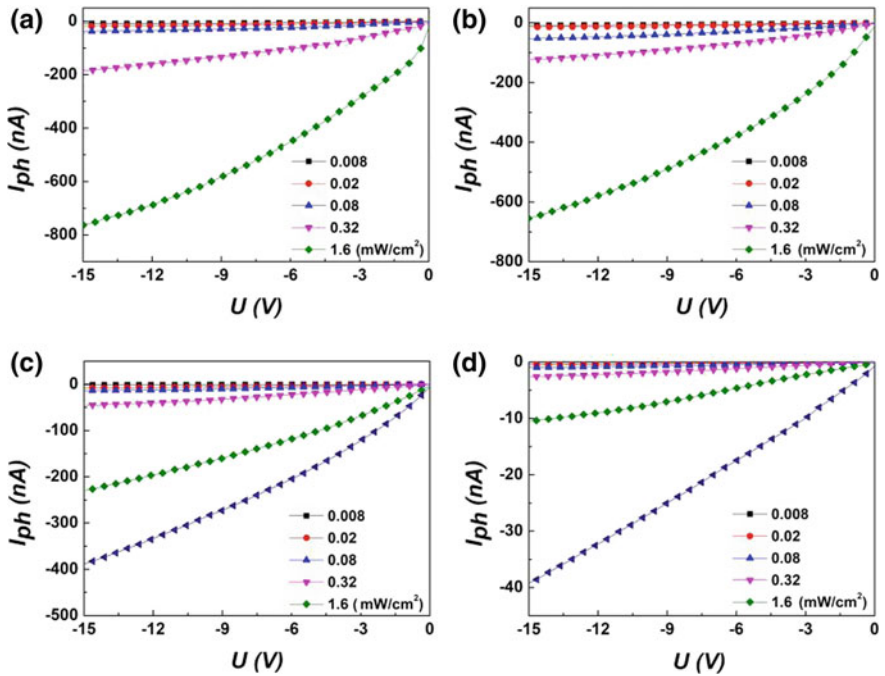


Fig. 3 Representative  $I$ - $V$  characteristics of devices at different wavelengths of 405 nm (a), 532 nm (b), 655 nm (c), and 808 nm (d), respectively

Figure 3 shows the representative  $I$ - $V$  characteristics of devices with a channel length of 35  $\mu\text{m}$  at different wavelengths (405, 532, 655, and 808 nm). It is seen that the photocurrent ( $I_{\text{ph}}$ ) increases as reverse bias voltage and incident light intensity, and



the  $I_{\text{ph}}$  is gradually reduced in the wavelength range from 405 to 808 nm. At the light intensity of  $1.6 \text{ mW/cm}^2$ , the significant  $I_{\text{ph}}$  value ( $\sim 700 \text{ nA}$ ) is obtained under 405 and 532 nm illumination compared to the  $I_{\text{ph}}$  value ( $\sim 10 \text{ nA}$ ) for 808-nm illumination.

For photodetectors, the photoresponsivity ( $R$ ) is a key performance parameter defined as the ratio of  $I_{\text{ph}}$  to the incident optical power ( $P_{\text{in}}$ ) that can be expressed as [10]

$$R = \frac{I_{\text{ph}}}{P_{\text{in}}}. \quad (1)$$

From the photoresponsivity ( $R$ ), the external quantum efficiency (EQE) can be described as [10]

$$\text{EQE} = \frac{hc}{q\lambda} R, \quad (2)$$

where  $h$  is the Planck constant,  $c$  is the velocity of light in vacuum,  $q$  is the elementary electric charge,  $\lambda$  is the wavelength of incident light.

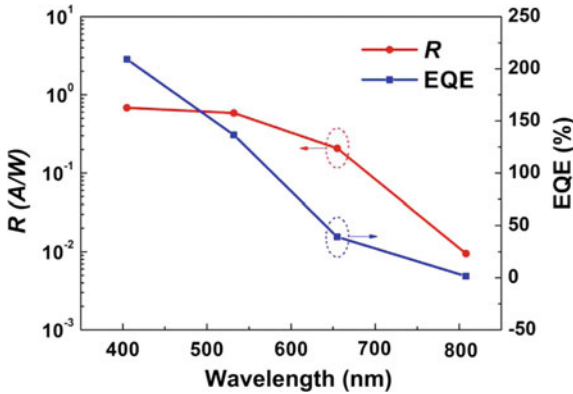


**Fig. 4** Dependence of photoresponsivity and the external quantum efficiency on the wavelength of incident light

Figure 4 shows the dependence of  $R$  and EQE on the wavelength of incident light for an incident optical power of  $\sim 1.6 \text{ mW/cm}^2$  at a reverse voltage bias of 15 V. Both  $R$  and EQE decrease with increasing wavelength from 400 to 700 nm, which demonstrates that the light absorption from visible light to near-infrared light of perovskite is gradually weakening.

Figure 5 shows the representative  $I$ - $V$  characteristics of perovskite planar photodiodes of different channel lengths irradiated by 405-nm laser with different light intensities. It can be found that the photo-generated currents of the devices of different channel lengths are not much different when the incident light intensity is less than

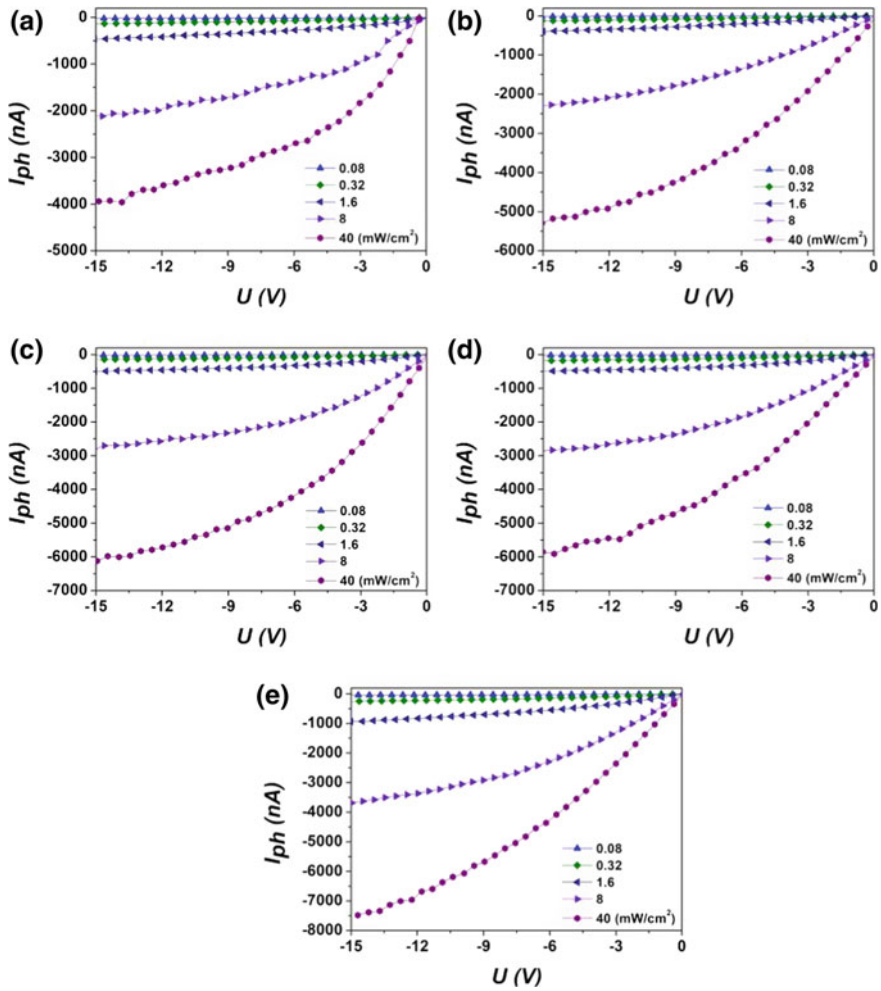


**Fig. 5** Representative  $I$ - $V$  characteristics of devices under illumination of  $\lambda = 405$  nm with channel lengths of 18  $\mu\text{m}$  (a), 25  $\mu\text{m}$  (b), 35  $\mu\text{m}$  (c), 50  $\mu\text{m}$  (d), and 130  $\mu\text{m}$  (e), respectively

1.6  $\text{mW}/\text{cm}^2$ . When the incident light intensity is increased to 8 and 40  $\text{mW}/\text{cm}^2$ , the photo-generated current increases as channel length. Moreover, it is worth noting that in Fig. 5d, e, the channel length is increased by 2.6 times, but the photo-generated current is only increased from 2800 to 3800 nA. For these interesting phenomena, we have analyzed the mechanism. When the perovskite thin film was illuminated by the incident light, excitons are generated, and the dissociated electrons and holes drift toward the anode and cathode under the action of the electric field. But the carrier diffusion length in perovskites is limited, which causes most of the carriers to recombine before being extracted by the electrodes. Therefore, the channel length hardly affects the photo-generated current below the light intensity of 1.6  $\text{mW}/\text{cm}^2$ .

However, when the incident light intensity is greater than  $1.6 \text{ mW/cm}^2$ , we infer that more high-energy excitons are easily generated by the device of longer channel, then there are carriers with greater probability of being extracted by the electrodes. But recombination of photoexcited carriers still exists, most carriers cannot reach electrodes. This may cause the photo-generated current to gradually increase as the length of the channel.

## 4 Conclusion

In summary, we have fabricated and characterized horizontal photodiodes with different channel lengths based on perovskite. The photo-generated current of the device is hardly affected by the channel length at weak light, owing to the carrier diffusion length in perovskites is limited, and most of the carriers have recombined before being extracted by the electrodes. As the incident light density increases, the photo-generated current gradually increases as the channel length, resulting from more high-energy excitons generated in longer channel under strong light, and more carriers extracted by the electrodes.

**Acknowledgements.** This work was supported by National Key R&D Program of China Grant No. 2016YFF0203605, and the Natural Science Foundation of Zhejiang Province Grant No. LY18F050009.

## References

1. Li, X., Yu, D., Chen, J., Wang, Y., Cao, F., Wei, Y., Wu, Y., Wang, L., Zhu, Y., Sun, Z.: Constructing fast carrier tracks into flexible perovskite photodetectors to greatly improve responsivity. *ACS Nano* **11**(2), 2015–2023 (2017)
2. Xu, X., Zhou, X., Zhou, K., Xia, Y., Ma, W., Inganäs, O.: Large-area, semitransparent, and flexible all-polymer photodetectors. *Adv. Funct. Mater.* **28**(48), 1805570 (2018)
3. De Fazio, D., Goykhman, I., Yoon, D., Bruna, M., Eiden, A., Milana, S., Sassi, U., Barbone, M., Dumcenco, D., Marinov, K.: High responsivity, large-area graphene/MoS<sub>2</sub> flexible photodetectors. *ACS Nano* **10**(9), 8252–8262 (2016)
4. Oliveira, J., Brito-Pereira, R., Gonçalves, B.F., Etxebarria, I., Lanceros-Mendez, S.: Recent developments on printed photodetectors for large area and flexible applications. *Org. Electron.* **66**, 216–226 (2019)
5. Woon, S.Y., Byung-Wook, P., Eui, H., Nam, J.J., Young, C.K., Dong, U.L., Seong, S.S., Jangwon, S., Eun, K.K., Jun, H.N.: Iodide management in formamidinium-lead-halide-based perovskite layers for efficient solar cells. *Science* **356**, 1376–1379 (2017)
6. Lin, K., Xing, J., Quan, L.N., de Arquer, F.P.G., Gong, X., Lu, J., Xie, L., Zhao, W., Zhang, D., Yan, C.: Perovskite light-emitting diodes with external quantum efficiency exceeding 20 per cent. *Nature* **562**(7726), 245–248 (2018)
7. Cao, Y., Wang, N., Tian, H., Guo, J., Wei, Y., Chen, H., Miao, Y., Zou, W., Pan, K., He, Y.: Perovskite light-emitting diodes based on spontaneously formed submicrometre-scale structures. *Nature* **562**(7726), 249–253 (2018)

8. Bao, C., Yang, J., Bai, S., Xu, W., Yan, Z., Xu, Q., Liu, J., Zhang, W., Gao, F.: High performance and stable all-inorganic metal halide perovskite-based photodetectors for optical communication applications. *Adv Mater* **30**(38), e1803422 (2018)
9. Wang, Y., Fullon, R., Acerce, M., Petoukhoff, C.E., Yang, J., Chen, C., Du, S., Lai, S.K., Lau, S.P., Voiry, D.: Solution-processed MoS<sub>2</sub>/organolead trihalide perovskite photodetectors. *Adv. Mater.* **29**(4) (2017)
10. Zhou, J., Huang, J.: Photodetectors based on organic-inorganic hybrid lead halide perovskites. *Adv. Sci.* **5**(1), 1700256 (2018)
11. Wang, Y., Li, X., Nalla, V., Zeng, H., Sun, H.: Solution-processed low threshold vertical cavity surface emitting lasers from all-inorganic perovskite nanocrystals. *Adv. Funct. Mater.* **27**(13), 1605088 (2017)
12. Kato, M., Fujiseki, T., Miyadera, T., Sugita, T., Fujimoto, S., Tamakoshi, M., Chikamatsu, M., Fujiwara, H.: Universal rules for visible-light absorption in hybrid perovskite materials. *J. Appl. Phys.* **121**(11), 115501 (2017)
13. Wehrenfennig, C., Eperon, G.E., Johnston, M.B., Snaith, H.J., Herz, L.M.: High charge carrier mobilities and lifetimes in organolead trihalide perovskites. *Adv. Mater.* **26**(10), 1584–1589 (2014)



# Green-Light Photoresponsive Organic Field-Effect Transistor by PTCDA/Pentacene Heterojunction

Ying Tang<sup>(✉)</sup> and Binghan Song

College of Optical and Electronic Technology, China Jiliang University,  
Hangzhou, China  
07a0403050@cjl.u.edu.cn

**Abstract.** The new organic photoelectric detector with great potential has been widely concerned and researched, especially for the photoresponsive organic field-effect transistor (photOFET). However, it is still rare for the researches on green-light photOFET. This paper aimed at green-light photOFET. The green-light photOFETs were fabricated by utilizing organic heterojunction based on PTCDA and pentacene. Under a green-light illumination (the wavelength is 532 nm), it exhibited a maximum photosensitivity of 56.15 (with power intensity of 16.5 mW/cm<sup>2</sup>) and a maximum photoresponsivity of 19.62 A/W (with power intensity of 0.0033 mW/cm<sup>2</sup>), which were greater than that of PTCDA single-layer photOFET. These results indicate that the heterojunction photOFET based on PTCDA and pentacene is proved to be a green-light photodetector with good performance.

**Keywords:** Green-light · PhotOFET · Pentacene · PTCDA · Heterojunction

## 1 Introduction

Electrophotonic detector has been widely used in various fields of military and national economy, and they are paid more and more attention because of their advantages of low cost, flexibility and large area. Common organic photodetectors included organic photodiodes [1], organic bipolar transistors [2] and photosensitive organic field-effect transistors [3–5] (photOFET). Due to the high photosensitivity and low noise [6–8], photOFET has played an important role in the field of light detection.

There are relatively few reports on green-light organic photodetector, while the other organic devices have received lots of attention. Leem et al. reported that an organic phototransistor formed with *N,N*-dimethylquinacridone and dicyanovinyl-terthiophene had a quantum effect of 52% under the wavelength of 540 nm, which could be used in full-color organic image sensor [9]. Lee et al. proposed a green sensitive organic photodetector with good photoresponsivity and spectral selectivity

based on boron subphthalocyanine chloride (SubPc) derivatives [10]. Kim et al. researched an organic photoelectric detector with excellent green translucent selection method with the detection sensitivity of  $2.1 \times 10^{-12} \text{ cm Hz}^{1/2}/\text{W}$  at 530 nm wavelength, which was better than those using metal electrodes [11]. In the current study, the research of green photOFET is relatively insufficient, especially in the research focused on perylene formic acid anhydride materials. PTCDA (3, 4, 9, 10-perylenetetracarboxylic dianhydride) is a kind of weak n-type organic semiconductor material with wide band gap of 2.5 eV. Although PTCDA's mobility is relatively low in organic semiconductors, it is an ideal material for great green-light photosensitivity with the absorption peak between 500 and 550 nm [12]. Pentacene is a representative *p*-type organic semiconductor material with a band gap of 1.9 eV and high hole mobility, which can form a heterojunction with PTCDA. The heterojunction structure is effective to improve the performance of photOFET, especially for heterotypic heterojunction consisting of the donors (*D*) and acceptors (*A*). The exciton at the *D*-*A* interface can be effectively separated into free electrons and holes that can effectively improve the device efficiency [13–15].

In the field of green photosensitive photOFET, this paper studied the photOFET devices with the structure of single layer of PTCDA and the structure of pentacene/PTCDA planar heterojunction. The photOFET with pentacene/PTCDA planar heterojunction has a better performance.

## 2 Experience

As shown in Fig. 1, it is a schematic diagram of the photOFET based on PTCDA and pentacene. The gate insulation is a layer of 1000 nm  $\text{SiO}_2$  through thermal oxide growth based on the substrate layer of heavily doped  $\text{n}^+\text{-Si}$ . The  $\text{SiO}_2$  substrate was cleaned by ultrasonication with acetone, ethanol, deionized water and blown dry by  $\text{N}_2$  and then dried in a vacuum oven at 60 °C for 10 min. Then, the modified layer of OTS

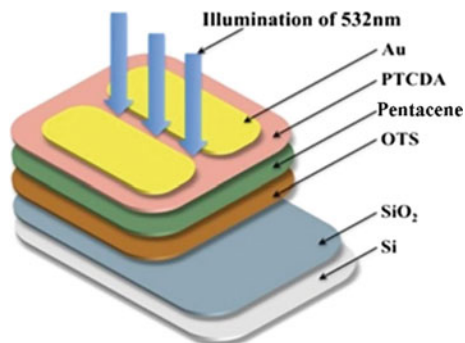


**Fig. 1** Schematic diagram of organic green photosensitive field-effect transistor based on pentacene/PTCDA planar heterojunction

monolayer was formed through OTS processing in the vacuum oven at 120 °C for 2 h. Hole transport layer was deposited on 50 nm pentacene film through evaporation at 0.5 nm/min with the substrate temperature of 75 °C and the PTCDA layer of 30 nm was evaporated on the pentacene layer with the same rate at room temperature. Source and drain electrodes of 30 nm thick were formed with Au at evaporation rate of 4.7 nm/min. The vacuum degree of the vacuum oven used for the forming of organic layer and metal electrode is  $2.1 \times 10^{-3}$  Pa. The length and width of the device channel in this paper are 50 and 2 nm, respectively, and the laser used for test is standard green laser with the output wavelength of 532 nm at the light intensity of 50 mW/cm<sup>2</sup>.

### 3 Results and Discussion

Figure 2 shows the output characteristic of single-layer PTCDA photOFET devices with the typical characteristic of n-channel. The output current is small for the reason of the limitation to low mobility of PTCDA. As a result, it is not suitable for the actual application with high threshold voltage and low 0.8 nA output current even at the gate voltage of -100 V and at the drain voltage of -50 V. Table 1 gives the summary sheet of the performance of different batches of single-layer PTCDA photOFET devices. It can be seen that the mobility of the device is in the order of  $10^{-5}$ - $10^{-4}$ , and the average mobility is  $8.01 \times 10^{-5}$  cm<sup>2</sup>/(V s), which shows the low mobility and poor performance. The device needs to add a large gate voltage to open with high power consumption and the threshold voltage between 65 and 90 V with the average voltage at 71.68 V. Therefore, it is not ideal to use single-layer PTCDA as the semiconductor channel layer of the field-effect transistor, and it is necessary to select the other high mobility semiconductor materials as the carrier channel transport layer. Figure 3 shows the absorption spectra of PTCDA films and pentacene films. As it is shown, PTCDA exhibits two significant absorption peaks at the wavelength of 483 and 561 nm, and the wavelength of green light is 532 nm just between those two peaks. That means PTCDA is a kind of good photosensitive material and can be used in green-light OFETs.

**Table 1** Performance of single-layer PTCDA photOFET devices

Heading level	Device 1	Device 2	Device 3	Device 4	Average
Mobility (cm <sup>2</sup> / (V s))	$9.53 \times 10^{-5}$	$1.14 \times 10^{-5}$	$8.72 \times 10^{-5}$	$2.38 \times 10^{-5}$	$8.01 \times 10^{-5}$
Threshold voltage (V)	66.36	66.01	66.06	88.29	71.68

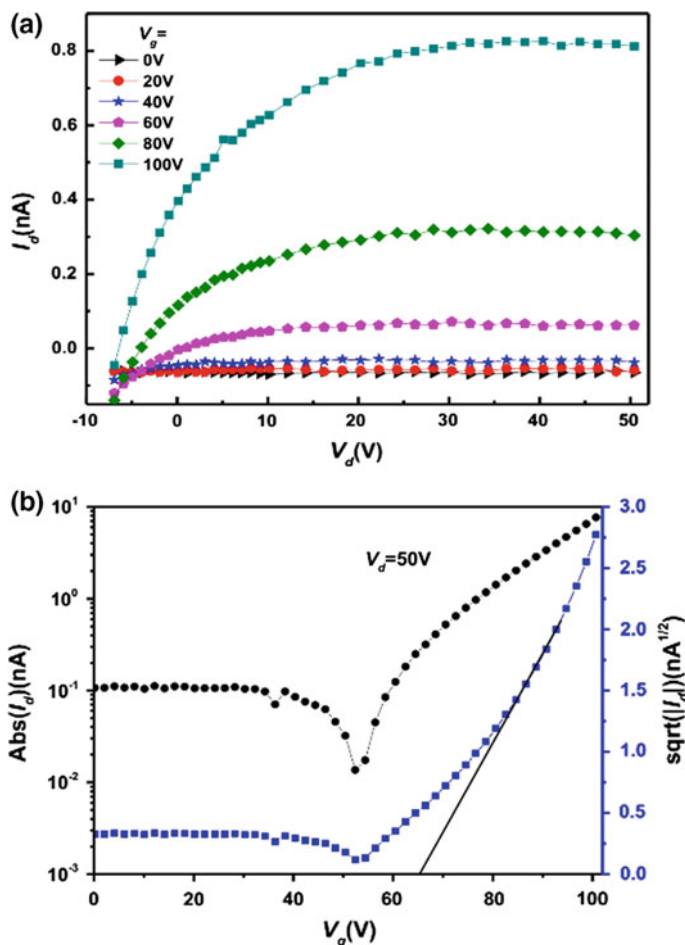


**Fig. 2** a Output characteristics and b transfer characteristics of pentacene/PTCDA photOFET devices

In the meantime, the absorption peaks of pentacene at 586 and 675 nm are still weak compared with PTCDA. And the photOFET based on pentacene/PTCDA is fabricated, in which the photoexciton generation and dissociation are realized mainly in the pentacene/PTCDA interface, while the transport of field-effect current occurs in high mobility channel layer based on pentacene. Additionally, bottom-gate top-contact geometry is used to fabricate the photOFETs.

In Fig. 1, the surface of  $\text{SiO}_2$  after OTS processing is changed from hydrophilic to hydrophobic, its flatness is improved, and the surface suspension keys and traps are reduced, which is conducive to the growth of organic compounds during vacuum evaporation and the preparation of high-quality organic films. Figure 4a shows the AFM image of pentacene film deposited on the OTS substrate, which demonstrates a flat film interface with uniform grain size, and RMS is 8.248 nm. After depositing



30 nm PTCDA on pentacene film, as shown in Fig. 4b, the RMS is slightly increased at 11.248 nm. It is concluded that photOFET based on pentacene/PTCDA demonstrates a good smoothness and medium grain size after OTS processing.

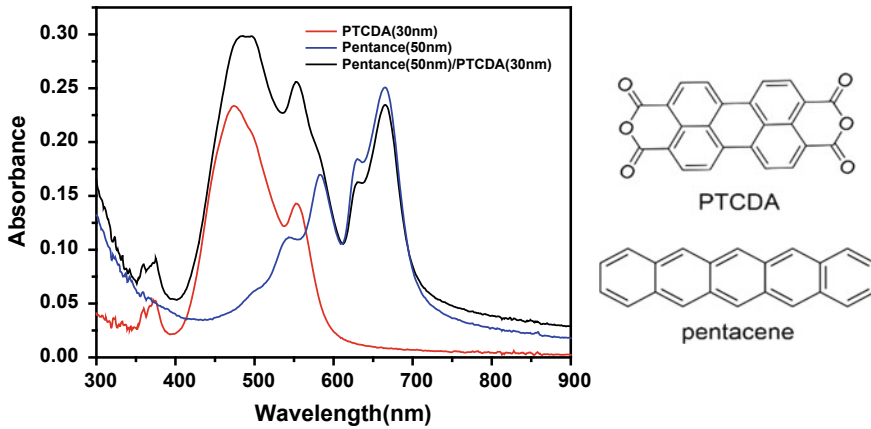


**Fig. 3** UV-Vis absorption spectra and molecular formula of PTCDA (30 nm) and pentacene (50 nm) thin films

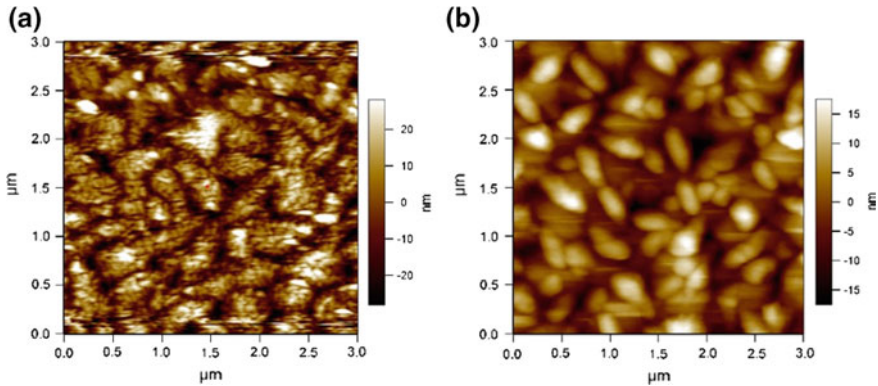


**Fig. 4** a AFM (pentacene) and b pentacene/PTCDA heterojunction thin films

The pentacene/PTCDA OFET devices exhibited a typical p-channel characteristic under the negative gate voltage and the negative drain voltage due to its pentacene heterojunction structure. From Fig. 5, we can see an obvious difference between the source-drain current ( $I_{ds}$ ) under the dark and light conditions. The reason for the great rise of device photocurrent is that the device produced a large number of excitons under the light and affected by the heterojunction interface strong electric field, and the excitons dissociated fast at the interface of pentacene/PTCDA leading to the formation of free holes and electrons. Figure 5a shows the output characteristic curve of

pentacene/PTCDA photOFET, even when the light intensity is weak to only  $0.033 \text{ mW/cm}^2$ , at the  $-50 \text{ V}$  gate voltage and drain voltage, the output current increased by 166.7%. The source-drain current under the condition of illumination increased rapidly, showing a good photosensitivity. The transfer curve is shown in Fig. 5b.

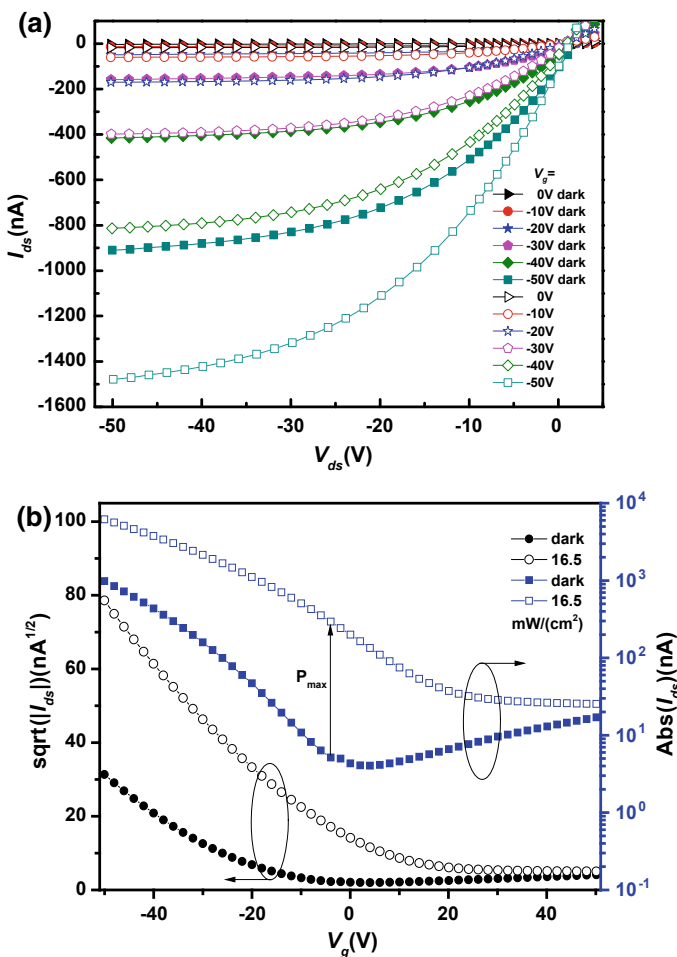


**Fig. 5** Output characteristics (a) and transfer characteristics (b) of a pentacene/PTCDA photOFET device (the solid symbol in the picture indicated a dark condition, and a hollow symbol indicated a light condition)

Light–dark current ratio  $P$  is an important parameter of organic photosensitive field-effect transistor, which is defined as follows [16]:

$$P = \frac{I_{\text{ph}}}{I_{\text{dark}}} = \frac{I_{\text{ill}} - I_{\text{dark}}}{I_{\text{dark}}} \quad (1)$$

where  $I_{\text{ph}}$  is the photocurrent,  $I_{\text{dark}}$  is the dark current, and the  $I_{\text{ill}}$  is the drain current under illumination. Another important parameter is the  $R$ , which is defined as [16]:

$$R = \frac{I_{\text{ph}}}{P_{\text{opt}}} = \frac{I_{\text{ill}} - I_{\text{dark}}}{P_{\text{inc}}A} \quad (2)$$

$P_{\text{opt}}$  is the incident light power,  $P_{\text{inc}}$  is the light intensity,  $A$  is the effective area of illumination.

As shown in Fig. 5, the device mobility  $\mu_{\text{FET}} = 1.73 \times 10^{-2} \text{ cm}^2/(\text{V s})$  and threshold voltage  $V_{\text{T}} = -20.26 \text{ V}$  in the dark. Under the illumination, the device mobility  $\mu_{\text{FET}} = 4.63 \times 10^{-2} \text{ cm}^2/(\text{V s})$  and the threshold  $V_{\text{T}} = -4.37 \text{ V}$ . While the incident intensity is  $16.5 \text{ mW/cm}^2$ , the  $V_{\text{g}} = -50 \text{ V}$  and the  $V_{\text{ds}} = -50 \text{ V}$ , the  $P_{\text{max}}$  of pentacene/PTCDA planar heterojunction devices is 56.15. When incident light intensity is  $0.0033 \text{ mW/cm}^2$ , the  $V_{\text{G}} = -50 \text{ V}$  and the  $V_{\text{D}} = -50 \text{ V}$ ,  $R$  of the device can reach at 19.62 A/W, showing a good photosensitivity.

The photogenerated carriers formed from the exciton dissociation in the PTCDA layer can be transmitted efficiently by using the high mobility material pentacene as the conductive channel layer of the device. The planar heterojunction interface formed by  $p$ -type pentacene and  $n$ -type material PTCDA is also favorable for the dissociation of excitons. The generation and transportation of photogenerated carriers can effectively improve the performance of devices. According to the analysis of AFM image mentioned above, the surface of the pentacene film exhibited a structure like cobblestone with low roughness. The large PTCDA grains cannot fill the concave on the surface of pentacene thin film while forming the PTCDA layer using vacuum evaporation so that the roughness of PTCDA layer increased slightly but the overall effect of film roughness is in the controllable range. In addition, structure like needle on the surface of PTCDA film increases the contact area with Au, improves the conductive efficiency of the electrode and makes the electrons and holes to composite faster in the channel, with the mobility and photosensitivity of device improving.

## 4 Conclusion

This paper analyzed two kinds of photOFETs with pentacene/PTCDA planar heterojunction structure and single PTCDA layer, respectively. The output characteristics of single-layer PTCDA photOFET devices indicate that it has a typical  $n$ -channel, weak output current and high threshold voltage. PhotOFET with pentacene/PTCDA planar heterojunction has a  $p$ -channel and achieves the highest photosensitivity of 56.15, while incident light intensity was  $16.5 \text{ mW/cm}^2$ , and both gate voltage and drain voltage was  $-50 \text{ V}$ . And while incident light intensity was  $0.0033 \text{ mW/cm}^2$  with the same gate voltage and drain voltage, the photoresponsivity reaches the maximum at 19.62 A/W. The performance gets significant optimization compared with the single-layer PTCDA photOFET.

## References

1. Torsi, L., Magliulo, M., Manoli, K., Palazzo, G.: Organic field-effect transistor sensors: a tutorial review. *Chem. Soc. Rev.* **42**(22), 8612–8628 (2013)
2. Mukherjee, B., Mukherjee, M., Choi, Y., Pyo, S.: Control over multifunctionality in optoelectronic device based on organic phototransistor. *ACS Appl. Mater. Interfaces* **2**(6), 1614–1620 (2010)
3. Wakayama, Y., Hayakawa, R., Seo, H.S.: Recent progress in photoactive organic field-effect transistors. *Sci. Technol. Adv. Mater.* **15**(2), 024202 (2014)
4. Li, H., Li, C., Duan, L., Qiu, Y.: Charge transport in amorphous organic semiconductors: effects of disorder, carrier density, traps, and scatters. *Isr. J. Chem.* **54**(7), 918–926 (2014)
5. Peng, Y., Lv, W., Yao, B., Xie, J., Yang, T.: Improved performance of photosensitive field-effect transistors based on palladium phthalocyanine by utilizing Al as source and drain electrodes. *IEEE Trans. Electron Devices* **60**(3), 1208–1212 (2013)
6. Ute, Z., Frederik, A., Tatsuya, Y., Kazuo, T., Hirokazu, K.: Flexible low-voltage organic transistors and circuits based on a high-mobility organic semiconductor with good air stability. *Adv. Mater.* **22**(9), 982–985 (2010)
7. Yasin, M., Tauqeer, T., Karimov, K.S., San, S.E., Kösemen, A.: P3HT: PCBM blend based photo organic field effect transistor. *Microelectron. Eng.* **130**, 13–17 (2014)
8. He, D.D., Nausieda, I.A., Ryu, K.K., Akinwande, A.I., Bulovic, V.: An integrated organic circuit array for flexible large-area temperature sensing. In: 2010 IEEE International Solid-State Circuits Conference (ISSCC). <https://doi.org/10.1109/isscc.2010.5434013>
9. Leem, D.S., Lee, K.H., Park, K.B., Lim, S.J., Kim, K.S.: Low dark current small molecule organic photodetectors with selective response to green light. *Appl. Phys. Lett.* **103**(4), 043305 (2013)
10. Lee, K.H., Leem, D.S., Castrucci, J.S., Park, K.B., Bulliard, X.: Green-sensitive organic photodetectors with high sensitivity and spectral selectivity using subphthalocyanine derivatives. *ACS Appl. Mater. Interfaces* **5**(24), 13089–13095 (2013)
11. Kim, D.H., Kim, K.S., Shim, H.S., Moon, C.K., Jin, Y.W.: A high performance semitransparent organic photodetector with green color selectivity. *Appl. Phys. Lett.* **105**(21), 213301 (2014)
12. Weszka, J., Jarka, P., Hajduk, B., Chwastekogierman, M.: Investigations of morphology and optical properties of thin films of TiOPc/PTCDA donor acceptor couple. *J. Achiev. Mater. Manuf. Eng.* **55**(2), 396–402 (2012)
13. Surya, S., Nagarkar, S., Ghosh, S., Sonar, P., Rao, V.: OFET based explosive sensors using diketopyrrolopyrrole and metal organic framework composite active channel material. *Sens. Actuators B Chem.* **223**, 114–122 (2016)
14. Islam, M.N.: Impact of film thickness of organic semiconductor on off-state current of organic thin film transistors. *J. Appl. Phys.* **110**(11), 114906 (2011)
15. Du, L., Luo, X., Wen, Z.: A striking performance improvement of fullerene n-channel field-effect transistors via synergistic interfacial modifications. *J. Phys. D: Appl. Phys.* **48**(40), 405105 (2015)
16. Hamilton, M.C., Martin, S., Kanicki, J.: Thin-film organic polymer phototransistors. *IEEE Trans. Electron Dev.* **51**(6), 877–885 (2004)



# Bending Characteristics of Flexible Organic Phototransistors Based on Copper Phthalocyanine

Huabiao Zhu<sup>1</sup>, Yuhuan Yang<sup>1</sup>, Yingquan Peng<sup>1</sup>(✉), Wenli Lv<sup>1</sup>, Sunan Xu<sup>1</sup>, Yi Wei<sup>1</sup>, Lei Sun<sup>1</sup>, Ying Wang<sup>2</sup>, and Fangzhi Guo<sup>1</sup>

<sup>1</sup> Institute of Microelectronics, College of Optical and Electronic Technology, China Jiliang University, Xueyuan Street 258#, 310016 Hangzhou, China  
yqpeng@cjlu.edu.cn

<sup>2</sup> College of Information Engineering, China Jiliang University, Xueyuan Street 258#, 310016 Hangzhou, China

**Abstract.** Highly photosensitive flexible organic phototransistors (OPTs) with an organic thin film of copper phthalocyanine (CuPc) as an active layer were prepared. The performance was investigated in different bending cycles. The photo responsivity reduced to 147.2 mA/W from the initial 253 mA/W and the photocurrent to 1510 nA from the initial 2300 nA after 20 cycles; while for bending cycle of 100 and 200, the photo responsivity and photocurrent kept almost unchanged.

**Keywords:** Phototransistor · Bending cycle · Mobility

## 1 Introduction

The field of plastic electronics is evolving at a rapid pace, particularly with the market entry of organic light-emitting diode based displays and screens [1]. Other applications include solar energy conversion, memory circuits for intelligent packaging, amplifiers ordered by light excitation, detection circuits and sensors of ultrasensitive images; in these last applications, the basic component is organic phototransistors (OPTs) [2–5]. Flexible organic phototransistors (FOPTs) based on conjugated polymers and small molecular materials have developed rapidly. The performance of FOPTs has been continuously improved by optimizing the FOPTs structure and synthesizing some soluble organic semiconductor materials. FOPT has the advantages of flexibility, large area feasibility, low cost, low operating temperature, etc. There are many potential applications of flexible display devices. These applications require better bending capability of the device, so a major challenge now is to enhance the stability and mechanical flexibility of the FOPTs for a variety of applications [6, 7]. In this paper, we have demonstrated FOPTs by using copper phthalocyanine (CuPc) active material with the structure of polyethylene terephthalate (PET)/indium tin oxide (ITO)/polyvinyl

alcohol (PVA)(700  $\mu\text{m}$ )/CuPc(50 nm)/Au(100 nm) and investigated the bending characteristics. The results show that the mobility decreases with the number of bending cycles.

## 2 Experiment

Organic semiconductor material CuPc was purchased from J&K Chemical Ltd., PVA from Alfa Aesar and PET coated with indium tin oxide (ITO) from Zhuhai Kaivo Optoelectronic Technology Co., Ltd. Organic phototransistors adopted the conventional bottom gate contact structure; the structure of this paper work was shown in Fig. 1a and was fabricated on 30 $\Omega$ /square (ITO) which coated flexible PET substrates. For the fabrication of device samples, at first, the PET/ITO substrates were cleaned in acetone, absolute ethanol and deionized water and were dried in a drying oven with a temperature of 60  $^{\circ}\text{C}$ . Then a 1- $\mu\text{m}$ -thick PVA film was spin coated with a speed of 3000 r/min from 0.2 g/ml water solution and baked for an hour in an oven at 200  $^{\circ}\text{C}$ . Thereafter, a monolayer of octadecyltrichlorosilane (OTS) was self-assembled by vacuum sublimation; by the self-assembling of an OTS monolayer, a culture dish with 20  $\mu\text{L}$  OTS liquid was quickly placed in the vacuum drying oven in which PET/ITO/PVA samples were loaded, and the temperature was then raised to 120  $^{\circ}\text{C}$ . After the OTS was volatilized, chloroform was used to rinse it. After that a 50-nm-thick CuPc films were deposited on the top of PET/ITO/PVA/OTS surface at a deposition rate of around 6.25  $\text{\AA}/\text{min}$ . At last, Au source-drain electrode film with a thickness of 200 nm was deposited through a shadow mask to define the channel length of 25  $\mu\text{m}$  and width of 20  $\mu\text{m}$ . The vacuum level during the film deposition was  $5 \times 10^{-4}$  Pa. All the current voltage ( $I$ - $V$ ) characteristics were measured in a vacuum chamber (10 Pa) by a home-made organic semiconductor characterization system OSDmeas8.0.

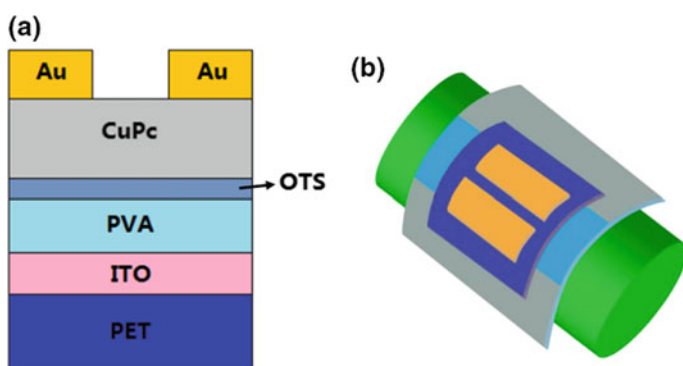


**Fig. 1** **a** The structure schematic of the FOPTs, **b** schematic of bending structure parallel to the channel direction

For the bending test, the device was attached to the glass rod with a radius of 10 mm for several cycles, as shown in Fig. 1b. The performance parameters of OPTs including threshold voltage ( $V_{th}$ ), mobility ( $\mu$ ), photocurrent ( $I_{ph}$ ) and photo responsivity ( $R$ ) in dependence of the bending cycle were extracted.

### 3 Results and Discussion

For OPTs, the saturation region field-effect mobility ( $\mu_{sat}$ ), threshold voltage ( $V_{th}$ ), photoresponsivity ( $R$ ) and photocurrent ( $I_{ph}$ ) are four key performance parameters.  $\mu$ ,  $I_{ph}$  and  $V_{th}$  can be extracted from the following equations [8]:

$$I_{ph} = I_{d,ill} - I_{d,dark} \quad (1)$$

$$I_d = \frac{W}{2L} C_{ox} \mu_{sat} (V_g - V_{th})^2, \dots (V_{ds} > V_g - V_{th}). \quad (2)$$

where  $I_{d,ill}$  and  $I_{d,dark}$  are drain current under illumination and drain current in dark, respectively.  $I_D$  is the drain current,  $W$  and  $L$  are the channel width and length, respectively. In this paper,  $W = 20$  mm,  $L = 25$   $\mu$ m,  $C_{OX}$  is the dielectric capacitance per unit area of the gate dielectric.

Another key parameter of OPTs,  $R$  is defined as the ratio of photocurrent to the incident optical power on the device channel [9]

$$R = \frac{I_{ph}}{P_{opt}} = \frac{I_{ph}}{P_{inc}A} \quad (3)$$

where  $P_{inc}$  is the incident light intensity on the channel of the device, and  $P_{opt}$  is the light power, which can be calculated from incident light intensity multiplied by the effective illuminated area ( $A$ ) of the device ( $W \times L$ ).

In order to study the effect of bending cycles on the device performance, the relationships between  $\mu$ ,  $I_{ph}$ ,  $V_{th}$  and  $R$  as a function of bending cycles were calculated by measuring the transfer characteristics and output characteristics of the devices. The cycles bending test of the horizontal direction of the transistors was performed for 20, 50, 100 and 200 cycles at a fixed bending radius of 10 mm. Figure 2a shows the output characteristics (source-drain current versus source-drain voltage) for the devices without bending measured at gate voltages ( $V_g$ ) varying from 0 to  $-20$  V with a step of 5 V. Figure 2c, e show the output characteristics for the devices when the bending cycles are 100 and 200 measured at  $V_g$  varying from 0 to  $-20$  V with a step of 5 V, respectively. Figure 2d, f show the transfer characteristics of the device in the dark and under illumination for the mechanical bending cycles of 100 and 200, respectively. It can be clearly seen from Fig. 2 that the dark current of the device increases with the number of bends cycles. According to the transfer characteristics and output characteristic curves in Fig. 2,  $\mu$ ,  $I_{ph}$ ,  $V_{th}$  and  $R$  were calculated for different bending cycles.

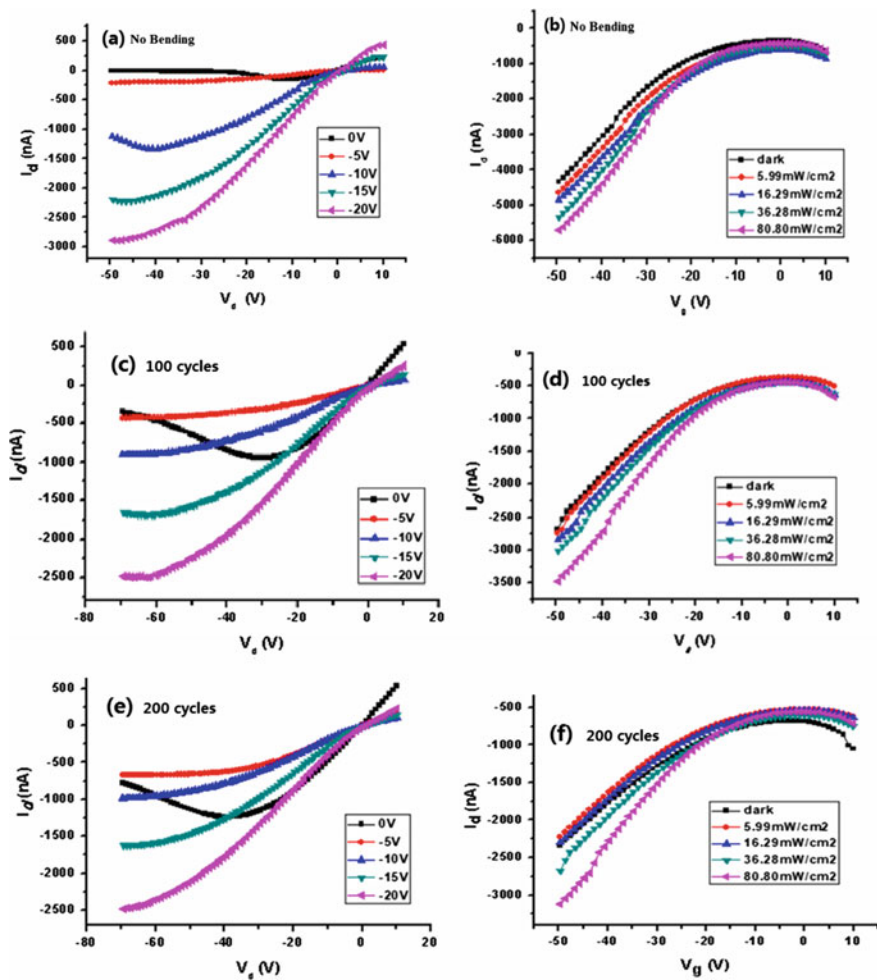
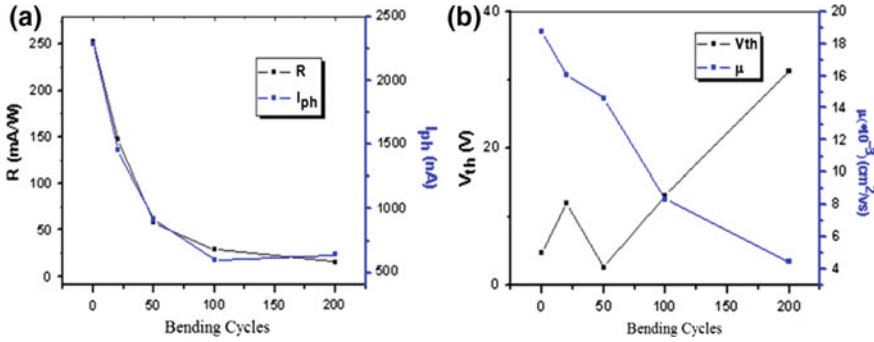


Fig. 2 Output and transfer characteristics of the device at a, b no bending, c, d 100 cycles bending, e, f 200 cycles bending

Figure 3 shows the variation trends of  $R$  and  $I_{ph}$  with the number of bending cycles. Both  $R$  and  $I_{ph}$  decrease rapidly at first and then kept almost constant at large bending cycles.  $R$  reduced to 147.2 mA/W from the initial 253 mA/W and  $I_{ph}$  to 1510 nA from the initial 2300 nA after 20 cycles; while for bending cycle of 100 and 200,  $R$  and  $I_{ph}$  kept almost unchanged. The decrease of  $R$  and  $I_{ph}$  may be related to the destruction of the channel layer during bending [10].

The  $V_{th}$  is directly related to the concentration of carriers in the conductive channel, which determines the conductivity of the device. As shown in Fig. 3b,  $V_{th}$  is always positive, and the reason may be the modification of PVA surface by OTS monolayer. After the surface processed with OTS, the contact between CuPc crystals increased and the conductivity of the channel during charge accumulation thus causes  $V_{th}$  of the





**Fig. 3** **a** Variations in photoresponsivity and photocurrent with bending cycles, **b** threshold voltage and mobility as a function of bending cycles

device to be positive [11]. During the increase of the number of bending cycles, the molecular spacing of the organic layer CuPc is affected by the bending and turns to larger, and the charge transport is hindered causes an increase in  $V_{th}$  and decrease in  $\mu$ .

## 4 Conclusion

In summary, we have demonstrated FOPTs by using CuPc active material, the bending cycles tests were performed. Both  $R$  and  $I_{ph}$  decrease rapidly at first and then kept almost constant at large bending cycles.  $R$  reduced to 147.2 mA/W from the initial 253 mA/W and  $I_{ph}$  reduced to 1510 nA from the initial 2300 nA after 20 cycles; while for bending cycle of 100 and 200,  $R$  and  $I_{ph}$  kept almost unchanged.

**Acknowledgements.** This work was supported by National Key R&D Program of China Grant No.2016YFF0203605, and the Natural Science Foundation of Zhejiang Province Grant No. LY18F050009 and LY18F040007.

## References

- Lucas, B., El Amrani, A., Chakaroun, M., Ratier, B., Antony, R., Moliton, A.: Ultraviolet light effect on electrical properties of a flexible organic thin film transistor. *Thin Solid Films* **517**(23), 6280–6282 (2009)
- Hamilton, M.C., Martin, S., Kanicki, J.: Thin-film organic polymer phototransistors. *IEEE Trans. Electron Devices* **51**(6), 877–885 (2004)
- Noh, Y.Y., Kim, D.Y., Yase, K.: Highly sensitive thin-film organic phototransistors: Effect of wavelength of light source on device performance. *J. Appl. Phys.* **98**(7), 074505 (2005)
- Hu, Y., Dong, G., Liu, C., Wang, L., Qiu, Y.: Dependency of organic phototransistor properties on the dielectric layers. *Appl. Phys. Lett.* **89**(7), 072108 (2006)
- Sheraw, C.D., Zhou, L., Huang, J.R., Gundlach, D.J., Jackson, T.N., Kane, M.G., Francl, J.: Organic thin-film transistor-driven polymer-dispersed liquid crystal displays on flexible polymeric substrates. *Appl. Phys. Lett.* **80**(6), 1088–1090 (2002)

6. Peng, Y., Lv, W., Yao, B., Fan, G., Chen, D., Gao, P., Zhou, M., Wang, Y.: High performance near infrared photosensitive organic field-effect transistors realized by an organic hybrid planar-bulk heterojunction. *Org. Electron.* **14**(4), 1045–1051 (2013)
7. Horowitz, G., Hajlaoui, R., Bouchriha, H., Bourguiga, R., Hajlaoui, M.: The concept of threshold voltage in organic field-effect transistors. *Adv. Mater.* **10**(12), 923–927 (1998)
8. Ren, Q., Xu, Q., Xia, H., Luo, X., Zhao, F., Sun, L., Zhao, Z.: High performance photoresponsive field-effect transistors based on MoS<sub>2</sub>/pentaceneheterojunction. *Org. Electron.* **51**, 142–148 (2017)
9. Peng, Y., Ding, S., Wen, Z., Xu, S., Lv, W., Xu, Z., Tang, Y.: Thin-film encapsulation of organic electronic devices based on vacuum evaporated lithium fluoride as protective buffer layer. *Appl. Phys. A* **123**(3), 178 (2017)
10. Park, J., Seo, J.H., Yeom, S.W., Yao, C., Yang, V.W., Cai, Z., Ju, B.K.: Flexible and transparent organic phototransistors on biodegradable cellulose nanofibrillated fiber substrates. *Adv. Opt. Mater.* **6**(9), 1701140 (2018)
11. Vivek, R., Deepak, B., Shree, T.: Flexible organic field-effect transistors with TIPS-pentacene crystals exhibiting high electrical stability upon bending. *Org. Electron.* **31**, 177–182 (2016)



# Preparation and Characterization of $(\text{C}_6\text{H}_5\text{C}_2\text{H}_4\text{NH}_3)_2\text{PbX}_4$ Perovskite Materials

Meimei Hu, Zungang Liu<sup>(✉)</sup>, Qingyang Meng, and Qianmin Dong

College of Optical and Electronic Technology, China Jiliang University,  
Hangzhou 310016, China

{zgliu78, qmdong}@cjlu.edu.cn

**Abstract.** The organic–inorganic hybrid perovskite is a new material obtained by compounding an inorganic component and an organic component on a molecular structure, and has the advantages of them, so that the material has good electroluminescence and photoluminescence effect, good mechanical processing characteristics, etc. In this paper, we synthesized  $(\text{C}_6\text{H}_5\text{C}_2\text{H}_4\text{NH}_3)_2\text{PbX}_4$  ( $X=\text{Cl}, \text{Br}, \text{I}$ ) by using a liquid phase method. The structure and luminescence properties of perovskite materials were controlled by adjusting the reaction temperature and using different halogen elements. The experimental results show that the  $(\text{C}_6\text{H}_5\text{C}_2\text{H}_4\text{NH}_3)_2\text{PbI}_4$  materials obtained at different reaction temperatures have a layered structure, and their crystallization quality decrease with increasing temperature. In addition, when the X ion is replaced by Br and Cl ions, both synthesized materials have an obvious layered crystal structure, indicating that the type of halogen ion does not affect the crystallization process and the layered structure. However, the photoluminescence spectrum peaks of the materials with different halogen ion are obviously different, verifying that the energy band structure of the material can be well regulated by changing the halogen ions.

**Keywords:** Liquid phase synthesis · Crystal quality · Perovskite

## 1 Introduction

Lead-halide perovskite materials have attracted the attention of researchers in recent years due to their perfect optoelectronic properties: high fluorescence quantum efficiency, low defect density, and continuous adjustable band [1–4]. Among the solar cells, light-emitting diodes and lasers, lead-halide perovskite materials have shown excellent application potential [5–7]. The structural formula of the perovskite material can be expressed as  $\text{ABX}_3$ . According to the A-site ion and the B-site ion, the material can be classified into organic perovskite material, inorganic perovskite material, and organic–inorganic hybrid perovskite material [8]. Organic–inorganic hybrid perovskite material has shown a combination of organic and inorganic components at the molecular level. This material combines good electrical properties, magnetic properties, thermal stability and mechanical stability of inorganic components [9–12], and the

structural variability and machinability of organic components [13]. This research use layer-structured perovskite material phenylethylamine ( $C_6H_5C_2H_4NH_2$ ) to study the structure and photoluminescent properties influenced by halogen ions.

## 2 Experiment

### 2.1 Materials Used

In this experiment, hydroiodic acid (45.0%, Aladdin company), hydrobromic acid (40.0%, Aladdin company), hydrochloric acid (36.0%~38.0%, Aladdin company), lead iodide (98.0%, Aladdin company), lead bromide (98.0%, Aladdin company), lead chloride (99.0%, Aladdin company), and  $\beta$ -phenylethylamine (98.0%) are used without further purification.

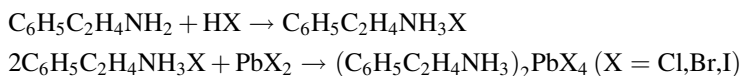
### 2.2 Equipment and Instrument

Constant temperature water bath heating pot (DF101S, Shanghai Yushen Instrument Co., Ltd.) and vacuum drying oven (DZF-6050, Shanghai Yushen Instrument Co., Ltd.) were used for synthesis.

X-ray diffraction (XRD) (D2 PHASER), field emission scanning electron microscopy (SEM) (su-8010), and photoluminescence spectrometer (FlexOne) were used for characterization.

### 2.3 Experimental Steps

In this experiment, crystal powder was synthesized by two-step reaction in liquid phase method, as described by the following equations:



**Synthesis of organic amine salts** The haloid acid and  $\beta$ -phenethylamine (molar ratio 1:1.2) were added to a beaker to react, taking well control the adding speed to avoid evaporation of phenethylamine, as the reaction is exothermic. After the reaction, heated the reacted liquid in 90 °C water bath to get preliminary dried solid powder, which was dried in a vacuum drying oven at 80 °C for two hours, a solid amine salt powder was obtained.

**Synthesis of target products** Haloid acid was selected as the solvent. The organic amine salt obtained in (1) and  $PbX_2$  (molar ratio 2:1) was added to the excessive solvent and stirred with a glass rod until the powder was completely dissolved. Then heated the solution in a water bath with 50, 65, 80 °C, respectively, for two hours, using magnetic stirring to make the reaction more complete. After completion of the reaction, the mixture was cooled down to room temperature, and the precipitate was filtered, dried in a vacuum drying oven for five hours at 80 °C to obtain a solid powder.

### 3 Results and Discussion

#### 3.1 Effect of Reaction Temperature

For studying the effect of reaction temperature, choose I ion as X ion, and select reaction temperatures as 50, 65, and 80 °C, respectively. It can be seen from Fig. 1 that different synthesis temperatures have none effect on the position of the fluorescence peak of the product, but the luminescence intensity is different, indicating a difference in crystal quality.

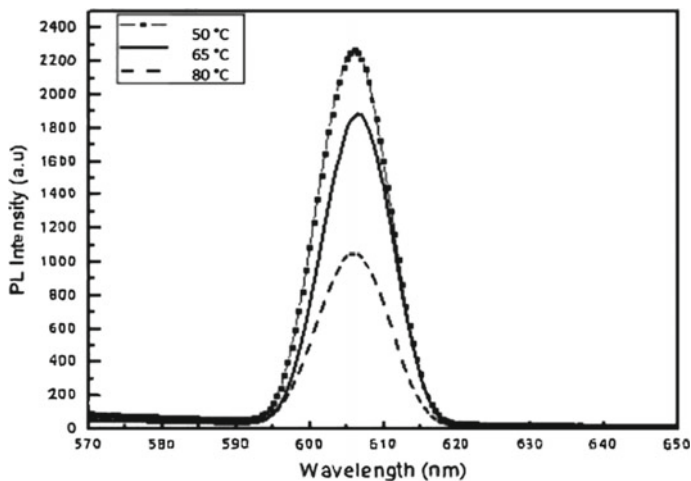


**Fig. 1** Fluorescence spectrum of  $(\text{C}_6\text{H}_5\text{C}_2\text{H}_4\text{NH}_3)_2\text{PbI}_4$  crystal powder prepared at different reaction temperatures (50 °C, 65 °C, 80 °C) (excitation wavelength: 300 nm)

Figure 2 shows the XRD diffraction pattern of the product crystal. For three different reaction temperatures, the distance among the diffraction peaks is obviously equal. The material has an obvious preferred orientation in the direction of (002*l*). Because the diffraction peaks are equidistant and perpendicular to the *c*-axis, the product has a two-dimensional layered structure. The best layered structure is with a product which was obtained at a reaction temperature of 50 °C, with the highest diffraction peaks. When the temperature is raised to 80 °C, the intensity of the diffraction peak become small, together with the appearance of other crystal planes, the layered structure is not as obvious as to those reacted at 50 and 65 °C. Such crystal structure characteristics are also consistent with the luminescence spectral properties of the material.

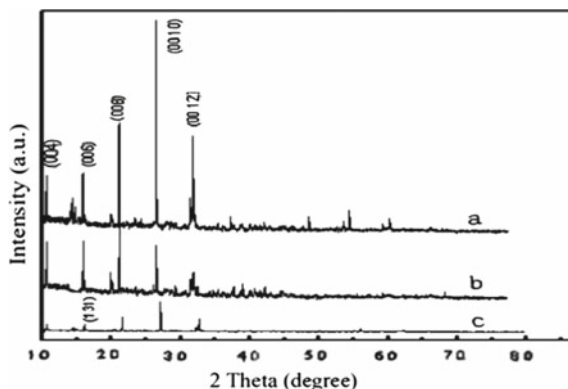


**Fig. 2** XRD pattern of  $(C_6H_5C_2H_4NH_3)_2PbI_4$  crystal powder prepared at different reaction temperatures **a** 50 °C, **b** 65 °C, **c** 80 °C

### 3.2 Effect of Halogen Species

Figure 3 is scanning electron micrographs of  $(C_6H_5C_2H_4NH_3)_2PbI_4$ ,  $(C_6H_5C_2H_4NH_3)_2PbBr_4$  and  $(C_6H_5C_2H_4NH_3)_2PbCl_4$ , and product crystal. It can be seen on the scale of 2  $\mu\text{m}$  that all crystal powders have layered structure. The layered structure characteristics of organic and inorganic hybrid perovskite materials mainly depend on the types of organic compounds rather than halogen ions; we infer that further structural adjustment of perovskite materials can focus on the selection of A-site ions.

Figures 4 and 5 show the XRD diffraction patterns of  $(C_6H_5C_2H_4NH_3)_2PbBr_4$  and  $(C_6H_5C_2H_4NH_3)_2PbCl_4$  prepared at a reaction temperature of 50 °C. It can be seen that the diffraction peaks are all from the direction of (002), indicating that the crystal has good selective growth in this direction and shows a good layered structure.

The specific comparison data of Fig. 6 is shown in Table 1. As the halogen passing from Cl to Br to I, the position of the fluorescent peak is redshifted, and the intensity is gradually enhanced. Because when halogen elements are different, the energy level structure of the material changes, resulting in the change of the material band gap. Verifying that the energy band structure of the material can be well regulated by changing the halogen ions. In addition, the spectrum of  $(C_6H_5C_2H_4NH_3)_2PbCl_4$  showed the characteristics of the superposition of multiple photoluminescence peak (main peak at 380 nm and three satellite peaks at 360, 400, and 480 nm). The full width at half maximum of the spectrum is wider than the previous two materials. Such spectral characteristics are due to the different luminescence mechanisms caused by the uneven particle size distribution of crystalline powder.

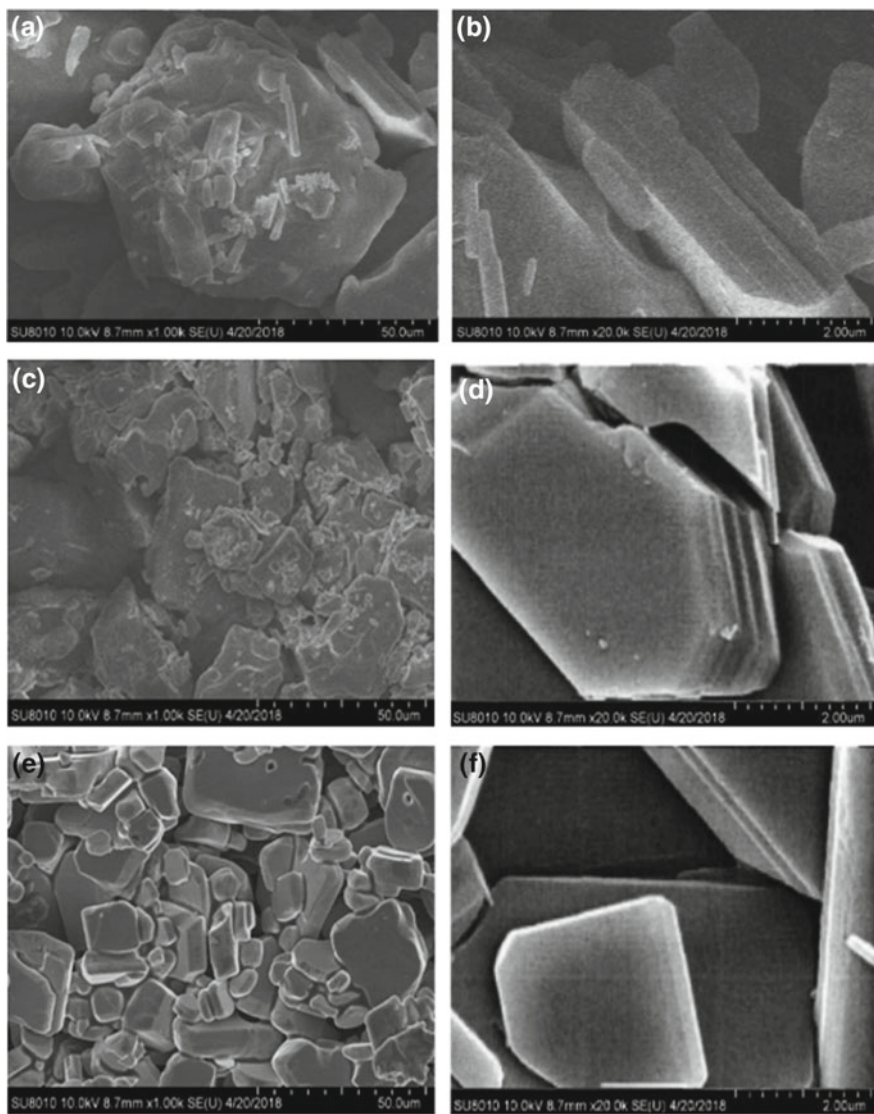


**Fig. 3** SEM of crystal powder under the conditions of 50 °C synthesis **a**, **b**  $(\text{C}_6\text{H}_5\text{C}_2\text{H}_4\text{NH}_3)_2\text{PbI}_4$ , **c**, **d**  $(\text{C}_6\text{H}_5\text{C}_2\text{H}_4\text{NH}_3)_2\text{PbBr}_4$ , **e**, **f**  $(\text{C}_6\text{H}_5\text{C}_2\text{H}_4\text{NH}_3)_2\text{PbCl}_4$  (left scale: 50  $\mu\text{m}$ , right scale: 2  $\mu\text{m}$ )

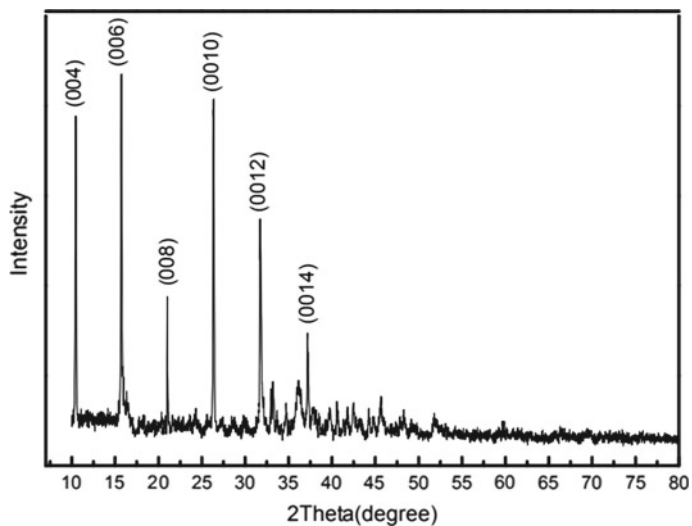


**Fig. 4** XRD pattern of  $(C_6H_5C_2H_4NH_3)_2PbBr_4$  crystal powder synthesized at 50 °C

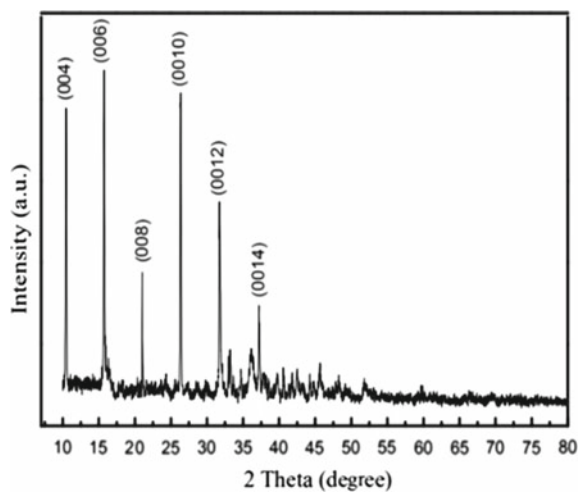


**Fig. 5** XRD pattern of  $(C_6H_5C_2H_4NH_3)_2PbCl_4$  crystal powder synthesized at 50 °C



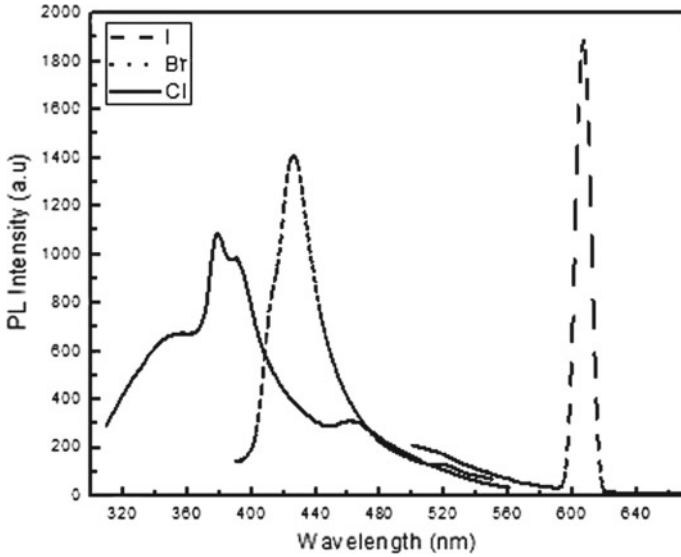


**Fig. 6** Fluorescence spectrum of  $(\text{C}_6\text{H}_5\text{C}_2\text{H}_4\text{NH}_3)_2\text{PbX}_4$  ( $X=\text{Cl}, \text{Br}, \text{I}$ ) crystal powder at  $50\text{ }^\circ\text{C}$

**Table 1** Different perovskite parameters of product crystal (reaction temperature is  $50\text{ }^\circ\text{C}$ )

Synthetic material	Central wavelength (nm)	FWHM (nm)	Maximum emission intensity (a.u.)
$(\text{C}_6\text{H}_5\text{C}_2\text{H}_4\text{NH}_3)_2\text{PbI}_4$	608	10	1875
$(\text{C}_6\text{H}_5\text{C}_2\text{H}_4\text{NH}_3)_2\text{PbBr}_4$	423	34	1392
$(\text{C}_6\text{H}_5\text{C}_2\text{H}_4\text{NH}_3)_2\text{PbCl}_4$	380	75	1080

## 4 Conclusion

In this paper, the perovskite  $(\text{C}_6\text{H}_5\text{C}_2\text{H}_4\text{NH}_3)_2\text{PbX}_4$  ( $X=\text{Cl}, \text{Br}, \text{I}$ ) was synthesized by the liquid phase method. The structure and luminescence properties of perovskite materials were controlled by adjusting the reaction temperature and using different halogen elements during the synthesis. The experiment results show that the layered structure of the composite material is not affected by temperature, but the quality of the material crystal will change.  $(\text{C}_6\text{H}_5\text{C}_2\text{H}_4\text{NH}_3)_2\text{-PbX}_4$  material has good, selectively, growth in the direction of (002*l*). The position of the materials' fluorescence peak shifts with the change of halogen ions, verifying that the band structure of the material can be well regulated by changing the halogen ions, so we can obtain perovskite materials with specific luminous wavelength.

## References

1. Qin, P.L.: High-performance rigid and flexible perovskite solar cells with low-temperature solution-processable binary metal oxide hole-transporting materials. *Solar RRL* **1**, 1700058 (2017)
2. Nishikubo, R.: Thermoresponsive emission switching via lower critical solution temperature behavior of organic-inorganic perovskite nanoparticles. *Adv. Mater.* **29**(23), 1700047 (2017)
3. Manisha, S.: Ultrathin, flexible organic-inorganic hybrid solar cells based on silicon nanowires and PEDOT:PSS. *ACS Appl. Mater. Interfaces.* **6**(6), 4356–4363 (2014)
4. Guichuan, X.: Low-temperature solution-processed wavelength-tunable perovskites for lasing. *Nat. Mater.* **13**(5), 476–480 (2014)
5. Xiao, J., Zhang, H.L.: Recent progress in organic-inorganic hybrid perovskite materials for luminescence applications. *Acta Phys. Chim. Sin.* **32**(8), 1894–1912 (2016)
6. Michael, M.L.: Efficient hybrid solar cells based on meso-super structured organometal halide perovskites. *Science* **338**(6107), 643–647 (2012)
7. Brenner, T.M.: Hybrid organic—inorganic perovskites: low-cost semiconductors with intriguing charge-transport properties. *Nat. Rev. Mater.* **1**(1), 15007 (2016)
8. Zhang, Z.: Research progress of solar cells based on organic-inorganic hybrid perovskites methylamine lead halide. *Energy Environ. Focus* **3**(4), 354–359 (2014)
9. Samuel, D.S.: Electron-hole diffusion lengths exceeding 1  $\mu\text{m}$  in an organometal trihalide perovskite absorber. *Science* **342**(6156), 341–344 (2013)
10. Guichuan, X.: Long-range balanced electron- and hole-transport lengths in organic-inorganic  $\text{CH}_3\text{NH}_3\text{PbI}_3$ . *Science* **342**(6156), 344–347 (2013)
11. Beal, R.E.: Cesium lead halide perovskites with improved stability for tandem solar cells. *J. Phys. Chem. Lett.* **7**(5), 746 (2016)
12. Mitzi, D.B.: High-mobility ultrathin semiconducting films prepared by spin coating. *Nature* **35**(22), 299–303 (2004)
13. Baikie, T.: Synthesis and crystal chemistry of the hybrid perovskite  $(\text{CH}_3\text{NH}_3)\text{PbI}_3$  for solid-state sensitised solar cell applications. *J. Mater. Chem. A* **1**(18), 5628–5641 (2013)



# Absolute Spectral Responsivity Calibration of Terahertz Detector

Bin Wu<sup>1,2(✉)</sup>, Hongchao Wang<sup>2</sup>, Peng Wang<sup>3</sup>, Peng Zhang<sup>2</sup>,  
Wancheng Zhang<sup>2</sup>, and Chengping Ying<sup>2</sup>

<sup>1</sup> Science and Technology on Electronic Test & Measurement Laboratory,  
Qingdao, China

wubinw@126.com

<sup>2</sup> The 41st Institute of China Electronics Technology Group Corporation,  
Qingdao, China

<sup>3</sup> IRay Technology Co., Ltd, Yantai, China

**Abstract.** Calibrating the absolute spectral responsivity is of great importance, because this guides the design and application of terahertz detectors. In this paper, we build a calibration system, and this system can be used to calibrate absolute spectral responsivity of terahertz detectors at a serial of frequencies such as 0.84, 1.63, 2.52, 4.25 THz et al. The key components of the system include a standard terahertz detector and a terahertz gas laser, and other components such as TPX lens and ultrasensitive voltmeter are also included. The calibration system was employed to calibrate a terahertz detector with the model of 12D-3S-VP produced by Gentec Inc., and the absolute spectral responsivity of 193.8 mV/W at 2.52 THz was obtained. The measurement uncertainty is analyzed to be 6.0%. This work not only offers method and system to terahertz detector calibration, but also contributes to high accuracy terahertz power measurement and terahertz device calibration.

**Keywords:** Terahertz detector · Absolute spectral responsivity · Calibration

## 1 Introduction

Absolute spectral responsivity is one of the key parameters of terahertz detector. Calibration of this parameter is very important, because it is the precondition to apply the detector to many areas such as remote sensing and security inspection.

Many groups report their fruitful works on this area. Researchers from PTB modified a cryogenic to make it as a measurable absorbance in the terahertz region, and they considered it as the primary standard detector in the terahertz region. In other words, they extended the application scope of cryogenic radiometer from the visible and infrared region to the terahertz region. In the calibration experiment, they measured the output power of a QCL at the frequency of 2.52 THz with the cryogenic radiometer, and the responsivity of a pyroelectric detector was calibrated from the

measured power and the electrical output of the pyroelectric detector. After this procedure, the pyroelectric detector became a transfer standard, and it has the qualification to calibrate the terahertz power for the industrial application, and the uncertainty was reported as 7.3% at the frequency of 2.52 THz [1–3]. PTB offered their terahertz power calibration service for the first time in the world in 2009 with this calibration system. Though the terahertz power metrology is realized by the modified cryogenic radiometer, the calibration uncertainty is not so satisfying because of the limited knowledge of the absorbance of the cryogenic radiometer cavity. Later, researchers from this group started to improve this calibration work, they modified a terahertz detector bought from Ophir Company and characterized the absorption of the absorber precisely. As a result, they got better terahertz power calibration accuracy by using this standard detector [4–6]. Deng and Sun [7, 8] from National Institute of Metrology of China (NIM) adopted the velvet material as absorber to design a standard terahertz detector. Its dynamic range was from several microwatts to milliwatt grades. They built an absolute spectral responsivity calibration system of terahertz detector based on this standard. In their calibration system, a BWO was employed as the radiation source.

Other works focusing on the standard detector design were also reported; these are not directly related to detector calibration, but as is known, standard detector is the key components of the calibration system, so we still make a brief summarization here. Researchers from NIST found the dense and ultra-long carbon nanotube array has high absorption to the incident terahertz wave, based on this they designed a standard detector which set the nanotube array as the absorber [9]. NIST, PTB and NIM participated in the international terahertz power comparison [10, 11] use their own detector, as a result, they obtained a satisfying result. More recently, researchers from National Metrology Institute of Japan presented a highly sensitive terahertz calorimeter developed using a magnetically loaded epoxy as a broadband absorber; the reflection loss of the absorber is less than 0.04, and measurement uncertainties of this detector at a 95% confidence level were 6.2% for 13  $\mu\text{W}$  at 300 GHz and 5.6% for 1.5  $\mu\text{W}$  at 1THz [12].

In this paper, a calibration system was built to calibrate absolute spectral responsivity of terahertz detectors. A terahertz detector with the model of 12D-3S-VP produced by Gentec Inc. was calibrated, and the measurement uncertainty was also analyzed.

## 2 Calibration Experiment

### 2.1 Calibration Method

The substitution method is commonly used to calibrate responsivity of detectors, because this method can eliminate some uncertainty factors caused by splitters and mirrors. In this method, a standard detector with known responsivity  $R_s$  is applied to detect the radiation from the laser source, and the output electric signal  $U_s$  is indexed as the response of the standard detector. Then, move the standard detector away from the light beam, and move the detector under test to the beam path. It is necessary to make the detector under test have the same position with the standard detector before moved

it away. Next, the output electric signal  $U_d$  is obtained, and the responsivity  $R_d$  of the detector under test can be depicted as follows:

$$R_d = \frac{U_d R_s}{U_s}$$

## 2.2 Calibration System and Experiment

Based on the substitution method above, we built an absolute spectral responsivity calibration system as shown in Fig. 1. The components of the system include a terahertz standard detector, a CO<sub>2</sub> pumped gas terahertz laser, two digital voltmeters, data acquisition and electric displacement guide controlling system.

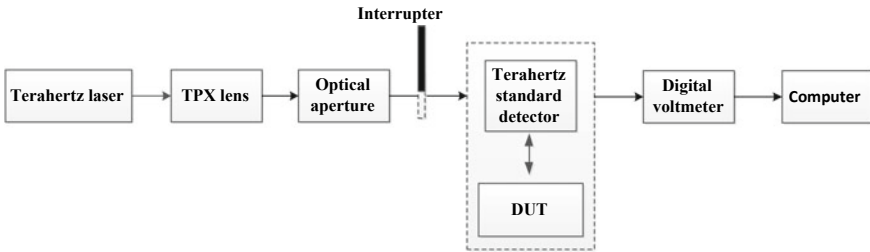


**Fig. 1** Schematic of the terahertz detector calibration system

The terahertz source used in the experiment is FIRL-100 CO<sub>2</sub> pumped gas THz laser produced by the Edinburgh Company. We use the CO<sub>2</sub> laser's 9P36 line as the pump light to excite methanol molecules to get terahertz wave with frequency of 2.52 THz. The terahertz standard detector has good absorption property in the whole terahertz range, and its traceability is resolved via National Institute of Metrology of China. The detector under test (DUT) is a commercial terahertz detector with the model of 12D-3S-VP produced by Gentec Inc., and its absolute spectral responsivity is given as 200 mV/W by the manufacturer. In addition, we use an interrupter to shut off the terahertz beam to measure the dark output signal of the detectors.

The calibration experiment was carried out by the following procedure.

- (1) Turn on the CO<sub>2</sub> pumped gas THz laser, and use the power stable module to realize a stable terahertz power output. Turn on and connect other electrical devices.
- (2) Tune the size of the optical aperture to make sure the terahertz power reached to the detectors has the proper value. In this paper, we adopt a power value of 10 mW.
- (3) Fix the standard detector and the detector under test in the electric displacement guide. Use the computer to control the movement of the electric displacement guide.

- (4) Move the standard detector into the terahertz beam. Use the interrupter to shut off the beam, and index the output dark electric signal  $U_{Ns}$  of the standard detector. Then move away the interrupter, and index the response voltage  $U_s$  when the voltage value is stable.
- (5) Move the detector under test into the terahertz beam, and the beam is also cut off by the interrupter to get the dark electric signal  $U_{Nd}$ . Then the interrupter is moved away to let the terahertz beam reach the detector, and the response voltage is indexed as  $U_d$ .
- (6) The absolute spectral responsivity  $R_d$  is calculated as the following equation:

$$R_d = \frac{U_d - U_{Nd}}{U_s - U_{Ns}} \cdot R_s$$

where  $R_s$  is the absolute spectral responsivity of the standard detector, in this paper,  $R_s = 274.4 \text{ mV/W}$ .

### 3 Results and Measurement Uncertainty Analysis

The experiment was carried out at room temperature, and the environment humidity was 42%. The data acquisition system was used to index the values of  $U_{Ns}$ ,  $U_s$ ,  $U_{Nd}$  and  $U_d$ . The experiment was carried out 6 times, and the result was shown in Table 1.

**Table 1** Experiment data and results

Times	$U_{Ns}$	$U_s$	$U_{Nd}$	$U_d$	$R_d$
1	2.457	0.005	1.726	0.007	192.371
2	2.406	0.006	1.742	0.006	198.483
3	2.339	0.004	1.657	0.006	194.019
4	2.316	0.006	1.636	0.005	193.743
5	2.337	0.005	1.658	0.008	194.151
6	2.322	0.006	1.612	0.007	190.160

The average of  $R_d$  at 2.52 THz was calculated as 193.8 mV/W, and this is in accordance with the value of 200 mV/W given by the manufacturer.

From the calibration method and procedure, the measurement uncertainty origins from the following factors: absolute spectral responsivity of the standard detector  $u_1$ , the output electric signal of the standard detector  $u_2$ , the output electric signal of the detector under test  $u_3$ , the stability of terahertz laser  $u_4$ , disturbance from the environment  $u_5$ , nonlinearity of the standard detector  $u_6$  and other unknown factors  $u_7$  (such as repeatability of the detector position and the stability of the standard detector). In addition, repeatability of the calibration results  $u_8$  is also one origin of uncertainty.

**Table 2** Summary of uncertainty

Uncertainty	Value	Type	Distribution
$u_1$	2.0%	B	Uniform
$u_2$	$9.0 \times 10^{-5}$	B	Uniform
$u_3$	$9.0 \times 10^{-5}$	B	Uniform
$u_4$	1.2%	B	Uniform
$u_5$	0.43%	B	Uniform
$u_6$	0.94%	B	Uniform
$u_7$	0.40%	B	Uniform
$u_8$	0.58%	A	Uniform

We analyzed the uncertainty as shown in Table 2. From the table, we can see the uncertainty information of each item. Among the eight items,  $u_1$ ,  $u_2$ ,  $u_3$ ,  $u_4$  and  $u_6$  were obtained from the certificates.  $u_5$  and  $u_7$  were cited from the data of our laboratory.  $u_8$  was calculated from the data of Rd in Table 1. The combined uncertainty is as follows:

$$u_c = \sqrt{\sum_{i=1}^8 u_i^2} = 3.0\%$$

Thus, an expanded uncertainty of  $U = 6.0\%$  ( $k = 2$ ) was obtained.

## 4 Conclusion

With the development of terahertz technology and its application, terahertz detector calibration becomes more and more important. In this study, we built a calibration system on absolute spectral responsivity of terahertz detector. A terahertz gas laser was adopted as terahertz source, and a novel terahertz radiometry was employed as a standard detector. We carried out calibration experiments in the laboratory, and a detector with the model of 12D-3S-VP was calibrated at 2.52 THz. The result showed the absolute spectral responsivity is 193.8 mV/W at 2.52 THz, and this is in accordance with the value given by the manufacture. The uncertainty was also analyzed, and we got an expanded uncertainty of 6.0%. The calibration system can work at a serial of frequencies, and thus, calibration at other frequencies is also available.

## References

1. Steiger, A., Gutschwager, B., Kehrt, M., Monte, C., Müller, R., Hollandt, J.: Optical methods for power measurement of terahertz radiation. *Opt. Express* **18**(21), 21804–21814 (2010)
2. Steiger, A., Muller, R.: Traceable calibration of Terahertz detectors. In: Conference on Precision Electromagnetic Measurements (CPEM), pp. 256–257. IEEE (2012)

3. Steiger, A., Bohmeyer, W., Kehrt, M., Lange, K., Monte, C., Muller, R.: THz radiometry traceable to SI and suitable detectors. In: 37th International Conference on Infrared, Millimeter, and Terahertz Waves (IRMMW-THz), pp. 1–2. IEEE (2012)
4. Steiger, A., Kehrt, M., Monte, C., Muller, R.: Traceable terahertz power measurement from 1 THz to 5 THz. *Opt. Express* **21**(12), 14466–14473 (2013)
5. Muller, R., Bohmeyer, W., Kehrt, M., Lange, K., Monte, C., Steiger, A.: Novel detectors for traceable THz power measurements. *J. Infrared, Millimeter, and Terahertz Waves* **35**(8), 659–670 (2014)
6. Muller, R., Gutschwager, B., Hollandt, J.: Characterization of a large-area pyroelectric detector from 300 GHz to 30 THz. *J. Infrared, Millimeter, and Terahertz Waves* **36**(163), 654–661 (2015)
7. Deng, Y.Q., Sun, Q., Yu, J., Lin, Y., Wang, J.: Broadband high-absorbance coating for terahertz radiometry. *Opt. Express* **21**(5), 5737–5742 (2013)
8. Deng, Y.Q., Sun, Q., Yu, J.: Broadband black coating for terahertz radiometry. In: 38th International Conference on Infrared, Millimeter, and Terahertz Waves (IRMMW-THz), pp. 1–2 (2013)
9. White, M.G., Dowell, M.L., Lehman, J.H.: Traceable terahertz power metrology at NIST. In: 39th International Conference on Infrared, Millimeter, and Terahertz waves (IRMMW-THz), p. 1. (2014)
10. Steiger, A., Müller, R., Oliva, A., Retal, : Terahertz laser power measurement comparison. *IEEE Trans. Terahertz Sci. Technol.* **6**(5), 664–669 (2016)
11. Deng, Y.Q., Sun, Q., Yu, J., Xu, N., Lin, Y.D.: Progress of terahertz radiometry and international comparison. *Chin. J. Lasers* **44**(3), 0314001 (2017)
12. Iida, H., Kinoshita, M., Amemiya, K.: Accurate measurement of absolute terahertz power using broadband calorimeter. *J. Infrared Milli Terahz Waves*. Published online, 08 March 2018



**Part IV**  
**Sensors and Measurement Technology**



# Determining Hole Mobility of Zinc Phthalocyanine Thin Films by Light-Intensity-Dependent Current–Voltage Characteristics

Yinqin Ye<sup>1</sup>, Fobao Huang<sup>2</sup>, Yingquan Peng<sup>1(✉)</sup>, Wenli Lv<sup>1</sup>,  
Sunan Xu<sup>1</sup>, Yi Wei<sup>1</sup>, Lei Sun<sup>1</sup>, and Ying Wang<sup>3</sup>

<sup>1</sup> Institute of Microelectronics, College of Optical and Electronic Technology, China Jiliang University, Xueyuan Street 258, Hangzhou 310018, China  
yqpeng@cjlu.edu.cn

<sup>2</sup> Institute of Microelectronics, School of Physical Science and Technology, Lanzhou University, South Tianshui Road 222#, Lanzhou 730000, China

<sup>3</sup> College of Information Engineering, China Jiliang University, Xueyuan Street 258, Hangzhou 310018, China

**Abstract.** Carrier mobility is a basic parameter of organic semiconductors. In this paper, hole mobility of zinc phthalocyanine (ZnPc) thin films was determined by light-intensity-dependent current–voltage characteristics. Firstly, built-in voltage,  $V_{bi}$ , of the organic diode with the structure of “ITO/zinc phthalocyanine (ZnPc)/2,9-dimethyl-4,7-diphenyl-1,10-phenanthroline (BCP)/Al” was measured as 0.45 V by using saturation photovoltage method. Based on the value of  $V_{bi}$ , the hole mobility of ZnPc thin film was  $(1.619 \pm 0.06) \times 10^{-6} \text{ cm}^2 \text{ V}^{-1} \text{ s}^{-1}$  by fitting the measured photocurrent–voltage characteristic with the established theory of space-charge-limited photocurrent conduction. The measured carrier mobility coincides with that reported in other literature.

**Keywords:** Carrier mobility · Built-in voltage · SCLC

## 1 Introduction

Phthalocyanines are aromatic organic compounds which have semiconductor properties. Its chemical stability and color density are used as pigments in textile. In the past few decades, metal-substituted phthalocyanine (MPc) film was often used as charge injection layer in organic light-emitting diodes and photovoltaic devices. In the materials of MPc, zinc phthalocyanine (ZnPc) is one of the most promising choices for photovoltaic electrical appliances, such as organic light-emitting devices (OLEDs), gas sensors, and perovskite solar cells [1, 2].

Most organic diodes exhibit built-in voltages, and organic diodes perform different potentials for samples composed of different active layers. There are many ways to measure the built-in voltage in organic diodes, in which saturation photovoltage method [3] has several advantages as simple and reliable. The carrier mobility is one of

the fundamental properties of semiconductors, so measuring the value of carrier mobility is crucial to the research of photovoltaic devices. The available transport characterization methods include space-charge-limited current (SCLC) [4], time of flight (TOF) [5], transient electroluminescence [6], however, SCLC is much more convenient than other existing methods.

In transient electroluminescent method, it needs a pulse generator connected to the two electrodes and provides square wave voltage pulses. In devices, the holes are injected from the anode and the electrons from the cathode. Because of the low carrier mobility of organic semiconductor materials, the holes and electrons' flow produce compound luminescence after a certain time-delay ( $t_d$ ), then use the light-intensity detector to capture the light-intensity signal. The mobility of minority carriers can be calculated by  $t_d$ . SCLC does not need expensive equipments as pulsed laser or high-speed amplifier in TOF neither. All the measuring devices used in SCLC include common laser diodes, light-intensity meters, conventional voltage, and current source meters.

In this paper, the carrier mobility was determined by light-intensity-dependent current–voltage characteristics. The built-in voltage  $V_{bi}$  of ZnPc in diodes was measured as 0.45 V by saturation photovoltage method, and the hole mobility of ZnPc thin film was  $(1.619 \pm 0.06) \times 10^{-6} \text{ cm}^2 \text{ V}^{-1} \text{ s}^{-1}$ , which is coincided with the results in other literatures.

## 2 Experimental

Organic semiconductor material zinc phthalocyanine (ZnPc) was purchased from J&K Chemical Ltd, and 2,7,9-dimethyl-4-diphenyl-1,10-phenanthroline (BCP) from Jilin OLED Co. Ltd. The organic films were deposited at a pressure of  $1.5 \times 10^{-3}$  pa, the deposition rate of the evaporated materials was 1–2 nm min<sup>-1</sup>, and the film thicknesses were controlled by a quartz crystal oscillator near the samples.

The manufacturing process of organic diodes is: Firstly, the substrates were cleaned with acetone, ethanol, and de-ionized water sequentially, then dried by blowing high-pure N<sub>2</sub> and baked in a vacuum oven with temperature of 60 °C about 45 min, next treated with ozone. Secondly, ZnPc and BCP were thermally evaporated on the ITO substrate in sequence. Finally, the top electrode was deposited by evaporation of aluminum (Al) through a shadow mask, defining a device area of 4 mm<sup>2</sup>. By the photoelectric measurements, a red light laser of 655 nm wavelength with power of 50 mW was used as the light source, and a home-made measurement system was used to measure the current–voltage ( $I$ – $V$ ) characteristics. For the  $I$ – $V$  measurements, the voltage was applied at the ITO electrode in reference to the Al electrode, and the device sample was located in a chamber with vacuum of below 10 Pa.

### 3 Results and Discussion

#### 3.1 The Built-in Voltage of ZnPc-Based Diodes

In order to get the hole mobility of ZnPc film, the saturation photovoltage method was used to measure the built-in voltage ( $V_{bi}$ ) of the organic diode. Figure 1 shows the  $I$ - $V$  curves under light irradiation of different intensities. It is seen that at reverse biases, the device current increases with the light intensities, and the position of  $|j_{ph}|$  minimum is the open-circuit voltage ( $V_{oc}$ ). Figure 2 shows the dependence of  $V_{oc}$  on the incident light power extracted from Fig. 1. It is clear that  $V_{oc}$  rises steeply at low-light intensities, flattens out at high-light intensities, and gradually gets the saturation value close to 0.45 V. Consequently, the  $V_{bi}$  of the device was 0.45 V, which is in the range of 0.4–0.5 V reported in literature [7].

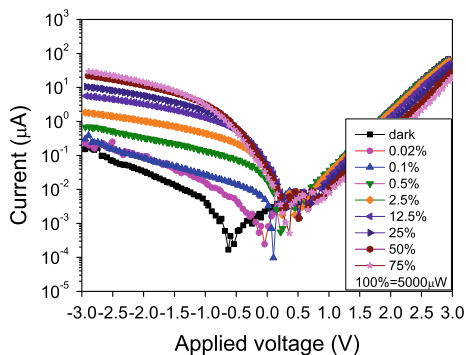


**Fig. 1**  $I$ - $V$  characteristics of ITO/ZnPc(200 nm)/BCP(15 nm)/Al diodes under 655-nm light illumination at different intensities

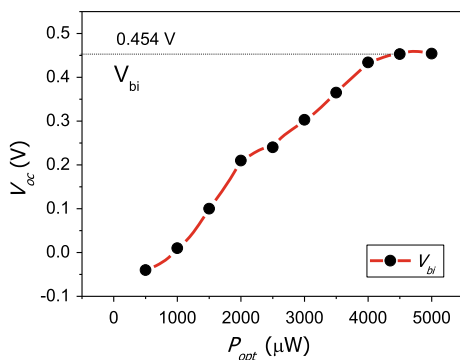


**Fig. 2**  $V_{oc}$ , as a function of the incident optical power, extracted from Fig. 1

In fact, the upper limit of  $V_{bi}$  in a single-layer organic diode can be estimated by using the metal-insulator-metal (MIM) model from the work functions of anode ( $W_a$ ) and cathode ( $W_c$ ), LUMO and HOMO energy levels of organic molecules [8]:

$$V_{bi} = \frac{1}{q} [\text{MIN}(W_a, \text{HOMO}) - \text{MAX}(W_c, \text{LUMO})] \quad (1)$$

where  $q$  is elementary charge. Figure 3 shows the energy level diagram with the structure of ‘ITO/ZnPc(200 nm)/BCP(15 nm)/Al’. As reported in other literature, the work function of the BCP/Al double-layer cathode is 4.2 eV. Taken the work function of ITO to be 4.7 eV, the  $V_{bi}$  in MIM model is calculated to be 0.5 V from Eq. (1), which is reasonably larger than the measured value of 0.45 V.

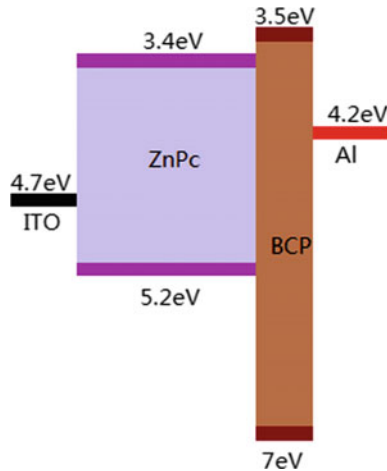


Fig. 3 Schematic energy level diagram of the diodes with the structure of ‘ITO/ZnPc/BCP/Al’

### 3.2 Hole Mobility of ZnPc Thin Film

Under light illumination, the photonic excitons are gathered near the Al electrode, where there form the photoholes and photoelectrons. At the positive bias, the applied electric field is opposite with the internal electric field, and the field is weakened, which results in low dissociation. At the reverse bias, the applied electric field is parallel with the internal electric field, so the ability of exciton dissociation is enhanced. The BCP/Al electrode collects the photoelectrons, causing the photoholes near the BCP/Al cathode to drift toward the ITO electrode. The contribution of the current flow in the device is dominantly from the drift of photoholes across the ZnPc layer toward the ITO electrode, and the current density is given by the equation:

$$j_{ph} = \frac{9}{8} \epsilon_0 \epsilon_r \mu \frac{(V - V_{bi})^2}{d^3} \tag{2}$$

where  $\epsilon_r$  is the dielectric constant of ZnPc film,  $\epsilon_0$  is the vacuum permittivity,  $d$  is film thickness, and  $\mu$  is the hole mobility. Change Eq. (2) to the following [9]:

$$\sqrt{j_{ph}} = \sqrt{\frac{9\epsilon_0\epsilon_r\mu}{8d^3}}(V - V_{bi}) \tag{3}$$

Figure 4 shows the current density  $\text{sqrt}(J_{ph})$  upon light in different intensities.

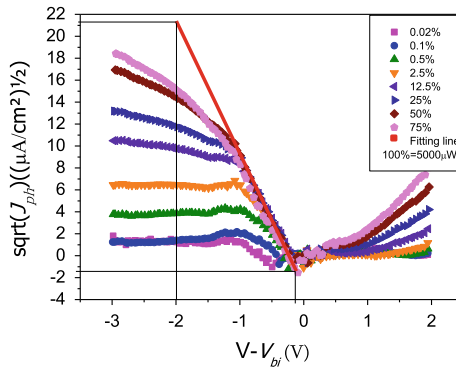


**Fig. 4**  $\text{sqrt}(J_{ph})-(V-V_{bi})$  characteristics of ITO/ZnPc(200 nm)/BCP(15 nm)/Al diode under 655-nm light at different intensities

Taken  $\epsilon_r = 5.4$  [10],  $d = 200$  nm, we can get the hole mobility  $\mu$  from Eq. (3) and the hole mobility of ZnPc thin film was measured to be  $(1.619 \pm 0.06) \times 10^{-6} \text{ cm}^2 \text{ V}^{-1} \text{ s}^{-1}$ , the hole mobility is in the range of  $10^{-7}$ – $10^{-5} \text{ cm}^2/\text{V s}$  [11].

### 4 Conclusion

The hole mobility of ZnPc thin films was measured by using the light-intensity-dependent  $I-V$  characteristics. The  $V_{bi}$  of the organic diodes with the structure of “ITO/ZnPc/BCP/Al” was measured as 0.45 V by saturation photovoltage method. Based on this value of  $V_{bi}$ , the hole mobility of ZnPc thin film was calculated as  $(1.619 \pm 0.06) \times 10^{-6} \text{ cm}^2 \text{ V}^{-1} \text{ s}^{-1}$  by fitting the measured photocurrent–voltage characteristic with the established theory of space-charge-limited photocurrent conduction. The measured value of carrier mobility coincides with that reported in other literatures.


**Acknowledgements.** This work was supported by National Key R&D Program of China Grant No. 2016YFF0203605, and the Natural Science Foundation of Zhejiang Province Grant No. LY18F050009 and LY18F040007.

## References

1. Liu, M., Michael, B.J., Henry, J.S.: Efficient planar heterojunction perovskite solar cells by vapour deposition. *Nature* **501**, 395–398 (2013)
2. Cole, A., McIlroy, R.J., Thorpe, S.C., Cook, M.J., McMurdo, J., Ray, A.K.: Substituted phthalocyanine gas sensors. *Sens. Actuators B* **13**, 416–419 (1993)
3. Ikram, I.M., Rabinal, M.K., Muliman, B.G.: A laboratory experiment to measure the built-in potential of a p–n junction by a photosaturation method. *Eur. J. Phys.* **30**, 127–134 (2009)
4. Mihailetschi, V.D., Wildeman, J., Blom, P.M.W.: Space-charge limited photocurrent. *Phys. Rev. Lett.* **94**, 126602 (2005)
5. Wiley, W.C., McLaren, I.H.: Time-of-flight mass spectrometer with improved resolution. *Rev. Sci. Instrum.* **26**, 1150 (1955)
6. Pinner, D.J., Friend, R.H., Tessler, N.: Transient electroluminescence of polymer light emitting diodes using electrical pulses. *J. Appl. Phys.* **86**, 5116 (1999)
7. Tyler, B.: Organic optoelectronic devices employing small molecules. Ph.D. Dissertation, Arizona State University (2014)
8. Wang, Y., Ma, C., Wang, R., Li, R., Peng, Y.: Model of mixing ratio dependence of built-in voltages in organic bulk heterojunction solar cells. *J. Optoelectron. Adv. Mater.* **13**, 165 (2011)
9. Huang, F., Peng, Y., Xu, K., Lv, W., Xu, S., Wang, Y., Tang, Y., Wei, Y., Yang, Y., Liu, G.: Simultaneous determination of built-in voltage and charge carrier mobility in organic diodes from light intensity dependent current–voltage characteristics. *J. Phys. D Appl. Phys.* **50**, 205106 (2017)
10. Wojdyła, M., Derkowska, B., Łukasiak, Z., Bała, W.: Absorption and photoreflectance spectroscopy of zinc phthalocyanine (ZnPc) thin films grown by thermal evaporation. *Mater. Lett.* **60**, 3441–3446 (2006)
11. Widmer, J., Fischer, J., Tress, W., Leo, K., Riede, M.: Electric potential mapping by thickness variation: a new method for model-free mobility determination in organic semiconductor thin films. *Org. Electron.* **14**, 3460–3471 (2013)



# Sensing Inter-dot Tunneling Using Nonlinear Absorption in Coupled Quantum Dots

Aihong Yang<sup>1,2</sup>(✉), Yan Xu<sup>1,2</sup>(✉), and Yandong Peng<sup>1,2</sup> 

<sup>1</sup> College of Electrical Engineering and Automation, Shandong University of Science and Technology, Qingdao 266590, China  
{yangah\_phys, xly5}@163.com

<sup>2</sup> College of Electronic Communication and Physics, Shandong University of Science and Technology, Qingdao 266590, China

**Abstract.** Tunneling-induced nonlinear absorption properties are investigated in coupled quantum dots. Tunneling causes constructive interference for the fifth nonlinearity and total absorption is enhanced dramatically. The nonlinear absorption provides sensitive detection for inter-dot tunneling.

**Keywords:** Tunneling measurement · Nonlinear absorption · Coupled quantum dots

## 1 Introduction

Coherent absorption is related with the imaginary part of medium susceptibility and is widely used in laser-matter interaction process. Broadband absorption spectrum is highly desirable for solar photovoltaics, stealth and optical modulator [1, 2]. Narrow absorption spectrum can be considered for sensor applications [3–6]. Many methods are proposed to enhance medium absorption by using, for example, electromagnetically induced transparency (EIT) [7], metamaterials [1], cavity quantum electrodynamics (CQED) [8] and tunneling-induced transparency (TIT) [9]. The main difference between TIT method and others is that TIT arises from tunneling-induced coherence that is an inherent coherence determined by structure. While EIT relies on external field-induced coherence for atoms, inter-mode interference for metamaterials and strong coupling for CQED.

In this work, we investigate tunneling-induced nonlinear absorption of coupled quantum dots (CQDs). Previously, we studied large nonlinear absorption in the weak-coupling regime [9]. Here we further consider strong nonlinear absorption in the strong-coupling regime. Resonant tunneling causes constructive interference for the fifth-order nonlinearity, whose strength is a few ten times larger than the linear absorption. The enhanced nonlinear absorption is very sensitive to inter-dot tunneling changes. The sensitivity with strong coupling is several times larger than that with the weak coupling.



## 2 Model, Equation and Results

The CQD model we considered is shown in Fig. 1. CQDs are produced on GaAs(001) substrates by a unique combination of precise in situ atomic layer etching and molecular beam epitaxy. It provides homogeneous ensembles of CQDs with a low density. The two dots of a CQD are aligned along the  $[1\bar{1}0]$  direction. We use the symbol  $X_{e_R, h_R}^{e_L, h_L}$  to denote the exciton states of the CQDs, where the superscript (subscript) represents the numbers of electrons and holes in the left (right) dot. The state  $X_{0,0}^{0,0}$  denotes the ground state  $|1\rangle$  without excitation.  $X_{0,0}^{1,1}$  represents the exciton state  $|2\rangle$  directly excited by a probe field.  $X_{1,0}^{0,1}$  denotes the indirect exciton state  $|3\rangle$ , where the excited electron tunnels to the neighbor dot with a bias voltage.  $X_{2,1}^{0,1}$  represents the biexciton state  $|4\rangle$  excited by another signal field. Using the density matrix master equation,  $\dot{\rho} = -i[H, \rho] + L\rho$  [7, 8] with the system Hamiltonian  $H$  [9] and the decay term  $L\rho$  [10], in the interaction picture and with rotating wave approximation, we get the medium susceptibility  $\chi = \chi_L + \chi_{NL}$  [10]. The linear susceptibility is

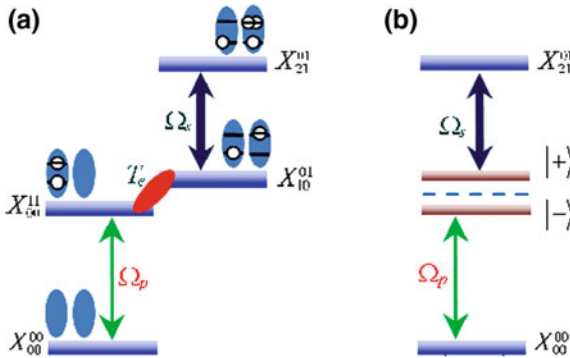


**Fig. 1** **a** Four-level CQD model with coupling configuration and **b** its dressed-state presentation

$$\chi_L/N = -[(i\Gamma_4 + \Delta_2 + \omega_{24})(\Delta_2 - \Delta_4 + \omega_{24}) - \Omega_c^2]/Z_1. \quad (1)$$

The nonlinear susceptibility is

$$\chi_{NL}/N = \chi^{(3)}/N + \chi^{(5)}/N, \quad (2)$$

where the third-order nonlinear term

$$\begin{aligned} \chi^{(3)} = & (\Delta_2 - \Delta_4 + \omega_{24})\{T_c^2(i\Gamma_4 + \Delta_4) - (\Delta_2 - \Delta_4 + \omega_{24})[\Gamma_4^2 + 2i\Gamma_4(\Delta_2 + \omega_{24}) \\ & + 3(\Delta_2 + \omega_{24})^2]\}\Omega_c^2 / (Z_3|Z_3|^2), \end{aligned} \quad (3)$$

and the fifth-order nonlinear term

$$\begin{aligned} \chi^{(5)} = & -[(T_e^2 - 3\Delta_2^2\Delta_4 - 6\Delta_2\omega_{24} + 3\Delta_4\omega_{24} - 3\omega_{24}^2) \\ & - i\Gamma_4(\Delta_2 - \Delta_4 + \omega_{24})]\Omega_c^4 / (Z_3|Z_3|^2), \end{aligned} \quad (4)$$

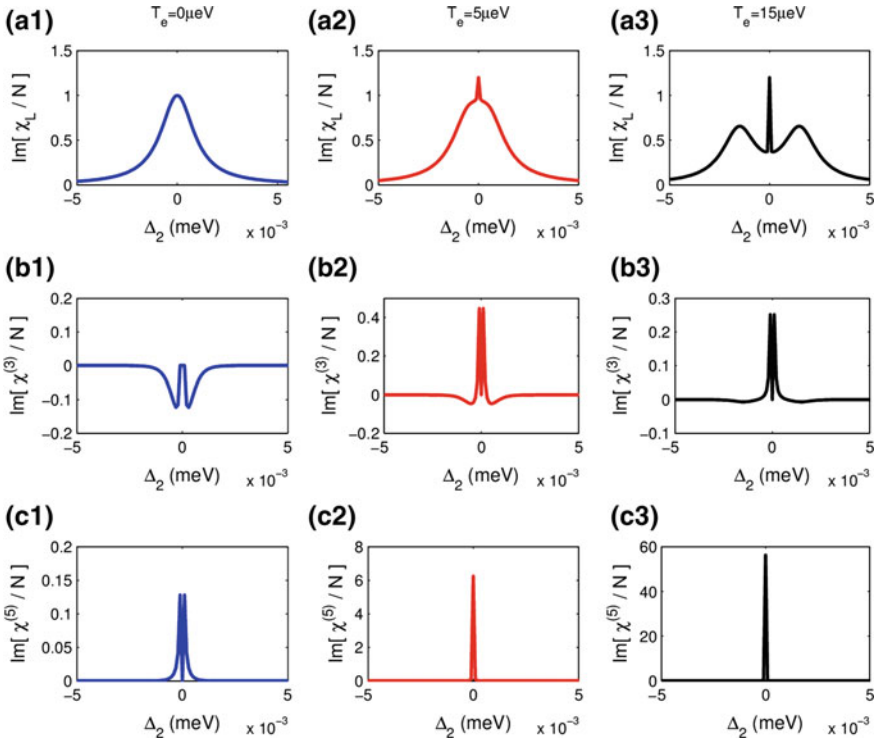
with

$$\begin{aligned} Z_1 = & -T_e^2(\Delta_2 - \Delta_4 + \omega_{24}) + (i\Gamma_2 + \Delta_1)[(i\Gamma_4 + \Delta_2 + \omega_{24})(\Delta_2 - \Delta_4 + \omega_{24}) - \Omega_c^2], \\ Z_2 = & (\Delta_2 - \Delta_4 + \omega_{24})\{T_e^2 + (\Gamma_2 + i\Delta_2)[\Gamma_4 + i(\Delta_2 + \omega_{24})]\} + (-i\Gamma_2 + \Delta_2)\Omega_c^2, \\ Z_3 = & T_e^2(\Delta_2 - \Delta_4 + \omega_{24}) + (\Gamma_2 - i\Delta_2)\{\Gamma_4(\Delta_2 - \Delta_4 + \omega_{24}) \\ & - i[\Delta_2^2 - \Delta_2\Delta_4 + |\Delta_2 - \Delta_4 + \omega_{24}| - \Omega_c^2]\}, \end{aligned}$$

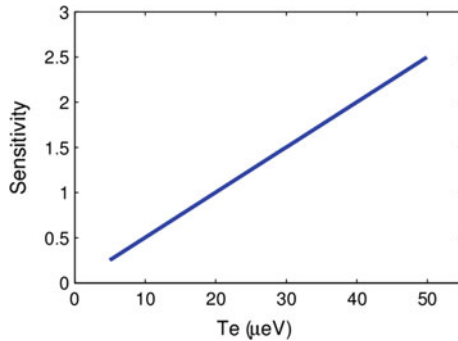
$N = 2|\mu_{21}|^2\Gamma_{\text{opt}}/(\varepsilon_0\hbar V\Omega_p)$ .  $\Gamma_{\text{opt}}$  is the optical confinement factor describing the fraction of power guided in QDs, and  $V$  is the volume of single CQDs.  $\Omega_j$  is Rabi frequency of coupling fields.  $\Delta_2$  and  $\Delta_4$  are their frequency detunings.

Figure 2 shows the linear and nonlinear absorptions, assuming  $\Gamma_2 = \Gamma_4 = \Gamma = 10$  eV for simplicity. When bias voltage turns off, inter-dot tunneling is weak and can be ignored due to different dot sizes. The CQDs behave like a two-level absorption medium. There is strong linear absorption (Fig. 2a1) and no nonlinear absorptions (Fig. 2b1, c1) at a resonance frequency ( $\Delta_2 = 0$ ). When the bias voltage is applied, electron levels in conductance bands come closely and tunneling arises. Resonant tunneling induced constructive interference in the linear and nonlinear absorptions. In the weak-coupling regime, e.g.,  $T_e = 5$   $\mu\text{eV}$ , a sharp peak appears on the top of the linear absorption spectrum  $\text{Im}[\chi_L]$  (Fig. 2a2), and a strong nonlinear peak appears in the fifth-order nonlinear term  $\text{Im}[\chi^{(5)}]$  (Fig. 2c2). In the strong-coupling regime, e.g.,  $T_e = 15$   $\mu\text{eV}$ , the linear absorption peak becomes separated from the background absorption with little change of the peak value (Fig. 2a3); the nonlinear absorption increases dramatically with amplitude of  $\sim 60\Gamma$  (Fig. 2c3), which is about ten times larger than the nonlinear absorption in weak-coupling regime,  $6\Gamma$ . This may be understood in the dress-state picture. The tunneling couples the states  $|2\rangle$  and  $|3\rangle$  and two new eigenstates appear,  $|\pm\rangle = (|2\rangle \pm |3\rangle)/2$ . There are two optical paths with coupling fields  $\Omega_p$  and  $\Omega_s$ ,  $|1\rangle - |\pm\rangle - |4\rangle$ . The inter-path interference leads to the enhanced nonlinear absorption.

We find the nonlinear absorption is sensitive to the tunneling strength, which can be used to probe inter-dot tunneling changes. The probe sensitivity of tunneling can be defined as  $S = |\partial\text{Im}[\chi_{\text{NL}}]/\partial T_e|$  according to sensitivity expression in Ref. [11]. The numerical results in Fig. 3 show that the sensitivity in the strong-coupling regime (e.g.,  $S \sim 2$  for  $T_e = 40$   $\mu\text{eV}$ ) is one order of magnitude of larger than that in the weak-coupling one (e.g.,  $S \sim 0.2$  for  $T_e = 5$   $\mu\text{eV}$ ). This can also be understood from Fig. 2. In the weak-coupling regime, FWHM is  $\sim 0.01$   $\mu\text{eV}$ . The narrower linewidth the absorption spectrum has, the better sensitivity the probe has. The scheme may help to design novel nonlinear optical sensing devices [12].



**Fig. 2** Linear  $\text{Im}[\chi_L/N]$  (first row), third nonlinear  $\text{Im}[\chi^{(3)}/N]$  (second row) and fifth-order nonlinear  $\text{Im}[\chi^{(5)}/N]$  (third row) absorptions with no tunneling  $T_e = 0$  (left column), weak coupling  $T_e = 0.5 \mu\text{eV}$  (central column) and strong coupling  $T_e = 15 \mu\text{eV}$  (right column).  $\Omega_s = 2 \mu\text{eV}$ ,  $\Delta_2 = 0$ ,  $\Delta_4 = 0$  and  $\omega_{23} = 0$



**Fig. 3** Sensitivity of nonlinear absorption about tunneling with other parameters as Fig. 2

**Acknowledgements.** The work is supported by the National Natural Science Foundation of China (Nos. 61675118, 11547037), the SDUST Research Fund (No. 2014JQJH104) and the innovation fund of postgraduate (Nos. SDKDYC170236, SDKDYC180365).

## References

1. Le, K., Bai, J.: Enhanced absorption efficiency of ultrathin metamaterial solar absorbers by plasmonic Fano resonance. *J. Opt. Soc. Am. B* **32**(4), 595–600 (2015)
2. Cossel, K., Waxman, E., Finneran, I., Blake, G., Ye J., Newbury.: Gas-phase broadband spectroscopy using active sources: progress, status, and applications. *J. Opt. Soc. Am. B* **34** (1), 104–129 (2017)
3. Luo, S., Zhao, J., Zuo, D., Wang, X.: Perfect narrow band absorber for sensing applications. *Opt. Express* **24**(9), 9288–9294 (2016)
4. Peng, Y., Yang, A., Chen, B., Li, L., Liu, S., Guo, H.: Tunable, high-sensitive measurement of inter-dot transition via tunneling induced absorption. *Appl. Phys. Lett.* **109**, 141101 (2016)
5. Wang, L., Di, K., Zhu, Y., Agarwal, G.: Interference control of perfect photon absorption in cavity quantum electrodynamics. *Phys. Rev. A* **95**, 013841 (2017)
6. Peng, Y., Yang, A., Xu, Y., Wang, P., Yu, Y., Guo, H., Ren, T.: Tunneling induced absorption with competing nonlinearities. *Sci. Rep.* **6**, 38251 (2016)
7. Scully, M., Zubairy, M.: *Quantum Optics*, 1st edn. Cambridge University Press, New York (1997)
8. Zhao, Q., Li, X.: A Bargmann system and the involutive solutions associated with a new 4-order lattice hierarchy. *Anal. Math. Phys.* **6**(3), 237–254 (2016)
9. Li, X., Zhao, Q.: A new integrable symplectic map by the binary nonlinearization to the super AKNS system. *J. Geom. Phys.* **121**, 123–137 (2017)
10. Zhang, Y., Belic, M., Wu, Z., Yuan, C., Wang, R., Lu, K., Zhang, Y.: Multicharged optical vortices induced in a dissipative atomic vapor system. *Phys. Rev. A* **88**, 013847 (2013)
11. Li, J., Yu, R., Ding, C., Wu, Y.: PT-symmetry-induced evolution of sharp asymmetric line shapes and high sensitivity refractive index sensors in a three-cavity array. *Phys. Rev. A* **93**, 023814 (2016)
12. Li, C., Wang, K., Wang, J., Zhang, Z., Peng, Y.: Application research of nonlinear optical sensing properties in coupled quantum dots system. *J. Shandong Univ. Sci. Tech. (Nat. Sci.)* **37**(6), 93–99 (2018)



# Study on the Pressure of HF Gas Detection in High-Voltage Electrical Equipment by TDLAS Technology

Shiling Zhang<sup>1</sup>(✉), Qiang Yao<sup>1</sup>, Xintian Li<sup>2</sup>, and Yunqi Yue<sup>2</sup>

<sup>1</sup> State Grid Chongqing Electric Power Company Electric Power Research Institute, Chongqing, China

526793305@qq.com

<sup>2</sup> Henan Province Rilixin Private Aviation Company, Zhengzhou, China

**Abstract.** The schematic diagram of the optical cavity design has been introduced in detail; meanwhile, the principle of measuring gas concentration with optical resonator is also introduced. Using the optical cavity spectroscopy technology, the gas component detection system is set up to realize high precision online monitoring of gas components such as HF. The detection system uses narrow line-width semiconductor laser to select the characteristic gas spectrum and output the absorption peak wavelength. Three kinds of gas concentration are measured by time division multiplexing, and the online sampling device of closed loop gas is integrated to complete the monitoring platform of high precision. The system needs the saw-tooth wave of 1 Hz, which can be generated by internal DA of ADSP-403. At the same time, the system needs a modulation signal of about 5 kHz, and the debugging signal with such high frequency cannot be generated by DA of micro-controller itself. The system uses DDS generator AD9850 to generate sinusoidal modulation signal which is superimposed on the saw-tooth wave to drive the laser. The paper has developed the SF<sub>6</sub> composition monitoring device based on optical attenuation technology, which provides the new research method for the online monitoring of gas components such as HF with the high accuracy of 3 ppm.

**Keywords:** Optical resonator · Online monitoring · Characteristic gas spectrum · Absorption peak wavelength

## 1 Introduction

Sulfur hexafluoride (SF<sub>6</sub>) gas as excellent insulation and arcing medium has been widely applied in the sulfur hexafluoride gas-insulated circuit breakers, gas-insulated combination electric appliance (gas-insulated substation-GIS), transformers, transformer, power cable, etc [1]. Electrical equipment in the process of running in the high-voltage electric arc or energetic factor will happen under the action of SF<sub>6</sub> gas decomposition, producing hydrogen fluoride (HF), sulfur dioxide (SO<sub>2</sub>), hydrogen sulfide (H<sub>2</sub>S), carbon monoxide (CO), fluoride thionyl SOF<sub>2</sub>, sulfuryl fluoride (SO<sub>2</sub>F<sub>2</sub>), and other compounds. With HF as important the decomposition product of the first, high-voltage equipment of HF gas detection is very important, but because of its

chemical properties and lively, strong physical adsorption, offline detection means is difficult to detect [2].

Based on the analysis of tunable laser technology (TDLAS), using the laser energy is absorbed by gas molecules frequency selective principle of high resolution spectrum of a gas concentration measurement and designs a suitable for high-voltage switch of the online detection system, to realize online detection of HF gas [3]. For high-voltage electrical equipment, HF gas pressure in the gas absorption spectral lines broadening serious problem through theoretical analysis put forward a kind of different concentration of high-voltage electrical equipment pressure correction algorithm, and algorithm is verified in the experiment.

## 2 Theoretical Analysis of HF Gas Concentration Detection

### 2.1 Principle of TDLAS Technology

The theoretical basis of TDLAS technology is Lambert–Beer law. It makes the laser emitted by the laser attenuation occurs after the absorption of the gas being measured, the absorption attenuation of laser signal is amplified when handling and collection, get information of measured gas concentration [4]. According to the Lambert–Beer’s law, the incoming light intensity of laser is  $I_0$ , and the absorption path of the laser is  $L$  (cm), and the outgoing light intensity after absorption attenuation is  $I_t$ , which is shown in Fig. 1.

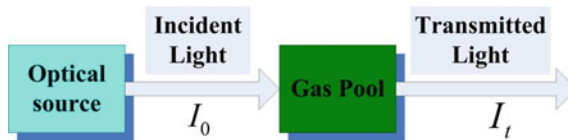


Fig. 1 Schematic diagram of Lambert–Beer law

The expression of Lambert–Bill’s law can be described as follows [5], where  $C$  is the concentration of the measured gas, the  $\phi(\nu)$ ,  $P$  and  $S(T)$  correspond to absorption coefficient, pressure, the linear intensity of lines, respectively. Using the TDLAS technology to detect the HF gas concentration, according to formula (1):

$$\frac{I_t}{I_0} = \exp[-S(T)\phi(\nu)pCL] \quad (1)$$

If the absorption line of HF gas is obtained, the spectral information of the attenuation can be obtained, and the gas concentration is deduced. In the study of gas detection, the linear form of gas spectra plays an important role in gas detection. The gas absorption spectrum observed by the spectrometer is a nonlinear geometric line of width, which is formed by the broadening mechanism of gas molecules. Common three kinds of molecular broadening are: Gaussian linear, Lorentz lines, and Voigt lines, by

detecting the absorption spectral lines of measured gas molecules can grasp information [6]. In view of the high gas pressure selected in this experiment, the main effect is collision broadening of HF gas, and the absorption spectrum line of the gas molecules can be described by Lorentz line, as shown below.

$$\phi_L(\nu, \nu_0) = \frac{2}{\Delta\nu_G} \left( \frac{\ln 2}{\pi} \right)^{1/2} \frac{a}{\pi} \int_{-\infty}^{+\infty} \frac{\exp(-y^2) dy}{a^2 + (w - y)^2} \quad (2)$$

## 2.2 Selection of HF Gas Absorption Line

The infrared absorption spectra of HF gas were obtained through the HITRAN standard spectral bank [6]. As shown in Fig. 2, the HF gas had a strong absorption peak at 2.47  $\mu\text{m}$  ( $4039 \text{ cm}^{-1}$ )–2.67  $\mu\text{m}$  ( $3742 \text{ cm}^{-1}$ ), while there was absorption peak around 1.26  $\mu\text{m}$  ( $7936 \text{ cm}^{-1}$ )–1.36  $\mu\text{m}$  ( $7352 \text{ cm}^{-1}$ ).

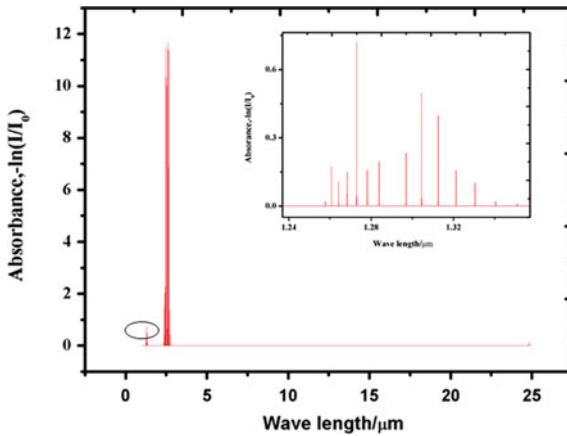


**Fig. 2** Infrared absorption spectra of HF gas (sub-graph is the effect of local amplification)

Considering that  $\text{SF}_6$  gas encountered arc and high temperature, it may produce  $\text{SO}_2$ ,  $\text{H}_2\text{S}$ ,  $\text{CO}$ ,  $\text{CO}_2$ ,  $\text{CF}_4$ ,  $\text{SOF}_2$ ,  $\text{SO}_2\text{F}_2$ , and other gases, due to the long-term use of gas leakage in high-voltage electrical equipment, there will be steam generation, and they may also interfere with HF measurement. Contrast material absorption spectra peaks above, further to determine the characteristics of the HF gas absorption lines,  $\text{H}_2\text{O}$ ,  $\text{H}_2\text{S}$ ,  $\text{SO}_2$  in 2.5  $\mu\text{m}$  (near  $4000 \text{ cm}^{-1}$ ) there are different levels of absorption, can produce interference of HF detection, on the other hand, although there is strong absorption peak near 2.5  $\mu\text{m}$ , but the laser's work in this area requires a higher cost of providing a cooling system for the light source and detector. To sum up, the absorption line of the circle is locally amplified, and 1.273  $\mu\text{m}$  ( $7855 \text{ cm}^{-1}$ ) is selected as the optimal absorption line for HF gas detection.

### 3 Experimental Equipment Overview

Based on the previous research results, a TDLAS detection system was developed. The laser driver and the detection adopt the second harmonic technique, temperature control, harmonic generation and harmonic detection, equipment display UI interface and communication parts are realized by chip MAX8520E, ADUC7026, and AM335X, respectively. In order to realize the online trace measurement of HF gas based on TDLAS technology, this research has developed a set of optical path structure suitable for the online detection of HF gas of high-voltage electrical equipment, as shown in Fig. 3. Mainly in selecting the appropriate measurement channel on both ends of the high-voltage equipment, a laser is emitted by a laser, after collaboration through the measured gas in the high-voltage equipment, reach high-voltage equipment at the other end this prism, the prism again through the high-voltage equipment after reflection, finally after focus into indium gallium arsenic detector is converted to electrical signals driven plate, after laser driver board for photoelectric conversion signal, through the synchronous demodulation second harmonic signal, the application of TDLAS detection system as shown in Fig. 4.

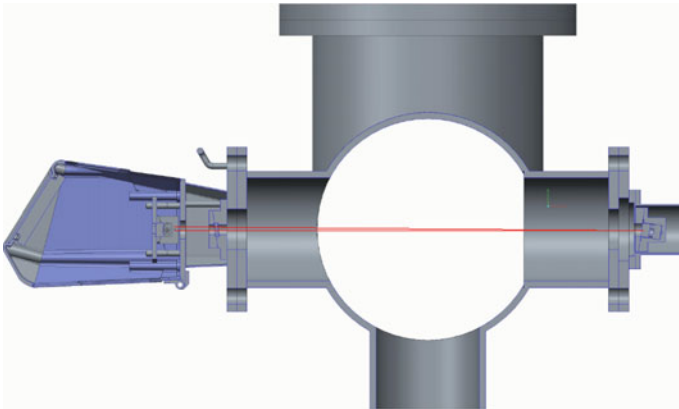


**Fig. 3** Optical path diagram of HF gas high-voltage online detection device

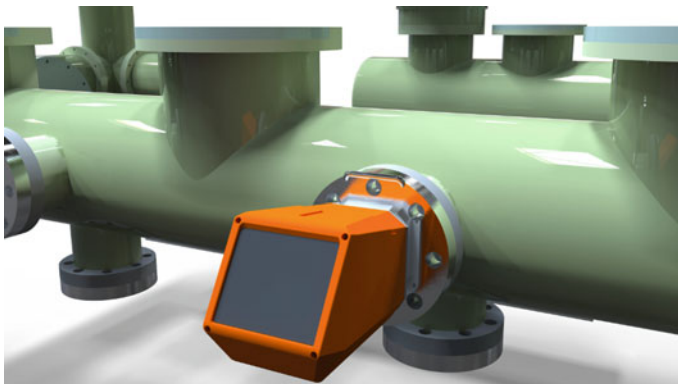


**Fig. 4** Physical diagram of HF gas high-voltage online detection device



## 4 Test Results and Analysis

After the TDLAS detection device is installed in the high-voltage equipment, the gas cylinder of the HF standard gas with a concentration of 20 ppm ( $\text{SF}_6$  gas as the background) will be connected with the equipment to minimize the length of pipeline connection between HF standard gas and high-voltage equipment. Before the experiment, vacuum treatment of high-pressure equipment gas chamber, first, the HF standard gas of 0.1 MPa is connected to the air chamber, and the pressure reducing valve is connected to the same amount of HF gas in the air chamber successively, and the pressure of the high-pressure equipment is gradually increased to 0.6 MPa. The current range of DC modulated signal is 20–70 mA, and the range of sine wave scanning signal is 8 mA. In the experimental process, the air chamber pressure recorded a set of data with each increment of 0.1 MPa, and 6 sets of data were recorded. The absorption spectrum line under different pressures was shown in Fig. 5.

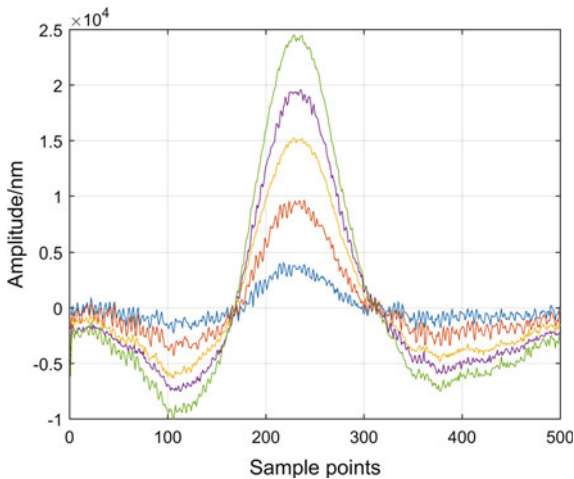


**Fig. 5** Absorption lines of HF gas under different pressure

With the increase of gas pressure, harmonic intensity of HF gas decreases and the broadening is increased. Because the HF gas increases the absorption line width with the pressure, the same tuning parameters cannot obtain excellent harmonic data to invert the gas concentration under high pressure. Based on previous experience, this study adjusted the amplitude of sinusoidal excitation signal and conducted set of experiments for each 5 mA sinusoidal signal, recording 10 sets of different data respectively. As shown in Fig. 6, the amplitude of the second harmonic signal increases with the amplitude of sinusoidal excitation in the pressure of 0.6 MPa. According to the data fitting function, the extreme value should be greater than 50 mA, but it is limited by the laser threshold current and cannot further increase the excitation current.

The increase of pressure makes the amplitude of the second harmonic signal decrease, which leads to the decrease of signal-to-noise ratio and inaccurate detection

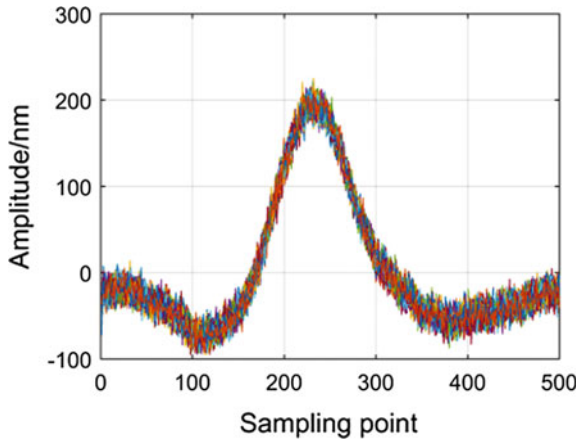


Fig. 6 Amplitude of the second harmonic signal varies with the sinusoidal signal

results. In order to solve this problem, this study applies AD5615 adjustable digital resistors combined with the adder to realize the dynamic adjustment of the sinusoidal excitation signal in the use of the equipment. The principle is shown in Fig. 7.

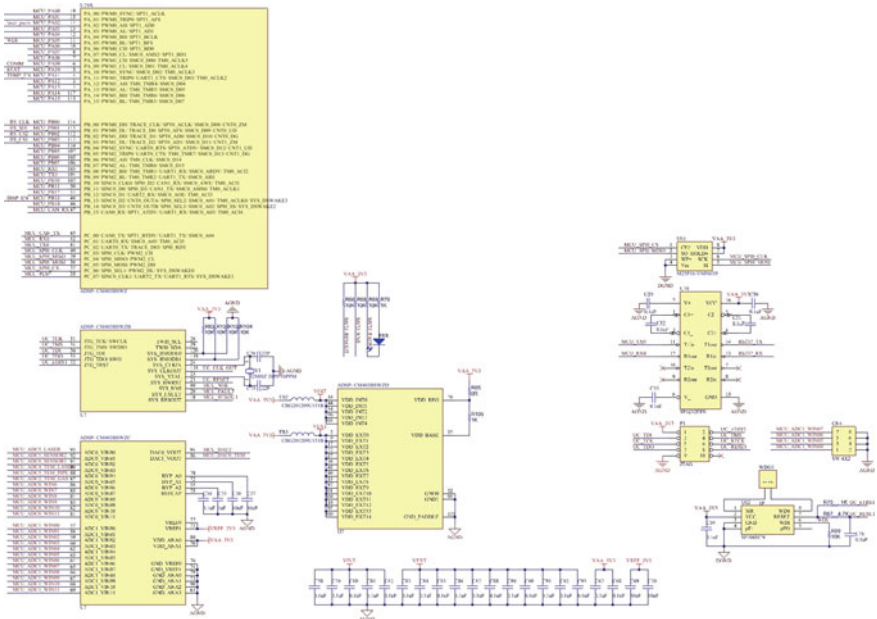
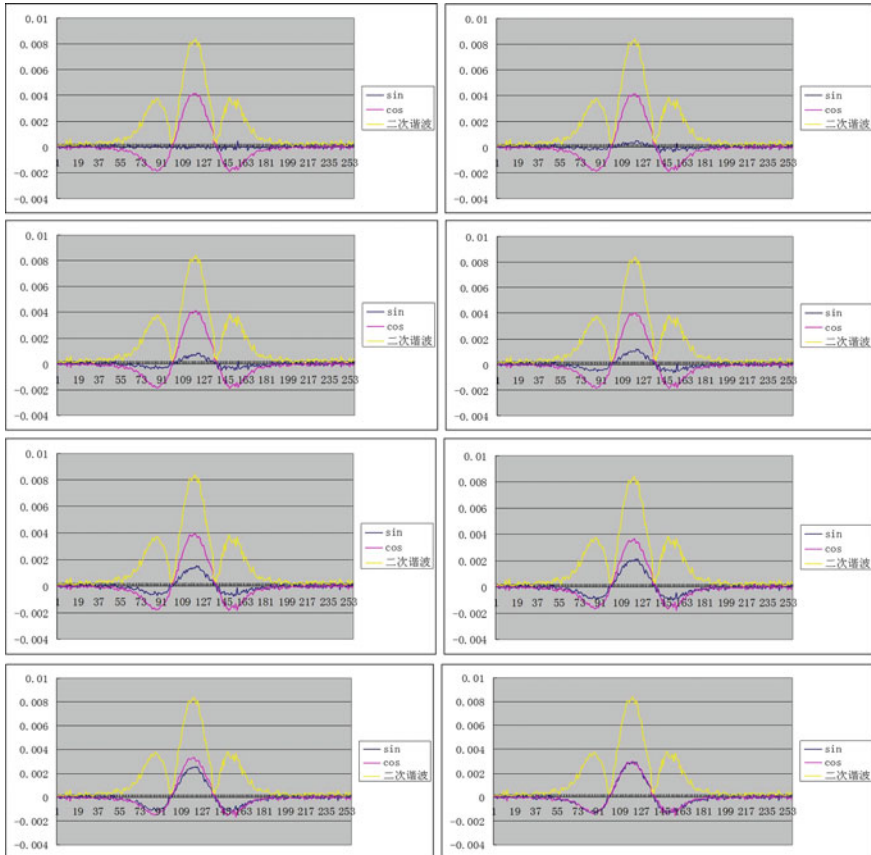


Fig. 7 Dynamic adjustment schematic of a sinusoidal signal

In the process of HF gas discharge in high-pressure electrical equipment gas chamber, the measured gas pressure parameters were dynamically compensated, and

the gas pressure in the experiment was reduced by 1 atm to collect a set of data. In each group of experiments, the control program to adjust the digital resistance tolerance of the sine wave amplitude change, and select the highest absorption peak, compared with fixed sine wave amplitude of the first set of experimental data, as shown in Fig. 8, second harmonic amplitude significantly increased after compensation, in the practical application of HF gas concentration detection effect is well.



**Fig. 8** Comparison of second harmonic amplitude before and after automatic compensation

The project team investigated the structural characteristics of high-voltage electrical equipment and proposed two optical structures suitable for online measurement of HF gas using TDLAS technology. One of them is the overhaul flange of 220 kV high-pressure equipment. As shown in Fig. 9, measuring chamber is set on it, and the HF gas in the high-pressure equipment and high voltage is diffused into the chamber for online measurement. Another form is based on the observation window of high-voltage equipment, on which a pair-through window is set so that the laser can pass through the whole high-voltage electrical equipment to realize the real-time online measurement of



**Fig. 9** High-voltage switching device for experiments

HF gas. The increase of pressure makes the amplitude of the second harmonic signal decrease, which leads to the decrease of signal-to-noise ratio and inaccurate detection results. In the process of the HF gas discharge in high-pressure electrical equipment gas chamber, the measured gas pressure parameters were dynamically compensated, and the gas pressure in the experiment was reduced by 1 atm to collect a set of data. In each group of experiments, the control program to adjust the digital resistance tolerance of the sine wave amplitude change, and select the highest absorption peak, compared with fixed sine wave amplitude of the first set of experimental data, as shown in Fig. 8, second harmonic amplitude significantly increased after compensation, in the practical application of HF gas concentration detection effect is well.

Compared with the direct absorption prototype, the laser driver circuit, the temperature control circuit, and pre-amplifier circuit are not much different because the phase-locked function is completely completed by software. Because of the superposition of harmonic signals, the analog signal modulation circuit is quite different from the direct absorption circuit. According to the design expectation, the system needs the saw-tooth wave of 1 Hz, which can be generated by internal DA of ADSP-403. At the same time, the system needs a modulation signal of about 5 kHz, and the debugging signal with such high frequency cannot be generated by DA of micro-controller itself. The system uses DDS generator AD9850 to generate sinusoidal modulation signal which is superimposed on the saw-tooth wave to drive the laser.

## 5 Conclusion

The optical cavity is the main body of laser, in order to meet the measurement of HF, CO, and H<sub>2</sub>S gas, and the absorption spectra of the three gases are 1568 nm, 1578 nm, and 1305 nm, respectively. Structure design of the gas absorption chamber can basically meet the requirement of the GIS gas pressure. According to the design expectation, the system needs the saw-tooth wave of 1 Hz, which can be generated by

internal DA of ADSP-403. At the same time, the system needs a modulation signal of about 5 kHz, and the debugging signal with such high frequency cannot be generated by DA of micro-controller itself. The system uses DDS generator AD9850 to generate sinusoidal modulation signal which is superimposed on the saw-tooth wave to drive the laser.

**Acknowledgements.** The paper is supported by the technology project of Chongqing Research Program of fundamental science and Advanced Technology (cstc2018jcyjAX0486); Science and Technology Project of Chongqing Power Company (2018 Science and Technology Project of Chongqing Power Company 4#).

## References

1. Qi, R.B., He, S.K., Li, X.T., Wang, X.Z.: Simulation of TDLAS direct absorption based on HITRAN database. *Spectrosc. Spectral Anal.* **35**, 172–177 (2015)
2. Li, Y., Zhang, X.X., Xiao, S., Chen, Q.: Decomposition properties of  $C_4F_7N/N_2$  gas mixture: An environmentally friendly gas to replace  $SF_6$ . *Ind. Eng. Chem. Res.* **57**, 5173–5182 (2018)
3. Zhang, Z.R., Dong, F.Z., Wu, B.: In-situ measurement of HF gas industrial situation based on TDLAS technology. *J. Optoelectron. Laser* **22**, 1691–1694 (2011)
4. Yao, Q., Yuan, Z.R., Li, X.T.: Using TDLAS technology to detect HF gas in  $SF_6$  high-voltage switches. *Instr. Techn. Sens.* **5**, 70–73 (2013)
5. Wu, Y., Wang, C.L., Sun, H., Murphy, A.B.: Properties of  $C_4F_7N-CO_2$  thermal plasmas: Thermodynamic properties, transport coefficients and emission coefficients. *J. Phys. D: Appl. Phys.* (2018)
6. Kieffel, Y., Biquez, F.:  $SF_6$  alternative development for high voltage switchgears. In: *Electrical Insulation Conference*, pp. 379–383. IEEE (2015)



# Application Research of Adjustable Frequency DC-Spark in Oil Analysis Spectrometer

Zhen Wang, Mingfan Dai, Shenghua Zhou, Bangning Mao,  
and Yanqing Qiu<sup>(✉)</sup>

China Jiliang University, Hang Zhou, China  
qyqhz@cjlu.edu.cn

**Abstract.** In order to improve the excitation efficiency and stability of the oil analysis spectrometer, this paper studies the application of adjustable frequency DC-Spark in oil analysis spectrometer and the feasibility of the excitation source is verified. The adjustable frequency DC-Spark is based on PWM (pulse width modulation) technology. By controlling the duty cycle of the PWM to affect the frequency and average energy of the spectral excitation, the warm-up time is shortened and the excitation frequency is optimized. The performance of the adjustable frequency DC-Spark and the AC arc excitation source were tested respectively in an oil analysis spectrometer system based on the rotating disk electrode (RDE: rotation disk electrode). The standard oil of 0, 10, 50 and 100 ppm of Conostan company was tested. The experimental results show that compared with the AC arc excitation source, the adjustable frequency DC-Spark has better excitation and less heat generation. The test results of Fe, Cu and Mg elements in the 100 ppm oil were taken as examples; the repeatabilities were 3.6, 3.5 and 4.1, and the reproducibilities were 2.6, 5.1 and 1.5, which were better than the detection values of AC arc excitation source.

**Keywords:** Spectrometer adjustable frequency DC-Spark · Repeatability · Reproducibility

## 1 Introduction

With the increase of the using time and the slight mismatch of the design and installation, the mechanical equipment will produce a small amount of abrasion during operation. These abrasions will produce metallic and non-metallic abrasive particles in the lubrication system of the equipment. It will affect the lubrication effect and even lead to serious accidents or complete damage of the equipment [1]. Therefore, in some mechanical operation situations that are likely to cause accidents, the conventional and accurate lubricating oil spectrum detection cannot only supervise the health condition of the mechanical equipment, but also provide early warning to the equipment abrasion failure, thus effectively ensuring the normal operation of the equipment [2–4]. At present, the domestic conventional testing of lubricating metal abrasive particles is mainly used in the aviation machinery. The main method is atomic emission spectrometry based on the rotating disk electrode (RED). AC arc or AC-Spark is widely used in excitation source, but its arc intensity varies with the level of the voltage, and

the stability is poor. Meanwhile, because of its difficulty to compress width of pulse, the peak energy is low and the average energy is high. Therefore, the background noise in element analysis is large, which is not conducive to the accuracy of elements analysis [5, 6]. However, the DC arc excitation source will cause strong self-absorption phenomenon, resulting in poor precision of analysis results, serious matrix effect and narrow linear dynamic range. These shortcomings hinder the development and application of this excitation source. Compared with the DC arc excitation source, the main advantages of adjustable frequency DC-Spark are high sensitivity to the elements that are difficult to be excited, wide dynamic range and good reproducibility of results [7]. With the emergence of high-power semiconductor devices, adjustable frequency DC-Spark has been widely used in the elements analysis. Besides, it has the advantages of simple structure, easy operation, low consumption and high sensitivity [8, 9]. However, as far as we know, there is no report of using adjustable frequency DC-Spark for lubricating oil spectrum detection. In view of the above shortcomings of AC arc and DC arc, considering the different excitation energies of different elements, in order to obtain high-quality atomic emission spectra, this paper uses a self-developed adjustable frequency DC-Spark for oil analysis spectrometer. The adjustable frequency DC-Spark has the advantages of short warm-up time, befitting excitation frequency and stable excitation spectrum [10, 11]. In this paper, the feasibility of applying adjustable frequency DC-Spark to oil analysis spectrometer is verified by experiments.

## 2 Test Principle

By measuring the concentration of various metal components in lubricating oil, we can assess the degree of abrasion of machinery and the health condition of equipment. In addition to this, we can predict mechanical failure. The detection of the metal component can be completed by measuring the atomic emission spectrum. When the atom receives the external energy, the outer electrons are excited to a higher energy level, and when the electrons at the high energy level return to the ground state, it will radiate energy in the form of photons. Each element has its own unique energy level and spectrum, so according to the position of the atomic emission spectrum line, the type of element contained in the object can be ascertained, and the content of the element can be determined according to the intensity of the emission spectrum. The relationship between the spectrum intensity ( $I$ ) and the content of the element ( $C$ ) is expressed by the Scheibe-Lomakin formula:

$$I = aCb \quad (1)$$

where  $a$  and  $b$  are constants related to experimental conditions.

### 3 System Structure

As shown in Fig. 1, the oil analysis spectrometer system is mainly composed of adjustable frequency DC-Spark, excitation chamber, spectral acquisition module and computer.

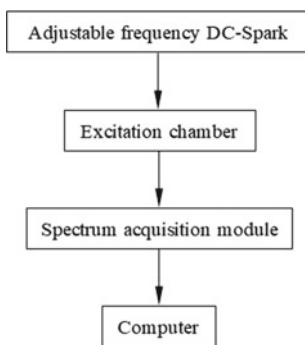


**Fig. 1** The system block diagram

The excitation chamber is used to excite the oil sample, including disk electrode, rod electrode and oil sample. The spectrum acquisition module is used to collect spectrum, mainly including collimating lens, grating and CCD. The computer is used to analyze the spectrum and calculate the content of metallic elements in the oil sample.

As shown in Fig. 2, the testing process is mainly divided into three steps. First step, turn on the power supply and set the disk electrode rotating at a certain speed, and then the oil sample can be partially transmitted to the gap between the rod electrode and disk electrode where the oil sample is heated and evaporated. After that, the atomic emission spectrum of the sample oil is acquired. In the second step, the spectrum is collimated through the lens and then transmitted to the ultraviolet spectrometer by the quartz fiber. In the third step, ultraviolet spectrometer transmits the spectrum data to computer for analysis, and then the software calculates the content of the element.

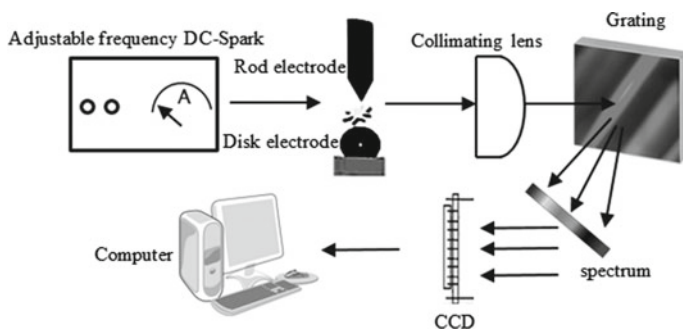


**Fig. 2** Flow diagram of lubricating oil spectrum detection



## 4 Experiment and Discussion

In order to study the application of adjustable frequency DC-Spark in oil analysis spectrometer and compare it with AC arc, the text designed the following experimental scheme. In the same oil analysis spectrometer system, AC arc and adjustable frequency DC-Spark are used respectively to detect the standard oil of different concentrations. The standard oil of each concentration needs to be tested 10 times. Analyze the test data, calculate its repeatability and reproducibility, then compare the test data of two power sources.

Respectively using AC arc and adjustable frequency DC-Spark, on the oil analysis spectrometer system, and then test 100 ppm standard oil of Conostan company, oil sample was tested 10 times, analyze the test data, calculate its repeatability and reproducibility.

Taking the most used elements of Fe, Cu and Mg as an example, calculate its repeatability and reproducibility of 10 times test data.

$$\text{Repeatability} = \frac{\sqrt{N(\sum X_i^2) - (\sum X_i)^2}}{N(N-1)} \quad (2)$$

$$\text{Reproducibility} = \text{Theoretical Value} - (\sum X_i)/N \quad (3)$$

N test times.

$X_i$  test data.

As shown in Table 1, under the AC arc conditions, the repeatability of Fe, Cu and Mg was 9.4, 7.7 and 10.8, and the reproducibility was 2.7, 4.2 and 6.9. As shown in

**Table 1** Test data of AC arc

Element	Fe	Cu	Mg
Value1	108	99.8	103.1
Value2	98.3	107.7	106.3
Value3	103.1	97.9	109.8
Value4	112.7	103.2	120.4
Value5	115.6	110.8	118.6
Value6	94.2	95.2	98.3
Value7	88.2	114	109.4
Value8	109.1	107.3	112.1
Value9	107	92.2	115.2
Value10	90.7	113.4	114.9
Repeatability	9.4	7.7	10.8
Reproducibility	2.7	4.2	6.9

**Table 2** Test data of adjustable frequency DC-Spark

Element	Fe	Cu	Mg
Value1	98.5	95.9	96.3
Value2	92.5	96.4	98.9
Value3	100.8	100	105.8
Value4	93.9	92.3	96.8
Value5	101.8	96.9	101.2
Value6	92	98.9	103.6
Value7	95.8	93.9	106.6
Value8	98.8	87.7	103.6
Value9	100.9	94.6	96
Value10	98.9	92.5	105.8
Repeatability	3.6	3.5	4.1
Reproducibility	2.6	5.1	1.5

Table 2, under the adjustable frequency DC-Spark conditions, the repeatability of Fe, Cu and Mg was 3.6, 3.5 and 4.1, and the reproducibility was 2.6, 5.1 and 1.5.

## 5 Conclusion

In this paper, according to the requirements for the determination of elements in lubricating oil, an adjustable frequency DC-Spark is used based on the principle of atomic emission spectrum, which has the short warm-up time and better excitation frequency. Take the test result of Fe, Cu and Mg in the 100 ppm standard oil as an example, the values of repeatability are 3.6, 3.5 and 4.1, respectively, the reproducibility are 2.6, 5.1 and 1.5, respectively, which are superior to the test values of the AC arc.

**Acknowledgements.** This work was supported by the Zhejiang Province public technology application research project 2017C33005.

## References

1. Zheng, C.S., Ma, B.: Based on oil spectrum analysis of comprehensive experimental study transmission condition monitoring. *Spectronic Instrum. Anal.* **29**(3), 749–751 (2009)
2. Wang, J., Yin, F.J., Xia, X.J.: The application of ICP-OES in the elemental analysis of engine oils. *Lubricating Oil* **2**, 45–49 (2015)
3. Zhang, Y.F.: Investigation on the behavior of single spark discharge in spark source atomic emission spectrometry. *Metall. Anal.* **36**(1), 4–10 (2016)
4. Wang, H., Ma, X.M., Zheng, W.: Determination of 10 trace impurity elements in titanium and titanium alloys with DC arc atomic emission spectrometry. *Rock Miner. Anal.* **33**(4), 506–511 (2014)

5. Yan, X.H., Peng, Y., Zhang, L.: Research of determination method for impurity elements in tantalum by full spectrum direct reading of DC arc emission spectrometer. *Cemented Carbide* **31**(2) (2014)
6. Ren, W.B., Jin, J.B., Guo, J.F.: Experimental research on voltage-current characteristics of carbon AC arc. *Trans. China Electrotechnical Soc.* **29**(2), 18–22 (2014)
7. Lei, H.T.: Determination of nitrogen in structural steel by spark source atomic emission spectrometry. In: *China Automotive Engineering Society Annual Meeting Proceedings*, vol. 3 (2015)
8. Ding, T.Y., Liu, J.L., Zhu, A.M.: Electrode configuration and plasma reactor of spark discharge. *Nucl. Fusion Plasma Phys.* **3**, 282–288 (2014)
9. Ye, M.Z.: Determination of trace aluminum in stainless steel by spark source atomic emission spectrometry. *Metall. Anal.* **35**(4), 13–18 (2015)
10. Xia, N.P., Shen, K., Xiang, W.H.: Spark source atomic emission spectrometer analyze high content phosphorus and stannum in steel. [www.gdchem.com](http://www.gdchem.com). **43**(1), 139–140 (2016)
11. Gao, C.Y., Wang, L., Fan, S.H.: Determination of trace potassium in electrolytic aluminum by flame atomic emission spectrometry. *Chin. J. Anal. Lab.* **2**, 164–166 (2016)



# A Three-Dimensional Measurement Method Based on Binary Structured Light Patterns for Medical Electronic Endoscope

Pei Tao, JiaMin Xia, Bo Yuan<sup>(✉)</sup>, and Liqiang Wang

Zhejiang University, Hangzhou, China  
yuanbo@zju.edu.cn

**Abstract.** One method for three-dimensional (3D) measurement based on 23 binary structured light patterns is proposed for the medical electronic endoscope in the present study. The patterns are designed by using simple logical operations and tools from combinatorial mathematics. First, we project these patterns onto the objects in proper order, and all the modulated patterns are captured by a CMOS camera. Then, a series of preprocessing methods which contain projector-camera calibration, reflection detection and suppression, radial and tangential distortion correction are used to process these modulated patterns. Finally, we decode the patterns and reconstruct the shape of objects by structured light triangulation. An experimental prototype endoscope is built and the results of experiments on real pig stomach show that the proposed method is effective. The precise of depth measurement at the working distance of 80 mm is better than 0.5 mm.

**Keywords:** Reconstruction · Structure light · Medical electric endoscope

## 1 Introduction

3D shape measurement plays an important role in several applications including industrial automation, human–computer interaction and surgery. It is particularly the case in medical applications for which the developments of robotic-assisted minimally invasive surgery (MIS) are remarkable. References [1, 2] use stereovision to reconstruct the soft tissue structures of the abdomen. However, stereovision principle always fails with poor textured scene. To tackle this, structured light-based methods are presented. The structured light technique replaces one of the cameras of the classical stereovision system by an active device which projects one or several known coded patterns onto the tissue [3]. Reference [4] combines two endoscopes, a laser-beam strip and a high-speed camera to obtain geometry of a given organ. This whole set of equipment is a little complicated. Reference [5] uses a miniature fiber probe to project a colored spot pattern onto the tissue surface. The probe has a small diameter and produces a pattern of high brightness making it suitable for use with biological tissue. However, the number of spots is not enough to obtain a high measurement accuracy, which is limited by the diameter of each fiber. Reference [6] computed monochromatic

patterns according to the theory of Perfect Map and presented non-grid-based patterns to speed up the decoding process. Although this technique can get real-time organs' surface reconstruction with GPU processing, it is not robust because of the organ's or tissue's surface is not always smooth. When the surface is wrinkled, it is hard to solve the well-known correspondences problem and thus get a wrong code of each window. Reference [7] generated the structured light of black and white strips by using four LED point sources to illuminate the grating mask plate. The same, this method is not robust when scene points receive illumination indirectly in the form of interreflections, subsurface or volumetric scattering.

In comparison with previous articles about the 3D measurement methods which applied in endoscope, in this article, we consider binary structured light patterns, which are perhaps the simplest to implement in medical electronic endoscope. On the other hand, structure light has good potential to be used in surgical environments as they have the advantage of performing well even on relatively featureless objects [8]. However, currently the applicability of most structured light techniques is limited to well-behaved scenes. Obviously, these techniques are not suitable for those surgical scenarios which have overexposed areas or shiny spots. Based on this analysis, the 10-bit binary Gray code with the maximum known min-SW that proposed by Goddyn in [9] is adopted, and the entire 3D reconstruction system only requires a single camera and a projector. We demonstrate reconstructions on scenes with complex geometry and material properties. In particular, the experiments on pig stomach show promising reconstruction results.

## 2 Methods

Figure 1 shows the synopsis of preprocessing and how the 3D medical electronic endoscope works. The projector projects 23 binary structured light patterns onto the objects in proper order, and the endoscope captures all these patterns which modulated by objects. Then, modulated patterns are processed with a series of methods which are all for decoding.

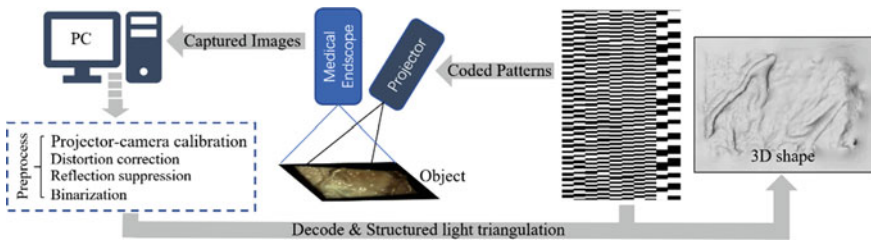


**Fig. 1** The proposed structured light system

## 2.1 Coded Patterns

For real-world scenarios, scene points receive illumination not only directly from the light source but also indirectly in the form of interreflections, subsurface or volumetric scattering [10]. To reduce the effect of indirect illumination, most currently used patterns contain a combination of both low and high spatial frequencies. Our design of patterns takes long-range interreflections and short-range subsurface scattering and requests to have large minimum stripe-widths (SW) and high frequencies.

The 10-bit binary Gray code with the maximum min-SW (8 pixels) was proposed by Goddyn et al. Because our projector resolution is  $1280 \times 720$ , 11-bit binary Gray code is needed to code all pixels' column. Based on 10-bit maximum min-SW Gray codes, 11-bit codes are designed to fit our experimental scene by us. Consequently, 21 patterns are designed as 11 patterns for column stripes (Fig. 2) and 10 for row stripes and 2 patterns that one is black for all pixels and one is white for all pixels are added to our patterns for restricting the illuminated area by the projector and the threshold for binarization. Therefore, every pixel in the projected pattern has its own unique 21-bit code.

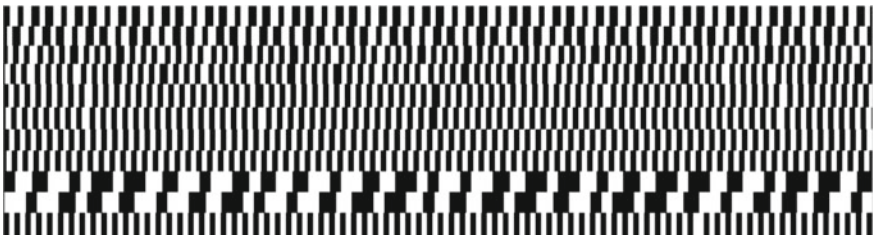


Fig. 2 The 11 Maximum min-SW gray coded patterns for column stripe

## 2.2 Projector-Camera Calibration

To determine the correspondence between the projected images and the 3D points is an indispensable step for reconstruction. Our structured light systems take projector-camera pair as experimental equipment to reconstruct the 3D shape. It is known that camera calibration is an indispensable part in the calibration of the system. There are already many calibration algorithms in the literature [11–14]. However, projector calibration algorithms are applied not in all 3D shape reconstruction system but just in the structured light system. Based on the fact that a projector can be regarded as an inverse pinhole model camera, Ref. [15] proposes a plane-based calibration technique that the camera and projector are calibrated separately. The camera is calibrated first and the projector is calibrated respect to the camera, using a projected pattern that is designed as a checkerboard. The design of the checkerboard and the algorithm is optimized by us and suits for our experimental environment.

### 2.3 Reflection Detection and Suppression

Specular reflections are a common problem causing inaccurate depth estimation and map reconstruction. Therefore, eliminating specular artifacts is a fundamental endoscopic image preprocessing step to ensure Lambertian surface properties and increase the quality of the 3D map. For the reflection detection task, we adopt the method that proposed by Turan et al. [16]. Then, the inpainting method proposed by Telea [17] is applied to suppress the saturated pixels by replacing the specularity by an intensity value derived from a combination of neighboring pixel values.

### 2.4 Pattern Decoding

The images taken by camera are shown in Fig. 3a. Each image should be preprocessed to reduce the effect of uneven illumination and binarize every pixel's code. The pre-processed image is shown in Fig. 3b. For the white and black pattern has restricted the illuminated area of projector and reflection effect on images has been suppressed, every pixel in the illuminated area has its own unique 21-bit code, which can be matched with the projected pattern pixel. Certainly, there are a number of mismatched points and points that are not matched, but these points can be removed in the process of reconstruction and will not affect the accuracy of the whole system for our dense reconstruction. Point clouds can be generated by calculating the 3D coordinates of matched points.

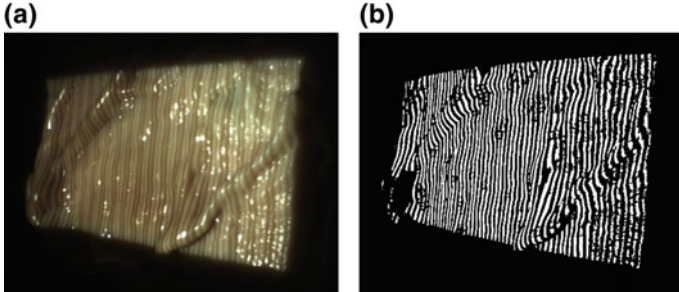


**Fig. 3** a The image taken by camera; b Image after preprocessing

## 3 Experiments and Results

An experimental prototype endoscope was built according to the proposed method. It is composed of a high-definition CMOS camera module developed by ourselves and a video-projector (see Fig. 4). Experiments were undertaken to evaluate the choice of the coded patterns and to validate the proposed methods in the laboratory environment.

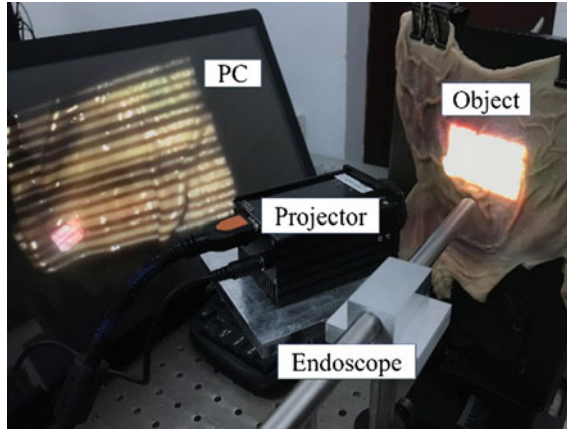


**Fig. 4** The experimental prototype endoscope with coded pattern

### 3.1 Reconstruction of Real Pig Stomach

For the application of interest, the 23 coded patterns were projected onto the inside surface of real pig stomach in succession, and the images were acquired with an endoscopic camera. Then, the series of methods proposed above were applied to process these images. Finally, structured light triangulation was used to reconstruct the 3D shape. Figure 5 shows that even the small rugae of mucosa is well reconstructed.

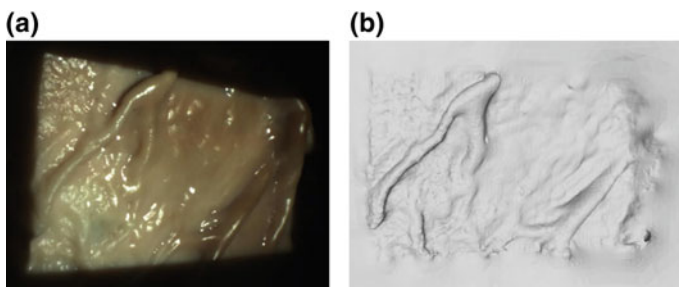


**Fig. 5** 3D reconstruction of real pig stomach. **a** The image captured by CMOS camera; **b** 3D reconstruction without texture mapping

### 3.2 Measurement Accuracy

To evaluate the measurement accuracy, we projected the patterns on parallel flat surfaces. First, one of the two flat surfaces is fitted with least square method after acquiring 3D coordinate. Then, the distance is measured from each point in another plane to the fit plane. The distance between the two flat surfaces is 9.75 mm. Figure 6b showcases the reconstruction result. The statistics demonstrate that the accuracy of surface reconstruction is very high using the proposed method under strict calibration



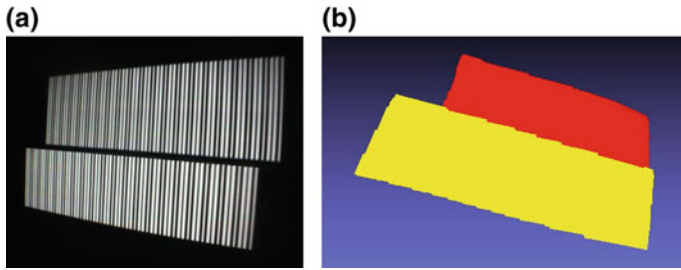


**Fig. 6** **a** The pattern projected on two flat surfaces; **b** 3D reconstruction

and perfect pattern decoding, with average error 0.475 mm and maximum error 0.985 mm.

## 4 Conclusions and Future Work

We adopted the maximum min-SW Gray codes as structured light and did 3D reconstruction for several static objects including real animal organ and tissue. The reconstruction results demonstrate our method is robust and effective. The result of real pig stomach shows that the proposed method is insensitive to fine shiny spots, thus this method has good potential application in surgical environments.

The final objective, which exceeds the framework of paper, is to reconstruct moving surfaces in real time and to integrate our patterns in an endoscopic tool taking advantage of the diffractive optics technology or other state of the art techniques.

## References

1. Hu, M., Penney, G., Edwards, P., Figl, M., Hawkes, D.: 3D reconstruction of internal organ surfaces for minimal invasive surgery. In: *Medical Image Computing and Computer Assisted Intervention*, pp. 68–77. Springer, Heidelberg (2007)
2. Stoyanov, D., Darzi, A., Yang, G.Z.: Dense 3D depth recovery for soft tissue deformation during robotically assisted laparoscopic surgery. In: *Medical Image Computing and Computer-Assisted Intervention, MICCAI 2004*, pp. 41–48. Springer, Heidelberg (2004)
3. Salvi, J., Pagès, J., Batlle, J.: Pattern codification strategies in structured light systems. *Pattern Recogn.* **37**(4), 827–849 (2004)
4. Hayashibe, M., Suzuki, N., Nakamura, Y.: Laser-scan endoscope system for intraoperative geometry acquisition and surgical robot safety management. *Med. Image Anal.* **10**(4), 509–519 (2006)
5. Clancy, N.T., Stoyanov, D., Maierhein, L., Groch, A., Yang, G.Z., Elson, D.S.: Spectrally encoded fiber-based structured lighting probe for intraoperative 3D imaging. *Biomed. Opt. Express* **2**(11), 3119–3128 (2011)
6. Maurice, X., Albitar, C., Doignon, C., De Mathelin, M.: A structured light-based laparoscope with real-time organs' surface reconstruction for minimally invasive surgery. In: *Engineering in Medicine and Biology Society*, pp. 5769–5772, IEEE (2012)

7. Zhou, T., Tao, P., Yuan, B., Wang, L.: A three-dimensional measurement method for medical electric endoscope. *Proc. SPIE* **102450**(A), 245 (2017)
8. Maierhein, L., Mountney, P., Bartoli, A., Elhawary, H., Elson, D., Groch, A.: Optical techniques for 3D surface reconstruction in computer-assisted laparoscopic surgery. *Med. Image Anal.* **17**(8), 974–996 (2013)
9. Goddyn, Luis; Gvozdzjak, Pavol,: Binary Gray Codes With Long Bit Runs. *Electron. J. Comb.* **10**(1), 10 (2003)
10. Gupta, M., Agrawal, A., Veeraraghavan, A., Narasimhan, S.G.: A practical approach to 3D scanning in the presence of interreflections, subsurface scattering and defocus. *Int. J. Comput. Vision* **102**(1–3), 33–55 (2013)
11. Jean-Yves Bouguet Homepage, [http://www.vision.caltech.edu/bouguetj/calib\\_doc/](http://www.vision.caltech.edu/bouguetj/calib_doc/). Last accessed 24 Jan 2019
12. Salvi, J., Armangué, X., Batlle, J.: A comparative review of camera calibrating methods with accuracy evaluation. *Pattern Recogn.* **35**(7), 1617–1635 (2002)
13. Zhang, Z.: A flexible new technique for camera calibration. *Microsoft Res.* **22**(11), 1330–1334 (2000)
14. Clarke, T.A., Fryer, J.G.: The development of camera calibration methods and models. *Photogram. Rec.* **16**(91), 51–66 (2010)
15. Falcao, G., Hurtos, N., Massich, J.: Plane-based calibration of a projector-camera system. *Vibot Master* **9**, 9 (2008)
16. Turan, M., Pilavci, Y.Y., Ganiyusufoglu, I., Araujo, H., Konukoglu, E., Sitti, M.: Sparse-then-dense alignment-based 3D map reconstruction method for endoscopic capsule robots. *Mach. Vis. Appl.* **29**(2), 345–359 (2018)
17. Telea, A.: An image inpainting technique based on the fast marching method. *J. Graph. Tools* **9**(1), 23–34 (2004)



# A Miniaturized Device for Measuring Flexure Angle of Flexible Fiber Data Gloves

Jin Zhang, Liqiang Wang<sup>(✉)</sup>, Bo Yuan, and Lei Zhang

State Key Laboratory of Modern Optical Instrumentation, Zhejiang University,  
Hangzhou, People's Republic of China  
wangliqing@zju.edu.cn

**Abstract.** Angle measuring devices are widely used in many fields, such as wearable devices, human-computer interaction interfaces, and intelligent surgical robots. Compared with electrical signal sensors, optical angle sensors provide a new way for the implementation of wearable data gloves because they are immune to electromagnetic interference and can be integrated in multiple channels. In this paper, an angle measuring device for flexible fiber data gloves is designed, which is composed of an LED light source, a CMOS image sensor, and two coupling lenses. Through a fiber coupling lens, the divergence angle of the LED light source matches with the numerical aperture of the flexible fiber and high-efficiency energy coupling is achieved. An imaging coupling lens with 3 mm length is used to ensure that each fiber image of the fiber bundles occupies more than 64 pixels on the CMOS photosensitive surface, achieving a 16-bit data accuracy of signal measurement. The experimental results show that the device can measure the angle change of the data gloves of 5 finger flexures at the same time, and the flexure resolution of each finger is better than  $0.5^\circ$ .

**Keywords:** Angle measuring device · CMOS image sensor · Multichannel integration

## 1 Introduction

The angle measurement is an important part of geometric measurement technology, and the comprehensive application of various measurement methods makes the measurement accuracy reach a high level. The earliest researches in angle measurement technology are mechanical angle measurement technology and electromagnetic angle measurement technology, such as multi-tooth indexing tables and circular magnetic grids. However, these methods need to be implemented manually, which are not easy to automate, and the measurement accuracies are limited. With the rapid developments of light sources, optoelectronic materials and devices, optical angle measurement technology has begun to develop rapidly. Optical angle measurement has higher precision than general mechanical and electromagnetic measurement [1]. In addition, it is easier to automate in the subdivision and measurement process, and it has the characteristics of non-contact measurement. Therefore, optical angle sensors are increasingly utilized in the fields of medicine [2], underwater exploration detections [3], aerospace [4], and wearable devices [5–7].

The bending characteristics of optical fibers provide a new way for optical angle measurement [8]. A spectrometer is used to measure the output light energy of the fiber, and the corresponding fiber bending angle is determined by the change of light intensity, so that the angle of measurement can be achieved. However, the cost of the spectrometer is high and the volume is large, which are difficult to meet the requirements of integration and multichannel measurements. In order to solve the above problems, we present a miniaturized device for measuring flexure angles of flexible fiber data gloves, which consists of a light-emitting diode (LED) light source, a complementary–metal–oxide semiconductor (CMOS) detector array and a 3 mm imaging objective lens. Meanwhile, the device has simple structure and can be integrated with multiple channels.

## 2 Design of the Device

### 2.1 General Design of the Device

As shown in Fig. 1, the device is composed of a light source module, a simulated hand bending module and an imaging module. In order to ensure the high-efficiency coupling of energy, a fiber-coupled lens is used to make that the divergence angle of the LED light source matches with the numerical aperture of mono-mode fiber. At the same time, the pitching table is used to simulate the bending of the hand joint, which can control angular flexure precisely. The imaging module consists of a Grey Point’s CMOS sensor, a self-designed imaging lens and a camera interface, to make sure that the fiber distal end has a clearly monochrome picture on the CMOS sensor.

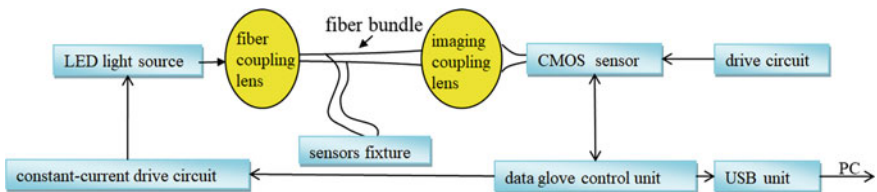


**Fig. 1** Device schematic diagram

In order to ensure wearable and miniaturized integration of data gloves, it is necessary to use a highly integrated detection unit to detect multiple optical fibers in parallel. As shown in Fig. 2, the self-designed optical coupling lens is used to amplify imaging, so that each fiber end can occupy as many pixels as possible on the CMOS sensor. A 16-bit data accuracy or higher can be achieved, in the case that the effective gray value of the CMOS sensor is only 8–10 bits. The lens has three spherical structures, and the fourth plane is the protective glass window of the CMOS sensor. The angles of the chief rays, which transfer from each field of view to the CMOS photo-sensitive unit, meet the chief ray angle (CRA) requirements. The lens parameters are optimized in the optical design software. As shown in Fig. 3, the modulation transfer function is obtained at the optimal imaging. In the 0.5 field of view, the modulation

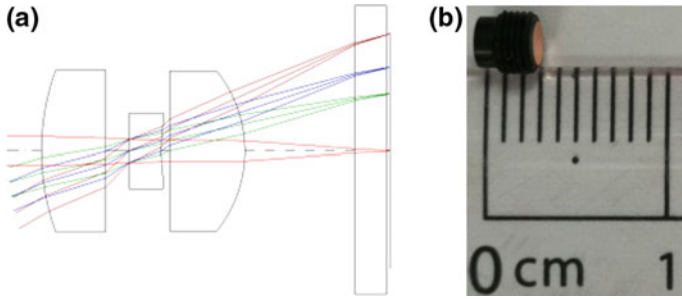


Fig. 2 a Ray trace of the lens, b picture of the lens

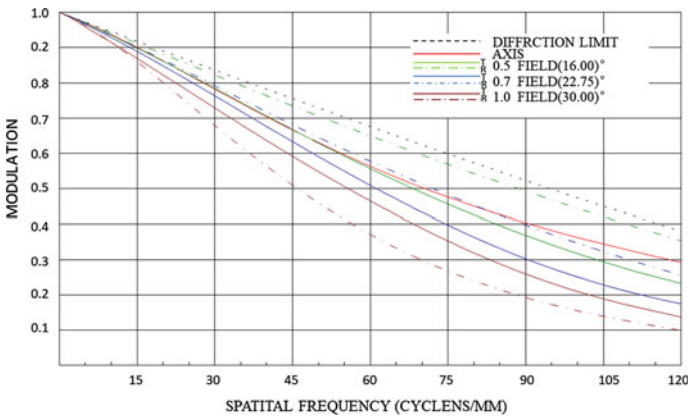


Fig. 3 MTF curve of the coupling lens

degree of the lens is reduced to 0.3, the resolution of the image plane is about 105 lp/mm, which ensures that each fiber image can occupy more than 64 pixels on the photosensitive surface of the CMOS.

## 2.2 Angle Measurement Method

The fiber coupling device couples the light emitted by the LED light source into the flexible fiber bundle. When the bending angle of a certain fiber in the flexible fiber bundle changes, the output light energy of that changes. The exit surface of the fiber distal end is clearly imaged on the photosensitive surface of the CMOS sensor through the imaging coupling lens, and the change of the light energy is finally reflected as the light and dark gray scale change of the image. The image is transmitted to the central processor through the Universal Serial Bus (USB) interface in real time. The gray value of the effective area of the image is calculated using Eq. (1), and the relationship between the change of the gray value and the bending angle is determined, thereby determining the accurate bending angle of the optical fiber. Here,  $I$  represents the

intensity of the effective image area, and  $p(i, j)$  is the gray value of a certain pixel in the effective area.

$$I = \sum p(i, j) \quad (1)$$

After obtaining the light intensity of each angle, the standard deviation is calculated using Eq. (2), where  $I_i$  represents the gray value of a certain angle, and  $\mu$  represents the average of the gray value.

$$\sigma = \sqrt{\frac{1}{N} \sum_{i=1}^N (I_i - \mu)^2} \quad (2)$$

According to the above standard deviation of the gray value of each angle, the average of the standard deviation can be calculated using Eq. (3), where  $\sigma_i$  represents the standard deviation of a certain angle.

$$\sigma_{\text{avg}} = \frac{1}{n} \sum_{i=1}^n \sigma_i \quad (3)$$

The sensitivity of the device is calculated using Eq. (4), where  $I_0$  represents the light intensity value of  $0^\circ$ ,  $I_n$  represents the light intensity value of  $90^\circ$ , and  $\sigma_{\text{avg}}$  represents the average value of the standard deviation.

$$S_{\text{avg}} = \frac{90^\circ}{(I_0 - I_n) / (3 \times \sigma_{\text{avg}})} \quad (4)$$

### 3 Device Characteristics

Firstly, the angle sensor of the flexible fiber is sensitive to the wavelength change of the light source. Therefore, the constant current drive mode LED light source is adopted to ensure the stability of the central wavelength. Because the CMOS image sensor has the highest sensitivity to yellow light, the LED selects the LYW5SN of the OSRAM, whose central wavelength is 590 nm. Secondly, the fiber coupling device couples the light emitted by the LED light source into the flexible fiber bundle as more efficiently as possible. The higher the coupling efficiency, the more power-saving the LED driver is, and the low power consumption can be achieved. Finally, the imaging objective lens can perform 3 mm imaging with a small size and chromatic aberration correction for the full range of visible to near-infrared light. The CMOS sensor surface can capture images of 5 or more angle sensors at the same time, ensuring that each fiber on the end face of the fiber bundle occupies more than 64 pixels on the CMOS photosensitive surface. The CMOS sensor has a data accuracy of 10 bits per pixel, thus ensuring that the data accuracy of each fiber reaches 16 bits. A wearable flexible fiber data glove with

five joint detection functions is shown in Fig. 4. Five flexible fiber-optic sensors are placed on the five finger joints of the glove. The light source and detector are packaged in a cassette and connected to the computer through the data line to realize the control of the movement of the artificial hand model.

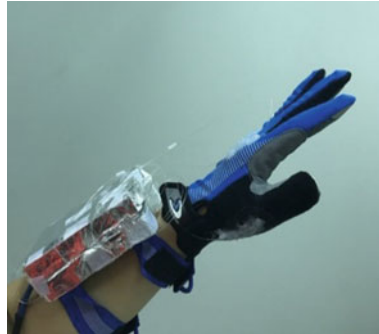


Fig. 4 Flexible fiber data glove and angle measuring device

### 4 Experimental Result

The curve of the gray value in the effective area of the CMOS sensor obtained by the experiment is shown in Fig. 5. In the figure, the abscissa is the bending angle of the fiber, and the ordinate is the gray value of the image in the effective area. In the actual calculation, 10 sets of different angles are selected, and 10 sets of gray values are selected for each angle to calculate the average of the standard deviation. The minimum angles that can be resolved by the five sets of experiments can be calculated by using Eqs. (2), (3), and (4). The result is shown in Table 1.

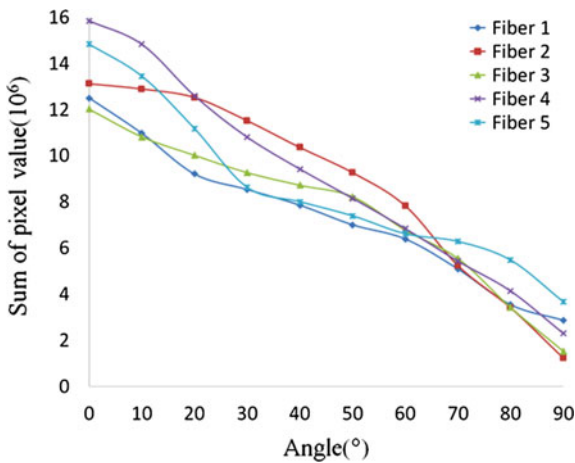


Fig. 5 Gray value of five fibers at different angles

**Table 1** Resolution of the device

No.	The gray value of 0°	The gray value of 90°	Mean of S.D	Angular resolution (°)
1	$1.25 \times 10^7$	$2.86 \times 10^6$	$1.6 \times 10^4$	0.45
2	$1.36 \times 10^7$	$1.26 \times 10^6$	$1.4 \times 10^4$	0.3
3	$1.20 \times 10^7$	$1.52 \times 10^6$	$1.90 \times 10^4$	0.49
4	$1.58 \times 10^7$	$4.12 \times 10^6$	$2.12 \times 10^4$	0.49
5	$1.48 \times 10^7$	$3.67 \times 10^6$	$1.88 \times 10^4$	0.46

## 5 Conclusion

The device for measuring flexure angle of flexible fiber data gloves has the advantages of small size and integration, which is designed and presented in this paper. The experimental results show that the data accuracy of the device can reach 16 bits, and the angle change of the data gloves of 5 parts can be measured at the same time. At the same time, the bending angle measurement of each part is better 0.5°. Therefore, the device can be well applied to flexible fiber data gloves.

## References

1. Yin, Y.H., Qiao, Y.F., Cai, S., Qiao, G.Y.: Optical method for angular deformation measurement of large structure. *Electro-Optic Technol. Appl.* **4**(29), 69–75 (2014)
2. Ito, S., Kawasaki, H., Ishigure, Y.: A design of fine motion assist equipment for disabled hand in robotic rehabilitation system. *J. Franklin Inst.* **1**(348), 79–89 (2011)
3. Yuh, J.: *Design and Control of Autonomous Underwater Robots: A Survey*. Kluwer Academic Publishers (2000)
4. Ambrose, R.O., Aldridge, H., Scott Askew, R.: Robonaut: NASA's space humanoid. *Intell. Syst. Appl. IEEE* **4**(15), 57–63 (2010)
5. Fujiwara, E., Suzuki, C.K.: Flexible optical fiber bending transducer for application in glove-based sensors. *IEEE Sens. J.* **14**(10), 3631–3636 (2014)
6. Hailian, W., Xiaodong, Z., Liang, M., et al.: Research on optic fiber perception of human motion for exoskeleton robot control. *Comput. Meas. Control* **11**(23), 3804–3806 (2015)
7. Zhang, Z.H., Zhang, X.D., Hou, Y.J.: Research on fiber-optic angle sensor with capturing human joint angles. *Sci. Technol. Eng.* **3**(12), 535–538 (2012)
8. Li, Z.G.: Bending characteristics and application of single-mode fiber. *Optical Commun. Technol.* **40**(80), 60–62 (2016)





# Research Progress on Artificial Intelligence Human Sensor

Tianqi Zhao, Aiming Feng<sup>(✉)</sup>, Shangzhong Jin<sup>(✉)</sup>, Yan Shi,  
Bin Hou, and Yongqiang Yan

China Jiliang University, Hangzhou, China  
{88a3600002, 86a0402001}@cjlu.edu.cn

**Abstract.** The artificial intelligence technology has achieved great progress recently and has potential in the applications of military, intelligent industry, transportation and logistics, intelligent security check, national security, biomedicine, intelligent agriculture, intelligent services, and so on. Human-like sensor and algorithm are two pillars of artificial intelligence technology, corresponding to the ‘senses’ and ‘brains’ of intelligent machines, respectively. Based on traditional sensor technology, the artificial intelligence human-like sensor combines the novel complementary metal oxide semiconductor (CMOS), micro-electro-mechanical systems (MEMS), nanotechnology, big data and cloud computing, Internet technology, and so on, leading to the great improvement of the sensors performance. In this paper, the artificial intelligence human perception is divided into five categories: vision, hearing, smell, taste, and touch, and corresponding research progress and application of the sensors were introduced.

**Keywords:** Artificial intelligence · Human-like perception · Visual sensing · Auditory sensing · Olfactory sensing · Taste sensing · Tactile sensing

## 1 Introduction

Artificial intelligence (AI) is a new technical science that studies and develops theories, methods, techniques, and application systems for simulating and extending the human intelligence. It has developed rapidly in recent years, in the applications of military and intellectual industry, transportation logistics, smart security, national security, biomedicine, smart agriculture, and services. It attempts to understand the essence of intelligence and produce a new intelligent machine that responds in a manner similar to human intelligence. Clouds and algorithms are the ‘brains’ of intelligent machines, and sensors with various functions are equivalent to the ‘sensory’ of intelligent machines. Analogous to human sensory functions, we divide artificial intelligence human-like sensor into five categories: visual, auditory, olfactory, taste, and touch. This article details the research progress of these five types of sensors.

## 2 Vision Sensor

Image sensor is the most widely used vision sensor, with a market share of more than 40%. It is widely used in driverless, robotic, drone, AR and VR, mobile phones, PC cameras, web cameras, security surveillance, driving recorders, video conferencing, traffic sign recognition, etc.

C. Soo proposed an offset pixel aperture technique implemented on a single CMOS image sensor chip to obtain depth information without increasing hardware cost and additional light sources [1]. F. Li proposed that the image acquisition and compression unit be integrated into the photodetector array chip, which greatly saves the power, volume, and weight of the common vehicle image compression unit [2]. E. Guerrero proposed a new continuous time equalization method to overcome the limited bandwidth of integrated CMOS photodetectors [3]. S. Seo developed a phase-locked pixel CMOS image sensor with large full-well capacity and low-time noise, achieving an internal response less than 500 ps at 635 nm [4].

E. R. Fossum first developed a new type of quantum imaging sensors (QISs) [5]. As a third-generation solid-state imaging detector technology (photon counting imaging), the device surpasses existing CMOS image sensor technology and photon counting technology, adopts 3-D back-illuminated CMOS image sensor technology, and has no avalanche at room temperature. Another type of detector with photon counting imaging capabilities is a single photon avalanche photodiode array (SPAD array) [6]. Each SPAD photocell implements a single photon response by avalanche multiplication, and a readout circuit is designed inside the cell to achieve independent output of the signal.

The future development trend of vision sensors is: (1) long distance, large field of view, high image resolution; (2) fast response, low detection limit, large dynamic range; (3) miniaturization, low power consumption, low cost, robustness; (4) highly integrated with image processing algorithms, Internet technologies, etc., with good remote intelligent imaging capabilities.

## 3 Auditory Sensor

The function of the auditory sensor is to convert the acoustic signal into an electrical signal and to be recognized by humans, similar to the function of the human ear. The sensors, with the capabilities of audio positioning and automatic speech recognition, have shown great application prospects in emerging fields such as wearable devices and voice-controlled vehicle systems. Compared with traditional electrical microphones, such as electret condenser microphones, MEMS microphones are ideal for smart hearing sensors because of their high sensitivity, high stability, good consistency, miniaturization, low power consumption, low cost, and compatibility with integrated circuit processes.

In order to meet the market demand for high sound quality, the key to the advancement of MEMS microphone technology is the improvement of sensitivity with following three methods. The first method is the improvements of the device structure. For example, J. Manz proposed a novel microphone read through a comb-like capacitor

to overcome the noise caused by viscous damping losses in conventional capacitive MEMS microphones [7]. I. Yoo improved the sensitivity of capacitive MEMS microphones with a signal-to-noise ratio of 70 dB through a flexible slit film [8]. The second method is to optimize the readout portion of the device. S. Walser programmatically fine-tunes the bias voltage of the capacitive film-backplane system and the gain factor of the output preamplifier to achieve a signal-to-noise ratio of 66 dB(A) and a sensitivity of  $-38$  dB [9]. The third method is the use of device arrays. For example, Z. Wang introduced a method of connecting four MEMS microphones in parallel to a single chip, reducing the overall acoustic noise by 6 dB while maintaining the same sensitivity [10].

In the field of artificial intelligence hearing sensing, MEMS microphones currently have two main applications. The first is sound source localization. J. Tiete developed a new sound sensor Sound Compass capable of measuring local noise levels and sound field directivity [11]. M. Turqueti introduced a new intelligent acoustic sensor array system consisting of a MEMS microphone array embedded in an FPGA platform for real-time data acquisition, signal processing, and network communication [12]. The second application is the speech recognition. A. Palla proposed a speech enhancement system based on MEMS microphone array and digital signal processor to increase the signal-to-noise ratio of user speech [13]. Z. Skordilis developed a new MEMS microphone array for multi-channel speech enhancement, exploring the effectiveness of array geometry for noise suppression in diffuse and local noise fields [14].

The performance of smart hearing sensors in the future includes: (1) high acoustic sensitivity, environmental noise reduction, active noise reduction; (2) positioning function; (3) miniaturization, low power consumption, low cost, and robustness; (4) combined with deep neural network, machine learning, Internet, and other technologies, it can realize remote intelligent speech recognition.

## 4 Olfactory Sensor

The olfactory sensor is similar to the human olfactory system, commonly known as ‘electronic nose,’ which can convert the type and concentration information of gaseous substances into electrical, optical, digital, and other signals. This kind of sensor has potential in the applications of industrial gas detection, environmental pollution, monitoring, human disease monitoring, food safety, explosive gas detection, and other fields.

G. McDowell proposed an illumination-based optical trace  $O_2$  sensor, which is one of the best techniques for detecting and quantifying  $O_2$  [15]. W. Ma proposed a Fabry–Perot interferometer (FPI) for sensitivity to  $CO_2$  gas at atmospheric pressure [16]. In order to achieve high-precision detection of  $NO_2$ , O. Chmela developed a series of parallel connected single nanowire sensor systems. Trace gas monitoring of nitric oxide (NO) is one of the important topics in environmental protection and human health monitoring [17]. C. Shi introduced quartz-enhanced photoacoustic detection of NO using ion beam configuration and distributed feedback quantum cascade lasers as excitation sources [18]. M. Fisser reported the measurement of dissolved hydrogen ( $H_2$ ) in transformer mineral oil by a fiber Bragg grating gas sensor [19]. B. Bierer proposed a quasi-continuous hydrogen sulfide ( $H_2S$ ) detection system with the

advantages of good selectivity, low cost, and easy mass promotion [20]. K. Schmitt proposed the use of a pH indicator as a gas sensing layer dip coated on a glass substrate to selectively and reversibly detect  $\text{NH}_3$  in the air [21]. O. Lupan proposed the integration of palladium (Pd) modified single ZnO nanowires (ZnO: Pd NW) in nanosensor devices for efficient and rapid detection of ultraviolet (UV) light and ( $\text{CH}_4$ ) gas at room temperature [22]. K. Mitsubayashi proposed a fluorescent acetone biosensor [23]. Mid-infrared (MIR) backscattering spectroscopy has proven to be a promising technique for non-contact detection of trace explosives on various surfaces [24]. S. Lee evaluated the feasibility of using commercial portable near-infrared spectrometers to detect the freshness of various foods [25]. The latest version of the MFIG sensor continuously and selectively detects the presence of high-quality contaminant molecules in HV vacuum with sensitivity as low as  $1\text{E-}13$  mbar [26].

The future development trends of the olfactory sensor are: (1) high olfactory sensitivity and specificity; (2) miniaturization, low power consumption, low cost, and robustness; (3) multi-functionality and high integration, enabling detection of multiple gases, it has powerful data processing, storage, and analysis capabilities and is highly intelligent; (4) compatible with Internet technology and capable of remote real-time analysis and processing.

## 5 Taste Sensor

The taste sensor is similar to human taste system, commonly known as ‘electronic tongue,’ which can convert the type and concentration information of characteristic molecules in liquid or solid matter into electric, optical, digital, and other signals. The application range is wide, including disease detection, biomedicine, food quality monitoring, intelligent cooking, and so on.

S. Martin developed a holographic sensor (an ion-selective optical nanosensor) for physiological metal ion detection that achieves a real-time response to  $\text{Na}^+$  concentration in a physiological range without the physical limitations of ion-selective electrodes and invasive, with good application prospects [27]. S. Deng proposed a low-cost, portable optical pH sensor for small volume measurements [28]. For the alcohol detection, J. Novak proposed a new methanol concentration sensor compatible with the GaP process [29]. For the detection of drug molecules, R. Galatus reported a hybrid platform for sensitive detection of  $\beta$ -lactam antibiotics, particularly ampicillin [30]. J. Lee proposed using a portable microscope camera to obtain images of sashimi and using the optimized image processing technique of polarized transmission images to detect kudoa thyrsites parasites in muscle fibers [31].

The future development trends of the taste sensor are: (1) high taste sensitivity and specificity; (2) miniaturization, low cost, portable, robust; (3) high integration, multi-functionality can achieve a variety of characteristic molecules in solid-liquid substances detection; (4) Intelligent and remote real-time detection capabilities.

## 6 Tactile Sensor

The tactile sensors in artificial intelligence mainly include a pressure sensing array, a force–torque sensor, and a dynamic tactile sensor. Information obtained from artificial sensing systems can be used to find contact locations, reconstruct and identify object shapes, and measure contact forces and temperatures. However, tactile sensing technology and research have not developed like other sensors. Current research focuses on the development of new tactile skin, the use of tactile sensors to cover robotic hands, new algorithms and new methods of using tactile information in autonomous operations, and so on.

For the pressure sensing, M. Fajkus proposed a prototype FBG sensor for human heart rate monitoring [32]. J. Ke developed a highly flexible piezoelectric composite fiber optic pressure sensor for measuring muscle movement on the surface of the human body [33].

For the strain sensing, Li Yuanqing prepared a strain sensitive material CT by pyrolyzing cotton in  $N_2$  gas environment and encapsulated it with PDMS elastomer to produce a linear CT/PDMS flexible strain sensor [34]. J. Yin proposed a biomimetic, flexible resistive microfluidic shear sensor skin [35].

For the slip feeling, M. Qian proposed a FBG-based sliding sensor to allow mechanical fingers to grip objects gently [36]. H. Chen fabricated an electronic skin system including a triboelectric generator (TENG), a hybrid porous microstructure (HPMS) pressure sensor, and a fabric porous supercapacitor (FPSC) [37].

For the force–torque sensing, U. Kim proposed a new six-axis force/torque (F/T) sensor for use in robots [38]. T. Phan designed a six-degree-of-freedom force/torque sensor and its readout circuit for cooperative robot working environment [39].

For the warm feeling, Z. Peng proposed a single-mode multimode single-mode (SMS) high-temperature fiber optic temperature sensor with polyimide coating [40]. U. Sampath proposed a polymer-coated FBG sensor for simultaneous strain and temperature monitoring at low temperatures [41].

For the wet feeling, J. Xu developed a ZnO nanorod humidity sensor for atmospheric humidity detection [42]. N. Lu proposed a polymer humidity sensor made of cellulose-based composite nanofibers to achieve sensing by impedance changes caused by humidity [43].

For the flexible wearable tactile sensing, the key to the realization of flexible wearable touch sensors is the design and manufacture of functional materials [44].

The development direction of the tactile sensors is: (1) flexible and appropriate shape to surround a given surface; (2) large area and high resolution; (3) long life, recoverability, consistency and robustness; (4) perception model tactile cognition; (5) research on new materials, especially rigid materials, flexible materials, and their fusion.

## 7 Summary

Artificial intelligence human-like sensor is based on traditional sensor technology, through the combination of new CMOS, MEMS technology, nanotechnology, big data and cloud computing technology and Internet technology, so that the performance of the sensor has made a qualitative leap. The artificial intelligence human-like sensor can be divided into five perspectives: visual, auditory, olfactory, taste, and touch. In the future, the development trend of artificial intelligence human-like sensor is high precision, high sensitivity, good consistency, high reliability, long service life, miniaturization, low cost, easy mass production, low power consumption, high integration, multi-function, intelligent, remote, safe to use, and free from environmental pollution.

## References

1. Choi, B.S., Bae, M., Kim, S.H.: CMOS image sensor for extracting depth information using offset pixel aperture technique. In: Proceedings of SPIE 10376, Novel Optical Systems Design and Optimization XX, 103760Y (2017)
2. Li, F., Xin, L., Liu, Y.: High efficient optical remote sensing images acquisition for nano-satellite-framework. In: Proceedings of SPIE 10423, Sensors, Systems, and Next-Generation Satellites XXI, 104231Q (2017)
3. Guerrero, E., Aguirre, J., Sánchez-Azqueta, C.: Equalizing Si photodetectors fabricated in standard CMOS processes. In: Proceedings of SPIE 10249, Integrated Photonics: Materials, Devices, and Applications IV, 102490N (2017)
4. Seo, M.W., Shirakawa, Y., Kagawa, K.: A high performance multi-tap CMOS lock-in pixel image sensor for biomedical applications. In: Proceedings of SPIE 10076, High-Speed Biomedical Imaging and Spectroscopy: Toward Big Data Instrumentation and Management II, 100760V (2017)
5. Ma, J., Masoodian, S., Starkey, D.: Photon-number-resolving megapixel image sensor at room temperature without avalanche gain. *Optica* **4**(12), 1474–1481 (2017)
6. Dutton, N.A.W., Parmesan, L., Holmes, A.J.: 320×240 oversampled digital single photon counting image sensor. In: Proceedings of the IEEE Symposium on VLSI Circuits Digest of Technical Papers (2014)
7. Manz, J., Dehe, A., Schrag, G.: Modeling high signal-to-noise ratio in a novel silicon MEMS microphone with comb readout. In: Proceedings of SPIE 10246, Smart Sensors, Actuators, and MEMS VIII, 1024608 (2017)
8. Yoo, I., Sim, J., Yang, S.: Development of capacitive MEMS microphone based on slit-edge for high signal-to-noise ratio. In: Proceedings of 2018 IEEE Micro Electro Mechanical Systems (MEMS), 17749094 (2018)
9. Walser, S., Siegel, C., Winter, M.: MEMS microphones with narrow sensitivity distribution. *Sens. Actuators A* **247**, 663–670 (2016)
10. Wang, Z., Zou, Q.B., Song, Q.L.: The era of silicon MEMS microphone and look beyond. In: Proceedings of 2015 Transducers - 2015 18th International Conference on Solid-State Sensors, Actuators and Microsystems (TRANSDUCERS), 15362431 (2015)
11. Tiete, J., Domínguez, F., Silva, B.D.: Sound compass: a distributed MEMS microphone array-based sensor for sound source localization. *Sensors* **14**(2), 1918–1949 (2014)

12. Turqueti, M., Oruklu, E., Saniie, J.: Smart acoustic sensor array system for real-time sound processing applications. In: *Smart Sensors and MEMs Intelligent Devices and Microsystems for Industrial Application*, pp. 492–517 (2014)
13. Alessandro, P., Luca, F., Roberto, S.: Wearable speech enhancement system based on MEMS microphone array for disabled people. In: *Proceedings of 2015 10th International Conference on Design & Technology of Integrated Systems in Nanoscale Era (DTIS)*, 15220405 (2015)
14. Skordilis, Z.I., Tsiami, A., Maragos, P.: Multichannel speech enhancement using MEMS microphones. In: *Proceedings of 2015 IEEE International Conference on Acoustics, Speech and Signal Processing (ICASSP)*, 15361564 (2015)
15. McDowell, G.R., Holmes-Smith, A.S., Uttamlal, M.: A robust and reliable optical trace oxygen sensor. In: *Proceedings of SPIE 10231, Optical Sensors 2017*, 102310T (2017)
16. Ma, W.W., He, Y.L., Zhao, Y.F.: CO<sub>2</sub> sensing at atmospheric pressure using fiber Fabry-Perot interferometer. In: *Proceedings of SPIE. 10231, Optical Sensors 2017*
17. Chmela, O., Sadílek, J., Samà, J.: Nanosensor array systems based on single functional wires selectively integrated and their sensing properties to C<sub>2</sub>H<sub>6</sub>O and NO<sub>2</sub>. In: *Proceedings of SPIE. 10248, Nanotechnology VIII* (2017)
18. Shi, C., Li, Z.L., Ren, W.: Experimental and modeling study of off-beam quartz-enhanced photoacoustic detection of nitrogen monoxide (NO) using a quantum cascade laser. In: *Proceedings of SPIE 10025, Advanced Sensor Systems and Applications VII*, 100250L (2016)
19. Fisser, M., Badcock, R.A., Teal, P.D.: Development of hydrogen sensors based on fiber Bragg grating with a palladium foil for online dissolved gas analysis in transformers. In: *Proceedings of SPIE 10329, Optical Measurement Systems for Industrial Inspection X*, 103292P (2017)
20. Bierer, B., Dinc, C., Gao, H., Wöllenstein, J.: MEMS-based array for hydrogen sulfide detection employing a phase transition. In: *Proceedings of SPIE 10246, Smart Sensors, Actuators, and MEMS VIII*, 102460D (2017)
21. Schmitt, K., Tarantik, K., Pannek, C.: Colorimetric sensor for bad odor detection using automated color correction. In: *Proceedings of SPIE 10246, Smart Sensors, Actuators, and MEMS VIII*, 102461F (2017)
22. Lupan, O., Adelung, R., Postica, V.: UV radiation and CH<sub>4</sub> gas detection with a single ZnO: Pd nanowire. In: *Proceedings of SPIE. 10105, Oxide-based Materials and Devices VIII* (2017)
23. Mitsubayashi, K., Chien, P.J., Ye, M.: Fluorometric biosniffer (biochemical gas sensor) for breath acetone as a volatile indicator of lipid metabolism. In: *Proceedings of SPIE 10013, SPIE BioPhotonics Australasia*, 100131T (2016)
24. Fuchs, F., Hugger, S., Jarvis, J.P.: Hyperspectral imaging for standoff trace detection of explosives using quantum cascade lasers. In: *Proceedings of SPIE. 10111, Quantum Sensing and Nano Electronics and Photonics XIV* (2017)
25. Lee, S., Noh, T.G., Choi, J.H.: NIR spectroscopic sensing for point-of-need freshness assessment of meat, fish, vegetables and fruits. In: *Proceedings of SPIE 10217, Sensing for Agriculture and Food Quality and Safety IX*, 1021708 (2017)
26. Maas, D., Muilwijk, P., Putten, M.: Lab- and field-test results of MFIG, the first real-time vacuum-contamination sensor. In: *Proceedings of SPIE 10145, Metrology, Inspection, and Process Control for Microlithography XXXI*, 101452I (2017)
27. Gul, S., Martin, S., Cassidy, J.: Development of sensitive holographic devices for physiological metal ion detection. In: *Proceedings of SPIE 10354, Nanoengineering: Fabrication, Properties, Optics, and Devices XIV*, 103540C (2017)

28. Deng, S.J., McAuliffe, M.A.P., Salaj-Kosla, U.: A pH sensing system using fluorescence-based fibre optical sensor capable of small volume sample measurement. In: Proceedings of SPIE 10110, Photonic Instrumentation Engineering IV, 101101C (2017)
29. Novák, J., Laurenčíková, A., Hasenohrl, S.: Methanol sensor for integration with GaP nanowire photocathode. In: Proceedings of SPIE 10248, Nanotechnology VIII, 102480E (2017)
30. Galatus, R., Feier, B., Cristea, C.: SPR based hybrid electro-optic biosensor for  $\beta$ -lactam antibiotics determination in water. In: Proceedings of SPIE 10405, Remote Sensing and Modeling of Ecosystems for Sustainability XIV, 104050C (2017)
31. Lee, J., Lee, H., Kim, M.: Rapid detection of parasite in muscle fibers of fishes using a portable microscope imaging technique. In: Proceedings of SPIE 10217, Sensing for Agriculture and Food Quality and Safety IX (2017)
32. Fajkus, M., Nedoma, J., Martinek, R.: Fiber optic sensor encapsulated in polydimethylsiloxane for heart rate monitoring. In: Proceedings of SPIE 10208, Fiber Optic Sensors and Applications XIV, 102080W (2017)
33. Ke, J.Y., Chu, H.J., Hsu, Y.H.: A highly flexible piezoelectric-fiber pressure sensor based on highly aligned P(VDF-TrFE) electrospun fibers. In: Proceedings of SPIE 10164, Active and Passive Smart Structures and Integrated Systems 2017, 101642X (2017)
34. Li, Y.Q., Huang, P., Zhu, W.B., Fu, S.Y., Hu, N., Liao, K.: Flexible wire-shaped strain sensor from cotton thread for human health and motion detection. *Scientific Reports* **7**, 45013 (2017)
35. Yin, J.Z., Santos, V.J., Posner, J.D.: Bioinspired flexible microfluidic shear force sensor skin. *Sens. Actuators A* **264**, 289–297 (2017)
36. Qian, M.Y., Yu, Y.L., Ren, N.K.: Sliding sensor using fiber Bragg grating for mechanical fingers. *Opt. Express* **26**(1), 254–264 (2018)
37. Chen, H.T., Song, Y., Guo, H.: Hybrid porous micro structured finger skin inspired self-powered electronic skin system for pressure sensing and sliding detection. *Nano Energy* **51**, 496–503 (2018)
38. Lee, D.H., Kim, U., Jung, H.: A capacitive-type novel six-axis force/torque sensor for robotic applications. *IEEE Sens. J.* **16**(8), 2290–2299 (2016)
39. Phan, T.P., Chao, P.C.P., Cai, J.J.: A novel 6-DOF force/torque sensor for COBOTs and its calibration method. In: Proceedings of 2018 IEEE International Conference on Applied System Invention (ICASI), 17861840 (2018)
40. Peng, Z.Z., Wang, L., Yan, H.H.: Research on high-temperature sensing characteristics based on modular interference of single-mode multimode single-mode fiber. In: Proceedings of SPIE 10025, Advanced Sensor Systems and Applications VII, 1002519 (2016)
41. Sampath, U., Kim, D., Song, M.: Coupled-fiber Bragg grating sensor structure for cryogenic conditions. In: Proceedings of SPIE 10374, Optical Modeling and Performance Predictions IX, 1037408 (2017)
42. Xu, J., Bertke, M., Li, X.: Gravimetric humidity sensor based on ZnO nanorods covered piezoresistive Si microcantilever. In: Proceedings of SPIE. 10246, Smart Sensors, Actuators, and MEMS VIII (2017)
43. Lu, N.S., Ameri, S.K., Ha, T.: Epidermal electronic systems for sensing and therapy. In: Proceedings of SPIE 10167, Nanosensors, Biosensors, Info-Tech Sensors and 3D Systems 2017, 101670J (2017)
44. Yang, T.T., Xie, D., Li, Z.H.: Recent advances in wearable tactile sensors: materials, sensing mechanisms, and device performance. *Mater. Sci. Eng. R* **115**, 1–37 (2017)





# Investigation on Oil Spectrum Detection Technology Based on Electrode Internal Standard Method

Mingfan Dai, Zhen Wang, Shenghua Zhou, Bangning Mao,  
and Yanqing Qiu<sup>(✉)</sup>

China Jiliang University, Hangzhou, China  
qyqhz@cjl.u.edu.cn

**Abstract.** In order to solve the problem that the internal standard elements cannot be added to the rotating disk electrode (RDE: Rotation disk electrode) oil spectrometer, which leads to the low stability and accuracy of the test results. In this paper, an internal standard detection technique using the components of the electrode itself as the internal standard is proposed. Firstly, the spectrum line of carbon element, which is the main component of the electrode under pulsed arc excitation, is used as the internal standard, and the actual test spectrum data obtained within the standard test time are normalized. Then, according to the internal standard method, the different elements needed to be tested are processed according to the peak-to-bottom ratio method. Finally, the method is applied to the oil analysis spectrometer developed by ourselves. The experimental results show that the test results using the electrode internal standard method are obviously better than those without the electrode internal standard method. The repeatability and reproducibility error of the measured values are within the allowable range of ASTM-D6595, especially the reproducibility and reproducibility of iron, copper, magnesium, aluminum, and so on are better than those of ASTM-D6595 standard. The RSD value is increased by nearly one order of magnitude, which can meet the needs of the actual lubricating oil detection and analysis, and the stability and accuracy are better.

**Keywords:** Atomic emission spectroscopy (AES) · High concentration · Internal standard method · ASTM-D6595

## 1 Introduction

With minor mismatches in the installation or the increase of service time of the machine, the mechanical equipment will produce a small amount of wear during operation. These wear will produce metallic or non-metallic abrasive particles in the lubrication system of the equipment, which will affect the lubricating effect of the oil and will cause serious accidents or even thorough damage to the equipment [1]. Therefore, in some mechanical operation places and occasions that are prone to serious accidents, conventional and accurate spectroscopic detection of lubricating oil can not only routinely detect the health status of equipment, it is also possible to give timely warnings before the equipment wear fault occurs, thus effectively ensuring the normal

operation of the equipment and avoiding the accident, which is with great significance [2–4].

The general internal standard method is to add a certain amount of pure substance as internal standard to the sample mixture to be analyzed and then test it [5]. However, the internal standard method proposed in this paper can be completed without adding any elements to the sample under analysis, which not only solves the problem that no elements can be added to the standard oil used in the test, but also improves the accuracy and stability of the test results.

### 1.1 Detection Principle and Experimental Device

**Detection Principle** The detection of metal composition can be done by measuring atomic emission spectra, and when an atom gets external energy, its outer electrons are excited to a higher energy level. Electrons at the high energy level radiate excess energy in the form of photons when they return to the ground state. Each element has its own energy level and characteristic spectrum, so the type of element to be tested can be judged by the atomic emission spectrum line. According to the intensity of the spectral line, the concentration of the corresponding elements can be determined. The relationship between the emission intensity ( $I$ ) of the spectral line and the concentration of the analyte ( $C$ ) is expressed by the Scheibe-Lomakin formula:

$$I = aC^b \quad (1)$$

In the formula,  $a$  and  $b$  are constants related to test conditions [6].

**Experimental Principle and Steps** As shown in Fig. 1, the spectroscopic detection of lubricating oil is based on the atomic emission spectrum theory, and the rotating disk electrode excitation device is used. The testing process is divided into three stages. In the first stage, the excitation discharge circuit is turned on, the disk electrode is rotated

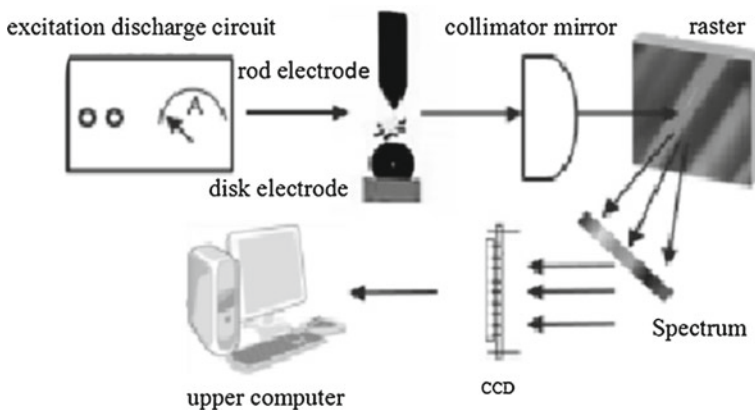


Fig. 1 Flow diagram of lubricating oil spectrum detection

at a certain speed, and the oil attached to the disk electrode is transferred to the spark discharge gap, then the oil to be measured at the discharge gap is heated and evaporated, dissociated into atoms or ionized into ions, which further excites the atoms or ions to produce radiation. In the second stage, the excited atomic emission spectrum is collimated through the lens and then transmitted to the ultraviolet spectrometer by quartz fiber. The radiation signal collected by the spectrometer is spacially dispersed by an optical grating. In the third stage, the one-dimension detector is used to detect the radiation at different wavelengths after light splitting, and the data are transmitted to the upper computer software. According to the line strength of the corresponding characteristic wavelength of the spectrum, the concentration is qualitatively analyzed.

The American Association for Testing and Materials Standard ASTM-D6595 is widely used for the detection and analysis of metal wear particles in used or new lubricating oil and hydraulic oil. The standard of test method for metal wear particles in lubricating oil and hydraulic oil is based on atomic emission spectrum of rotating disk electrode. The existing national standard GB/T 17476 is also established on the basis of the former. The testing procedure involved in this paper is strictly in accordance with the ASTM-D6595 standard.

**Experimental Preparation** In the case of high concentration test, the standard oil in the instrument is calibrated with the test results of the standard oil of 0, 100, and 900 ppm produced by Conostan Company. Then test the standard oils of 0, 50, 100, 300, 500, and 900 ppm three times under the test conditions with and without the internal standard method. The test data were calculated and analyzed by using MATLAB software to verify the stability and accuracy of using the internal standard method to improve the experimental results.

## 2 Detection Principle and Experimental Device

A set of spectrometers is composed of three polychromatic instruments, named as CC, CD, and CE. Using MATLAB software to process the off-line data generated in the experiment operation, we can obtain the spectrum of CC, CD, CE, corresponding to Fig. 2a–c, respectively. The horizontal coordinate is the pixel number, and the vertical coordinate is the response intensity. According to the metal elements and their recommended lines in Table 1, the required peak lines were marked and the elements named in Fig. 2a–c.

Without the use of internal standard method, Fig. 3a–c can be obtained by the off-line data processing, of which the horizontal coordinate is the ppm value, and the vertical coordinate is the characteristic value denotes the line strength. As can be seen from the three linear slope spectra of Fig. 3a–c, the linearity slope of most elements is very small, which leads to a great change in the corresponding ppm value if the characteristic value changes a little bit, leading to the instability and the large deviation of the test results.

With the help of the internal standard method, we can process the off-line data by MATLAB to obtain the Fig. 4a–c, of which the horizontal coordinate is the ppm value, and the vertical coordinate is the characteristic value. As can be seen from the three

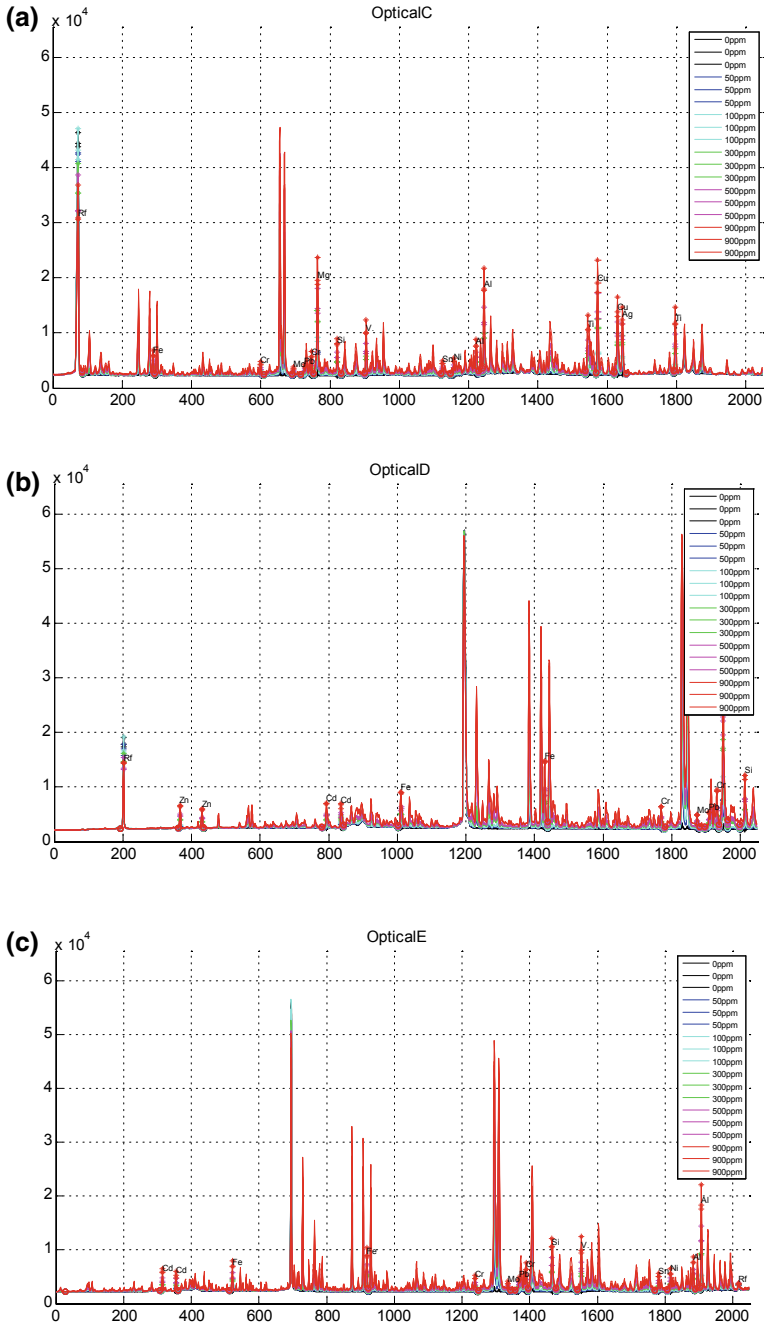


**Fig. 2** a CC spectrogram. b CD spectrogram. c CE spectrogram

**Table 1** Metallic element and recommended characteristic lines

Element	Wavelength
Fe	259.94
Cu	324.75, 224.26
Mg	280.20, 518.36
Al	308.21
Ni	341.48
Cd	393.37, 445.48
Sn	317.51
Pb	283.31
Ti	334.94
Cr	425.43
Zn	213.86
Si	251.60
Ag	328.07, 243.78

linear slope spectra of Fig. 4a–c, the linearity slope of each element is obviously increased after the internal standard method is enabled. Compared with the non-enabled internal standard method, its characteristic values change to a certain extent and the corresponding ppm values do not change much, which makes the test results more stable.

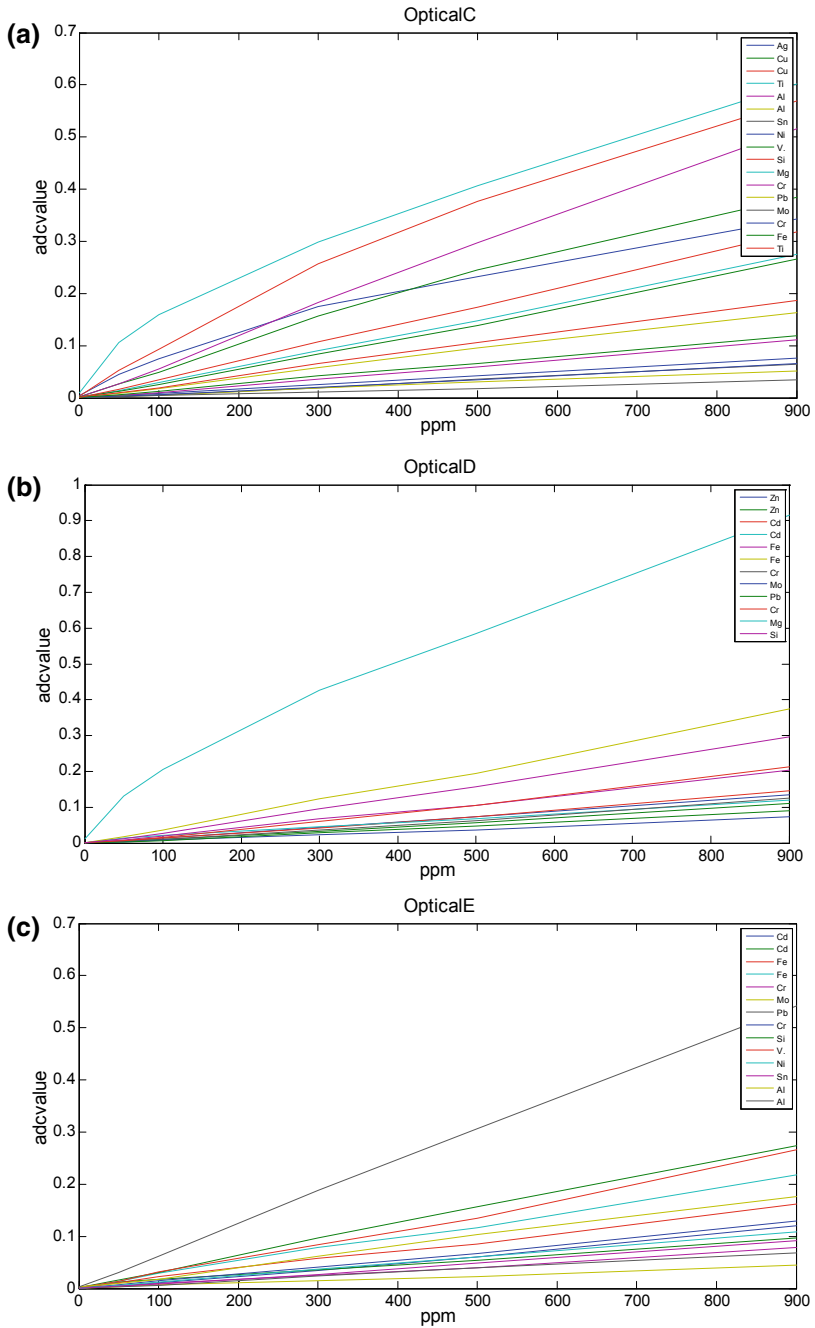
The test results were taken as examples of the focused element Fe, Cu, Mg, and Al.

Table 2 shows the test results without the internal standard method. It can be seen that the stability of the experimental results is good at the concentration of 0, 50, and 100 ppm. The fluctuation of individual elements is relatively large at the concentration of 300 ppm. At the concentration of 500 and 900 ppm, more than half of the elements are volatile. As can be seen in conjunction with Fig. 3a–c, the linearity slope of these elements is very small, if the characteristic value of the same concentration changes a little, the corresponding ppm value will change a lot, which leads to the instability of the test results.

Table 3 shows the test results of the internal standard method. It can be seen that the stability and accuracy of the test results at low concentrations are not particularly obvious. However, the stability and accuracy of the test results at high concentration are significantly improved compared with the results without using the internal standard method.

In combination with Tables 2 and 3, the reproducibility and repeatability of Fe, Cu, Mg, Al at different concentrations are calculated according to the national standard GB/T 17476.

From Tables 4, 5, 6, and 7, we can see that the test results with the internal standard method are better than those without the internal standard method in terms of reproducibility and repeatability.



**Fig. 3** **a** Non-internal standard CC linear slope spectrogram. **b** Non-internal standard CD linear slope spectrogram. **c** Non-internal standard CE linear slope spectrogram

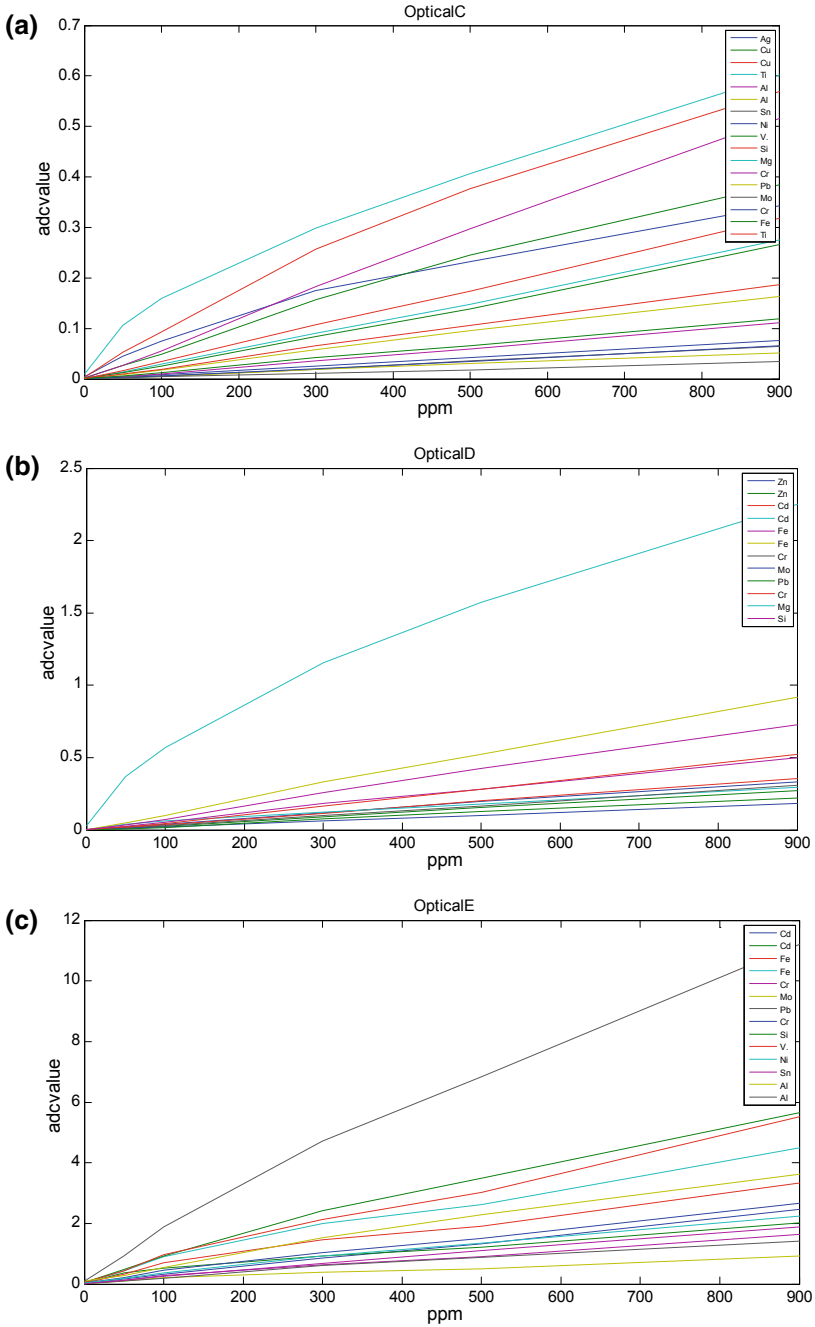


**Fig. 4** **a** With internal standard CC linear slope spectrogram. **b** With internal standard CD linear slope spectrogram. **c** With internal standard CE linear slope spectrogram

**Table 2** Test results without internal standard method

Element	900 ppm	500 ppm	300 ppm	100 ppm	50 ppm	0 ppm
Fe	810.7	339	284.3	97.9	50	0
	857.4	404.6	286.7	97.5	45.3	0
	960.6	463.8	287.8	99.5	48.6	0
Cu	961.9	302.7	295.7	97.2	52.6	0
	737.8	468.3	267.7	97.4	51.9	0
	1055.8	390.9	254.7	88.4	50	0
Mg	795.7	355.1	262.4	90.8	51.9	1.3
	589	408.1	271.3	91.3	47.7	0
	717.4	397.2	275.3	92.6	51.1	0
Al	910.9	459.3	308.8	101.1	52.4	0
	763.5	509.5	266.4	105.6	50.7	0
	984.2	427.5	294.1	98.1	52.5	0

**Table 3** Test results with internal standard method

Element	900 ppm	500 ppm	300 ppm	100 ppm	50 ppm	0 ppm
Fe	889.3	479.8	264.9	96.1	45.4	0
	863.7	488.1	269.8	95.6	45.5	0
	884.9	473.9	275	96	46.8	0
Cu	882.7	524.3	278.3	93.5	44	0
	916.2	487.1	282.7	92.1	45	0
	905.4	470.5	275.6	98	46.7	0
Mg	864.3	514.9	269.8	100.3	45.9	0
	895.1	487	284.8	97.7	48	0
	858.9	453.8	273.3	98.4	47.1	0
Al	899.8	502.9	278.4	96.4	47	0
	897.5	486.7	270.1	93.7	45.4	0
	845.9	474.8	283.2	95.4	49.9	0

**Table 4** Reproducibility without internal standard method

Reproducibility	Fe	Cu	Mg	Al
500 ppm	97.88	81.16	112.12	35.16
900 ppm	30.32	22.72	189.8	11.33

**Table 5** Repeatability without internal standard method

Repeatability	Fe	Cu	Mg	Al
500 ppm	50.98	34.52	23.11	33.81
900 ppm	65.97	134.07	90.35	92.11



**Table 6** Reproducibility with internal standard method

Reproducibility	Fe	Cu	Mg	Al
500 ppm	20.07	3	11.8	25.39
900 ppm	22.12	8.5	28.62	19.88

**Table 7** Repeatability with internal standard method

Reproducibility	Fe	Cu	Mg	Al
500 ppm	6.2	24.45	10.39	12.43
900 ppm	9.83	25.3	16.54	25.06

### 3 Conclusion


In this paper, an internal standard detection technique using the components of the electrode itself as the internal standard is proposed, according to the ASTM-D6595 test standard of the American Association of Materials and Testing, the electrode internal standard detection technology is used to test different concentrations of standard oil. The experimental results show that when the concentration of the standard oil is less than or equal to 100 ppm, the stability and reliability of the test results with and without the internal standard method are not very different. However, when the standard oil concentration is higher than 100 ppm, the test result using the internal standard method is obviously superior to the test result without using the internal standard method. At the same time, the repeatability and reproducibility error of the measured values are within the allowable range of the ASTM-D6595 standard, especially the repeatability and reproducibility of the key elements such as Fe, Cu, Mg, Al are better than the requirements of the ASTM-D6595 standard. It can meet the needs of actual detection and analysis of lubricating oil, and the stability and accuracy are better.

### References

1. Zheng, C.S., Ma, B.: Based on oil spectrum analysis of comprehensive experimental study transmission condition monitoring. *Spectronic Instrum. Anal.* **29**(3), 749–751 (2009)
2. Wang, J., Yin, F.J., Xia, X.J.: The application of ICP-OES in the elemental analysis of engine oils. *Lubricating Oil* **2**, 45–49 (2015)
3. Zhang, Y.F.: Investigation on the behavior of single spark discharge in spark source atomic emission spectrometry. *Metallurgical Anal.* **36**(1), 4–10 (2016)
4. Wang, H., Ma, X.M., Zheng, W.: Determination of 10 trace impurity elements in titanium and titanium alloys with DC arc Atomic Emission Spectrometry. *Rock Mineral Anal.* **33**(4), 506–511 (2014)
5. Wang, X.P., Sun, P.Y., Zhou, Q., Li, M., Cao, L.X., Zhao, Y.H.: Internal standard analysis of saturated hydrocarbon fingerprint of crude oil. *Anal. Chem.* (08), 1121–1126 (2007)
6. Lei, H.T.: Determination of nitrogen in structural steel by spark source Atomic Emission Spectrometry. In: China Automotive Engineering Society Annual Meeting Proceedings, 3 (2015)



# Design of Compact Oil Particle Counter System Based on Microscopic Imaging

Zhonghui Cheng, Bin Shen, Dong Fu, Shangzhi Zhong, Yan Xuan, Tianhu Zhang, and Yanqing Qiu 

China Jiliang University, Hangzhou, China  
qyqhz@cjlu.edu.cn

**Abstract.** In this paper, a compact oil particle counter system based on microscopic imaging and smart camera was developed. An optical lens system with 2 times optical magnification and 105 mm conjugate distance was designed. The image data acquired from the high-definition CMOS module (based on Hi3516A) was processed by a CPU on the camera. A control circuit board was developed to display the results in a TFT screen and control the working process of the whole system. Finally, a compact particle counter system with the optical resolution better than 2  $\mu\text{m}$  was acquired. Compared with similar commercial products as we know, this system was accurate and portable, especially suitable for field and online testing.

**Keywords:** Compact oil particle counter system · Microscopic imaging · Smart camera · Control circuit board

## 1 Introduction

With the rapid development of emerging industries, safe and reliable equipment has become an important guarantee for its continued rapid development. Among them, lubricating oil, hydraulic oil, transformer oil, fuel oil, and other oils play a pivotal role in the operation of related equipment. The existence forms of pollutants in oil can be divided into solid particles, bubbles, moisture, etc. [1], and solid particles have the greatest influence of the equipment, because the equipment will be damaged by solid particles. Therefore, the solid particles have become the focus and difficulty in system of oil pollution control [2]. In this context, oil contamination detection technology for indicating the degree of oil contamination has emerged.

At present, oil particle counters are used to detect the concentration of oil particles. And the manufacturers are mainly foreign companies, such as the American Pacific Instruments. Most of these domestic instruments rely on imports, which has the drawbacks of high price. Desktop computer is also taken as the current processor of the oil particle counter, which is large in size and not conducive to carry and inconvenient in on-site monitoring. Hence, there are great development prospects and economic benefits for this kind of instruments.

According to the actual requirements, a compact oil particle counter system based on microscopic imaging method was designed to detect the solid particles pollution degree of oil including lubricating oil, hydraulic oil, transformer oil, and fuel oil.

Compared with similar commercial products as we know, this system has the advantages of accurate and portable, especially suitable for field and online testing.

## 2 System Composition and Working Principle

### 2.1 System Hardware Composition

This paper was dedicated to the design and development of a compact oil particle counter system based on microscopic imaging. The method used in this system was part of the flow image analysis method of automatic oil particle counter. As shown in Fig. 1, an illumination source illuminates the oil sample in the chip sampling device. Through the optical microscopy system, the small particles are imaged on the sensor of the smart camera. A custom algorithm was written on the built-in system of the smart camera instead of a computer to meet the compact requirements. On the basis of previous studies, this paper will combine the related knowledge of optics, electricity, image processing, and single-chip microcomputer to study the system design.

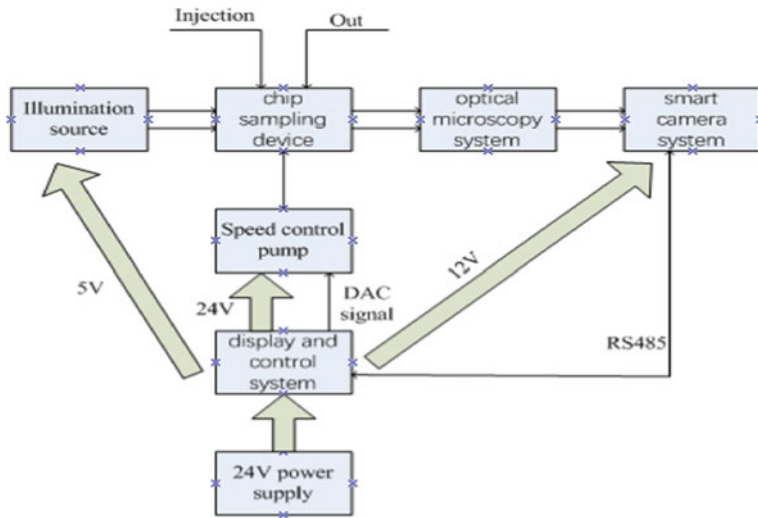
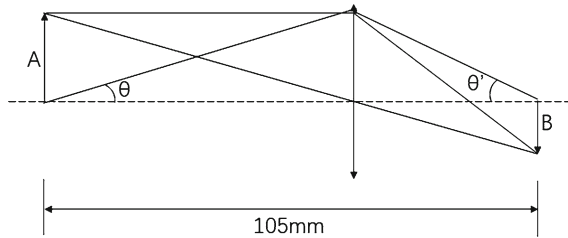


Fig. 1 System logic structure

According to the established scheme, this system consists of four main parts—a chip sampling device, an optical microscopy system, a smart camera system, and a display and control system, as shown in Fig. 1. The chip sampling device had been designed by the relevant research group and was not within the scope of this paper. The sensor part of the system was formed by the optical microscopy system and the smart camera system. The main functions were optical imaging, image acquisition and data processing, and sending the processing results to the display and control system.

## 2.2 Design of High-Resolution Microscopy Imaging Optical Lens

This paper was devoted to the design of a compact and portable oil particle counter system. Considering the volume and weight requirements of such instruments, according to the scheme, the optical system needed to follow the image sensor size and size of the smart camera to develop parameters related to microscopic imaging lenses [3]. The basic principle of the micro-imaging lens is shown in Fig. 2.



**Fig. 2** Basic principle of micro-imaging lens

In consideration of the improvement of the confidence and the existing microscopic imaging lens on the market was difficult to meet the requirements of the system, it was decided to redesign the microscopic imaging lens to achieving the goals.

Imaging requirements:

Illumination source: 850 nm wavelength LD;

Numerical aperture (NA): 0.2;

Microscopic magnification: 2 times;

System imaging conjugate distance: no more than 105 mm;

Depth of field: not less than 15  $\mu\text{m}$ ;

Optical resolution: better than 2  $\mu\text{m}$  (based on minimum particle size);

Resolution: no less than 2 million pixels;

Modulation Transfer Function (MTF) > 0.2.

An optical microscopy imaging system designed based on the above requirements will have the following advantages: (1) Using two times magnification to improve the field of view and increase the sampling rate and the accuracy of statistics. (2) Using 850 nm light source can further equalize the sensitivity of RGB three pixels, thereby improving the image gain balance of the system. (3) The use of laser light source can further reduce the color difference of the optical system.

**Initial Structure Setting and Optimization** According to the guidance of the instructor, the design of the micro-magnification lens with two sets of cemented lenses combined with a single lens was selected. As shown in Fig. 3. Among them, the glass used in the first set of double cemented lenses was H-LAK8A, H-ZLAF53A, the second set of double cemented lenses was H-LAK61, H-SFS6, and the last single lens was H-LAF54.

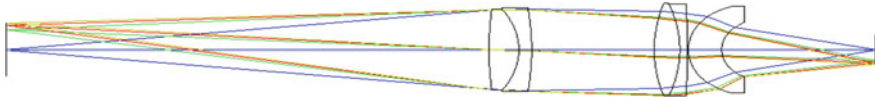


**Fig. 3** System selected lens design

After determining the design, the basic parameters according to the imaging requirements were calculated. It was known that the microscopic magnifying optical system usually adopted the reverse design idea that was the tracking direction of the light reached the object surface from the image plane. And Fig. 3 shows the reverse design of the lens system.

In the reverse design, the object value was set to 0.1 in the system general configuration. Since the laser light source of 850 nm wavelength was selected, the wavelength setting was 820, 850, and 870 nm, and the weights were set to 1, 2, and 1. Because the selected sensor was IMX185, and the size was 1/1.8, so selected the height of the object when the field of view was set, and selected four fields of view for optimization analysis, their y field values were 0, 2.2, 3.1, 4.4, which were 0 field of view, 50% of the maximum field of view, 70% of the maximum field of view and 100% of the maximum field of view.

Calculation of spatial resolution: By the formula  $1/2D = 1/(2 \times 2 \mu\text{m}) = 250 \text{ lp/mm}$ , the  $D$  in the formula referred to the sensor's single pixel size. Actually, the  $2 \mu\text{m}$  substituted in our calculation was approximately substituted according to the actual size of the sensor of  $3.75 \mu\text{m}$ . The calculation of this value was used in the MTF that was the MTF met the required 0.2 at an abscissa of 250 lp/mm. The system modulation evaluation function (MTF) is shown in Fig. 4. As can be seen from the figure, the system's MTF has met the design requirements.

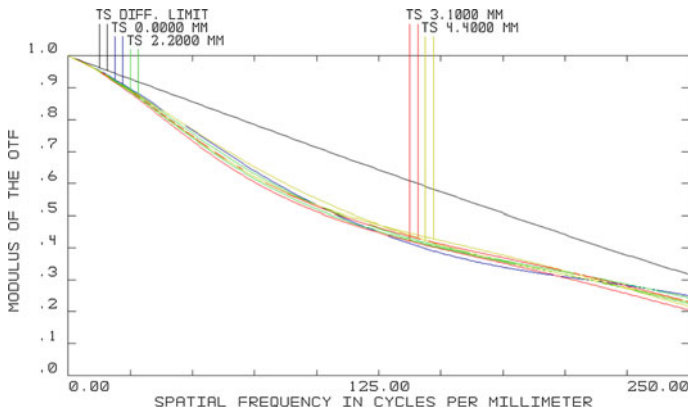


**Fig. 4** System MTF

**Microscopic Imaging Lens Mechanical Structure** For easy processing and assembling, a reasonable mechanical designed was made, as shown in Fig. 5, which is compact in structure, low cost, and easy for assembling.

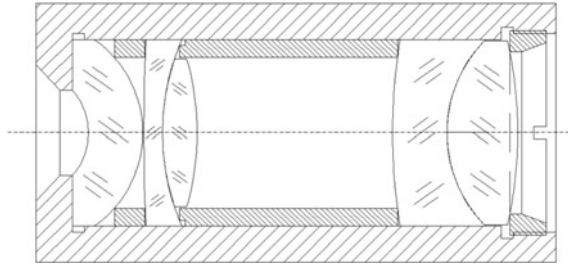


**Fig. 5** Microscopic imaging lens mechanical structure

### Smart Camera System Design

*Smart camera selection.* The smart camera selected million star-level module—Hi3516A+IMX185, which has functions of image acquisition, data processing, network communication, etc., which provided convenient help for the research and development system of this paper (Fig. 6).

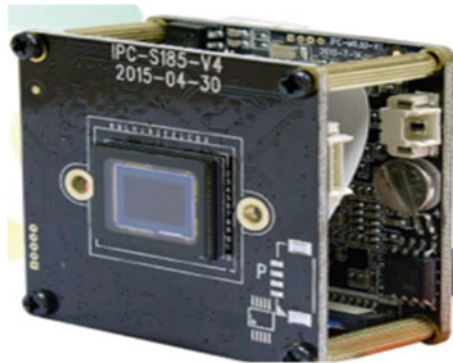


**Fig. 6** Smart camera with Hi3516A as the main control chip

This smart camera integrated the image acquisition, processing, and communication functions into a single camera, which had greatly helped the system developed in this paper.

Hi3516A was a professional high-end system on chip (SOC) developed by HiSilicon for high-definition IP camera (network camera) products. Its 1080P@30fps H264 multi-stream encoding performance, excellent image processing, high-performance intelligent acceleration engine and other features. Significantly reduced ebom (engineering design) costs while meeting customer differentiated IP camera product features, performance, and image quality requirements [4], and IMX185 is a CMOS color image sensor manufactured by Sony Corporation.

### 3 Measurement Experiments and Results

#### 3.1 Application

The physical system for testing based on the system logic structure diagram is shown in Fig. 7.

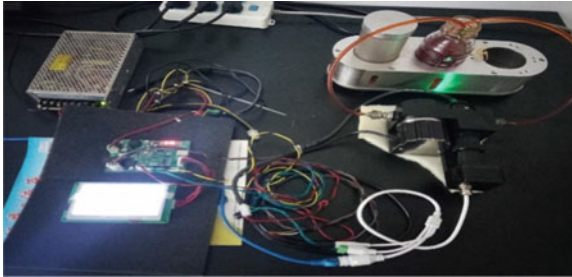


Fig. 7 Physical test system

#### 3.2 Test Process and Results

Confirm a test standard, such as GJB420B-2006, print, and save the test results to obtain the test results in paper and electronic versions for archiving. The corresponding test was done. Result of a test result is shown in Fig. 8.

Plane NO:	012345	Oil NO:	012345
counts/100ml:			
size(um):	cum1:	class:	
>1(>4)	255856	9	
>5(>6)	67545	8	
>15(>14)	17281	9	
>25(>21)	5420	10	
>50(>38)	16	4	
>100(>70)	0	0	
test standard:	GJB420B-2006	class:	10

Fig. 8 Version test results

### 4 Conclusion

The test results showed:

The current oil particle sensor is portable, and the overall performance of online detection is still not good, and oil online monitoring technology is currently developing

toward integration, automation, and intelligence. Now research hotspots focus on basic theory research, new online oil sensors, and integration of integrated online monitoring technologies. Compared with similar commercial products as we know, this system was accurate and portable, especially suitable for field and online testing.

**Acknowledgements.** This work was supported by Zhejiang University Student Research Innovation Program (project No. 2018R409012).

## References

1. Wu, S.Y., Wang, S.F.: Sources, hazards and control measures of hydraulic oil pollution. *Equipment Manufact. Technol.* **3**, 80–82 (2008)
2. Yang, M., Xiong, C.H.: Determination of oil contamination: particle counting method and automatic particle counter. *Hydraulics Pneumatics & Seals* **31**(04), 1–3 (2011)
3. Zhang, W.H., Li, X.N.: A practical method for testing MTF of imaging lens using CMOS image sensor. *Opt. Instrum.* **28**(6), 17–22 (2006)
4. <http://www.travellinux.com/product-solutions/hi35xx-sdk-edb-ip-Camera-dvr-nvr-rdk.html>. Last accessed 21 Dec 2018





# Adaptive Phase Estimation in the Presence of Nonlinear Phase Noise for Coherent Optical Detection

Faith Kwaku Deynu<sup>1,2</sup>(✉), Bo Xu<sup>1</sup>, and Evans Wilson Akpari<sup>2</sup>

<sup>1</sup> University of Electronic Science and Technology of China, Chengdu 611731, China

faithdeynu@yahoo.com

<sup>2</sup> Ho Technical University, P.O. Box HP 217, Ho, Ghana

**Abstract.** For phase-modulated systems, digital carrier phase estimation (CPE) has been generally accepted as the fundamental solution to suppressing the challenging effects of laser phase noise (LPN). The optimal average length FIR filter used in carrier phase estimation algorithms, which is the best trade-off between tracking the time-varying phase offset and reducing effects of the Gaussian noise, has been identified as crucial to estimating phase reference from consecutive multi-symbols and impacts performance of digital coherent receivers. The optimal average length depends on factors such as laser linewidth and optical signal-to-noise ratio (OSNR) as well as nonlinearities of the channel, factors that are very difficult to observe in actual networks because they differ device by device, channel by channel, and subject to change with time, since their statistical knowledge may be unknown especially in reconfigurable optical systems. This paper proposes a simple adaptive phase estimation scheme that uses a phase noise reference to suitably set the properties of the FIR filter (i.e., average length) in phase tracking circuits under different channel conditions to mitigate the combined effects of both intrinsic laser phase noise and nonlinear phase noise in coherent phase-modulated optical systems.

**Keywords:** Coherent optical fiber communication · Phase noise · Adaptive carrier phase estimation

## 1 Introduction

The recent commercialization of the digital coherent transceiver applications for 50 Gb/s BPSK, 100 Gb/s QPSK, and 200 Gb/s 16-QAM in submarine links, terrestrial long-haul systems, and metro/regional networks, respectively, confirmed the trend toward coherent systems in future optical communication systems in order to enhance fiber capacity and overcome the nonlinear limit to avoid capacity crunch [1]. For phase-modulated systems, digital carrier phase estimation (CPE) [2] has been generally accepted as the fundamental solution to suppressing the challenging effects of laser phase noise (LPN). In realistic long-haul coherent optical fiber communication systems, there exists not only LPN but also nonlinear phase noise (NLPN) due to fiber nonlinearities caused by Kerr effects. As a result, mitigating phase shifts due to fiber

nonlinearity becomes the next logical step to improving transmission performance of coherent optical phase-modulated systems. The NLPN in a single channel has two effects: the average fixed phase shift due to signal–signal self-phase modulation (SPM) and the signal–noise interactions known as Gordon–Mollenauer (GM) effect [3]. On the other hand, digital back-propagation (DBP) [3] effectively mitigates the former effect but often fails in the presence of the latter to converge to the exact transmitted signal. Hence, DBP cannot avoid performance degradation caused by the GM effect. Furthermore, prior works have identified the average length used in carrier phase estimation algorithms as crucial to estimating phase reference from consecutive multi-symbols and can be optimized blindly [4] or based on phase noise statistics to influence the performance of digital coherent receivers in the presence of cross-phase modulation (XPM). The optimal average length, which is the best trade-off between the varying speed of the phase offset and reducing effects of the Gaussian noise, depends on factors such as laser linewidth and optical signal-to-noise ratio (OSNR) as well as nonlinearities of the channel. Since these factors differ device by device, channel by channel, and subject to change with time and are very difficult to observe in actual networks because their statistical knowledge may be unknown especially in reconfigurable optical systems, it is desirable that the carrier phase estimator be adaptive. It is therefore very useful to adaptively choose the average length under different channel conditions to get the best performance in coherent optical systems. In this paper, the authors propose a simple adaptive phase estimation scheme that uses the phase noise reference to appropriately set the properties of the FIR filter (i.e., average length) in the phase tracking circuit to mitigate the combined effects of both the intrinsic laser phase noise (LPN) and GM effect.

## 2 Adaptive Filtering

Under the conventional CPE scheme which uses a fixed optimum FIR filter, a case of ASE-noise-limited channel requires a large tap number of FIR filters for superior performance. Contrarily, a case of phase-noise-limited channel requires a short FIR filter to dynamically track the phase rotation caused by the large phase noise fluctuation. In real system implementations, condition of system noises is probably subject to vary with time and from channel to channel frequently. This suggests that the conventional CPE scheme with a fixed property of the FIR filter may be ineffective to precisely follow the phase rotation under any of the above channel conditions and offers only a limited gain. Hence, the FIR filter needs to be automatically adjusted in systems under different conditions to get the best performance. Furthermore, when launch power is low, the dominant limiting factor in the system is ASE noise. In contrast, with increasing launch power as is the case during fiber nonlinearity regime, a larger reduction in ASE noise eventually occurs and the system becomes phase-noise limited. As a consequence of the large phase noise, the optimal FIR filter subsequently becomes quite small. As ASE noise is Gaussian distributed, medium-to-low noise occurs frequently than large noise. Any occurring large ASE noise signal at the instance of large phase noise can be difficult to average out which can skew the overall phase estimation from the actual value significantly. Thus, any symbol with

such large phase noise is likely to severely distort the phase estimation and cause performance degradation. To improve upon the stability of the CPE performance in situations of large phase noise, the proposed CPE scheme eliminates those symbols with large noise in the phase reference (PR) signal from averaging process by setting the PR signal to zero during such instances. The proposed scheme therefore seeks to divide the channel into a case of phase-and-ASE-noise-limited subchannels and adaptively selects the tap number of the FIR filter to match the strength of the prevailing system noise condition in each subchannel. For the first step, the proposed scheme derives a PR value  $\theta_k$  which seems to contain complete information about the phase noise at each sample by raising the received signal to the  $M$ th-power [4] to remove the data modulation. Next, the PR value  $\theta_k$  is compared to a pre-defined threshold  $\theta_T$  controlled by a thresholding factor  $\beta$ , where  $0 \leq \beta \leq 1$ . If the PR value  $\theta_k$  is equal to or greater than the threshold  $\theta_T$ , a smaller tap number suitable for tracking large phase noise is selected. Conversely, if the PR value is less than the threshold  $\theta_T$ , a large tap number suitable for small phase noise is selected. Mathematically, the scheme can be summarized as:

$$N = \begin{cases} N_s, & \theta_k \geq \beta\theta_T \\ N_l, & \theta_k < \beta\theta_T \end{cases} \quad (1)$$

where the  $N$  is the appropriate selected averaging length and  $\theta_T$  is the maximum possible phase change between signal with and without ASE noise, but can also be the nonlinear threshold. Note that the phase rotation characteristic of the phase noise differs from that of the ASE noise. Because  $\theta_k$  is correlated to the phase noise, performance is expected to improve with adaptive tap selection. Finally, based on the tap number selected, the averaged phase rotation  $\psi$  is derived using the  $M$ th-power CPE as:

$$\psi = \text{PU} \left\{ \frac{1}{M} \arg \left[ \sum_{i=1}^N (y_k)^M \right] \right\} \quad (2)$$

where PU refers to the phase unwrapping function applied. Differential encoding and decoding is employed to deal with the resultant cycle slips.

### 3 Simulation and Results Discussion

A 112-Gb/s coherent optical standard single mode fiber (SSMF) link is simulated with polarization-multiplexed quadrature phase shift keying (PM-QPSK) transmission constellation in VPI to evaluate the performance of the proposed phase noise compensation scheme. At the transmitter, QPSK symbols are generated using MATLAB and modulated by IQ modulator. The fiber link is a recirculating loop made up of identical 80-km spans of an uncompensated SSMF with 0.2 db/km fiber loss, 16 ps/nm km dispersion coefficient, and  $1.22 \text{ W}^{-1} \text{ km}^{-1}$  fiber nonlinearity coefficient. The span loss was compensated by Erbium-doped fiber amplifiers (EDFA) modeled with a gain of 16 dB and noise figure of 4 dB. The ASE noise is added inline to guarantee that the interaction

between signal and noise is acceptably captured. The laser linewidth is either zero when no LPN is considered, or approximately 100 kHz (counting for the sum of both transmit and receive LO laser) when LPN is considered. At the receiver, the signal is demodulated by a standard phase and polarization diversity coherent homodyne optical receiver followed by DSP modules that digitized the received signal and mitigated simultaneously chromatic dispersion and the average fixed phase shift due to SPM using DBP as well as polarization demultiplexing [3]. This is followed by the adaptive CPE proposed here, which is done independently on each of the two polarizations but averaged to estimate the phase noise which stems from same lasers.

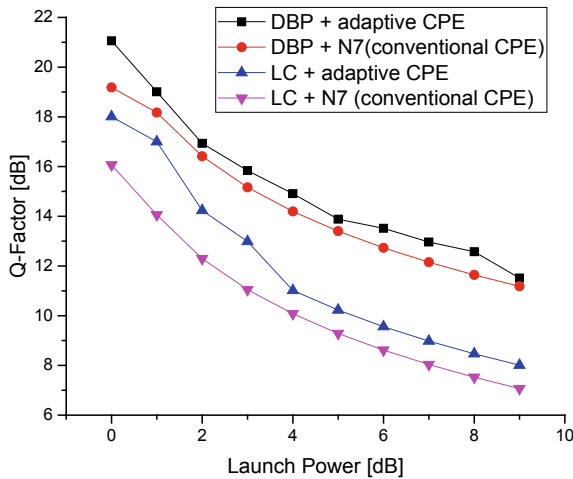


**Fig. 1** Performance analysis after 1200 km fiber transmission. LC: Linear compensation

We study the performance of our adaptive CPE in terms of  $Q$ -factor based on AWGN distribution and phase estimation error as a function of launch power with respect to fiber length. In order to demonstrate the nonlinear noise cancelation effect of CPE methods, the ASE noise was first turned off and on later to exploit the impact of the average length of CPE on system performance and its dependence on  $Q$ -factor as a function of launch power variation in the presence of phase noise with or without ASE noise in optical fiber transmissions. In cases of NLPN only where there is no laser linewidth and requires no CPE in the DSP, yet the NLPN was affected by the CPE. Note that even in the absence of ASE noise, some filtering operation was still necessary to ensure optimal phase tracking. Due to limited space, such results are not presented here. After extensive simulation, the optimum block size was found to be 7 for the convention CPE. We proceed to compare such a scheme with our adaptive CPE scheme with the optimized values  $\beta = 0.8$ ,  $N_s = 3$ , and  $N_l = 15$ . Figure 1 shows the performance analysis of 112 Gb/s PMD-QPSK for the two schemes in terms of  $Q$ -factor as a function of launch power variation in the presence of phase noise with ASE noise. As obvious from Fig. 1, the  $Q$ -factor improvements achieved by our adaptive phase noise estimation scheme over the conventional scheme are roughly about 1 dB, which agrees with our prediction.

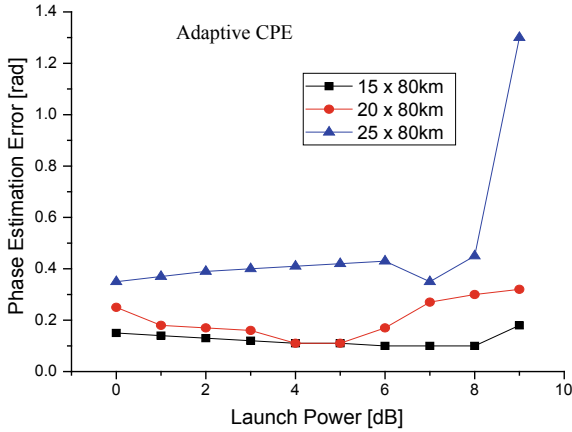


**Fig. 2** Phase estimation error as a function of launch power for various fiber transmission lengths

The performance of our adaptive filter is further assessed in terms of phase estimation error  $\Delta\varphi_k$ , defined as the absolute maximum difference between the original and estimated phase noise in [4] as:

$$\Delta\varphi_k = \theta_k - \psi \tag{3}$$

Figure 2 shows the result of such an assessment of the phase estimation error as a function of launch power for various fiber spans. For different fiber transmission lengths, the scheme shows similar performance no matter the value of the launch power, even though there are fluctuations. The dependency of the optimal average length dynamics on the phase of each sample may be responsible for these fluctuations. Furthermore, we compared our blockwise averaging method with the sliding (moving) average method defined as [2]:

$$\psi = \text{PU} \left\{ \frac{1}{M} \arg \left[ \sum_{i=-N}^N (y_k)^M \right] \right\} \tag{4}$$

The result as indicated in Fig. 3 shows that the sliding method achieves better performance than the blockwise method because it uses both past and future symbols to estimate the carrier phase and the phase thus estimated is taken as the phase for the central symbol. In the blockwise method, since all the symbols within the block share same phase estimate, it is likely that symbols at the edges of the block may differ in phases from the central symbol in reality.

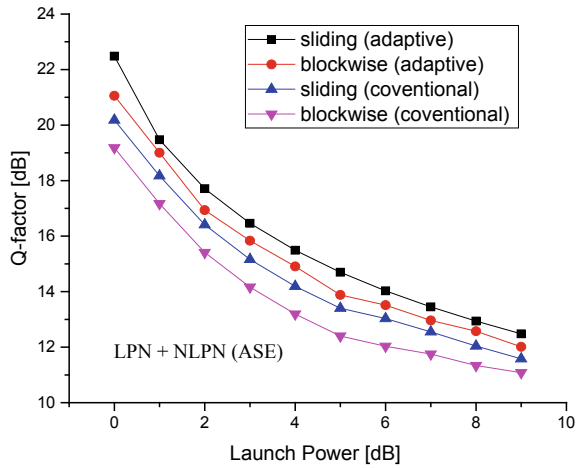


Fig. 3 Blockwise versus sliding averaging methods

## 4 Conclusion

Compared with the conventional optimal fixed-tap filter scheme, performance of the proposed adaptive scheme is superior since it adaptively selects an adequate number of FIR filters according to the strength of the phase noise as measured in phase estimating circuits. In addition, the proposed adaptive scheme recognizes and excludes symbols with significantly large noise during the phase estimation process. It can be concluded that the proposed scheme offers superior performance for high-rate coherent optical fiber transmission systems even though the complexity of its additional hardware is quite simple.


**Acknowledgements.** This work is supported by the National Natural Science Foundation of China (#61471088).

## References

1. Agrell, E.: Roadmap of optical communications. *J. Opt.* **18**(6), 1–40 (2016)
2. Deynu, F.: Adaptive phase estimation in the presence of nonlinear phase noise for carrier phase recovery of PM-QPSK Signals in Coherent Optical Receivers, submitted to ICOM (2018)
3. Lin, C., Asif, R.: Nonlinear mitigation using carrier phase estimation and digital backward propagation in coherent QAM transmission. *Opt. Express* **20**(26), B405–B412 (2012)
4. Goldfarb, G., Li G.: BER estimation of QPSK homodyne detection with carrier phase estimation using digital signal processing. *Opt. Express* **14**(18), 8043–8053 (2006)



# Preparation and Application of Semiconductor Fluorescent Probe

Xin Wang , Jiaqi Chen, Jie Huang, Yuxue Feng, Zhenhuan Gu,  
and Zugang Liu

China Jiliang University, Hangzhou 310018, China  
xwcjlu@163.com

**Abstract.** This paper describes the investigation of surface modified CdTe/ZnS nanoparticle as a sensing receptor for Hg<sup>2+</sup> ion detection by optical approach. Glutathione-modified CdTe/ZnS nanoparticles were used as a fluorescence sensor for Hg ion which involved in the fluorescence quenching. The experiment results show that fluorescence intensity is the highest when the mol ratio of CdTe and ZnS is 1:2 in nanoparticle structure, and the fluorescence intensity of nanoparticle depends linearly on mercury ion concentration, and the correlation coefficient  $R = 0.9823$ , and simulation error less than four percent. This technique demonstrated an effective detection of mercury in aquatic environment.

**Keywords:** Cd/ZnS nanoparticle · Glutathione modification · Hg ion

## 1 Introduction

Semiconductor materials are widely used in telecommunications, industrial manufacturing, and aerospace field. Currently, the range of semiconductor materials and their application are widely extended. The semiconductor materials can be used in energy, display, medical, and biological fields [1–3]. Among them, semiconductor fluorescent probe is the one that is most widely used in medical field. The fluorescence material has wide excitation spectrum and good light stability and is used to detect heavy metal ions [4–6]. Functionalized modification is needed for the detection of different heavy metal ions, and different nanoparticle shall be modified according to different characteristics of heavy metal ion. CdSe and CdTe, which can be used to detect heavy metal ions by looking the change in the emission spectra of the nanoparticle in the UV-visible range, have received special attention [7–9]. In 2002, Yongfen Chen et al. [10] established a new method for detecting Cu<sup>2+</sup> and Zn<sup>2+</sup> with functionalized nanoparticles. In 2014, LiMi Zhu [11] successfully synthesizes L-cysteine/mercaptopropionic acid-modified CdTe nanoparticle with high quantum yield, good fluorescence stability, and good biocompatibility. However, the preparation of functionally modified nanoparticle still either requires nitrogen protection, or requires higher temperatures, or requires special treatment, and the preparation process is still complicated. This paper uses ultrasonic chemical reaction to synthesize CdTe/ZnS nanoparticles and uses glutathione to modify the nanoparticles to detect Hg ions, which is convenient to prepare and may provide new direction for Hg ion detection research.

## 2 Experiment

### 2.1 Reagents

Sodium tellurite (99.99%), hydrazine hydrate (>98.0%), mercaptoacetic acid (99.0%), were used as received zinc sulfate, white vitriol, sodium sulfide, glutathione, phosphate buffer, mercury (GSB 04-1729-2004) were of analytical grade.

### 2.2 Apparatus

The structures of these samples were analyzed with an X-ray diffraction (XRD) (BRUKER-AXS), and UV-VIS spectroscopy was measured with UV-vis spectrophotometer (Hitachi, F2700).

### 2.3 Experimental Steps

The CdTe nanoparticles were synthesized by ultrasonic chemistry [12], reacting  $\text{Na}_2\text{TeO}_3$  with  $\text{CdCl}_2$  solution with hydrazine hydrate as a reducing agent.

**Synthesis of CdTe/ZnS Compounds**  $\text{Na}_2\text{TeO}_3$  was added to the  $\text{CdCl}_2$  solution and 6 mL of hydrazine hydrate until the pH of 10.5 and then ultrasonically reacted for two hours. Then, mix the above CdTe solution with ZnS solution on the ratio of CdTe: ZnS at 2:1 to 1:4 and ultrasonically oscillate for two hours.

**Preparation of Glutathione-Modified CdTe/ZnS Nanoparticles** The synthesized CdTe/ZnS nanoparticles were dissolved in the PB buffer solution, and then different amounts of glutathione (reducing) were added and oscillated for two hours, and the surface modification was completed by self-assembly.

**Hg<sup>2+</sup> Solution Preparation and Concentration Test** Use the national standard sample (GSB 04-1729-2004), to prepare different concentrations of  $\text{Hg}^{2+}$  solution. Then, a mixed solution of CdTe/ZnS quantum dots and glutathione is dissolved in PB buffer solution, and different concentrations  $\text{Hg}^{2+}$  solution is added, mechanically stir for one minute, and let stand for 10–30 min before test. The CdTe/ZnS core-shell quantum dot fluorescence quenching is caused by the absorption of  $\text{Hg}^{2+}$  on glutathione. The quench at peak intensity of fluorescence is used to establish the relationship between the  $\text{Hg}^{2+}$  concentration and the fluorescence intensity.

## 3 Results and Discussion

The XRD pattern shown in Fig. 1a shows that the phase of the material is CdTe (JPCDS No. 43-712), and its three strong peaks are  $23.763^\circ$ ,  $39.293^\circ$ , and  $46.438^\circ$ , correspond crystal plane to (111), (220), and (311), and the crystal purity is high, and the particle size of the sample can be calculated to be about 10 nm according to the half-height Scherrer formula of the diffraction peak corresponding to the (111) plane.

The XRD pattern shown in Fig. 1b indicates that the phases of the synthesized substance are CdTe (JPCDS No. 43-712) and ZnS (JPCDS No. 60-378). The peak



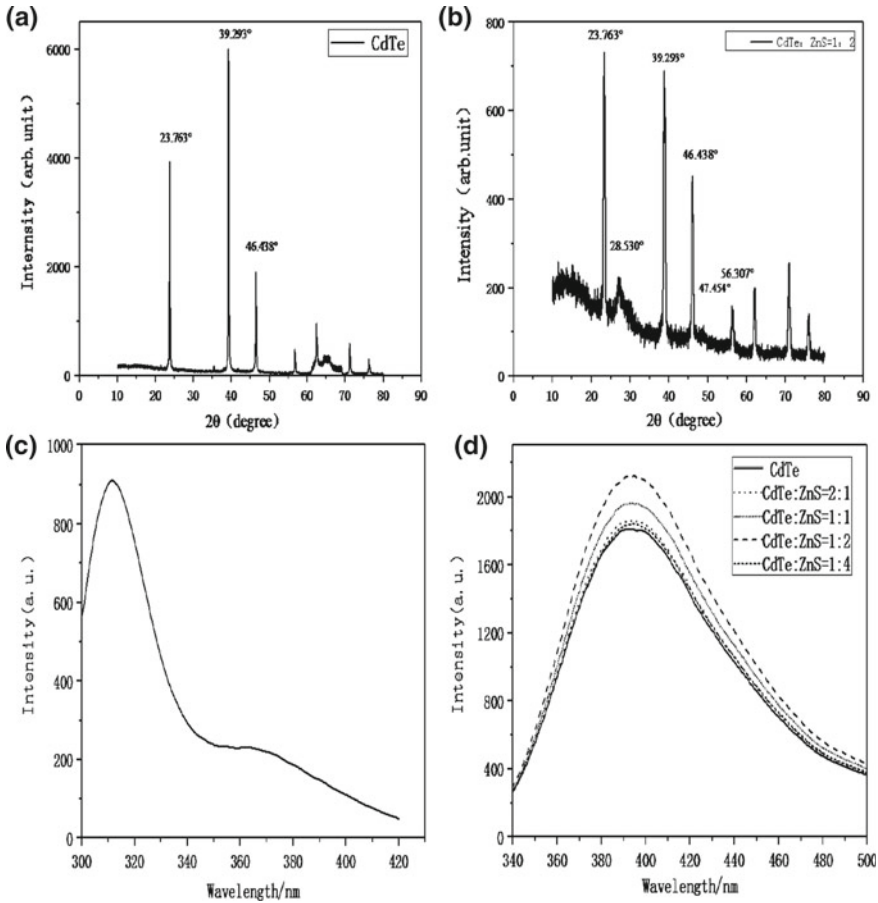


**Fig. 1** **a** XRD pattern of CdTe sample, **b** CdTe/ZnS nanoparticles XRD pattern with CdTe: ZnS molar ratio of 1:2, **c** excitation spectra of CdTe/ZnS nanoparticles, **d** emission spectra of CdTe/ZnS nanoparticles (CdTe: ZnS = 2:1, 1:1, 1:2, 1:4)

indicated by the black dot is the diffraction peak belonging to ZnS, and the three strong peaks are 28.530°, 47.454°, and 56.307°, correspond crystal plane to (111), (220), and (311); the peak indicated by the white dot is the diffraction peak belonging to CdTe, and the three strong peaks are 23.763°, 39.293°, and 46.438°, correspond crystal plane to (111), (220), and (311). According to the three strong peaks, it can be judged that the crystal purity of the CdTe/ZnS core-shell nanocrystalline is high, and the particle size of the sample can be calculated to be about 10 nm according to the half-height Scherrer formula of the diffraction peak.

From Fig. 1c, d, we can see the excitation spectrum and the emission spectra at different CdTe: ZnS ratio. When the CdTe/ZnS nanocrystalline with the CdTe: ZnS molar ratio at 1:2, it has the strongest fluorescence intensity.

From Fig. 2a, when the CdTe nanocrystalline is 1:1 with the modified glutathione, the fluorescence intensity is the strongest, which can be used as the best ratio for the detection of heavy metals.

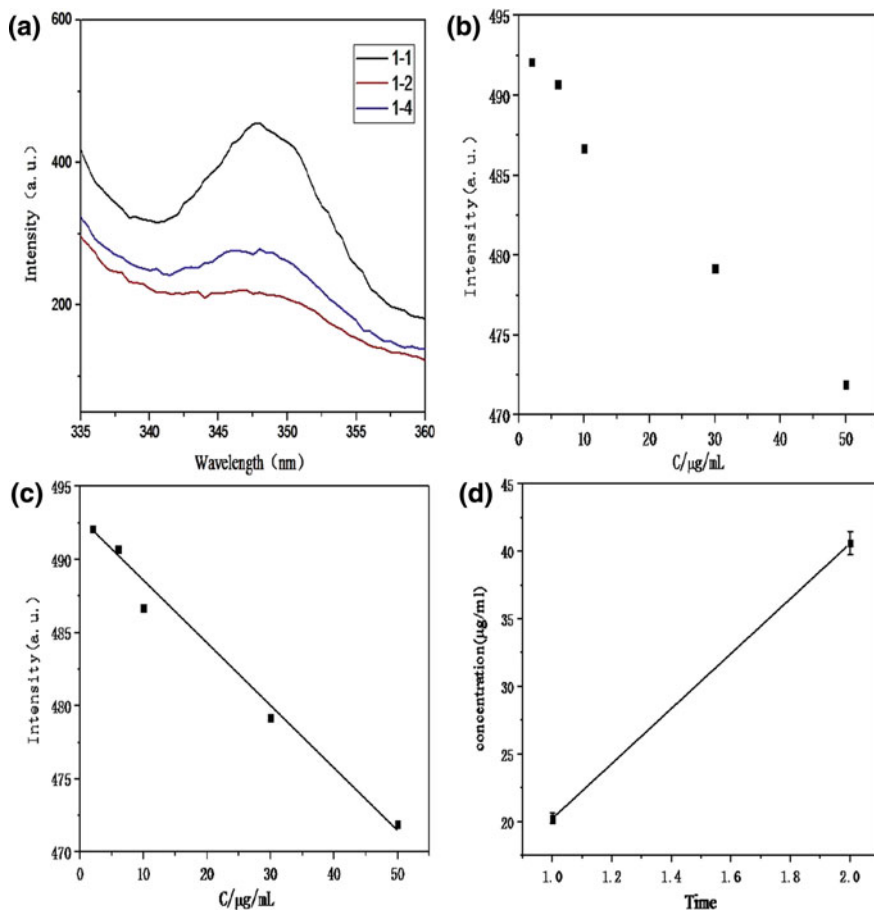


**Fig. 2** a Fluorescence characteristic curve of CdTe nanoparticles modified with different proportions of glutathione, b relationship between  $Hg^{2+}$  concentration and fluorescence quenching intensity, c a fitted graph, d  $Hg^{2+}$  concentration test error diagram

According to Fig. 2b, c, it can be seen that the  $Hg^{2+}$  concentration has a good linear relationship with the fluorescence intensity of the CdTe/ZnS nanoparticles, and the equation is established by a one-way linear regression fit:

$$I = 492.32 - 0.42 C \quad (1)$$

Here,  $I$  is the fluorescence intensity, and  $C$  is the  $Hg^{2+}$  concentration. The linear correlation coefficient  $R$ -square factor is 0.9823, indicates that  $I$  and  $C$  have high

linearity. In order to verify the accuracy of the model, the same measuring procedure was used to test the fluorescence intensity, and the concentration value was calculated by formula (1), and the relative error was calculated. From Fig. 2d, the calculated measurement model and the actual concentration of the  $\text{Hg}^{2+}$  concentration formulation relative error is less than 4%, indicating that the test model having a high degree of accuracy.

## 4 Conclusion

In this paper, CdTe/ZnS was prepared by ultrasonically chemical reaction, and CdTe/ZnS nanoparticles were modified with glutathione to detect heavy metal  $\text{Hg}^{2+}$  concentration. The experimental results show that the best CdTe to ZnS ratio as 1:2 and 1:1 as best glutathione to CdTe/ZnS quantum dots ratio for achieving the best fluorescence characteristics and the strongest fluorescence intensity. The linear relationship between the  $\text{Hg}^{2+}$  concentration and the fluorescence intensity of CdTe/ZnS nanoparticles is found with experimental results. It shows that the  $\text{Hg}^{2+}$  concentration can be effectively detected with this method in biotic environment.

## References

1. Del, S.S., Leonardo, A., Ezio, C., Maria, M.A., Andrea, Z., Pietro, U.: Progress in the development of CdTe and CdZnTe semiconductor radiation detectors for astrophysical and medical applications. *Sensors* **9**, 3491–3526 (2009)
2. Barbas, M.J., Schultko, J.B.: Semiconductor nanocrystals as fluorescent biological labels. *Science* **281**, 2013–2016 (1998)
3. Yang, R.H., Zhang, Y., Li, K.A., Liu, F., Chan, W.H.: Fluorescent ratioable recognition of  $\text{Cu}^{2+}$  in water using a pyrene-attached macrocycle/ $\gamma$ -cyclodextrin complex. *Anal. Chim. Acta* **525**, 97–103 (2004)
4. Chen, D., Ray, A.K.: Removal of toxic metal ions from wastewater by semiconductor photocatalysis. *Chem. Eng. Sci.* **56**, 1561–1570 (2001)
5. Chan, W.C.W., Maxwell, D.J., Gao, X., Bailey, R.E., Han, M., Nie, S.: Luminescent QDs for multiplexed biological detection and imaging. *Curr. Opin. Biotechnol.* **13**, 40–46 (2002)
6. Wu, C.S., Khaing, M.K., Fan, X.: Highly sensitive multiplexed heavy metal detection using quantum-dot-labeled DNazymes. *ACS Nano* **4**, 5897–5904 (2010)
7. Weiss, S., Alivisatos, A.P.: Semiconductor nanocrystals as fluorescent biological labels. (fluorescent probes in biological experiments). *Science* **281**, 2013–2016 (1998)
8. Chan, W.C.W., Nie, S.: Quantum dot bioconjugates for ultrasensitive nonisotopic detection. *Science* **281**, 2016–2018 (1998)
9. Zhu, L.M., Ding, Z.Q., Nie, H.L.: Preparation of L-cysteine/ mercapto propion ic acid modified CdTe quantum dots, CN (2014)
10. Dabbousi, B., Rodriguez-Viejo, J.: (CdSe)ZnS Core-Shell Quantum Dots: Synthesis and Characterization of a Size Series of Highly Luminescent Nanocrystallites, ASC Publication, 1997
11. Liu, Y., Zhou, J.G., Shen, Q.H., Yu, D.D., Jin, L., Fan, H.L.: Ultrasonic wave-assisted synthesis of CdTe semiconductor nanocrystals in water applied to biolabel of microorganism. *Chem. J. Chin. Univ.* **29**, 1166–1170 (2008)

12. He, Y., Sai, L.M., Lu, H.T., Hu, M., Lai, W.Y., Fan, Q.L.: Microwave-assisted synthesis of water-dispersed CdTe nanocrystals with high luminescent efficiency and narrow size distribution. *Chem. Inform.* **38**, 359–365 (2007)



# Online Monitoring Study for SF<sub>6</sub> Composition by Optical Cavity Sensing Technology in High-Voltage GIS

Shiling Zhang<sup>1(✉)</sup>, Qiang Yao<sup>1</sup>, and Meng Jiang<sup>2</sup>

<sup>1</sup> State Grid Chongqing Electric Power Company Electric Power Research Institute, Chongqing, China  
526793305@qq.com

<sup>2</sup> Beijing Optical Fiber Sensing System Engineering Technology Research Center, Beijing Institute of Aerospace Control Devices, Beijing, China

**Abstract.** The schematic diagram of optical cavity design has been introduced in detail; meanwhile, the principle of measuring the gas concentration with optical resonator is also introduced. The pressure distribution and the velocity distribution of the optical cavity have been simulated by finite element method. Finally, the field performance of the optical cavity has been tested. Using the optical cavity spectroscopy technology, the gas component detection system is set up to realize high precision online monitoring of gas components such as CO, H<sub>2</sub>S and HF. The detection system uses narrow line-width semiconductor laser to select the characteristic gas spectrum and output the absorption peak wavelength. Three kinds of gas concentration are measured by time division multiplexing, and the online sampling device of closed loop gas is integrated to complete the monitoring platform of high precision. The paper has developed the SF<sub>6</sub> composition monitoring device based on optical attenuation technology, which provides the new research method for the online monitoring of gas components such as CO, H<sub>2</sub>S and HF with the high accuracy of 3 ppm.

**Keywords:** Optical cavity design · Online monitoring · Characteristic gas spectrum

## 1 Introduction

SF<sub>6</sub> gas as excellent insulation and arcing medium has been widely applied in the SF<sub>6</sub> gas insulated circuit breakers, the gas insulated combination electric appliance, such as GIS, transformers, transformer, and power cable [1]. Electrical equipment in the process of running in the high-voltage electric arc or energetic factor will happen under the action of SF<sub>6</sub> gas decomposition, producing hydrogen fluoride (HF), sulfur dioxide (SO<sub>2</sub>), hydrogen sulfide (H<sub>2</sub>S), carbon monoxide (CO) and other compounds. With HF as important the decomposition product of the first, in the high-voltage equipment of HF gas detection is very important, but because of its chemical properties and lively, strong physical adsorption, offline detection means is difficult to detect [2, 3].

In this paper, the schematic diagram of the optical cavity design has been introduced in detail; meanwhile, the principle of measuring the gas concentration with

optical resonator is also introduced. The pressure distribution and the velocity distribution of the optical cavity have been simulated by finite element method. Finally, the field performance of the optical cavity has been tested. Using the optical cavity spectroscopy technology, the gas component detection system is set up to realize high precision online monitoring of gas components such as CO, H<sub>2</sub>S and HF. The detection system uses narrow line-width semiconductor laser to select the characteristic gas spectrum and output the absorption peak wavelength. Three kinds of gas concentration are measured by time division multiplexing, and the online sampling device of closed loop gas is integrated to complete the monitoring platform of high precision. The paper has developed the SF<sub>6</sub> composition monitoring device based on optical attenuation technology, which provides the new research method for the online monitoring of gas components such as CO, H<sub>2</sub>S and HF with high accuracy.

## 2 Technical Principle

HF, CO and H<sub>2</sub>S are three typical fault gases in SF<sub>6</sub> insulated equipment. These gases have rich absorption spectrum in the infrared band, take into account the reasons for the price and absorption of the laser, the common absorption lines are selected [4]. The optical cavity is the main body of laser, in order to meet the measurement of HF, CO and H<sub>2</sub>S gas, and the absorption spectra of the three gases are 1568, 1578 and 1305 nm, respectively. The high reflectivity film system is 1300–1600 nm. When the cavity length is 0.4 m, and the absorption time is 80 ns, the detection accuracy is  $0.3 \times 10^{-6}$ . The reflector is strictly fixed on the stable device, the average optical input of the cavity is reflected thousands of times in the fluid tube through a mirror, and the light output through another mirror is accepted by the photo-multiplier tube (Fig. 1).

After the reflection, the light intensity will be weakened by the transmission of the mirror in the cavity. By measuring the gradual decreasing of the optical pulse ring, the relationship between the pulse intensity of the cavity and the time can be obtained. The reflectivity of the cavity lens *M1* and *M2* is *R1* and *R2*, respectively. The initial energy

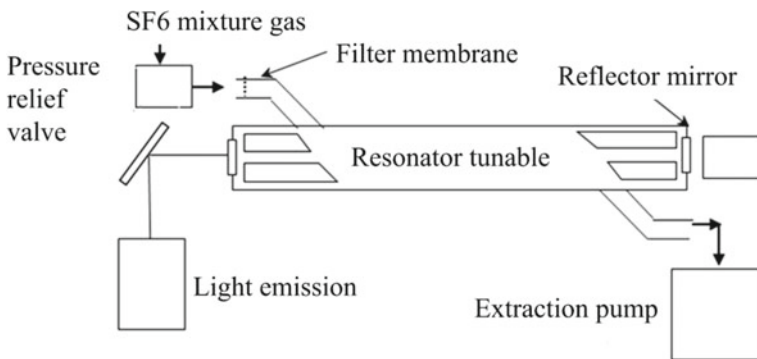


**Fig. 1** Schematic diagram of the optical cavity design

of the optical pulse in the coupled ring down cavity is  $I_0$  and the center wavelength is  $\lambda$ . The intensity of optical pulse at the time of  $t$  can be expressed as:

$$I(t, \lambda) = I_0 \exp[-\tau(\lambda)/t] \quad (1)$$

The oscillation time is determined by the reflectivity  $R_1$  and  $R_2$  of the two mirrors. The mathematical expression of  $\tau$  is:

$$\tau(\lambda) = \frac{t_r}{\ln(R_1 R_2)^{-1}} \quad (2)$$

$t_r = 2L/c$  is the time required to express in the light cavity, and  $c$  is the light speed,  $L$  is the length of the resonator. Assuming that the absorption coefficient of the cavity sample is  $\alpha$ , the formula (1) can also be expressed as:

$$I = I_0(1 - R^2) \exp(-\alpha L) \quad (3)$$

The intensity of light attenuates exponentially with time, that:

$$\tau = nL/[c(1 - R + \alpha L)] \quad (4)$$

When there is no gas or liquid in the cavity,  $\tau_0$  also can be expressed as:

$$\tau = nL/[c(1 - R)] \quad (5)$$

The change of the decay time before and after the absorption sample was detected:

$$\alpha = (n/c) \cdot \left( \frac{1}{\tau} - \frac{1}{\tau_0} \right) \quad (6)$$

Equation (6) shows that the numerical change of the intensity of the pulse light source does not have direct effect on the sensing measurement, but the stability of the cavity will limit the calculation accuracy of the absorption coefficient. And the gas concentration  $N$  is:

$$N = \frac{1}{c\sigma(v)} \left[ \frac{1}{\tau(v)} - \frac{1}{\tau_0} \right] \quad (7)$$

From (7), the gas concentration  $N$  can be calculated.

### 3 Design of the Optical Cavity

The system can not only meet the testing requirements of high pressure in SF6 gas insulated electrical equipment, but also meet requirement of circulating gas detection. The configuration of the device design is shown in Fig. 2. In order to better display the internal condition of the device, a section of the device is shown in Fig. 3. The optical

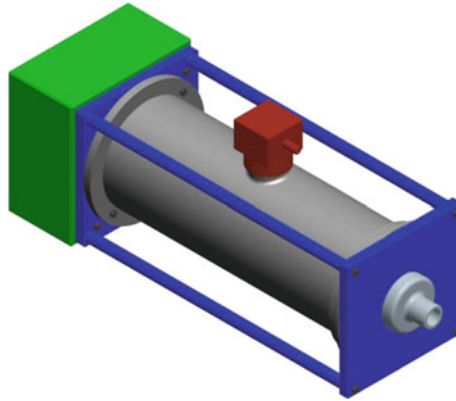


**Fig. 2** Configuration of the device design

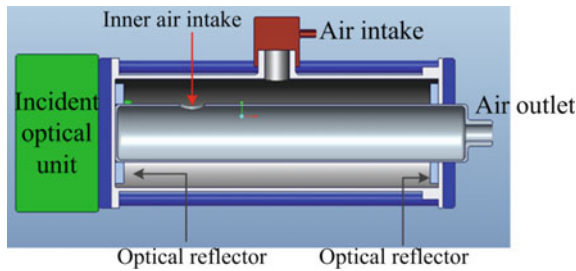


**Fig. 3** Section of the device

cavity is divided into the internal and external two layers, the blue part is the reinforcement of the structure parts, gas enters through the upper air inlet into the interior of the absorption chamber, light incident into the gas chamber, multiple laser oscillations are formed on both sides by optical mirrors [5]. In order to maintain the stability of the internal airflow, increase inner air intake. The optical reflection diagram of the optical cavity is shown in Fig. 4.



**Fig. 4** Optical reflection diagram of the optical cavity



Figure 4 shows that the use of reflectors at the end of photo-acoustic cell can increase the absorption optical path, to improve the detection sensitivity of the system, the photo-acoustic pool is required to work in resonant mode [6, 7]. The modulation frequency  $f$  of chopper is equal to the resonant frequency  $f_0$  of photo-acoustic cell. At 25 °C, propagation speed of sound wave in SF6 gas is about 135.4 m/s; therefore, the theoretical value of one-dimensional resonant frequency of photo-acoustic cell designed is 1120 Hz, the frequency response curve is shown in Fig. 5, shown that the maximum peak value is around 1050 Hz, which is close to the designed value 1120 Hz.

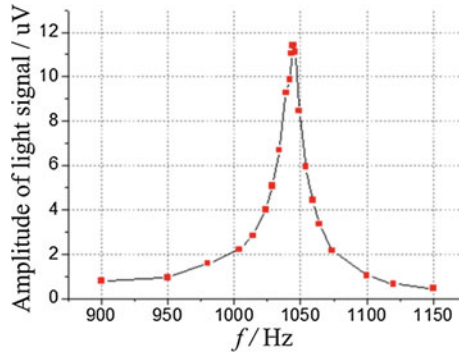


Fig. 5 Frequency response curve

#### 4 Simulation of Optical Cavity with FEM

The SF6 gas pressure in the GIS is always 0.4–0.6 MPa, so set the air intake 0.1–0.5 MPa, and in the outlet pump with the vacuum, so the pressure is 0.05 MPa. The finite element model (FEM) of the gas chamber structure is shown in Fig. 6.

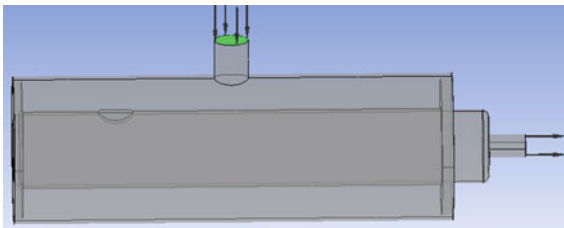
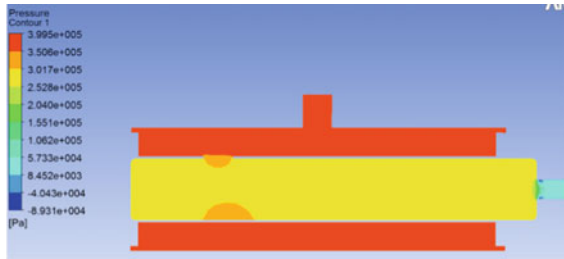


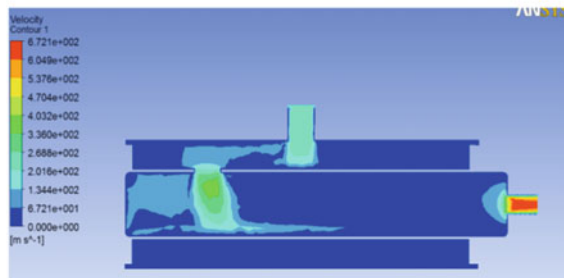
Fig. 6 FEM model of the gas chamber

The upper part is an air inlet, and the mirror is fixed on both sides of the air chamber. In the middle is the outlet pipe, in order to stabilize the airflow, there is a hole in the middle of the outlet pipe, and the right side is the air outlet. Take the inlet pressure as 0.4 MPa for an example, the simulation results are shown in Fig. 7.

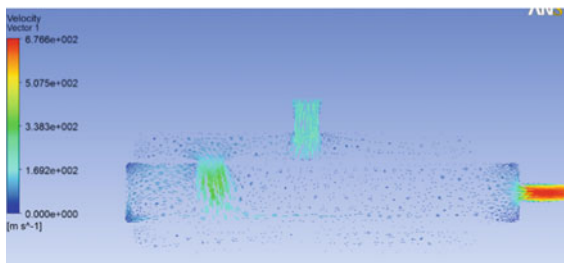
Figure 7a indicates that the whole chamber is uniform, and the maximum pressure is the outermost chamber shell. The inlet area of the internal outlet is orange and the pressure is larger. In other area, due to the larger size of the chamber, the force is uniform. Figure 7b indicates the gas velocity vector diagram, and the direction and trend of gas flow can be seen. It can be seen that the structure design of the gas absorption chamber can basically meet the requirement of the GIS gas pressure. The force is uniform, and the flow and pressure values are reasonable.



(a) Pressure distribution



(b) Velocity distribution



(c) Velocity vector graph

**Fig. 7** FEM model of the gas chamber

### 5 Hardware and Software Design of Optical Cavity

The design of laser cavity spectroscopy detection system for three gases of H<sub>2</sub>S, CO and HF is shown in Fig. 8. Three different laser output wavelengths for three kinds of gas absorption peaks to be measured. The light emitted by the laser is modulated by the modulation signal generated by the signal generator into the beam closing device. The beam closing device combines the multi-wavelength light into a sound light modulator, then enters the high reflectivity cavity through the collimator, and outputs the switch through the detector [8, 9]. By switching the time division of the switch channel, the AD converter is converted into a digital signal and enters the micro-control unit, and the inversion of the concentration is realized by compiling the algorithm. Data output to the human-machine interaction interface, to achieve three kinds of different gas concentration display, switch machine and online self-calibration process control. The index of laser selection is center wavelength at 1305, 1568 and 1578 nm, respectively. The LIV characteristics curve is tested, and the test results are shown in Fig. 9.

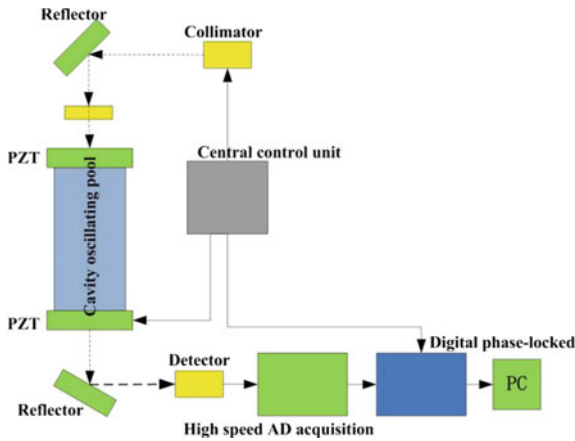


Fig. 8 Technical scheme for detecting content of dissolved gas

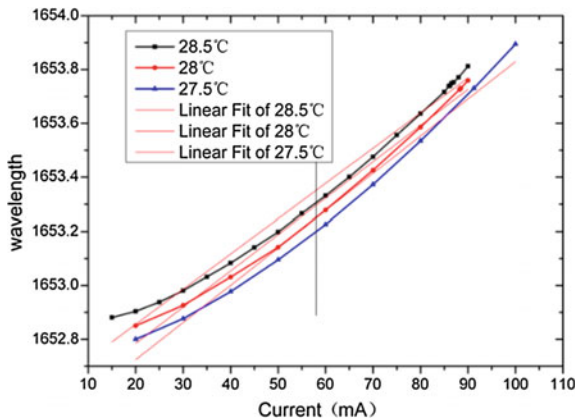


Fig. 9 The LIV curves of the laser

At the different temperatures, the wavelength varies with the current drift coefficient, linear fitting is used and approximate equation is:

$$\lambda = 0.101 * T + 1652.888 \quad (8)$$

At 25 °C, the standard thermistor value is  $10 \pm 0.5 \text{ k}\Omega$ , and negative temperature coefficient is  $-4.4\%/^{\circ}\text{C}$ , the relationship between the thermistor  $R$  and the absolute temperature  $T$  is  $R = 10,000 * \exp(-4400 * (1/298.15 - 1/T))$ . According to the laser performance test curve in Fig. 9, the laser driving current and operating point temperature can be determined.

## 6 Field Testing Results of Optical Cavity

Plunge certain amount of N<sub>2</sub> into the device, it should change around 0 ppm, Fig. 10 is the baseline change of 30 min at 20 °C.

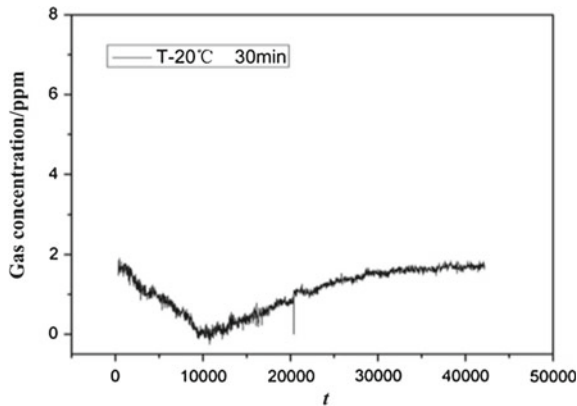


**Fig. 10** Baseline change curve at  $T = 20 \text{ }^{\circ}\text{C}$

It can be seen that the baseline fluctuation is at 0–2 ppm, which satisfies the accuracy of 3 ppm, the 3 ppm H<sub>2</sub>S, CO and HF gas can be distinguished because of the baseline fluctuation. From 20 to 0 °C, the baseline variation curve can be seen from Fig. 11, the baseline fluctuation is 3.5 ppm at 0 °C, which can not meet detection accuracy of 3 ppm.

To improve the detection accuracy of system, it is necessary to improve the weak signal detection ability of the system. The modulated signal is loaded into the laser to obtain the modulated wavelength output, and optical signal is converted into electrical signal. The signal enters the FPGA through AD to carry out the digital phase-locked calculation. The overall structure of the circuit board is shown in Fig. 12.

Figure 12 shows that under different temperature conditions, the optical circuit for gas detection has high accuracy.

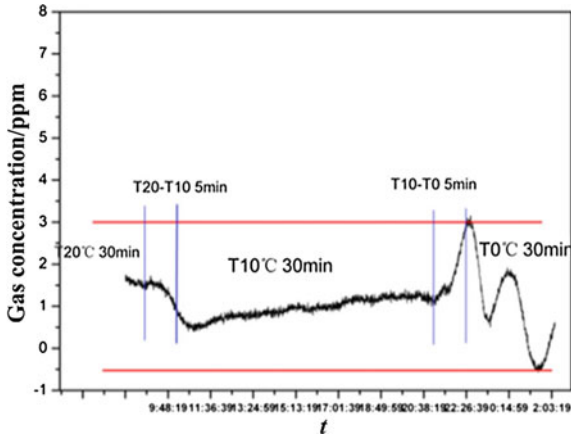


Fig. 11 Baseline change curve of 0–20 °C

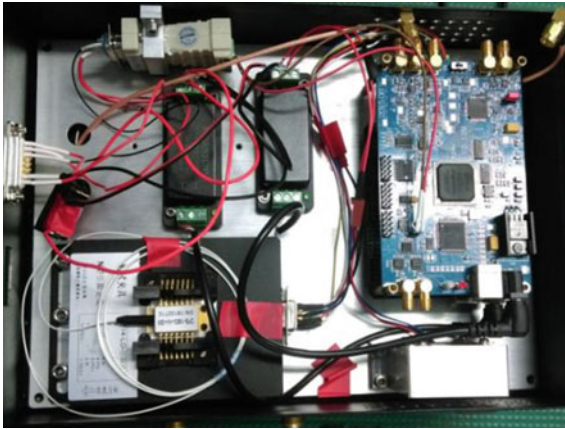


Fig. 12 Optical circuit for gas detection

## 7 Conclusion

The optical cavity is the main body of laser, in order to meet the measurement of HF, CO and H<sub>2</sub>S gas, and the absorption spectra of the three gases are 1568, 1578 and 1305 nm, respectively. Structure design of the gas absorption chamber can basically meet the requirement of the GIS gas pressure. The force is uniform, and the flow and pressure values are reasonable. The relationship between the thermistor  $R$  and the absolute temperature  $T$  is  $R = 10,000 \cdot \exp(-4400 \cdot (1/298.15 - 1/T))$ . According to the laser performance test curve, the laser driving current and operating point temperature can be determined. Moreover, the signal enters the FPGA through AD to carry out the digital phase-locked calculation which can realize the gas detection with high accuracy.

**Acknowledgements.** The paper is supported by the technology project of Chongqing Research Program of fundamental science and Advanced Technology (cstc2018jcyjAX0486); Science and Technology Project of Chongqing Power Company (2018 Science and Technology Project of Chongqing Power Company 4#).

## References

1. Qi, R.B., He, S.K., Li, X.T., Wang, X.Z.: Simulation of TDLAS direct absorption based on HITRAN database. *Spectrosc. Spectral Anal.* **35**, 172–177 (2015)
2. Hosokawa, M., Okumura, K., Yamagiwa, T.: Dielectric performance of improved gas insulated bushing for UHV GIS. *IEEE Trans. Power Delivery* **2**(2), 359–366 (1987)
3. Li, Y., Zhang, X.X., Xiao, S., Chen, Q.: Decomposition properties of C<sub>4</sub>F<sub>7</sub>N/N<sub>2</sub> gas mixture: An environmentally friendly gas to replace SF<sub>6</sub>. *Ind. Eng. Chem. Res.* **57**, 5173–5182 (2018)
4. Zhang, Z.R., Dong, F.Z., Wu, B.: In-situ measurement of HF gas industrial situation based on TDLAS technology. *J. Optoelectron. Laser* **22**, 1691–1694 (2011)
5. Yao, Q., Yuan, Z.R., Li, X.T.: Using TDLAS technology to detect HF gas in SF<sub>6</sub> high-voltage switches. *Instrum Technique Sens.* **5**, 70–73 (2013)
6. Wu, Y., Wang, C.L., Sun, H., Murphy, A.B.: Properties of C<sub>4</sub>F<sub>7</sub>N–CO<sub>2</sub> thermal plasmas: thermodynamic properties, transport coefficients and emission coefficients. *J. Phys. D: Appl. Phys.* (2018)
7. Kieffel, Y., Biquez, F.: SF<sub>6</sub> alternative development for high voltage switchgears. In: *Electrical Insulation Conference*, pp. 379–383. IEEE (2015)
8. Gugat, J.L., Krantz, M.C., Gerken, M.: Two-dimensional versus three-dimensional finite-element method simulations of cantilever magnetoelectric sensors. *IEEE Tran. Magn.* **49**(10), 5287–5293 (2013)
9. Luo, X.Q., Hu, W., Xu, T.: Air gap flashover characteristics and selection of gap distance for ± 1100 kV DC U-shaped wall bushing. *High Voltage Eng.* **43**, 946–952 (2017)